Graz University of Technology

Doctoral Thesis

Calibration of elemental and isotope proxies by inorganic precipitation experiments

Author:
Anja Füger

A thesis submitted in order to obtain the doctoral degree of natural sciences
-Doctor rerum naturalium-
(Dr. rer. nat.)
at the
Graz University of Technology
Institute of Applied Geosciences

Graz, May 2019

Primary Supervisor
Dr. Vasileios Mavromatis
Graz University of Technology
Institute of Applied Geosciences
Rechbauerstraße 12
8010 Graz
Austria

Supervisor & Examiner
Dipl. Chem. Dr. Albrecht Leis
JR-AquaConSol GmbH
Steyrergasse 21
8010 Graz
Austria

Supervisor & Primary Reviewer
Univ.-Prof. Dr. Martin Dietzel
Graz University of Technology
Institute of Applied Geosciences
Rechbauerstraße 12
8010 Graz
Austria

Secondary Reviewer
Prof. Dr. habil. Michael E. Böttcher
Leibniz-Institute for Baltic Sea Research
Seestraße 15
18119 Warnemünde
Germany

Statutory Declaration

I, Anja Füger, declare that I have authored this thesis independently, that I have not used other than the declared sources / resources, and that I have explicitly marked all material which has been quoted either literally or by content from the used sources. The text document uploaded to TUGRAZonline is identical to the printed version.

Graz, ____________________________ ____________________________
Date Signature

Eidesstattliche Erklärung

Ich, Anja Füger, erkläre an Eides statt, dass ich die vorliegende Arbeit selbstständig verfasst, andere als die angegebenen Quellen / Hilfsmittel nicht benutzt, und die den benutzten Quellen wörtlich und inhaltlich entnommene Stellen als solche kenntlich gemacht habe. Das in TUGRAZonline hochgeladene Textdokument ist mit der gedruckten Dissertation identisch.

Graz, ____________________________ ____________________________
Datum Unterschrift

„Ein Gelehrter in seinem Laboratorium
ist nicht nur ein Techniker;
er steht auch vor den Naturgesetzen
wie ein Kind vor der Märchenwelt.“

Marie Curie

Abstract

The chemical composition of seawater is an essential tool in providing information about land-ocean distribution, the chemical evolution of the composition of seawater and the Earth`s atmosphere as well as long-term climate change at all geological time scales. Therefore, geological archives such as marine skeletal carbonates (e.g. brachiopods), which preserve the chemical composition of the ancient seawater, are routinely analyzed for elemental and isotope concentration and distribution. The interpretation of elemental and isotope signals in natural carbonate minerals requires a detailed understanding of the controlling mechanism related to their distribution during carbonate mineral formation. Conducting precipitation experiments is an essential tool in order to unravel the formation conditions in natural surroundings. This project includes new elemental and isotopic data from inorganic carbonate mineral precipitates, which are formed using advanced experimental approaches, in order to develop and adjust new proxies e.g. for the reconstruction of the ambient water composition during carbonate mineral formation.

The first part of this PhD thesis involves traditional stable oxygen isotope data ($\delta^{18}O$) of smithsonite, a secondary zinc carbonate, as a function of formation time and temperature. The observed temporal evolution of the oxygen isotope fractionation between smithsonite and water ($10^3\ln\alpha_{smithsonite\text{-}water} \approx \Delta^{18}O_{smithsonite\text{-}water} = \delta^{18}O_{smithsonite} - \delta^{18}O_{water}$) indicates isotopic equilibrium was achieved after 7 days of reaction time. At isotopic equilibrium, the oxygen isotope fractionation is decreasing with increasing temperature ($25 \leq T \leq 80$ °C). This trend fits within (i) the range of theoretical calculations; and (ii) the sequence of various trigonal Me-carbonates, i.e. smaller cation radii yield in higher $10^3\ln\alpha_{carbonate\text{-}water}$ values. Moreover, the oxygen isotope fractionation between smithsonite and water might be a useful tool for the determination of formation temperatures or constraining post-depositional changes in environmental settings applying a multi metal carbonate approach considering siderite formation.

The focus of the second and third experimental study of this thesis is given on the molar Li/Ca ratio and lithium isotope fractionation (δ^7Li) behavior during the growth of calcite as a function of pH and growth rate. The positive correlation of the partitioning coefficient D^*_{Li} ($D^*_{Li} = \frac{(c_{Li}/c_{Ca})_{calcite}}{(m_{Li^+}/m_{Ca^{2+}})_{solution}}$) with calcite growth rate (r_p) can be explained by an increasing entrapment of Li at the rapidly growing calcite surfaces. At high growth rates with $r_p > 10^{-7.7}$ mol m^{-2} s^{-1} the lighter Li isotopes are preferentially incorporated into the growing calcite. This can be explained by kinetically controlled transport and surface entrapment of the lighter lithium isotopes at calcite surface defect sites related to their higher reaction rates. The dependence of lithium incorporation and its isotope fractionation on mineral growth rate may provide a tool to determine the precipitation rate of natural grown carbonates. The dependence of D^*_{Li} on pH can be explained by coupled incorporation of Li^+ and HCO_3^- for charge balance. The incorporated $LiHCO_3°$ complex is favoring ^6Li in $LiHCO_3°$ vs. $Li(H_2O)_n^+$ ($n = 1 – 6$) according to the longer Li-O bond length in aqueous $LiHCO_3°$. Therefore, in the pH rage between 6.3 and 8.3, the smaller Li isotope fractionation during the uptake in the growing calcite is consistent with the decreasing availability of $LiHCO_3°$ for the incorporation in calcite at elevated pH. At pH > 8.3 the Li incorporation mechanism is mainly based on the adsorption of Li^+ onto the negatively charged calcite surface, which is dominated by adsorption and subsequent

entrapment kinetics. These mechanisms cause preferential uptake of lighter Li isotopes. The pH-dependence of Li/Ca ratio may provide insights on formation conditions in continental carbonate deposits according to significant pH variations in these deposits.

The forth contribution of this thesis is focused on the incorporation of the redox-sensitive element Cr in calcite in the form of chromate (Cr(VI): CrO_4^{2-}) and on its corresponding isotope composition ($\delta^{53}Cr$) during calcite growth as a function of pH. The experimental results clearly show that the Cr(VI) uptake during calcite growth is significantly affected by the formation of aqueous $CaCrO_4^0$ species ($8 \leq pH \leq 9.4$) and by the additional uptake of aqueous CrO_4^{2-} species when the reaction solution has a $pH \geq 9.4$. The uptake of Cr(VI) during calcite growth is consistent with the decreasing availability of Ca^{2+}, $CaCrO_4^0$ complexation and its incorporation at elevated pH. Owing to the longer Cr-O bond lengths in aqueous $CaCrO_4^0$ compared to CrO_4^{2-} species the lighter $^{52}Cr(VI)$ isotope is preferentially incorporated in the aqueous $CaCrO_4^0$. Moreover, at $pH \geq 9.4$ an almost constant molar $(CaCrO_4^0)/(CrO_4^{2-})$ ratio yields in constant $Cr(VI)_{calcite}$ values and $\Delta^{53}Cr_{calcite\text{-}solution}$ values close to zero ($\Delta^{53}Cr_{calcite\text{-}solution} = 0.05 \pm 0.01$ ‰). These new insights of Cr(VI) incorporation and its isotope fractionation during the growth of calcite show that the Cr(VI) isotope fractionation is not solely reflecting redox effects in the aqueous solution from which the carbonates precipitate. But in fact, it is also suggested to be reasonably used at alkaline conditions to directly predict the Cr(VI) isotopic signature of the aqueous solution from which the calcite forms.

Kurzfassung

Die chemische Zusammensetzung von Meerwasser stellt eine wesentliche Kenngröße dar, die Informationen über die Verteilung von Land und Ozean, die chemische Entwicklung der Meerwasserzusammensetzung sowie über die Entwicklung von atmosphärischen und langzeitlichen Klimaveränderungen auf der Erde während allen geologischen Zeitepochen wiedergibt. Die Zusammensetzung von ursprünglichem Meerwasser ist in geologischen Archiven wie marinen, skeletartigen Karbonaten (z.B. Brachiopoden) gespeichert. Diese natürlichen Karbonate werden bezüglich ihrer Elementkonzentration, -verteilung und Isotopenverteilung analysiert. Die Interpretation dieser Signale in natürlichen Karbonaten erfordert jedoch ein detailliertes Verständnis der Mechanismen, welche das elementare und isotopische Verteilungsverhalten während des Wachstums von Karbonatmineralen kontrollieren. Die Durchführung von anorganischen Fällungsexperimenten stellt ein wertvolles Werkzeug dar, um diese kontrollierenden Fällungsmechanismen in natürlichen Umgebungen zu entschlüsseln. In der vorliegenden Arbeit werden neue Daten bezüglich Element- und Isotopenverteilungen in Karbonaten aus anorganischen Fällungsexperimenten präsentiert, die auf der Grundlage hochentwickelter experimentelle Methoden ermittelt wurden. Diese Daten können genutzt werden, um neue Tracer zu erschließen und deren Einsatz für geowissenschaftliche Fragestellungen zu etablieren z.B. für die Rekonstruktion der ehemaligen Meerwasserzusammensetzung.

Der erste Teil der vorliegenden Dissertation beinhaltet die Untersuchung traditioneller, stabiler Isotope ($\delta^{18}O$) in sekundären Zinkkarbonaten (Smithsonit), in Hinblick auf deren Bildungszeit und -temperatur. Die zeitabhängige Entwicklung der Sauerstoffisotopenfraktionierung ($10^3\ln\alpha_{\text{Smithsonit-Wasser}} \approx \Delta^{18}O_{\text{Smithsonit-Wasser}} = \delta^{18}O_{\text{Smithsonit}} - \delta^{18}O_{\text{Wasser}}$) zwischen Smithsonit und Wasser zeigt, dass sich nach 7 Tagen Reaktionszeit thermodynamisches Isotopen-Gleichgewicht einstellt. Des Weiteren verringert sich mit zunehmender Reaktionstemperatur ($25 \leq T \leq 80$ °C) die Sauerstoffisotopenfraktionierung im isotopischen Gleichgewicht. Dieser Trend liegt (i) im Bereich verschiedener theoretischer Kalkulationen und (ii) stimmt mit der Reihenfolge verschiedener trigonaler Me-Karbonate überein. Dabei gilt, je kleiner der Kationenradius, umso größer die $10^3\ln\alpha_{\text{Karbonat-Wasser}}$ Werte. Die gewonnenen Erkenntnisse über die Sauerstoffisotopenfraktionierung in Smithsonit können genutzt werden, um sowohl die Bildungstemperatur von Karbonatmineralen als auch Änderungen der ökologischen Begebenheiten nach deren Ablagerung zu bestimmen. Dies ist vor allem in Kombination mit den Isotopensignaturen von Siderit in Form eines Multi-Proxy Ansatzes möglich.

Der Fokus der zweiten und dritten experimentellen Studie dieser Arbeit liegt in der Betrachtung des molaren Li/Ca Verhältnis und des Fraktionierungsverhaltens von Lithiumisotopen (δ^7Li) während des Wachstums von Kalzit in Abhängigkeit vom pH-Wert und der Wachstumsrate. Die zu erkennende positive Korrelation der Verteilungskoeffizienten D^*_{Li} ($D^*_{Li} = \frac{(c_{Li}/c_{Ca})_{Kalzit}}{(m_{Li^+}/m_{Ca^{2+}})_{Lösung}}$) mit der Wachstumsrate von Kalzit (r_p) ist erklärbar mit dem zunehmenden Einschluss von Lithium an der schnell wachsenden Kalzitoberfläche. Diese kinetisch kontrollierte Einbindung von Li in die Kalzitoberfläche bei $r_p > 10^{-7.7}$ mol m^{-2} s^{-1} begünstigt, insbesondere an Fehlstellen, den Einbau des leichteren Li Isotopes (^{6}Li) aufgrund dessen höherer Reaktionsrate. Daher kann die

Ratenabhängigkeit des Lithiumeinbaus und die mit diesem Prozess in Verbindung stehende Isotopenfraktionierung als möglicher Indikator für die Bestimmung von Bildungsraten natürlich wachsender Karbonate genutzt werden. Die Abhängigkeit des D_{Li}^{*} vom pH-Wert kann durch den gekoppelten Einbau von Li^+ und HCO_3^- erklärt werden. Aufgrund der längeren Li-O Bindungslängen in gelöstem $LiHCO_3^{\circ}$ bevorzugen die eingebauten $LiHCO_3$ Komplexe ^6Li im Vergleich zu den $Li(H_2O)_n^+$ (n = 1 – 6) Aqua-Komplexen, d.h. je mehr $LiHCO_3^{\circ}$ für den Einschluss in Kalzit zur Verfügung steht, desto leichter wird der Kalzit. Bei steigenden pH-Werten (von 6.3 zu 8.3) nimmt die Verfügbarkeit von Hydrogenkarbonat und damit die Verfügbarkeit von $LiHCO_3^{\circ}$ in der Lösung ab, sodass der Kalzit isotopisch schwerer wird. Bei einem pH-Wert > 8.3 ist der Li Einbau hauptsächlich auf die Adsorption von Li^+ an der negativ geladenen Kalzitoberfläche zurückzuführen. Dieser Mechanismus wird dominiert über die Adsorptionskinetik und nachfolgendem Einbau in Kalzit, verbunden mit einer bevorzugten Aufnahme von leichteren Li Isotopen. Die beobachtete pH-Abhängigkeit der Li/Ca Verteilung kann dazu verwendet werden, Rückschlüsse auf Bildungsbedingungen bei kontinentalen Karbonatablagerungen, aufgrund der dort herrschenden signifikanten pH Variationen, zu ziehen.

Der Fokus des 4. Teils der vorliegenden Arbeit liegt im Elementverhältnis des Redox sensitiven Elements Chrom, in der Form von Chromat (Cr(VI): CrO_4^{2-}), und dessen isotopischer Zusammensetzung ($\delta^{53}Cr$) in Abhängigkeit des pH-Wertes während des Wachstums von Kalzit. Die experimentellen Resultate zeigen, dass die Cr(VI) Aufnahme während des Wachstums von Kalzit signifikant von der Bildung von gelösten $CaCrO_4^0$ Spezies beeinflusst wird ($8 \leq pH \leq 9.4$). Bei einer Reaktionslösung mit pH-Werten ≥ 9.4 wird der Einbau von Cr(VI) in Kalzit durch die zusätzliche Aufnahme von gelösten CrO_4^{2-} Spezies bestimmt. Die abnehmende Verfügbarkeit von Ca^{2+} in der Reaktionslösung mit zunehmendem pH-Wert mindert dabei die Komplexbildung zu $CaCrO_4^0$ und damit den Einbau von Cr(VI). Aufgrund der längeren Cr-O Bindungslängen im gelösten $CaCrO_4^0$, im Vergleich zur CrO_4^{2-} Spezies, wird im gelösten $CaCrO_4^0$ bevorzugt das leichtere $^{52}Cr(VI)$ Isotop gebunden. Ein konstantes Molarverhältnis von $(CaCrO_4^0)/(CrO_4^{2-})$ bei pH-Werten ≥ 9.4 liefert konstante $Cr(VI)_{Kalzit}$ und $\Delta^{53}Cr_{Kalzit\text{-}Lösung}$ Werte, welche ungefähr bei null ($\Delta^{53}Cr_{Kalzit\text{-}Lösung} = 0.05 \pm 0.01$ ‰) liegen. Diese neuen Einblicke in Bezug auf den Cr(VI) Einbau und dessen Isotopenfraktionierung während des Wachstums von Kalzit zeigen, dass die Cr(VI) Isotopenfraktionierung in wässrigen Lösungen nicht nur Redox-Effekte reflektiert. Die Cr(VI) Isotopenzusammensetzung von natürlich gewachsenen Karbonaten kann möglicherweise auch dazu genutzt werden, um direkt die Cr(VI) Isotopensignatur von alkalischen, wässrigen Lösungen wiederzugeben.

Acknowledgements

First and foremost, I would like to thank my supervisors Martin Dietzel, Albrecht Leis and Vasileios Mavromatis for your great support, encouragement and guidance throughout the last years. I appreciate our scientific and personal discussions which helped to develop concepts and improve skills. I want to especially thank Vasileios Mavromatis, who went beyond the call of duty for which I’m extremely grateful. Special thank goes to Michael Böttcher for reviewing this PhD thesis.

I want to thank all people who are involved in the BASE-LiNE Earth Project for great scientific meetings, networking and discussions.

In this respect, a huge thank you goes to Robert Frei and Claire Rollion-Bard for the possibility of two great secondments at the University of Copenhagen and at the Institute de Physique du Globe de Paris. I would especially like to thank Marie Küssner and Sylvie Bruggmann for your support concerning interpretation of Li and Cr isotope data and your useful suggestions and remarks during writing our manuscripts. Above all, I am grateful to you for sharing your valuable time of your PhD to help me improve my clean lab skills and knowledge about Li and Cr isotope geochemistry. Thank you for the great time we had.

In general, I would like to thank all the people who were involved in any kind of help during my PhD work. Stefanie Eichinger and Andre Baldermann are thanked for great support concerning ICP-OES measurements. Andrea Wolf, Maria Hierz, Sylvia Perchthold, Judith Jernej, Alexandra Geisinger-Haslinger, Sabine Lindbichler and Barbara Zirngast are thanked for excellent support in the laboratory, in particular, your help with analytical and technical issues.

Moreover, I would like to thank my colleagues: Isaac Kell-Duivestein, Dorothee Hippler, Peter Schreiber, Christoph Zambanini, Walter Poltnig, Till Harum, Dominik Janisch, Sandra Murg, Lisa Brückner Judith Mach and Johannes Draxler for your support, the good time we had and the great working environment.

A huge thank you goes to the best office mates in the world: Cyrill Grengg, Florian Konrad, Jessica Stammeier, Bettina Purgstaller and Katja Götschl. Thanks for your support concerning suggestions, discussions, help during the experimental work and the great time we spent together during coffee, beer, lunch and ice cream breaks. I want to express my sincere gratitude, in particular, to Jessica Stammeier for all your help, humor and advice during isotope measurements, writing, clean lab work and discussions. You cheered me up whenever I felt lost and encouraged me to find my own way. I am thankful for the great time we spent together.

Dennis Volz, thank you for standing by my side. You managed all my moods and I’m endless grateful that you took this journey with me.

Last but not least, I want to thank my family and close friends for your patience as well as moral and personal support. In particular, the deepest thank goes to my wonderful parents who making me laugh even on bad days and always believed in me.

Content

Statutory Declaration V

Abstract IX

Kurzfassung XI

Acknowledgements XIII

List of Figures XIX

List of Tables XXI

Chapter 1 - Introduction 1

- 1.1 BASE-LiNE Earth 1
- 1.2 Occurrence and behavior of calcium carbonate in aqueous environments 2
  - 1.2.1 Implications of elemental and isotopic distribution on calcium carbonate in aqueous solutions 2
  - 1.2.2 Precipitation experiments of carbonate minerals 4
- 1.3 Oxygen isotopes in the global water cycle 6
- 1.4 Lithium flux and its isotopic fractionation behavior 7
- 1.5 Chromium cycle and the Cr(VI) isotopic signal 8
- 1.6 Outline of the Doctoral Thesis 9

Chapter 2 - Oxygen Isotope Fractionation During Smithsonite Formation From Aqueous Solution 13

- 2.1 Introduction 14
- 2.2 Methods 16
  - 2.2.1 Experimental Setup 16
  - 2.2.2 Analytics 17
    - 2.2.2.1 Solid characterization 17
    - 2.2.2.2 Chemical analyses 17
    - 2.2.2.3 Geochemical modeling 17
    - 2.2.2.4 Oxygen isotopic analyses 18
  - 2.2.3 Ab initio calculations of mineral-water vapor oxygen isotopic fractionation factors at the harmonic level 19
- 2.3 Results 20
  - 2.3.1 Mineralogy of the precipitates 20
  - 2.3.2 Chemical composition of the reactive solution 23
  - 2.3.3 Oxygen isotopic fractionation factor between smithsonite and solution at 25°C 24
  - 2.3.4 Oxygen isotopic fractionation factor between 25 and 80 °C 25
  - 2.3.5 Theoretical calculations of calcite-water and smithsonite-water oxygen isotope fractionation at equilibrium 26
- 2.4 Discussion 28
  - 2.4.1 Reaction mechanisms and pathways 28
  - 2.4.2 Kinetics versus isotope equilibrium conditions 29
  - 2.4.3 Oxygen isotope equilibrium fractionation between different metal carbonate minerals and water 30

2.4.4 Ab initio calculations of smithsonite-water fractionation and comparison to experimental data. 31
2.4.5 Revisiting oxygen isotope fractionation between theoretical calculations and experimental data of various carbonates 31
2.4.6 Implications for natural systems 32
2.5 Summary and Conclusions 33
Chapter 3 - Effect of growth rate and pH on lithium incorporation in calcite 35
3.1 Introduction 36
3.1.1 General Background 36
3.1.2 Mechanisms of monovalent cation incorporation in carbonate minerals 37
3.1.3 Partitioning coefficients 37
3.2 Methods 38
3.2.1 Experimental set-up 38
3.2.2 Analytical procedures 40
3.2.2.1 Solution characterization 40
3.2.2.2 Solid characterization 41
3.3 Results 41
3.3.1 Mineralogy of the precipitated solids 41
3.3.2 Chemical composition of reactive fluids and growth rate calculation 42
3.3.3 Lithium and sodium partitioning between calcite and solution 43
3.4 Discussion 45
3.4.1 The role of growth rate on Li incorporation in calcite 45
3.4.2 The role of pH on Li incorporation in calcite 46
3.4.3 Implications for the Li content of natural calcite 48
3.5 Conclusions 49
Chapter 4 - The role of growth rate and pH on lithium isotope fractionation during its incorporation in calcite 51
4.1 Introduction 52
4.2 Methods 53
4.2.1 Calcite precipitation 53
4.2.2 Solution and precipitate characterization 54
4.2.3 Li isotope analyses 55
4.3 Results 56
4.4 Discussion 58
4.4.1 Effect of growth rate on Li isotopic fractionation 58
4.4.1.1 Approaching equilibrium isotope fractionation 58
4.4.1.2 Kinetic isotope fractionation 59
4.4.2 Effect of pH on the Li isotopic fractionation 60
4.4.3 Implications for Li isotope composition of natural calcites 62
4.5 Conclusions 63

Chapter 5 - The role of pH on chromium partitioning and isotopic fractionation during its incorporation in calcite 65
5.1 Introduction........ 66
5.2 Methods........ 67
5.2.1 Precipitation experiments........ 67
5.2.2 Solution characterization........ 70
5.2.3 Solid characterization........ 70
5.2.4 Chromium isotope separation........ 70
5.2.5 Chromium isotope analyses........ 71
5.3 Results 71
5.3.1 Mineralogy of the precipitates 71
5.3.2 Chemical composition of the fluid and precipitation rate 72
5.3.3 Cr(VI) distribution between calcite and solution........ 73
5.3.4 Cr(VI) isotopic fractionation between reactive solution and precipitate 74
5.4 Discussion........ 75
5.4.1 Effect of pH on chromate incorporation into calcite 75
5.4.2 Cr(VI) isotope fractionation during calcite growth 78
5.4.3 Implications for Cr(VI) incorporation and isotope fractionation in natural calcite........ 80
5.5 Conclusions........ 82
Chapter 6 - Conclusions and Perspectives 85
6.1 Conclusions........ 85
6.2 Perspectives........ 86
References…………… 91
Appendix A - Supplementary to Chapter 2........ 111
Appendix B - Supplementary to Chapter 3........ 115
Appendix C - Supplementary to Chapter 4 119
Appendix D - Supplementary to Chapter 5 123
Appendix E - Author's Contribution 125

List of Figures

Figure 1.1: Experimental setup for the inorganic precipitation and co-precipitation of carbonate minerals. 5

Figure 1.2: Schematic of oxygen in the global water cycle. 6

Figure 1.3: Schematic of the surface lithium flux. 8

Figure 1.4: Schematic of the surface chemistry of chromium. 9

Figure 2.1: Experimental set-up of the high pressure titanium batch reactor. 16

Figure 2.2: FT-IR spectra and X-ray diffraction pattern of precipitated hydrozincite and smithsonite. 21

Figure 2.3: SEM image of precipitated hydrozincite and smithsonite. 22

Figure 2.4: Temporal evolution of pH and saturation degree of precipitating solution. 23

Figure 2.5: Temporal evolution of the $10^3\ln\alpha(^{18}O)_{smithsonite\text{-}water}$ value. 24

Figure 2.6: Oxygen isotope fractionation between smithsonite and water as a function of temperatur. 25

Figure 2.7: Stability fields of zincite, hydrozincite versus smithsonite at 25°C as a function of CO_2 partial pressure and pH. 28

Figure 2.8: Oxygen isotope fractionation between smithsonite and water as a function of temperature for trigonal-cation Me-carbonate minerals. 30

Figure 2.9: Dependence of oxygen isotope fractionation between endmember metal carbonate minerals and water at 25 °C on the respective ionic metal radius. 32

Figure 3.1: Experimental set-up for the calcite growth experiments. 39

Figure 3.2: SEM image of calcite seeds and final overgrow precipitates. 41

Figure 3.3: Temporal evolution of Ca, Li and Na as a function of time. 42

Figure 3.4: Apparent partition coefficient of Li and Na between calcite and reactive fluid plotted as a function of calcite growth rate. 43

Figure 3.5: Apparent partition coefficient of Li and Na between calcite and reactive fluid plotted as a function of pH. 44

Figure 3.6: Apparent partition coefficient of Li in calcite and reactive fluid plotted as a function of activity of aqueous bicarbonate ion. 47

Figure 3.7: Apparent partition coefficient of Li vs Na. in calcite. 49

Figure 4.1: $\Delta^7Li_{calcite\text{-}solution}$ plotted as a function of calcite growth rate. 57

Figure 4.2: $\Delta^7Li_{calcite\text{-}solution}$ values plotted as a function of pH. 58

Figure 4.3: $\Delta^7Li_{calcite\text{-}solution}$ shown as a function of lithium distribution coefficient and aqueous HCO_3^- activity. 61

Figure 5.1: Experimental set-up for the Cr(VI) incorporation in calcite. 68

Figure 5.2: SEM image of calcite seeds and final overgrow precipitates. 72

Figure 5.3: Temporal evolution of Ca and Cr(VI) aqueous concentration and pH as a function of time. 72

Figure 5.4: Cr(VI) partitioning coefficient in calcite as a function of pH and amount of chromate incorporated in calcite. 74

Figure 5.5: Cr(VI) isotope fractionation plotted as a function of pH in the synthetic precipitates of this study and literature data. 75

Figure 5.6: Species distribution as a function of experimental pH for aqueous CrO_4^{2-}, $CaCrO_4^0$, Ca^{2+} and CO_3^{2-}. 76

Figure 5.7: Relationship between the amount of incorporated chromate ($Cr(VI)_{calcite}$) and the concentration of the aqueous $CaCrO_4^0$ complex. 77

Figure 5.8: Relation between Cr(VI) isotope fractionation and amount of incorporated chromate and aqueous $CaCrO_4^0$ concentration. 79

Figure 5.9: Correlation between $\Delta^{53}Cr_{calcite-solution}$ and the concentration of $CaCrO_4^0$ complex and the aqueous ratio of $CaCrO_4^0$ complexes and total Cr(VI) of our experimental and natural carbonate samples from the literature. 81

Figure 6.1: Oxygen isotope fractionation between smithsonite, calcite, minrecordite and water plotted as a function of temperature. 87

List of Tables

Table 2.1: Temperature, pH, duration, added $NaHCO_3$ and $Zn(NO_3)_2$ of the experimental solution. 18
Table 2.2: Structural parameters of calcite and smithsonite. 26
Table 2.3: Comparison of model phonon frequencies in smithsonite and calcite. 26
Table 2.4: Fits of $10^3\ln\alpha(^{18}O)_{\text{mineral-water(vapor)}}$ for 0 - 400°C, with $x = 10^3/T$. 27
Table 3.1: Chemical composition of Li and Ca in the reactive fluid. 40
Table 4.1: Physicochemical conditions, elemental and isotope fractionation of Li during experimentally growing calcite. 54
Table 5.1: Chemical and isotopic composition of Cr(VI). 69

Chapter 1

Introduction

1.1 BASE-LiNE Earth

The chemical composition of the seawater reflects the mass balance of all fluxes in and out of the ocean. In particular, the seawater composition is affected by (bio-)chemical and (bio-)geological processes in the Earth’s atmosphere-hydrosphere-lithosphere system through geological time. In the Phanerozoic eon (~540 million years ago) the seawater composition provides important information on the mass balances due to these controlling processes such as extinction events, volcanic activity, the evolution of the chemical composition of seawater and of the Earth`s atmosphere, diagenetic processes, land-ocean interaction / distribution and plate tectonic (e.g. Burke et al., 1982; Renne et al., 1995; Veizer et al., 1997; 1999; Palmer et al., 1998; Pearson and Palmer, 1999; 2000; Lemarchand et al., 2000; Wallmann, 2001; 2004; Steuber and Veizer, 2002; Kampschulte and Strauss, 2004; Miller et al., 2005; Came et al., 2007; Farkaš et al., 2007; Vollstaedt et al., 2014).

Therefore, one of the main research goal of the geoscience community is to reconstruct the paleo-seawater composition on the basis of elemental and isotopic data through geological time scales. Up to date, geochemical processes such as alteration of geological archives and the lack of advanced methodical approaches limits the interpretation of Phanerozoic seawater records. In order to fill this gap, the BASE-LiNE Earth project was established: “Brachiopods As SEnsitive tracers of gLobal mariNe Environment: Insights from alkaline, alkaline earth metal, and metalloid trace element ratios and isotope systems” (https://www.baseline-earth.eu/). BASE-LiNE Earth is an Innovative Training Network funded by the European Commission within the Marie Skłodowska-Curie Actions in Horizon 2020 'European Union Funding Programme for Research and Innovation'. The goal of BASE-LiNE Earth is to explore new hydrocarbon reservoirs and to develop innovative methods to determine primary signals which are preserved in suitable ancient geological archives. These new insights can be used in order to extend the knowledge of Phanerozoic seawater records (Eisenhauer et al., 2014).

The obstacle in (ancient) seawater reconstructions is the inability to directly investigate / analyze pristine seawater. Thus, the chemical condition of paleo-seawater has to be reconstructed, e.g. by analyzing the (trace-)element and isotope composition of marine skeletal carbonates (e.g. Veizer et al., 1997; 1999; Steuber and Veizer, 2002; Kampschulte and Strauss, 2004; Farkaš et al., 2007, Vollstaedt et al., 2014). Brachiopods are highly abundant throughout the Phanerozoic eon and were thus chosen as main focus of the BASE-LiNE Earth project. The brachiopod shells are composed of low-Mg calcite, a stable skeletal carbonate. Thus, the shells are quite resistant to post-depositional alteration, preserving the physical and chemical properties of the ambient seawater during formation. As a consequence, their shells are promising to determine primary elemental and isotopic signals of environmental changes in ancient oceans (e.g. Lowenstam, 1961; Popp et al., 1986; Veizer et al., 1986; 1999; Delaney et al., 1989; Carpenter and Lohmann, 1995; Brand et al., 2003; 2013; 2015; Parkinson et al., 2005; Farkaš et al., 2007; Ushatinskaya, 2008).

1.2 Occurrence and behavior of calcium carbonate in aqueous environments

The formation of calcium carbonate ($CaCO_3$) occurs mostly during the precipitation from aqueous solutions and can be induced inorganically or biogenically (e.g. Morse and Mackenzie, 1990; Dove et al., 2003; Morse et al., 2007, Dietzel, 2011). Inorganic precipitation of calcium carbonate minerals is forced by supersaturation, e.g. induced by evaporation in marine environments, hydrothermal processes and by degassing of carbon dioxide during speleothem formation. In contrast, biogenic formation of calcium carbonate minerals occurs during biomineralization of skeletal parts of marine and non-marine organisms such as foraminifera, corals and brachiopods (e.g. Dietzel, 2011, and references therein).

In low pressure environments, four distinct polymorphs of anhydrous calcium carbonate are known: calcite, aragonite, vaterite and amorphous calcium carbonate as well as two hydrated forms: monohydrocalcite and ikaite (e.g. Morse and Mackenzie, 1990; Dietzel, 2011). In seawater reactions, however, calcite and aragonite are the most common and important forms of calcium carbonate (e.g. Morse et al., 2007).

In nature, carbonate minerals are usually not pure substances. Impurities within the carbonate mineral lattice are common, caused by, for instance, incorporation in interstitial positions and substitution of a host ion by foreign ions (e.g. Ishikawa and Ichikuni, 1984; Dietzel, 2011, and references therein). Because carbonate minerals preserve the primary elemental and isotopic composition of the aqueous environments during the formation, the element ratios and isotopic distribution in carbonate minerals are routinely used by the geoscientific community to reconstruct e.g. ancient temperatures, past continental weathering rates and the evolution of seawater as well as the Earth’s atmosphere (e.g. Rosenthal et al., 1997; Palmer et al., 1998; Steuber and Veizer, 2002; Farkaš et al., 2007; Rollion-Bard et al., 2009; Frei et al., 2011; Hathorne et al., 2013; Vigier et al., 2015).

1.2.1 Implications of elemental and isotopic distribution on calcium carbonate in aqueous solutions

The incorporation and isotopic fractionation behavior of major and trace elements in precipitating calcium carbonate is on one hand controlled by physicochemical parameters such as temperature (e.g. Dietzel et al., 2004; Marriott et al., 2004a; Tang et al., 2008a), growth rate (e.g. Lorens, 1981; Mucci and Morse, 1983; Tesoriero and Pankow, 1996; Tang et al., 2008a; Rimstidt et al., 1998; Böhm et al., 2012; Mavromatis et al., 2013; 2018; Füger et al., 2019) and pH (e.g. Mavromatis et al., 2015; 2019; Füger et al., 2019). On the other hand, it is also affected by the crystal structure of the precipitating mineral phase and by the chemical properties of each element such as ionic radius and the dehydration of ions at the mineral surface (e.g. Nielsen, 1984; Okumura and Kitano, 1986; Reeder et al., 1999; Morse et al., 2007).

The incorporation of divalent cations (e.g. Mg^{2+}, Sr^{2+}, Ba^{2+} and Zn^{2+}) in calcium carbonate can be described by ideal ion substitution of the Ca^{2+} ion in the crystal structure, influenced by distortion and relaxation due to the size of the substituting ion (e.g. Pingitore et al., 1992; Cheng et al., 1998; Reeder et al., 1999; Finch and Allison, 2007). However, monovalent cations (i.e. Li^+, Na^+, Rb^+ and K^+) are assumed to be incorporated in interstitial positions between carbonate ions and CaO_6 octahedra at the growing crystal surface, affected by initial aquo-complex formation and charge balance processes at the mineral surface during the incorporation (e.g. White, 1977; Ishikawa and Ichikuni, 1984; Busenberg and Plummer; 1985; Okumura and Kitano, 1986; Füger et al., 2019). The substitution of foreign anions and uncharged species (i.e. SeO_4^{2-}, SO_4^{2-}, CrO_4^{2-}, H_3BO_3, $B(OH)_4^-$, H_3AsO_3; $H_2AsO_4^-$ and $HAsO_4^{2-}$) follows a substitution for the carbonate ion in the calcite lattice. The substitution is affected by initial aquo-complex formation, distortion of the local structure and coordination changes during the incorporation (e.g. Reeder et al., 1994; Alexandratos, 2004; Tang et al., 2007; Yokoyama et al., 2012; Mavromatis et al., 2015; Wynn et al., 2018).

For example, for divalent cations, it is known that the incorporation of Mg in carbonate minerals can be used as paleo-thermometer of seawater as well as to identify continental weathering, dolomitization and hydrothermal activities (e.g. Rosenthal et al., 1997; Steuber and Veizer, 2002; Saenger and Wang, 2014). The Sr/Ca ratio of carbonates can be used as a multi-proxy approach to reconstruct environmental conditions (i.e. temperature, precipitation rate) of calcite growth (e.g. Smith et al., 1979; Lorenz, 1981; Tesoriero and Pankow, 1996; Stoll and Schrag, 2000; Tang et al., 2012). Moreover, the Ba partitioning in calcite and aragonite has the potential to provide information on the environmental conditions of natural waters in the past due to carbonate formation rates (e.g. Mavromatis et al., 2018). Mavromatis et al. (2019) demonstrated that the Zn isotope composition in calcite can potentially be used to reconstruct the paleo-pH at the time of mineral formation. With respect to monovalent cations, the well-studied Li/Ca ratio in carbonate shells can be used as proxy for environmental parameters such as dissolved inorganic carbon, salinity, growth rate and temperature (e.g. Delaney et al., 1985; 1989; Hall and Chan, 2004; Marriott et al., 2004a; 2004b; Lear et al., 2010; Vigier et al., 2015; Füger et al., 2019). The Li isotope distribution in carbonate minerals are widely used in order to reconstruct the paleo-δ^7Li of seawater as an indicator for continental weathering rates (e.g. Huh et al., 1998; Marriott et al., 2004a; Rollion-Bard et al., 2009; Dellinger et al, 2018). Concerning anions, the Cr isotope distribution in carbonates is commonly used as proxy for past continental weathering and to reconstruct the redox state of the ancient ocean (e.g. Frei et al., 2011; Bonnand et al., 2013; Gilleaudeau et al., 2016; Rodler et al., 2016; 2017). The B species distribution and the corresponding δ^{11}B isotope composition in carbonates can be used in order to determine the pH of paleo-seawater (e.g. Hemming and Hanson, 1992; Hönisch and Hemming, 2005; Trotter et al., 2011; Mavromatis et al., 2015; Uchikawa et al., 2015). Wynn et al. (2018) showed that the partition coefficient between sulfate and carbonate might be used in speleothem records in order to reconstruct environmental drivers such as cave ventilation and external temperature dynamics. At last, one of the most important and studied parameter in order to reconstruct past environmental changes is the oxygen isotope distribution in carbonates which provides an excellent tool to unravel the temperature during the carbonate formation (e.g. Clayton and Epstein, 1961; O'Neil and Clayton, 1964; Becker and Clayton 1976;

Popp et al., 1986; Carpenter and Lohmann, 1995; Veizer et a., 1997; Melchiorre et al., 2001; Boni et al., 2003; Lécuyer et al., 2012).

1.2.2 Precipitation experiments of carbonate minerals

The successful applications of the above elemental and isotopic proxies in carbonate minerals requires a precise understanding of the controlling mechanisms which influence the elemental and isotopic distribution during the growth of calcium carbonate. This requirement can be obtained and assessed by experimental and modelling studies. Accordingly, an enormous number of experiments in controlled environments were conducted in the past.

For example, the rapid carbonate co-precipitation technique that is illustrated in Fig. 1.1A. Within this method, two different solutions (solution A contains Ca^{2+} and solution B CO_3^{2-}) are slowly and simultaneously mixed in a reactor vessel. One of the two solutions contain the element which should be co-precipitated depending on the physicochemical properties of the element. The mixing of the solutions leads to turbidity which indicates that the precipitation started instantly. An incubation period allows the precipitates to settle down (e.g. Wray and Daniels, 1957; Reddy and Nancollas, 1976; Clarkson et al., 1992; Hales and Frost, 2007; Hua et al., 2007; Rodler et al., 2015; Füger et al., 2018). Another co-precipitation technique involves a flow-through system using double diffusion silica hydrogel experiments (Fig 1.1B). Two solutions (solution A contains Ca^{2+} and solution B CO_3^{2-}) are located in two vertical branches, separated by a column of silica hydrogel which contains the element that should to be co-precipitated. In order to start the crystal growth within the gel column the two separated reactive solutions are brought together by diffusing through the silica hydrogel (e.g. Henisch, 1970; Prieto et al., 1997; Sánchez-Pastor et al., 2011; Rodler et al., 2015; van Zuilen et al., 2016). Moreover, diffusion and mixing techniques are used mimicking natural systems. The experimental setup of the membrane diffusion technique involves a polyethylene (PE) bottle with a membrane containing an inner solution A (CO_3^{2-} enriched) saturated with CO_2 gas which is placed in a vessel of an outer solution B. The outer solution exhibits Ca^{2+}, significantly lower pCO_2 values and the element that should be co-precipitated (Fig 1.1C). During the experimental run, CO_2 diffuses through the membrane from the inner to the outer solution due to the CO_2 gradient between both solutions and provokes calcium carbonate precipitation. During the precipitation the pH is kept constant by using pH-stat titration. The precipitation rate of calcite thereby is controlled by the flux of CO_2 through the membrane, adjusted by the thickness of the membrane and the pH difference between the inner and outer solution (e.g. Dietzel and Usdowski, 1996; Dietzel et al., 2004; Tang et al., 2008a; Dietzel et al., 2009; Rodler, 2015). Furthermore, a constant-addition technique can be used in order to precipitate carbonate minerals using a dual syringe pump or a peristaltic pump (Fig. 1.1D). Note here, the precipitation technique using a peristaltic pump was inspired and modified after the experimental setup using a dual syringe pump. In both experimental setups two inlet solutions (solution A containing Ca^{2+} and B CO_3^{2-}) are delivered to the reaction vessel. One of the added solutions as well as the reactor solution contain the element which should be co-precipitated depending on the physicochemical properties of the element. The addition of CO_3^{2-} to the reactor solution leads to precipitation of calcium carbonate. During the experimental run, the pCO2 and the pH are maintained constant by bubbling gas into the reactor solution and a thermostatic bath is holding the temperature constant in the reactor solution. Using the dual syringe pump technique, however, the inlet solutions are added to the reactor solution in narrow bore diameter tubes which extended below the water level. In order to start the addition of the inlet solutions, the reactor solution is sampled with a syringe. Due to the resulting different water-levels between the dual syringe pump solutions and the reactor solution, the inlet solutions are added. In contrast, using a peristaltic pump the inlet solution is permanently delivered to the reactor solution and the precipitation rate can be easily modified by changing the flow rate. In order to keep the volume of the reactor solution constant, a volume of the reactive solution equal to the volume of the inlet solutions delivered in 24 h by the peristaltic pump is sampled with a syringe (e.g. Mucci, 1981; Mucci and Morse, 1983; Tesoriero and Pankow, 1996; Marriott et al., 2004a; 2004b; Tang et al., 2007; Mavromatis et al., 2013; 2015; 2017b; 2018; Gautier et al., 2014; Füger et al., 2019).

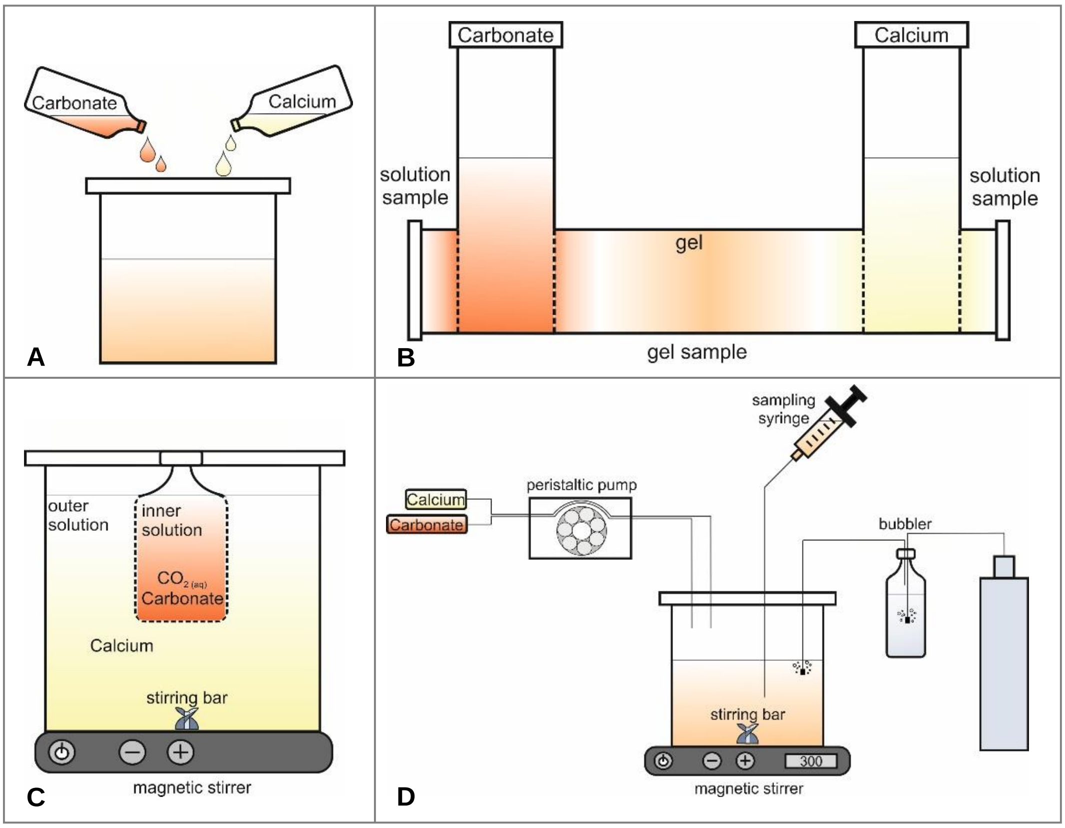
Carbonate
Calcium
A
Carbonate
Calcium
solution sample
solution sample
gel
gel sample
B
outer solution
inner solution
$CO_{2\,(aq)}$
Carbonate
Calcium
stirring bar
magnetic stirrer
C
sampling syringe
peristaltic pump
Calcium
Carbonate
bubbler
stirring bar
300
magnetic stirrer
D

Figure 1.1: Experimental setup for the inorganic precipitation and co-precipitation of carbonate minerals with various elements using (A) rapid carbonate co-precipitation experiments; (B) double diffusion silica hydrogel experiments (modified after Henisch, 1970 and Prieto et al., 1997); (C) membrane diffusion technique (modified after Dietzel and Usdowski, 1996); and (D) constant-addition technique by a peristaltic pump (modified after Mavromatis et al., 2013).

1.3 Oxygen isotopes in the global water cycle

Oxygen is the most abundant element in Earth's crust. It has three stable isotopes: ^{16}O (99.757 %; relative abundance), ^{17}O (0.038 %) and ^{18}O (0.205 %; e.g. Rosman and Taylor, 1998). The isotope composition of water ($\delta^{18}O_{water}$) within the global water cycle shows a wide range of variations (see Fig. 1.2). Evaporation of seawater from the ocean surface leads to gaseous H_2O which is enriched in ^{16}O related to a higher vapor pressure of $H_2{}^{16}O$. When this water vapor reaches supersaturation, the water condensates and clouds are formed. During condensation of H_2O again when the dew point is reached, the lighter oxygen isotopes preferentially remain in the vapor phase, leaving the water, commonly known as rain, enriched in heavy isotopes. Thereafter different pathways (i.e. groundwater or river water) introduce the precipitated water back to the oceans. During the overall global water cycle the oxygen isotope fractionation is influenced by the distance from the coast and the meteorological conditions (e.g. Appelo and Postma, 2007; Hoefs, 2018, and references therein).

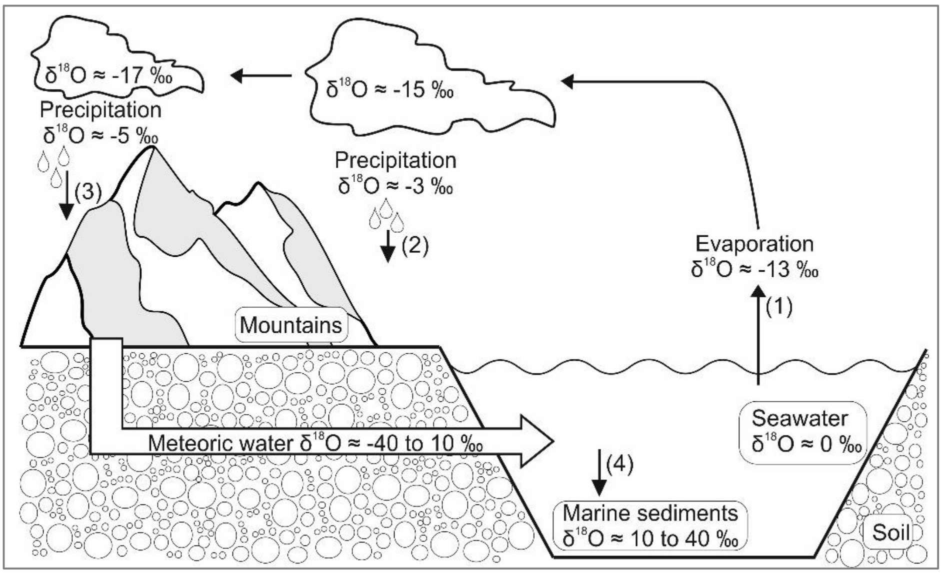

Figure 1.2: Simplified schematic view of the oxygen isotope distribution within the global water cycle: (1) Evaporation of the seawater leads to heavier oxygen isotopes preferentially remaining in the seawater; (2) Due to cooling clouds start to precipitate and leads to heavier oxygen isotopes in the landscape; (3) Ongoing precipitation introduces the preferential the heavier oxygen isotopes to the landscape; and (4) Removal of oxygen from the ocean via incorporation in marine sediments as a function of temperature (modified after Hoefs, 2018, and references therein).

However, in the global water cycle carbonate minerals such as marine carbonates precipitate. This includes oxygen isotope exchange with the surrounding aqueous medium (e.g. Hoefs, 2018) according to the expression

$$\frac{1}{3}CaC^{16}O_3 + H_2{}^{18}O = \frac{1}{3}CaC^{18}O_3 + H_2{}^{16}O \quad (1.1)$$

In 1947, Urey supported the theoretical basis for the use of $\delta^{18}O$ values in carbonate minerals as a paleo-temperature proxy. All $\delta^{18}O_{water}$ values are reported relative to Vienna Standard Mean Ocean

Water (VSMOW) standard. The measured low-temperature carbonates ($\delta^{18}O_{carbonate}$) are expressed on the Vienna Pee Dee Belemnite (VPDB) scale and are reported relative to VSMOW standard (e.g. Hoefs, 2018) using the following equation by Coplen et al. (1983):

$$\delta^{18}O_{VSMOW} = 30.91 + 1.03091 * \delta^{18}O_{VPDB} \quad (1.2)$$

Subsequent, the oxygen isotope fractionation between carbonate and water (e.g. Hoefs, 2018) can be calculated using the expression (Eq. 1.3):

$$10^3 \ln\alpha_{carbonate\ -water} \approx \Delta^{18}O_{carbonate\ -water} = \delta^{18}O_{carbonate} - \delta^{18}O_{water} \quad (1.3)$$

Knowledge and understanding of all these processes is an important key for paleo-climate research and reconstruction of paleo-temperatures. Since Urey's work in 1947 a large number of experimental (e.g. McCrea, 1950; O'Neil et al., 1969; Tarutani et al., 1969; McConnaughey, 1989; Kim and O'Neil, 1997; Kim et al., 2006; Dietzel et al., 2009; Mavromatis et al., 2012; Füger et al., 2018) and theoretical (e.g. Zheng, 1999; Watson, 2004; Schauble et al., 2006; Chacko and Deines, 2008; Zheng, 2011; Füger et al., 2018) studies demonstrated that oxygen isotopes fractionate strongly between carbonate minerals and aqueous solution. However, question remain, especially in respect to equilibrium and kinetic conditions.

1.4 Lithium flux and its isotopic fractionation behavior

Lithium has two stable isotopes: ^{6}Li (7.59 %; relative abundance) and ^{7}Li (92.41 %; e.g. Rosman and Taylor, 1998). The large relative mass difference (~16.67 %) between the two isotopes exhibits a very large range of Li isotopic composition ($\Delta^7Li_{carbonate\ -water} = \delta^7Li_{carbonate} - \delta^7Li_{water}$) in natural surroundings (e.g. Hoefs, 2018). Therefore, Li is a powerful tracer for low-temperature geochemical processes during weathering of continental siliceous rocks and secondary mineral formation (e.g. Chan and Edmond, 1988; Chan et al., 1992; Hoefs and Sywall, 1997; Huh et al., 1998; 2001; Rudnick et al., 2004; Kisakűrek et al., 2005; Vigier et al., 2008; Misra and Froelich, 2012).

As it can be seen in Fig. 1.3, Li is introduced into the ocean by (i) hydrothermal fluids; and (ii) continental / riverine run-off (e.g. Chan et al., 1992; 1994; 2002; Huh et al., 1998; 2001; Bray et al., 2001; Kisakűrek et al., 2005; Misra and Froelich, 2012). The first process occurs during high-temperature leaching of oceanic silicate rocks. Hydrothermal fluids from mid-ocean ridges are highly enriched in Li concentration compared to seawater. Yet, isotope fractionation between these hydrothermal fluids and basaltic source rocks is negligible. In contrast, the riverine input of Li (low-temperature geochemical weathering of continental silicate rocks) is enriched in heavy isotopes compared to their continental source rocks (e.g. Chan et al., 1994; Elderfield and Schultz, 1996; Tomascak et al., 2008; Misra and Froelich, 2012).

The most important sink for lithium in the ocean is the formation of marine sediments and clays (e.g. Chan et al., 1992; 2006; Vigier et al., 2008; Verney-Carron et al., 2011). A lesser sink is the incorporation during carbonate formation (e.g. Hoefs and Sywall, 1997).

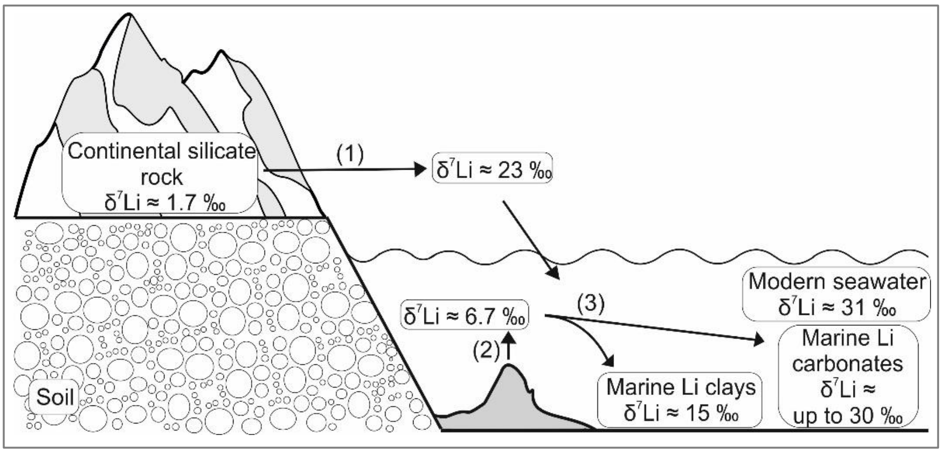

Figure 1.3: Simplified schematic view of the Li fluxes and its isotopic composition within the Earth`s crust (modified after Misra and Froelich, 2012): (1) Input of preferential heavier Li isotopes into the seawater via rivers is based on chemical weathering of silicate rocks; (2) Input of Li into the ocean via hydrothermal fluids (value taken from Bray et al., 2001); and (3) Removal of preferentially lighter Li isotopes from the ocean into marine sediments such as clays and carbonates (value taken from Rollion-Bard et al., 2009; Vigier et al., 2015; Roberts et al., 2018).

Investigating the incorporation and fractionation of Li in carbonate minerals, could facilitate determining the Li fluxes within the Earth`s crust and seawater.

1.5 Chromium cycle and the Cr(VI) isotopic signal

Chromium mainly occurs in the oxidation states (III) and (VI). The oxidized Cr(VI) is present as either chromate (CrO_4^{2-} under alkaline pH) or bichromate ($HCrO_4^-$ under acidic pH) oxyanion. The Cr(VI) is highly toxic, soluble and mobile (e.g. Hoefs, 2018). In nature, four isotopes of Cr with their relative abundances occur: ^{50}Cr (4.35 %), ^{52}Cr (83.79 %), ^{53}Cr (9.50 %) and ^{54}Cr (2.36 %; e.g. Rosman and Taylor, 1998).

Cr(III) is abundant in ultramarfic rocks and can be found in igneous terrestrial reservoirs. The oxidation, i.e. weathering, of Cr(III) in soils catalyzed by MnO_2 (Fig. 1.4) leads to the input of ^{53}Cr enriched Cr(VI) into river, groundwater and at least into the ocean (e.g. Fendorf, 1995; Robles-Camacho and Armienta, 2000; Oze et al., 2004; 2007; Izbicki et al., 2008; Frei et al., 2009; 2014; Bonnand et al., 2013). In the ocean the Cr(VI) can be reduced to Cr(III) either influenced by microorganisms or proceed in the presence of Fe-bearing minerals to Fe(III), Cr(III) (hydr-)oxides. This reduction enriches the Cr(VI) in heavy isotopes, leaving an isotopically light Cr(III) precipitate (e.g. Fendorf, 1995; Ellis et al., 2002; Sikora et al., 2008; Frei et al., 2009; Døssing et al., 2011; Jamieson-Hanes et al., 2012; Kitchen et al., 2012). The redox sensitivity makes the Cr isotope ($\Delta^{53}Cr_{carbonate\text{ -water}} = \delta^{53}Cr_{carbonate} - \delta^{53}Cr_{water}$) system to become a novel tool in sedimentary rocks to study the evolution of ocean and atmosphere O_2 levels in Earth’s history (e.g. Frei et al., 2009; 2011; Lyons and Reinhard, 2009; Konhauser et al., 2011; Frei and Polat, 2013; Bonnand et al., 2013; Crowe et al., 2013; Planavsky et al., 2014; Gilleaudeau et al., 2016; Rodler et al., 2016; 2017).

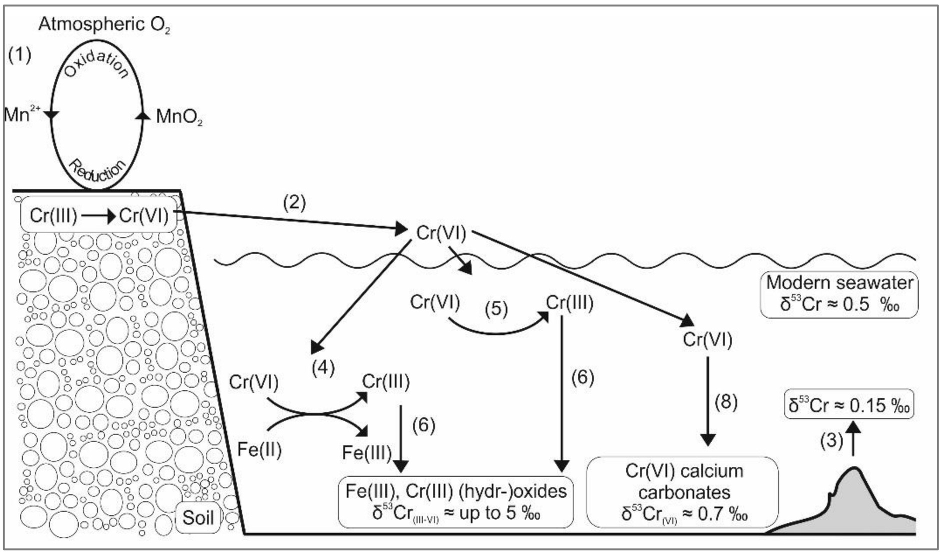
Atmospheric O_2
(1)
Oxidation
Mn^{2+}
MnO_2
Reduction
Cr(III) → Cr(VI)
(2)
Cr(VI)
Modern seawater
$\delta^{53}Cr \approx 0.5$ ‰
Cr(VI)
(5)
Cr(III)
Cr(VI)
(4)
Cr(VI)
Cr(III)
(6)
(6)
(8)
$\delta^{53}Cr \approx 0.15$ ‰
(3)
Fe(II)
Fe(III)
Fe(III), Cr(III) (hydr-)oxides
$\delta^{53}Cr_{(III-VI)} \approx$ up to 5 ‰
Cr(VI) calcium carbonates
$\delta^{53}Cr_{(VI)} \approx 0.7$ ‰
Soil

Figure 1.4: Schematic of the surface chemistry of chromium (modified after Frei et al., 2009): (1) Oxidation of Cr(III) in soils to Cr(VI); (2) Transport of the positive fractionated Cr(VI) into the ocean (value taken from Frei et al., 2011); (3) Cr(III) input into seawater by hydrothermal vents; (4) Abiotic reduction of Cr(VI) to Cr(III) in the ocean by upwelling iron; (5) Biotic reduction of Cr(VI) to Cr(III) in the ocean by bacteria; (6) Removal of Cr(III) from the ocean via Fe(III), Cr(III) (hydr-)oxides; (7) Direct removal of Cr(VI) from the ocean via marine carbonate (values taken from Holmden et al., 2016).

However, under conditions, where reduction is not possible, Cr(VI) remains mobile in the seawater (Rai et al., 1987; Palmer and Puls, 1994). Therefore, the interaction between Cr(VI) and calcium carbonate becomes more significance based on the widespread occurrence and precipitation of calcium carbonate in low-temperature aqueous environments (e.g. Frei et al., 2011; Bonnand et al., 2013; Gilleaudeau et al., 2016; 2018; Holmden et al., 2016; Farkaš et al., 2018).

1.6 Outline of the Doctoral Thesis

Marine carbonates, i.e. brachiopod shells, of the above developed elemental and isotope proxies exhibit limited knowledge about the controlling mechanisms which influence the incorporation behavior of foreign components and their isotope fractionation (see **Chapter 1**). Therefore, laboratory experiments are constraint in need for the evaluation and most importantly for the calibration of such proxies.

The goal of this PhD thesis is to develop and evaluate elemental and isotope proxies during the formation of inorganic precipitated carbonate minerals which can be used for the reconstruction of environmental conditions. The present experimental studies are embedded within the BASE-LiNE Earth initiative. The overall aim of this multi-disciplinary project is to use brachiopod shells as a proxy for the evolution of Phanerozoic seawater and its implication for past climate changes. This study is focused on the element partitioning and isotope fractionation processes in inorganic carbonates precipitated under controlled laboratory conditions establishing methods as well as developing new experimental and proxy approaches. The carbonate formation is monitored by using mineralogical and microstructural methods as well as advanced multi proxy techniques. The applied proxies involve traditional stable isotopes ($\delta^{18}O$) in secondary zinc carbonates (e.g. hydrozincite and smithsonite). Emphasis is given on the elemental ratio Li/Ca during the growth of calcite and the Li isotope system (δ^7Li). Further, the incorporation of the redox-sensitive element chromium, i.e. chromate (Cr(VI): CrO_4^{2-}), in calcium carbonates is assessed as well as its corresponding isotope distribution ($\delta^{53}Cr$). Selected isotopes (e.g. $\delta^{18}O$) were measured in Graz at the isotope laboratory of JR-AquaConSol GmbH and others by cooperating institutions (δ^7Li at the Institute de Physique du Globe de Paris and $\delta^{53}Cr$ at the University of Copenhagen). The obtained results are introduced and discussed in **Chapters 2** to **5** in detail.

Chapter 2 deals with the oxygen isotope fractionation between smithsonite and water as a function of formation time and temperature. We present first data from experimental work on smithsonite synthesis coupled with ab initio-based molecular dynamic calculations modeled by M. Méheut. Smithsonite synthesis is comparable rare in the laboratory due to the strong dependence of its formation conditions on the partial pressure of CO_2. Therefore, we use a CO_2 high pressure reactor in order to provoke low pH conditions that lead to the dissolution of initially formed hydrozincite to yield smithsonite formation. Chapter 2 is published in Chemical Geology (2018), Vol. 495, pp. 76 – 89 (A. Füger, M. Méheut, V. Mavromatis, A. Leis, M. Dietzel).

Chapter 3 provides new insights on two major physicochemical parameters that control the incorporation of Li in calcite. Essentially, the effect of calcite growth rate and pH is assessed and discussed. Considering that Li/Ca ratios in natural calcite are increasingly studied as indicators of silicate weathering activity, this study provides fundamental background to understand the incorporation of Li in calcite. Chapter 3 is published in Geochimica et Cosmochimica Acta (2019), Vol. 248, pp. 14 - 24 (A. Füger, F. Konrad, A. Leis, M. Dietzel, V. Mavromatis).

Chapter 4 shows the effect of calcite growth rate and pH on the Li isotope fractionation between calcite and solution during the growth of calcite. Given that Li isotopes are used in natural calcite as tracer of silicate weathering processes, the correlation between growth rate and Li isotopes indicates a great opportunity for Li isotopes as proxy for formation rats during secondary carbonate mineral formation in natural environments. Chapter 4 is currently prepared for publication (A. Füger, M. Kuessner, C. Rollion-Bard, A. Leis, M. Dietzel, V. Mavromatis).

Chapter 5 deals with new insights on the effect of pH on Cr(VI)/(CO_3^{2-}) values and the Cr(VI) isotope fractionation between calcite and solution during calcite formation. Cr(VI) isotopes in the nature are mostly used as proxy for atmospheric and seawater O_2 levels related to the reduction of Cr(VI) to Cr(III) and the following fractionation. This study clearly shows that if reduction is not occurring, Cr(VI) isotopes fractionate as a function of pH during calcite growth. This new insight provides information which has to be considered for natural carbonates. Chapter 5 is currently under review (A. Füger, S. Bruggmann, R. Frei, A. Leis, M. Dietzel, V. Mavromatis).

Chapter 6 provides a conclusion of the new insights for proxies which are introduced in this PhD thesis concerning the oxygen isotope fractionation in smithsonite, the Li/Ca ratio and its isotope fractionation between calcite and solution as a function of pH and growth rate as well as the

$Cr(VI)/(CO_3^{2-})$ ratio and its isotope composition as a function of pH. In addition, perspectives for further developments and a better understanding of natural phenomena related to the observed proxies in this PhD thesis are given. These perspectives involve the analysis of controlling parameters during the incorporation of Cr(VI) and Li in calcite (e.g. temperature, growth rate and seed material), further investigations concerning double carbonates and additional measurements such as clumped isotopes, Zn isotopes and high resolution spectroscopy of the precipitates.

Chapter 2

Oxygen Isotope Fractionation During Smithsonite Formation From Aqueous Solutions

A. Füger[1,2], M. Méheut[3], V. Mavromatis[2,3], A. Leis[1], M. Dietzel[2]

[1] JR-AquaConSol GmbH, Steyrergasse 21, 8010, Graz, Austria
[2] Institute of Applied Geosciences, Graz University of Technology, Rechbauerstraße 12, 8010, Graz, Austria
[3] Géosciences Environnement Toulouse (GET), CNRS, UMR 5563, Observatoire Midi-Pyrénées, 14 Avenue Edouard Belin, 31400 Toulouse, France

Published in Chemical Geology, 20 September 2018, Vol. 495, Pages 76-89
(https://doi.org/10.1016/j.chemgeo.2018.08.005)

Abstract - Oxygen isotope fractionation between carbonate minerals and water is used as an environmental proxy to estimate mineral formation temperatures or isotopic composition of precipitating fluids. To date no experimental data on the oxygen isotope fractionation factor between smithsonite ($ZnCO_3$) and water, $\alpha(^{18}O)_{smithsonite\text{-}water}$ = $(^{18}O/^{16}O)_{smithsonite}$ / $(^{18}O/^{16}O)_{water}$, exist. Therefore, in the present study experimental work on smithsonite synthesis in the temperature range between 25 and 80 °C is coupled with ab-initio based theoretical calculations.

Laboratory precipitation experiments took place in titanium reactors at elevated pCO_2 (~10 atm) in order to induce the formation of smithsonite from hydrozincite ($Zn_5(CO_3)_2(OH)_6$), which is the precursor phase initially formed at 25 °C and low pCO_2 (pH ~ 6.8). The constant $\alpha(^{18}O)_{smithsonite\text{-}water} = (1000 + \delta^{18}O_{smithonite}) / (1000 + \delta^{18}O_{water})$ value reached at a reaction time ≥ 10000 min (7 days) suggests near equilibrium conditions. Based on the experimentally obtained temperature relation of $\alpha(^{18}O)_{smithsonite\text{-}water}$ at 25, 40, 60, and 80 °C the integrated equation can be linearly described by the function:

$$10^3\ln\alpha(^{18}O)_{smithsonite\text{-}water} = (2.79 * 10^6/T^2 - 0.95) \pm (0.06 * 10^6/T^2 + 0.60)$$

where the temperature is in Kelvin. The ab initio calculations suggest that this relation can be described in the temperature range from 0 to 100°C as:

$$10^3\ln\alpha_{smithsonite\text{-}liquid\ water} = (3.21 * 10^6/T^2 - 3.63) \pm (0.025 * 10^6/T^2 + 0.90)$$

The $\alpha(^{18}O)_{smithsonite\text{-}water}$ values from the experimental approach fit within error to the theoretical relationship from the literature and the above ab initio calculations. Difference in slope between the

experiment and theoretical obtained equation likely reflects modelling inaccuracies, whereas kinetic effects cannot be completely ruled out in the experimental approach.

The obtained $\alpha(^{18}O)_{smithsonite\text{-}water}$ values match with the general sequence of $Zn^{2+} < Fe^{2+} < Mn^{2+} < Ca^{2+}$ for mono-cation trigonal Me-carbonate minerals suggesting incorporation of lighter oxygen isotopes in the carbonate mineral at increasing cation radius as indicated from thermodynamic considerations. Potential applications of oxygen isotope fractionation during smithsonite formation for natural aqueous surroundings are discussed.

2.1 Introduction

Zinc carbonate minerals are typically formed within the oxidation zone of zinc bearing ore bodies (Anthony et al., 2003). Two zinc carbonate minerals are known, smithsonite ($ZnCO_3$) and hydrozincite ($Zn_5(CO_3)_2(OH)_6$). Hydrozincite can be readily synthesized in the laboratory, whereas smithsonite synthesis is comparatively more complicated (Jambor, 1964; Bouchard and Smith, 2001; Zhu et al., 2001). Until now no experimental data exist for the oxygen isotope fractionation between smithsonite and water ($\alpha_{smithsonite\text{-}water} = (^{18}O/^{16}O)_{smithsonite} / (^{18}O/^{16}O)_{water}$) and its temperature dependence. This lack of data is likely caused by the seldom occurrence of the physicochemical conditions required for smithsonite formation in Earth`s surface environments and the competitive precipitation of hydrozincite. The formation conditions for smithsonite versus hydrozincite are strongly controlled by the partial pressure of $CO_2$. Under Earth`s atmospheric conditions (CO_2 partial pressure of about $10^{-3.5}$ atm) hydrozincite is the stable zinc carbonate phase. If the partial pressure of CO_2 increases smithsonite formation is favored, depending in particular on pH and on dissolved inorganic carbon (DIC refers to $CO_{2(aq)}$, H_2CO_3, HCO_3^-, and CO_3^{2-}) concentration (Alwan and Williams, 1979; Williams, 1990).

Since Urey's work in 1947 and from a large number of experimental (e.g. McCrea, 1950; O'Neil et al., 1969; Tarutani et al., 1969; McConnaughey, 1989; Kim and O'Neil, 1997; Kim et al., 2006; Dietzel et al., 2009; Mavromatis et al., 2012) and theoretical (e.g. Urey, 1947; Zheng, 1999; Watson, 2004; Schauble et al., 2006; Chacko and Deines, 2008; Zheng, 2011) studies thereafter, it is well established that oxygen isotopes fractionate strongly between carbonate minerals and the aqueous fluid from which they are formed. The respective isotope fractionation factor α, defined as the ratio of the abundance of the isotopomers ^{18}O and ^{16}O in the two phases, significantly depends on temperature (Urey, 1947; McCrea, 1950). Thus, oxygen isotopes in carbonates provide an excellent tool to unravel formation temperature, providing that the isotopic composition of their parent solution is known or can be reasonably estimated. Typically, the equilibrium oxygen isotope fractionation factor decreases as temperature increases (e.g. Hoefs, 2015). In order to use oxygen isotope fractionation as geological thermometer besides equilibrium fractionation kinetic effects also have to be evaluated (e.g. Dietzel et al., 2009). The kinetics of isotopic exchange and the reaction mechanisms between carbonate minerals and water, as well as between the DIC species and water have to be considered (e.g. McCrea, 1950; Beck et al., 2005; Kim et al., 2006) as each species has a distinct oxygen isotope fractionation compared to water (McCrea, 1950).

Already in 1953, Epstein and co-workers documented oxygen isotope fractionation of various alkaline earth carbonates to differ up to several per mil. After the study of McCrea (1950) on temperature variation of the fractionation of oxygen isotopes between dissolved inorganic carbon and water as well as between calcite and water, the isotopic compositions of a large variety of carbonate minerals such as strontianite and witherite (O'Neil et al. 1969), biogenic induced aragonite (Tarutani et al. 1969), siderite (Becker and Clayton 1976; Carothers et al. 1988; van Dijk et al. 2017), inorganic aragonite (Zhou and Zheng, 2002; 2003; Kim et al. 2006) have been investigated. The oxygen isotope fractionation ($10^3\ln\alpha_{carbonate\_mineral-water} \approx \Delta^{18}O_{carbonate\_mineral-water} = \delta^{18}O_{carbonate\_mineral} - \delta^{18}O_{water}$) among carbonate minerals varies from 23 ‰ for strontianite (Chacko and Deines, 2008) up to 32 ‰ for dolomite at 25 °C (Schmidt et al., 2005). Up to date, for smithsonite only theoretical studies on oxygen isotope fractionation exist (e.g. Zheng, 1999; Chacko and Deines, 2008).

Theoretical studies are based on the vibrational properties of the phases of interest. Accordingly, Chacko and Deines (2008) have computed the mineral-CO_2 fractionation for many carbonate minerals, including smithsonite, based on the experimentally measured vibrational properties of these phases. The mineral-liquid water fractionation (e.g. 32.18 ± 0.21 ‰ for smithsonite at 25 °C) is obtained accordingly by combining CO_2-H_2O experimental data (see Rosenbaum, 1997). However, Chacko and Deines (2008) base their work on several simplifying assumptions (see Deines, 2004) and rely on the quality of available experimental data, which can differ for two different minerals such as calcite and smithsonite (see the Methodology section of Chacko and Deines (2008), for further details). Another approach to assess the full vibrational properties of those phases, independently of any experiment, is based on the electronic structure modeling of minerals and molecules that was developed for mineral-water fractionation behaviors (e.g. Méheut et al., 2007). In the case of the electronic structure-based calculation, there are two principal sources of critical uncertainties: (1) the inevitable choice of an approximate exchange-correlation functional, at the foundation of the electronic structure calculation, induces errors on the harmonic vibrational properties. This corresponds at first order to an identical relative underestimation of all vibrational frequencies (e.g. around 5 %). (2) The model does not include anharmonic effects for the water molecule. A new ab initio modelling for oxygen isotope fractionation is herein applied to yield theoretical $\alpha(^{18}O)_{smithsonite-vapour\_H2O}$ values, further combined with the experimental vapor-liquid fractionations of Horita and Wesolowski (1994) to obtain $\alpha(^{18}O)_{smithsonite-water}$. We provide this by an approach based on the electronic structure modeling of minerals and molecules with correction for the above mentioned uncertainties (e.g. Méheut et al., 2007). This approach is first validated on the well constrained case of the calcite-water equilibrium and then applied to smithsonite.

In the present study we experimentally determine the until now poorly constrained oxygen isotope fractionation between smithsonite and water as a function of temperature. The formation of smithsonite was induced by the transformation of hydrozincite between 25 and 80 °C. The experimental fractionation coefficients were assessed in comparison to the theoretical values generated in this study and from the literature. The obtained temperature-controlled oxygen isotope fractionation kinetics, reaction mechanisms and the implications to natural smithsonites and smithsonite forming environments are addressed.

2.2 Methods

2.2.1 Experimental Setup

Smithsonite was synthesized at the temperature range 25 to 80 °C (± 0.5 °C) at 10 atm CO_2 pressure in either a PARR© non-stirred high-pressure titanium batch reactor (4601-4622 General Purpose Reactors), or a PARR© stirred high pressure titanium batch reactor (4560 Mini Reactors) both equipped with electrical heaters. An illustration of the experimental set-up used in this study can be seen in Fig. 2.1.

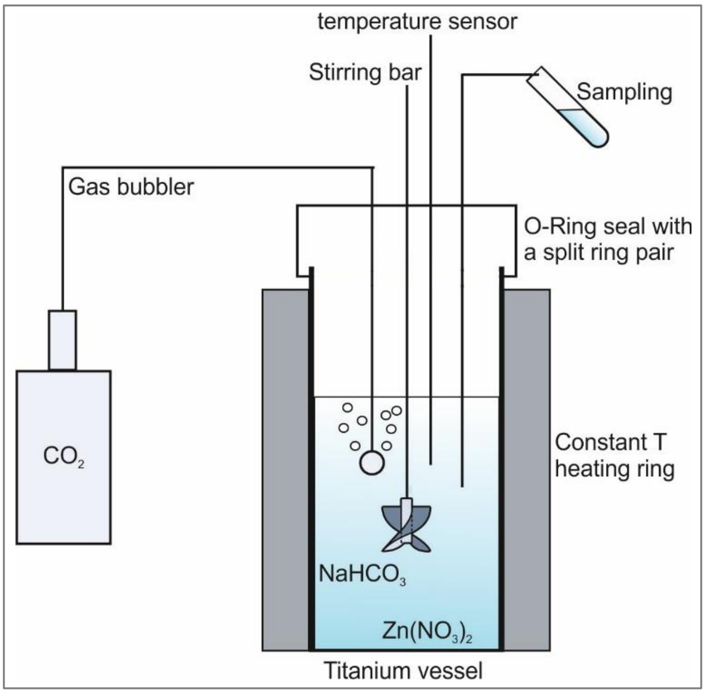

Figure 2.1: Experimental set-up of the high pressure titanium batch reactor which was used for experiments with and without using the stirring bar.

The use of two different setups (with and without stirring) served as a control of the reproducibility of the obtained experimental results. The experimental solution was prepared by mixing 250 mL of two stock solutions, the first containing 0.2 M of $NaHCO_3$ (Carl Roth, ≥ 99.5 %, p.a., ACS, ISO) and the second containing 0.04 M of $Zn(NO_3)_2$ (Merck, ≥ 98.5 %, p.a.), in the reactor at ambient temperature. Owing to the high supersaturation of the reactive solution with respect to hydrozincite, this zinc hydroxide carbonate mineral (pH 6.83 ± 0.17) is formed instantaneously after the mixing of the two stock solutions at ambient conditions according to the overall reaction

$$5\ Zn^{2+} + 10\ HCO_3^- = Zn_5(CO_3)_2(OH)_{6\ (s)} + 8\ CO_2 + 2\ H_2O \qquad (2.1)$$

After the mixing of the stock solutions the reactors were immediately sealed and pressurized at pCO_2 ~ 10 atm (within ~10 min after mixing). The low pH conditions (pH 5.4 ± 0.2), provoked by the prevailing elevated pCO_2, lead to the dissolution of hydrozincite and the subsequent formation of smithsonite according to the overall reaction

$$Zn_5(CO_3)_2(OH)_{6\,(s)} + 3\ CO_2 \rightarrow 5\ ZnCO_{3\,(s)} + 3\ H_2O. \qquad (2.2)$$

In total 20 experiments were performed, with reaction times ranging from 465 to 72620 min (about 8 hours to 50 days) in order to follow the temporal evolution of smithsonite formation as well as its oxygen isotope composition. At the end of each experiment the reactor was quenched and subsequently the solution was separated from the precipitate using vacuum filtration and 0.1 µm filters (Millipore, cellulose acetate). Aliquots (1 mL) were sampled from the reactive solution in-situ for alkalinity and 10 mL aliquots for oxygen isotope analyses of the solution. Additional, an aliquot was acidified to a 2 % HNO_3 matrix for analysis of Zn and Na concentrations using HNO_3 of suprapure grade (Roth ROTIPURAN®). The separated precipitates were thoroughly rinsed with MilliQ water three times to remove adsorbed Zn ions from the solid surface and subsequently dried at 40 °C for solid phase characterization.

2.2.2 Analytics

2.2.2.1 Solid characterization

The collected solids were analyzed using Attenuated Total Reflectance – Fourier Transform Infrared Spectroscopy (ATR-FTIR; Perkin Elmer Spektrum 100) equipped with a $ZnSeO_4$ crystal in the wavenumber range from 650 to 4000 cm^{-1}. X-ray powder diffraction (XRD) patterns of the precipitates were measured using a PANalytical X´Pert PRO diffractometer and Co-Kα-radiation (40 mA, 40 kV) over 50 min at a range from 4° to 85° and a scan speed of 0.03° min^{-1}. The mineral phases were quantified by Rietveld refinement using the PANalytical X'Pert HighScore Plus software with its associated PDF-2 database. Selected solids were imaged using a ZEISS DSM 982 Gemini scanning electron microscope (SEM) operating at 2 kV accelerating voltage.

2.2.2.2 Chemical analyses

Alkalinity of the reactive solutions was measured by potentiometric titration using 0.01 M HCl and a Schott TitroLine alpha plus titrator with an uncertainty of ± 2 %. The pH of the same aliquots was measured using a WTW IDS pH-meter combined with a SenTix® 945 pH gel electrode with a glass shaft from WTW, calibrated against NIST standard buffers at pH = 4.01, 7.00 and 10.01 at 20 °C (analytical error: ± 0.03 pH units). Aqueous concentrations of Zn and Na were analyzed in acidified (2% HNO_3) aliquots by inductively coupled plasma optical emission spectroscopy using a Perkin Elmer Optima 8300 DV ICP-OES. A range of SPS-SW2 Batch 130 and NIST 1640a standards were measured at the beginning and end of a sample series and had an analytical error (2s, 3 replicates) of ± 3 % for all elements relative to the standards.

2.2.2.3 Geochemical modeling

Aqueous speciation of the reactive solutions, ion activities and saturation degree (Ω = IAP/solubility constant) of the reactive solutions with respect to smithsonite (see Table 2.1), hydrozincite, and zincite were calculated using PHREEQC software (Parkhurst and Appelo, 1999) together with its MINTEQ.V4 database as well as PHREEPLOT (Kinniburgh and Cooper, 2011) to establish a stability diagram of the Zn-CO_2-H_2O system.

Table 2.1: Temperature, pH, duration, added $NaHCO_3$ and $Zn(NO_3)_2$ of the experimental solution. $\delta^{18}O$ values of the precipitates relative to Vienna Standard Mean Ocean Water (VSMOW). $10^3 ln\alpha(^{18}O)_{precipitate–water}$: Oxygen isotopic fractionation between the precipitate and water ($\delta^{18}O_{water}$ = −9.58 ± 0.33, ‰; VSMOW).
[1] hydrozincite precipitated at the initial stage of the experiments at 25 °C
s = precipitation of smithsonite by using a stirred reactor

No.	T (°C)	pH	t (min)	added $NaHCO_3$ (mM)	added $Zn(NO_3)_2$ (mM)	$\Delta^{18}O$ precipitate	$10^3(^{18}O)$ precipitate-water	Ω precipiate
Precursor phase (hydrozincite)								
T25_0[1]	25	5.83	0	199.8	40.9	22.75	32.11	$10^{-7.01}$
Smithsonite (non-stirring)								
T25_1.1	25	5.31	465	228.7	43.5	19.43	28.97	13.49
T25_1.2	25	5.42	1160	199.5	44.2	20.11	29.64	26.30
T25_1.3	25	5.35	1410	249.5	43.2	20.49	29.95	13.80
T25_1.4	25	5.46	4485	199.6	42.1	21.24	30.69	8.32
T25_1.5	25	5.41	10050	201.4	42.8	20.77	30.32	3.80
T25_1.6	25	5.40	20150	199.4	43.2	20.74	30.26	3.24
T25_1.7	25	5.48	30270	202.0	42.8	20.87	30.36	2.09
T25_1.8	25	5.39	58790	201.2	43.0	21.05	30.41	1.74
T25_1.9	25	5.38	72620	207.7	44.2	21.06	30.50	1.05
T40_1	40	5.32	24240	98.1	21.8	17.93	27.35	3.89
T40_2	40	5.54	4125	199.8	39.1	18.09	27.28	6.17
T60_1	60	5.50	18815	100.2	20.0	14.41	23.79	7.24
T60_2	60	5.06	26930	103.0	21.1	14.23	24.32	2.14
T80	80	5.48	10035	100.0	21.0	12.22	21.38	10.96
Smithsonite (stirring)								
T25s_1.1	25	5.61	490	226.4	36.9	21.06	30.44	57.54
T25s_1.2	25	5.51	930	188.5	39.8	20.6	30.02	44.67
T25s_1.3	25	5.45	1345	170.1	39.8	19.99	29.51	39.81
T25s_1.4	25	5.40	4490	179.0	38.5	20.14	29.64	28.18
T25s_1.5	25	5.38	10170	166.4	39.5	19.87	29.34	26.92
T25s_1.6	25	5.43	20040	202.1	39.9	19.84	29.35	3.80

2.2.2.4 Oxygen isotopic analyses

The most common way to analyze the oxygen isotope composition of solid carbonates is to use a modification of the original phosphoric acid reaction technique developed by McCrea (1950). The oxygen isotope composition of smithsonite ($\delta^{18}O_{smithsonite}$) was measured with a Gasbench II sample preparation device interfaced to a Thermo Finnigan DeltaplusXP a Finnigan GasBench II mass spectrometer using the common phosphoric acid method (Révész and Landwehr, 2002; Spötl and Vennemann, 2003; Paul and Skrzypek, 2007). To measure the oxygen isotope composition of the precipitates, aliquots of approximately 500 µg material were transferred into 10 mL glass vials and flushed with helium, using a gas flow of 100 mL/min to remove residual air from the sample vials. Phosphoric acid (99 %) added a couple of drops into each sample vial; the produced CO_2 is manually transferred onto a Gas Chromatography column using a flow rate of 1.5 mL/min at 72 °C, where the CO_2 was chromatographically separated from other components of the gas sample. The analytical error of the $\delta^{18}O_{smithsonite}$ values, reported relative to the VPDB standard, was ± 0.1 %.

The oxygen isotope ratios of the final reactive solution were measured in 0.3 mL sub-samples with the classical CO_2–H_2O equilibration method (Epstein and Mayeda, 1953) using a dual inlet Thermo Finnigan Deltaplus mass spectrometer coupled to an automated preparation unit adopted from Horita et al. (1989). The measurements were carried out at 24 °C with a precision < 0.1 ‰. All $\delta^{18}O_{water}$ values are reported relative to VSMOW (Vienna Standard Mean Ocean Water), calculated using equations by Coplen et al. (1983).

The measured $\delta^{18}O_{smithsonite}$ values were expressed on the VPDB scale using the normalization protocol IUPAC developed by Kim et al. (2015) coupled with the phosphoric acid fractionation factor for smithsonite reported by Gilg et al. (2003) for the reference materials NBS 19 and NBS 18 at 72 °C. The $\delta^{18}O_{smithsonite}$ values were converted to the VSMOW scale using the expression

$$\delta^{18}O_{VSMOW} = 30.92 + 1.03092 * \delta^{18}O_{VPDB} \qquad (2.3)$$

The oxygen isotopic fractionation factor between smithsonite and water was calculated using the equation

$$\alpha_{smithsonite\text{-}water} = (1000 + \delta^{18}O_{smithsonite}) / (1000 + \delta^{18}O_{water}) \qquad (2.4)$$

2.2.3 Ab initio calculations of mineral-water vapor oxygen isotopic fractionation factors at the harmonic level

The equilibrium mineral-water vapor fractionation of oxygen isotopes is obtained by combining the β-factors of both phases. The isotopic fractionation factor of an element between two phases *A* and *B*, is defined as the overall ratio of isotopes *Y* and *Y** in the phase *A* as compared with the same ratio in *B*. Both phases *A* and *B* contain two isotopic forms *Y* and *Y**. *Y** corresponds to the least abundant isotope. The β-factor corresponds to the isotopic fractionation factor of *Y* between the phase *A* and a perfect gas of *Y* atoms. This quantity can be computed, with the harmonic approximation, from the vibrational frequencies of the phase of interest (Bigeleisen and Mayer, 1947). The β-factor of water vapor in the harmonic approximation is computed following Méheut et al. (2007). The β-factors of calcite and smithsonite are computed from their phonon frequencies with equations (8) and (16) of Méheut et al. (2007). The phonon frequencies are computed from first-principles using density functional theory (DFT) (Hohenberg and Kohn, 1964; Kohn and Sham, 1965). The calculation was based on the exchange-correlation functional of Perdew, Burke and Ernzerhof (PBE) (Perdew et al., 1996), a plane-wave basis set, and atomic pseudopotentials as implemented in the Quantum Espresso package. The pseudopotentials used for O and H are described in the electronic annexes of Méheut et al. (2007). The pseudopotentials used for Ca and Zn were taken from the PSlibrary (Dal Corso, 2014). For the C pseudopotential, we used the $1s^2$, $2s^2$, $2p^2$ configuration, with core radius 1.23, 1.23 a. u., respectively.

Computational details for water vapor are the same as in Méheut et al. (2007). For calcite and smithsonite, electronic wave-functions are expanded in plane-waves up to an energy cutoff $\varepsilon_{cut} = 80$ Ry and the charge density cut-off is set to 4 ε_{cut}. The electronic structure integration is performed by sampling the first Brillouin zone with a 3x3x3 k-points grid according to the Monkhorst-Pack scheme (Monkhorst and Pack, 1976).

Phonon frequencies are computed using linear response theory (Baroni et al., 2001) with the Quantum Espresso package (Giannozzi et al., 2009). Interatomic force-constants are obtained from the dynamical matrices computed exactly (within DFT) on a 3 x 3 x 3 grid of q-vectors.

Long-range effects are taken into account by computing Born effective-charges and static dielectric constants (Baroni et al., 2001). Dynamical matrices and thus phonon frequencies can then be obtained in any point of the reciprocal space by Fourier-interpolation of the force constants. For smithsonite, the β-factor is converged with a 6 x 6 x 6 interpolation grid.

2.3 Results

2.3.1 Mineralogy of the precipitates

The collected FT-IR spectra of synthetic smithsonite compared to those of the intermediate reaction product hydrozincite can be seen in Fig. 2.2A. Smithsonite exhibits vibration bands at 742 (carbonate v_4 in phase bending mode), 841 (carbonate v_2 bending mode), 1078 (carbonate v_1 stretching mode) and 1378 cm^{-1} (carbonate v_3 vibrational mode) in agreement with Hales and Frost (2007). Note here that it is generally expected that the v_2 bending mode of carbonates lay within the frequency range from 890 to 850 cm^{-1} (Farmer, 1974), a range of values that is somewhat higher compared to those of our study (Fig. 2.2A). The occurrence however of the v_2 band at 841 cm^{-1} – observed in this study – is in excellent agreement with that reported by Hales and Frost (2007) for smithsonite. The infrared spectrum of hydrozincite shows additional infrared bands to smithsonite at 949 cm^{-1} and 3306 $cm^{-}1$, both attributed to hydroxide vibrations (Stoilova et al., 2002). The X-ray diffraction pattern of the precipitated solid is compared to a reference smithsonite spectrum in Fig. 2.2B, which suggests smithsonite to be the sole reaction product in all experiments performed at elevated CO_2 pressure.

From SEM imaging (Fig. 2.3A) it can be seen that the initially precipitated hydrozincite consists of nanosized spherical particles with less than 1 µm in diameter that are similar in form to the hydrozincite shape documented earlier by Wahab et al. (2008), whereas in the final reaction product no hydrozincite is present as it is confirmed by both XRD and SEM. In addition, Fig. 2.3 illustrates changes in the texture of the growing smithsonite crystals throughout the experimental runs and for distinct formation temperatures. For instance, in experiments at 25 °C, the size of crystal aggregates increased with reaction time. Smithsonite incubated for 1160 and 20150 min (Fig. 2.3B and C) comprised of crystal aggregates with a diameter of 5 µm. At 30270 min reaction time the diameter of the crystal aggregates is about 10 µm (Fig. 2.3D), whereas at 72620 min reaction time the diameter of the crystal aggregates increased up to about 20 µm (Fig. 2.3F). The crystal aggregates of smithsonite consist of rhombohedral crystals with an edge length of about 1 µm. In contrast, at higher temperatures the edge length of the rhombohedral smithsonite crystals increased, but crystal aggregates are in the same dimension (Fig. 2.3G at 60 °C for 26930 min).

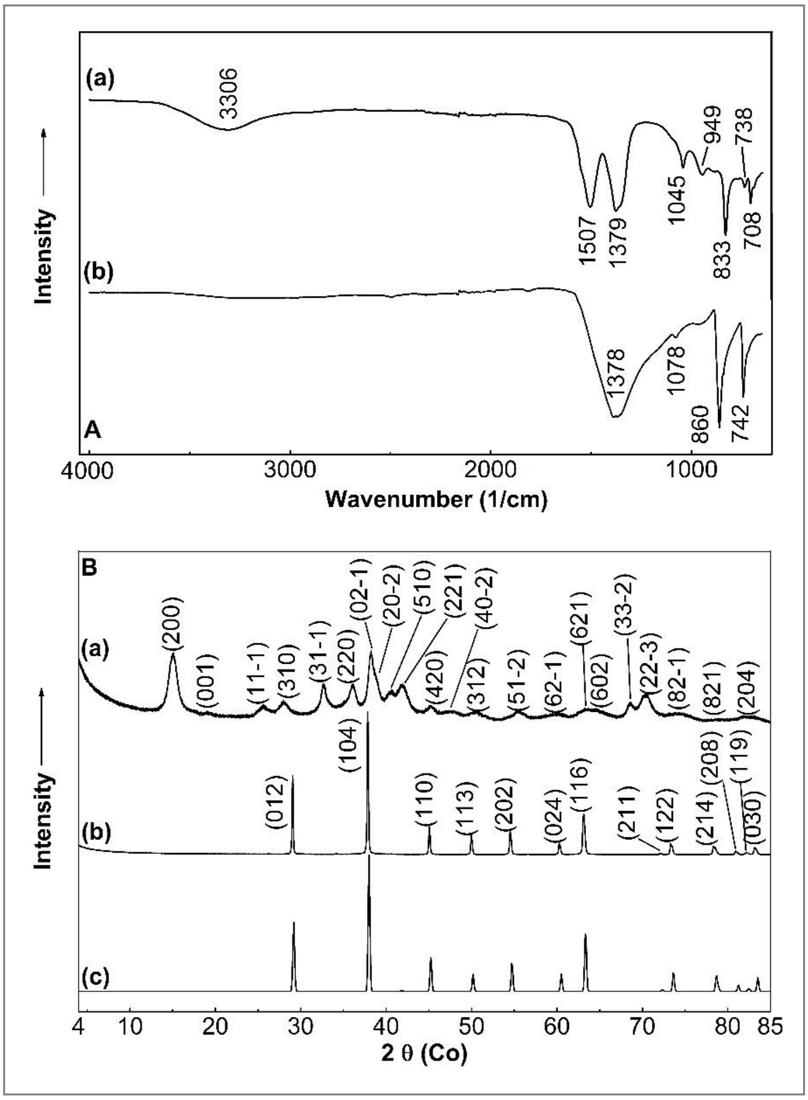

Figure 2.2: (A) Typical FT-IR spectra of (a) precipitated hydrozincite (exp. T25_0) from the beginning of each experiment at ambient conditions at a reaction time of 1 min and (b) precipitated smithsonite from exp. T25_1.1 at 10 pCO_2 (atm) and 25 °C at a reaction time of 480 min; and (B) Characteristic X-ray diffraction pattern of (a) precipitated hydrozincite (exp. T25_0) from the beginning of each experiment at ambient conditions at a reaction time of 1 min, (b) precipitated smithsonite from exp. T25_1.1 at 10 pCO_2 (atm) and 25 °C at a reaction time of 480 min and (c) smithsonite (FIZ Karlsruhe, ICSD database; PDF-number: 01-083-1765 8-449).

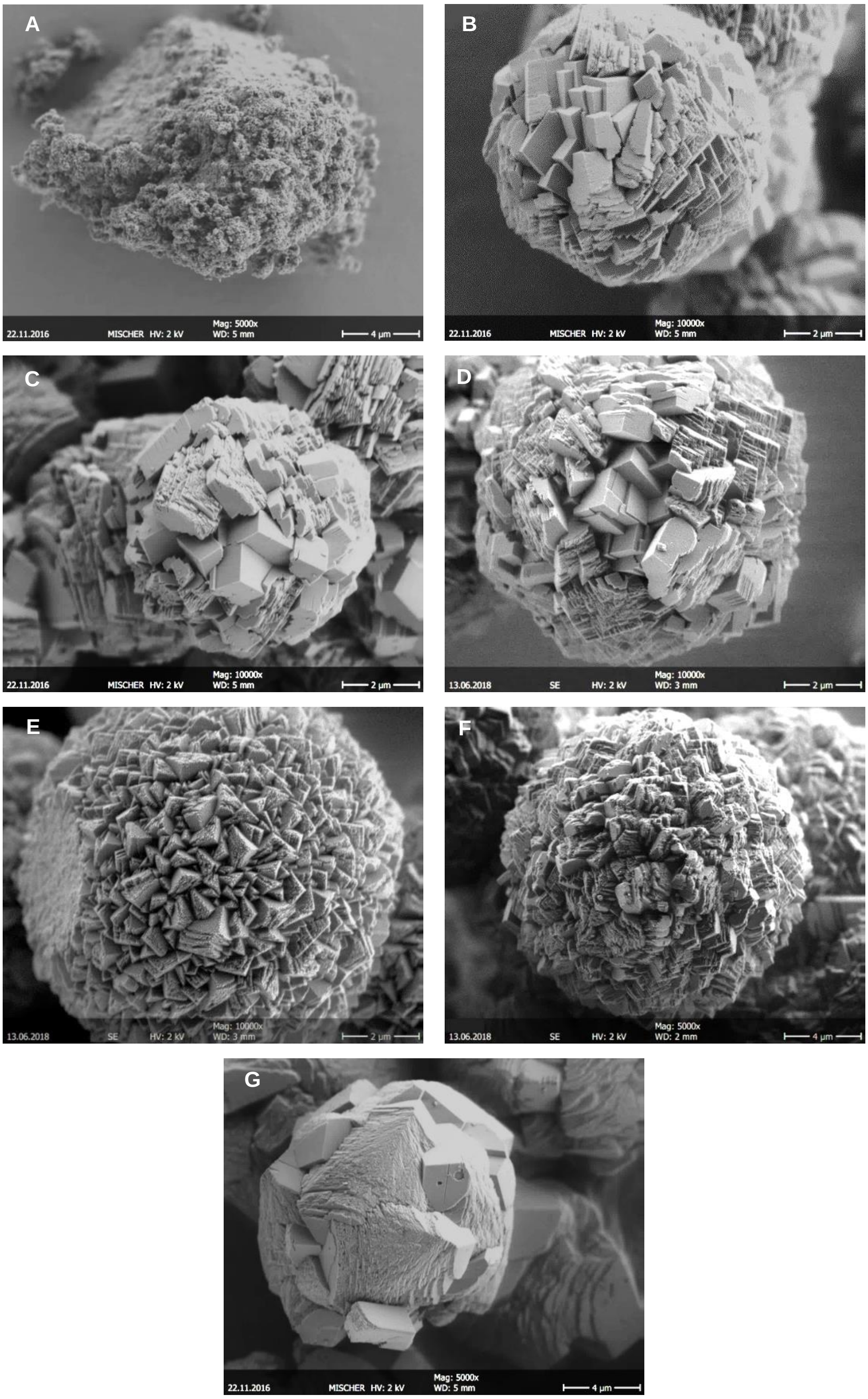
A
22.11.2016 MISCHER HV: 2 kV Mag: 5000x WD: 5 mm 4 µm
B
22.11.2016 MISCHER HV: 2 kV Mag: 10000x WD: 5 mm 2 µm
C
22.11.2016 MISCHER HV: 2 kV Mag: 10000x WD: 5 mm 2 µm
D
13.06.2018 SE HV: 2 kV Mag: 10000x WD: 3 mm 2 µm
E
13.06.2018 SE HV: 2 kV Mag: 10000x WD: 3 mm 2 µm
F
13.06.2018 SE HV: 2 kV Mag: 5000x WD: 2 mm 4 µm
G
22.11.2016 MISCHER HV: 2 kV Mag: 5000x WD: 5 mm 4 µm

Figure 2.3: Scanning electron microphotographs of precipitated (A) hydrozincite (characteristic transition phase precipitated at 25 °C in all experiments; exp. T25_0) and (B) typically precipitated smithsonite (exp. T25_1.2; pCO_2 = 10 atm; 25 °C; 1160 min), (C) smithsonite (exp. T25_1.6; pCO_2 = 10 atm and 25 °C at 20150 min reaction time), (D) smithsonite (exp. T25_1.7; pCO_2 = 10 atm; 25 °C; 30270 min), (E) smithsonite (exp. T25_1.8; pCO_2 = 10 atm; 25 °C; 58790 min), (F) smithsonite (exp. T25_1.9; pCO_2 = 10 atm; 25 °C; 72620 min), and (G) smithsonite (exp. T60_2; pCO_2 = 10 atm; 60 °C; 26930 min).

2.3.2 Chemical composition of the reactive solution

The chemical composition of the reactive solution was used to calculate the temporal evolution of pH and supersaturation in respect to smithsonite. The pH of the reactive solution (see Fig. 2.4A) for the experiments using the non-stirring reactor is increasing between 465 and 1410 min with a maximum at about 1160 min, whereas the pH for the experiments using the stirring reactor decreased over the same time interval. The pH for both experiments - using the stirring and non-stirring reactor - is approaching a constant pH of 5.4 ± 0.05 with increasing reaction time.

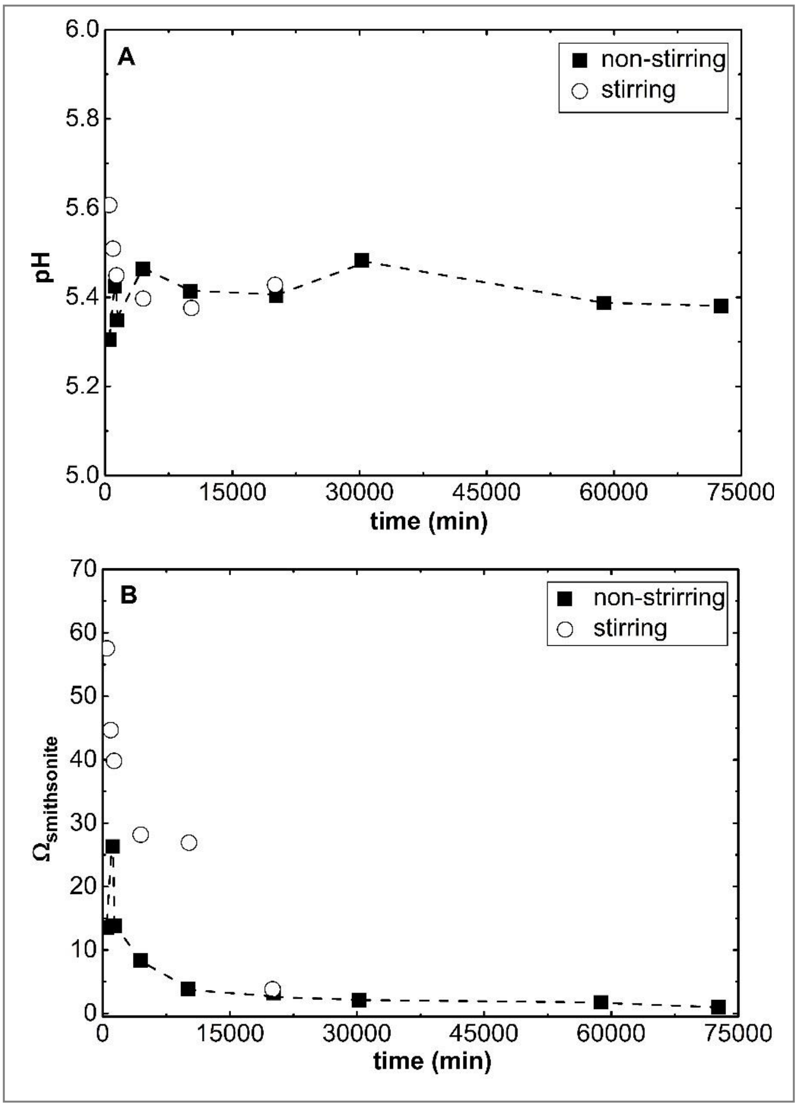

Figure 2.4: (A) pH of precipitating solution as a function of reaction time at 25 °C in the stirring versus non-stirring reactor; and (B) Saturation degree in respect to smithsonite (at steady state Ωsmithsonite = 1.1 ± 0.3) plotted as a function of reaction time at 25 °C in the stirring versus non-stirring reactor. The curve was connected via two points by a single line.

The supersaturation of the reactive solution in respect to smithsonite follows the evolution of pH, i.e. decreasing between 490 and 1345 min (Fig. 2.4B) for the experiments using the stirring reactor. In contrast, between 465 and 1410 min the $\Omega_{smithsonite}$ for the experiments using the non-stirring reactor show a maximum at about 1160 min. As with pH, the supersaturation of the reactive solution with respect to smithsonite reaches an approximately equal value in both experiments of $\Omega_{smithsonite} = 1.1 \pm 0.3$. The pH and the supersaturation state evolution indicates the approach of chemical equilibrium conditions for smithsonite and confirms the accuracy of solubility data from Schindler et al. (1969). The pH-induced $\Omega_{smithsonite}$ evolution is strongly based on the pH dependence of DIC species distribution. The pH difference in the non-stirring versus stirring reactive solutions can be likely explained by the delayed neutralization of the in CO_2 loaded solution due to hydrozincite transformation to smithsonite at non-stirring conditions.

2.3.3 Oxygen isotopic fractionation factor between smithsonite and solution at 25°C

The temporal evolution of the oxygen isotope fractionation between carbonate precipitate and water has been studied in detail for experiments performed at 25 ˚C. The oxygen isotopic composition of the water used in our experiments was measured to be $\delta^{18}O_{water} = -9.58 \pm 0.33$ ‰ (VSMOW; n = 20). The temporal evolution of the $10^3\ln\alpha_{smithsonite\text{-}water}$ values is displayed in Fig. 2.5.

The $10^3\ln\alpha_{smithsonite\text{-}water}$ value at ≥ 10000 min (i.e. 7 days) of the experimental run time is about 30.5 ± 0.1 ‰ using the non-stirring reactor, whereas it is about 29.4 ± 0.1 ‰ in experiments conducted with the stirring reactor (Table 2.1). Note here, that the apparent $10^3\ln\alpha_{hydrozincite\text{-}water}$ value between hydrozincite and water is slightly higher (32.1 ± 0.1 ‰ at 25 °C; see Table 2.1) compared to that measured between smithsonite and water. Although the final $\alpha_{smithsonite\text{-}water}$ values are almost identical within the overall accuracy of the used experimental approach, the temporal evolution using the stirring and non-stirring reactor were significantly different at the beginning of the runs. The $10^3\ln\alpha_{smithsonite\text{-}water}$ values decrease by using the stirring reactor, whereas the experiments performed in the non-stirring reactor indicate an increase of $\alpha_{smithsonite\text{-}water}$ with time.

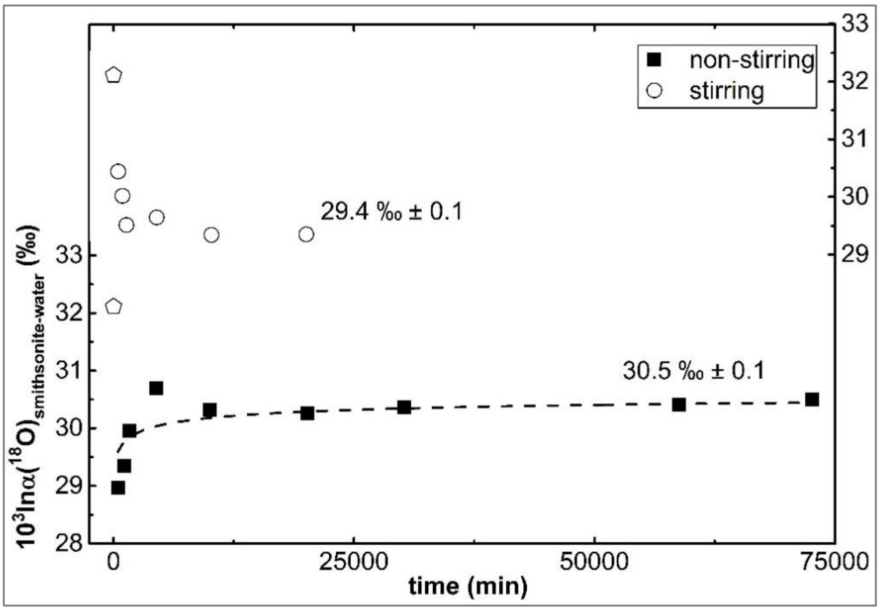

Figure 2.5: Temporal evolution of the $10^3\ln\alpha(^{18}O)$smithsonite-water value for the oxygen isotope fractionation between the precipitate and water for experiments conducted at 25 °C as a function of reaction time in the stirring versus non-stirring reactor. The pentagon symbol represents the oxygen isotope fractionation of the precipitated hydrozincite (t = 0 min). The curves were fitted using a calculation of Origin: $10^3\ln\alpha_{smithsonite\text{-}water} = a - b * \log(c * \text{time [min]})$. Errors are with the size of the symbols.

These findings indicate that a synthesis duration of about 10000 min (Fig. 2.5) is likely needed in the experimental runs to approach a constant isotopic fractionation between smithsonite and water at 25 °C, where also thermodynamic equilibrium is approached (see Fig. 2.4A and B). Accordingly, less time for approaching constant isotope composition can be expected for the experiments at elevated temperatures.

2.3.4 Oxygen isotopic fractionation factor between 25 and 80 °C

As a constant isotopic fractionation between smithsonite and water is reached at about 10000 min for T ≥ 25 °C, the obtained $10^3\ln\alpha_{\text{smithsonite-water}}$ values at t ≥ 10000 min were used to obtain a T dependence of apparent oxygen isotope fractionation between smithsonite and water up to 80 °C (see Table 2.1; Fig. 2.6).

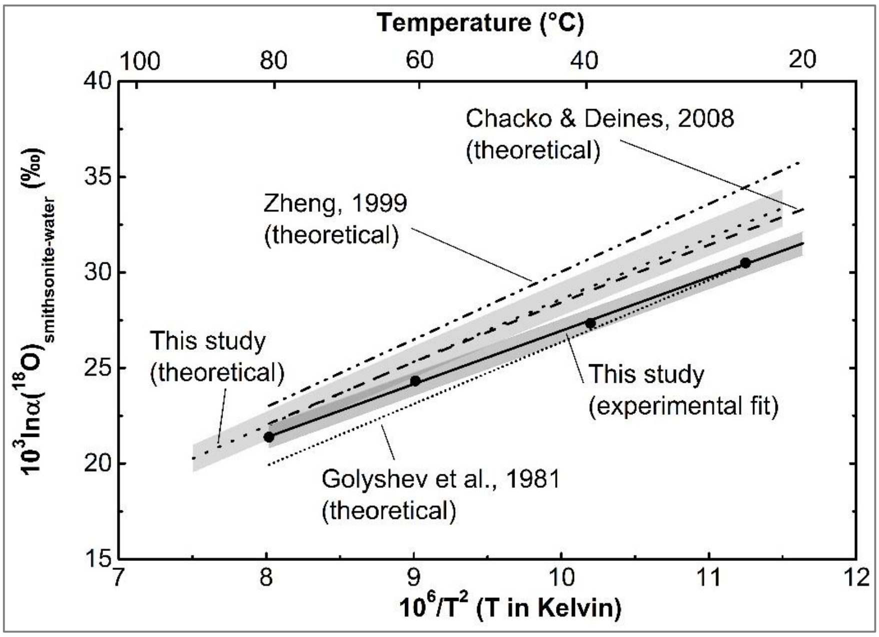

Figure 2.6: Oxygen isotope fractionation between smithsonite and water as a function of temperature. Solid symbols represent the obtained data from this study for smithsonite formation in the non-stirring reactor (only isotope values between 25 °C and 80°C for a reaction time ≥ 10000 min are shown, where oxygen isotope fractionation is approaching equilibrium). Dashed line represents the theoretical calculation of Chacko and Deines (2008), dashed-dotted line of Zheng (1999), small dotted line of Golyshev et al. (1981) and the dotted line shows the ab-initio calculation (of the present study).

The experimental findings indicate a strong negative temperature control on $10^3\ln\alpha_{\text{smithsonite-water}}$ according to the expression

$$10^3\ln\alpha_{\text{smithsonite-water}} = (2.79 * 10^6/T^2 - 0.95) \pm (0.06 * 10^6/T^2 + 0.60) \quad (2.5)$$

where high temperatures result in lower α values that can be attributed to near isotopic equilibrium conditions.

2.3.5 Theoretical calculations of calcite-water and smithsonite-water oxygen isotope fractionation at equilibrium

Cell parameters of calcite and smithsonite are obtained at zero pressure until the residual forces are less than 10^{-3} Ry/Å (Table 2.2). They are generally overestimated by around 1 - 2 %, which is the usual trend with GGA PBE functional. A good agreement is observed between calculated frequencies and experimental ones (Table 2.3).

Table 2.2: Structural parameters of calcite and smithsonite, compared with experiment (exp.) and previous calculations (PBE). The numbers in parenthesis refer to uncertainties on the last significant digit.

[1] Effenberger et al. (1981)

[2] Schauble et al. (2006)

[3] Ducher et al. (2016)

	Calcite			**Smithsonite**		
	This work	**Exp[1]**	**PBE[2]**	**This work**	**Exp[1]**	**PBE[3]**
a (Å)	5.0600	4.9896[2]	5.0352	4.7207	4.6526[7]	4.714
c (Å)	17.2046	17.0610[11]	17.2194	15.3211	15.0257[22]	15.28
x(O)	0.25729	0.25682[11]		0.27550	0.27636[11]	

Table 2.3: Comparison of model phonon frequencies in smithsonite and calcite with experimental data and other calculations (PBE). E_g and A_{1g} are Raman-active, A_{2u} and E_u are IR-active, A_{1u} and A_{2g} are silent modes. For IR-active modes, LO and TO frequencies are reported. For smithsonite, measurements (exp.) are from Frost et al. (2008a) for Raman, and Frost et al. (2008b) for infrared. For calcite, measurements (exp.) are from Gillet et al. (1993) for Raman, and from Hellwege et al. (1970), Cowley and Pant (1973), White (1974), and Gillet et al. (1996) for infrared.

	Calcite			**Smithsonite**		
mode	**This work**	**Exp**	**PBE**	**This work**	**Exp**	**PBE**
E_g	177	196	78	152	156	151
	277	304	278	264	281	264
	693	730	697	680	711,709	689
	1342	1405-1409	1371	1372	1434	1392
A_{1g}	1047	1092	1063	1045	1086	1059
A_{2u}	139-231			114-142	92-132	112-140
	311-355			276-385	303-387	275-386
	810-827	(842),870	818	824-838	872-900	840-854
E_u	149			117-129	102-123	114-127
	183-222			205-216	223-239	205-216
	260-336			268-363	297-380	267-364
	705-707	(729),744		680-681	711	689-690
	1339-1496	(1335),1440	1369	1342-1486	1407-1549	1361-1506
A_{1u}	208			274		
	1047			1045		
A_{2g}	281			180		
	372			299		
	817			828		

Generally, the calculated frequencies underestimate experimental results by a few %, but the relative difference is varying depending on the modes. The ratio between calculated harmonic frequencies and corresponding experimental frequencies is discussed in detail in Appendix A. For calcite and smithsonite this ratio was found to be essentially identical for the two carbonate minerals, and equal to 0.957 ± 0.006, where the error stands for the standard error on this ratio. This is consistent with the results from Schauble et al. (2006) who concluded on the adequacy of a unique scale factor for several anhydrous carbonate minerals.

The mineral-water vapor fractionation factors, calculated from the raw ab initio-based harmonic frequencies, are given as a function of temperature in Table 2.4 and represented on Figure A.3 (Appendix A). These calculations are affected by two errors of different origin. First, harmonic frequencies calculated within our approach underestimate experimental harmonic frequencies by a few percent. This underestimation was corrected by multiplying all mode frequencies of a given material by an identical scale factor, deduced from the comparison of experimental harmonic frequencies and calculated harmonic frequencies (see details in Appendix A). For water vapor, experimental harmonic frequencies are available, and can be compared to our calculation (see Table 1 of Méheut et al., 2007). The obtained scaling factor is 0.954 ± 0.003 (1SE) (see details in Appendix A). For calcite and smithsonite, however, the only available experimental frequencies are anharmonic. Anharmonic effects in calcite and smithsonite are nevertheless expected to be small (see below), and we therefore used the experiment over calculation frequency ratio discussed above (0.957 ± 0.006) as our scaling factor.

Table 2.4: Fits of $10^3\ln\alpha(^{18}O)_{\text{mineral-water(vapor)}}$ for 0 - 400°C, with $x = 10^3/T$. PBE refers to the uncorrected calculation. For the correction, see text. The estimated error on the corrected laws results from the propagation of the uncertainty on the scaling factor (1SE, see Appendix A) and from the 0.5‰ error (treated as an uncertainty) due to the neglect of anharmonicity for calcite and smithsonite (see text).

Mineral	Regression
calcite (PBE)	$4.257 - 14.305x + 8.863x^2 - 0.656x^3$
smithsonite (PBE)	$4.367 - 14.502x + 9.416x^2 - 0.7378x^3$
Calcite (corrected)	$3.9 - 13.8x + 9.42x^2 - 0.712x^3$
Smithsonite (corrected)	$4.0 - 14.0x + 10.02x^2 - 0.737x^3$
error of corrected laws	$0.7 + 0.07x - 0.004x^2 + 9.10^{-5}x^3$

Second, the expressions used for the β-factors (equation (11) of Méheut et al., 2007 for water vapor, equation (16) of Méheut et al., 2007 for the carbonates) are based on the harmonic approximation. For water vapor, Richet et al. (1977) proposed a simple correction for anharmonic effects based on experimental frequencies (equation 49 of Richet et al., 1977). We simply added this correction to our water vapor β-factor. For calcite and smithsonite, the vibrations were assumed to be harmonic, and therefore no anharmonic correction was applied. This situation – a gas treated anharmonically, and carbonates considered harmonic – has been discussed by Chacko and Deines (2008) study. Based on the estimation of anharmonic effects in calcite by Gillet et al. (1996) and Polyakov (1998), these authors concluded that these hypotheses may lead to an over- or underestimation by about 0.5 ‰ of gas-carbonate fractionation.

The corrected mineral-water vapor fractionation factors are given as a function of temperature in Table 2.4 and represented in Figure A.3 (Appendix A). The uncertainty on the obtained corrected law, resulting both from the uncertainty on the scaling factor and from the estimated 0.5 ‰ additional error discussed above, is also given on Table 2.4 and represented on Figure A.3 (Appendix A). To obtain a mineral / liquid-water fractionation (calcite: Fig. A.2 in Appendix A; smithsonite: Fig. 2.6), we combined our calculated calcite / gas-water fractionation with the liquid / gas-water experimental fractionation determined by Horita and Wesolowski (1994). If we limit ourselves to the 0 – 100 °C temperature interval, these laws can be given as:

$$10^3\ln\alpha_{\text{calcite-liquid water}} = (2.65 * 10^6/T^2 - 4.87) \pm (0.025 * 10^6/T^2 + 0.90) \qquad (2.6)$$

$$10^3\ln\alpha_{\text{smithsonite-liquid water}} = (3.21 * 10^6/T^2 - 3.63) \pm (0.025 * 10^6/T^2 + 0.90). \qquad (2.7)$$

2.4 Discussion

2.4.1 Reaction mechanisms and pathways

Figure 2.7 shows the individual stability fields of zincite, hydrozincite and smithsonite as a function of the partial pressure of CO_2 and pH according to the used thermodynamic data. At the beginning of each experiment hydrozincite is immediately precipitating at quasi neutral pH conditions (pH ~ 6.8) at 25 °C, and consistently the solution composition is plotting within the stability field of hydrozincite (Fig. 2.7). The increase of the pCO_2 pressure to about 10 atm results in a pH decrease.

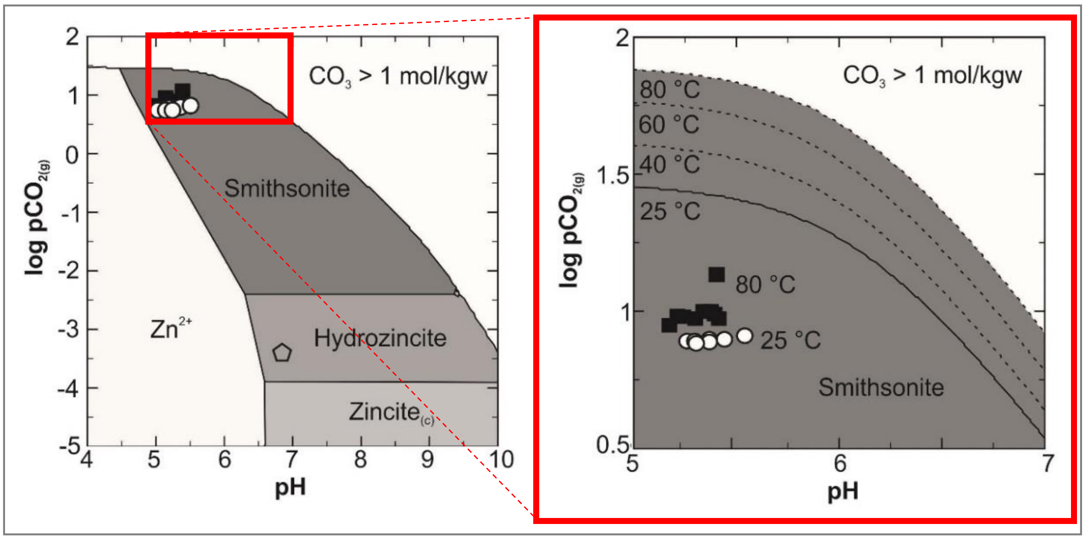

Figure 2.7: Stability fields of zincite, hydrozincite versus smithsonite at 25°C as a function of CO_2 partial pressure (pCO_2 in atm) and pH calculated using PHREEPLOT combined with PHREEQC software (see text for details). The pentagon symbol in the left diagram represents the initial experimental solution indicating hydrozincite formation as transition step at 25 °C and low pCO_2. The enhanced detail on the right side shows the smithsonite stability field from 25, 40, 60 to 80 °C. The open circles (stirred experiments) and closed squares (non-stirred experiments) refer to the chemical composition and the CO_2 partial pressure shift of the experimental solutions for the temperature of 25 and 80 °C calculated with PhreeqC; 40 and 60 °C data points are lying in between those for 25 and 80 °C (this study).

Accordingly, the solution composition shifts into the stability field of smithsonite at temperatures between 25 and 80 °C. Smithsonite is subsequently formed via dissolution of hydrozincite. For the final experimental solutions chemical equilibrium in respect to smithsonite solubility is reached (see saturation degrees in Table 2.1 and exemplarily shown for T = 25 °C; Fig. 2.4).

2.4.2 Kinetics versus isotope equilibrium conditions

In earlier studies it has been well established that deviation from isotopic equilibrium in carbonate systems may affect apparent $10^3\ln\alpha_{carbonate\_mineral-water}$ values (Mills and Urey, 1940; McConnaughey, 1989; Kim et al., 2006; Dietzel et al., 2009; Gabitov et al., 2012; 2013; Watkins et al., 2014). Due to the lack of oxygen isotopic equilibrium data for smithsonite precipitated in the laboratory, this study explores the temporal evolution of $\alpha_{smithsonite-water}$ at 25 °C, in order to verify the achievement of a constant oxygen isotopic fractionation between smithsonite and water as a function of reaction time (see Fig. 2.5).

As it can be seen in Fig. 2.5 $\alpha_{smithsonite-water}$ achieves quasi constant values that can be attributed to near isotopic equilibrium conditions. We note here that at a given reaction stage of the experiments kinetic effects might occur. These effects can be related to isotopic dis-equilibrium conditions among DIC species and / or high precipitation rates of carbonate minerals from solution, that can induce non-equilibrium isotopic conditions at the solid-liquid interface (e.g. Jiménez-López et al., 2001 for Mg-calcite; Dietzel et al., 2009 for calcite; Mavromatis et al., 2012 for Mg-calcite). In particular, the later effect might be valid in this study for initial hydrozincite formation due to mixing of the two stock solutions inducing extremely high supersaturation of the resulting solution with respect to hydrozincite ($\Omega_{hydrozincite} = 10^{7.01}$; see Table 2.1). On the other hand, the long term temporal evolution of the $\alpha_{smithsonite-water}$ value as it is depicted in Fig. 2.5, together with the increase in the average diameter of the formed crystal (Fig. 2.3B - F) rather suggest near equilibrium isotope exchange between smithsonite and the reactive fluid.

The temporal evolution of the oxygen isotope fractionation between smithsonite and water is divided into two parts. The first part (in the range from 465 to 1410 min) shows a contrasting behavior of the $10^3\ln\alpha_{smithsonite-water}$ values between the experiments using the non-stirring and stirring reactor (see Fig. 2.5 and discussion above). This contrasting behavior, in analogy to experiments with different agitation and shaking frequencies of Chacko et al. (1991) and Fortier (1994), might be caused by the continuous agitation of the solution in the experiments using the stirring reactor. The agitation of the solution might lead to a fast oxygen exchange rate between smithsonite and the CO_2 and follows higher oxygen isotope fractionation.

In the second part (≥ 1410 min) of the experiments the evolution of $10^3\ln\alpha_{smithsonite-water}$ values using the non-stirring and stirring reactor shows a similar behavior. With increasing reaction time (≥ 10000 min) $10^3\ln\alpha_{smithsonite-water}$ reached a constant value, suggesting near isotopic equilibrium conditions, at a similar reaction time, where isotope equilibrium between Mg-calcite and precipitating solution is reached (see Mavromatis et al., 2012; t ~ 14400 min). Note here that the transformation of hydrozincite to smithsonite proceeds via a dissolution and re-precipitation process. Therefore, isotopic memory effects from the precursor phase hydrozincite are unlikely to occur at the final stage of the experiments.

2.4.3 Oxygen isotope equilibrium fractionation between different metal carbonate minerals and water

In the present study experimental times of ≥ 10000 min were used to study oxygen isotopic between smithsonite and solution at temperatures ranging from 25 to 80 °C, at close isotopic equilibrium conditions (see discussion above; Fig. 2.6). The obtained decrease of $10^3\ln\alpha_{\text{smithsonite-water}}$ values with increasing temperature is a common feature when isotopic equilibrium is achieved also shown by other experimental studies, e.g. for calcite, aragonite, dolomite and siderite (e.g. McCrea, 1950; O'Neil et al., 1969; Tarutani et al., 1969; McConnaughey, 1989; Kim et al., 2006; Dietzel et al., 2009; Mavromatis et al., 2012; van Dijk et al., 2017), as well as in theoretical studies (Urey, 1947; Zheng, 1999; Watson, 2004; Schauble et al., 2006; Chacko and Deines, 2008; Zheng, 2011). In order to verify our experimental data in the scope of oxygen isotope fractionation between various carbonate minerals and water from other experimental studies Fig. 2.8 illustrates the respective $10^3\ln\alpha(^{18}O)$ values as a function of temperature.

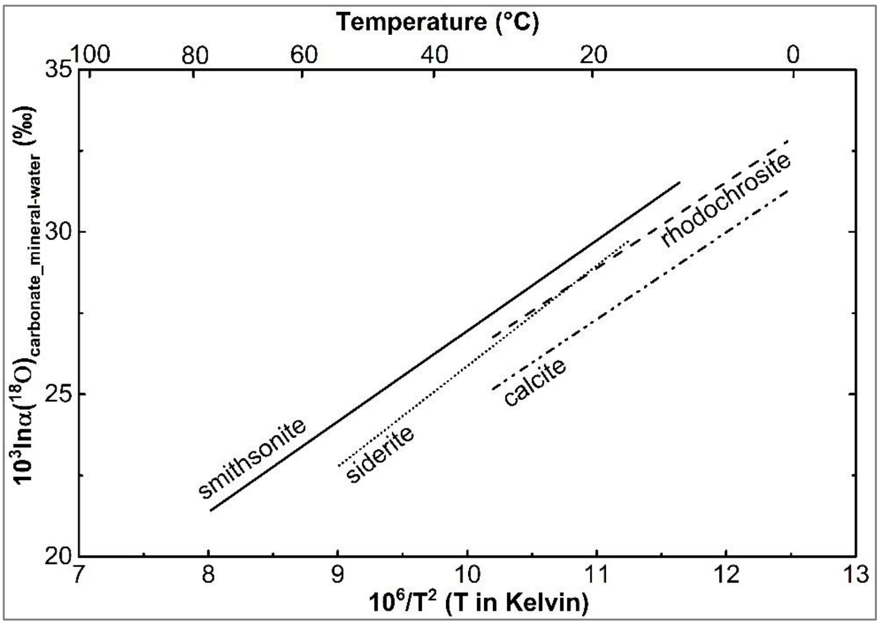

Figure 2.8: Oxygen isotope fractionation between smithsonite and water (see Eq. 2.5) as a function of temperature for those of mono-cation trigonal Me-carbonate minerals: siderite (van Dijk et al., 2017); rhodochrosite (Kim et al., 2009); calcite (Kim and O'Neil, 1997).

The most noticeable result for the oxygen isotope fractionation as a function of temperature is that all carbonate-water fractionation curves are positioned parallel to one another indicating different oxygen isotope fractionation up to several per mil between various carbonates (see also O'Neil et al. (1969) and Chacko et al. in 2001). The general finding is: the smaller the cation radius the higher the $10^3\ln\alpha(^{18}O)$ value. Chacko and Deines (2008) pointed out that both, the increase in cationic size and cationic mass, influence the preferentially incorporation of lighter oxygen isotopes in the carbonate mineral, based on internal vibrations of the carbonate and structure motions (e.g. O'Neil et al., 1969; Golyshev et al., 1981; Kim and O'Neil, 1997). Our experimental data fit into the obtained sequence of $Zn^{2+} < Fe^{2+} < Mn^{2+} < Ca^{2+}$ for mono-cation trigonal Me-carbonate minerals at isotopic equilibrium (Fig. 2.8).

2.4.4 Ab initio calculations of smithsonite-water fractionation and comparison to experimental data

The corrected theoretical oxygen isotopic fractionation factor between calcite and water obtained in our study is in good agreement both with earlier theoretical calculations (i.e. Chacko and Deines, 2008) and with experimental data sets, at least in temperatures above 40 °C (Fig. A.2 of the Appendix A). This confirms the quality of Chacko and Deines (2008) calculations and underlines the use of this correction procedure.

The three computational ab initio models exhibit the general trend of decreasing oxygen isotope fractionation with increasing temperature such as with the experimental data (see Fig. 2.6). However, the existing theoretical data (e.g. Zheng, 1999; Chacko and Deines, 2008) as well as the data from the new ab initio calculation are slightly heavier compared to the measured oxygen isotopic fractionation factors of this study. As different simulation types of liquid water can be used for theoretical calculations, we assume that the discrepancy between the theoretical calculations (e.g. Zheng, 1999; Chacko and Deines, 2008 and this study) and the experimental data from this study may be explained by less precisely described anharmonicity of liquid water and / or not completely reaching isotopic equilibrium through kinetic effect in the experiments (see discussion above). Kinetic effects might be an additional cause for the deviation between experimental and calculated data.

2.4.5 Revisiting oxygen isotope fractionation between theoretical calculations and experimental data of various carbonates

In order to classify our experimental and theoretical data, in Fig. 2.9 oxygen isotope fractionation between various carbonate minerals and water is combined as a function of their ion radius at 25 °C. As it can be seen the $10^3\ln\alpha_{\text{carbonate\_mineral-water}}$ values of the experimental data are located above for Zn, Fe and Cd, underneath for Pb and Ba and on an equal level for Mn, Ca and Sr in comparison to the theoretical calculations of Chacko and Deines (2008).

The interesting finding is that the theoretical $10^3\ln\alpha_{\text{carbonate\_mineral-water}}$ values not completely follow the trend of decreasing oxygen isotope fractionation with increasing ionic radius. For instance, though the sequence of the ionic radius is $Fe^{2+} < Mn^{2+} < Cd^{2+}$ the theoretical $10^3\ln\alpha_{\text{carbonate\_mineral-water}}$ values are increasing. Furthermore, the sequence of the ionic radius is $Sr^{2+} < Pb^{2+} < Ba^{2+}$, certainly the theoretical $10^3\ln\alpha_{\text{carbonate\_mineral-water}}$ value of cerussite forms a downward peak between strontianite and witherite. In addition, the difference between theoretical and experimental $10^3\ln\alpha_{\text{carbonate\_mineral-water}}$ values is up to 4 ‰ for Cd and 6 ‰ for Pb. In contrast, our experimental data fit well into the experimental data of the literature following the finding: the smaller the cation radius the larger the oxygen isotope fractionation.

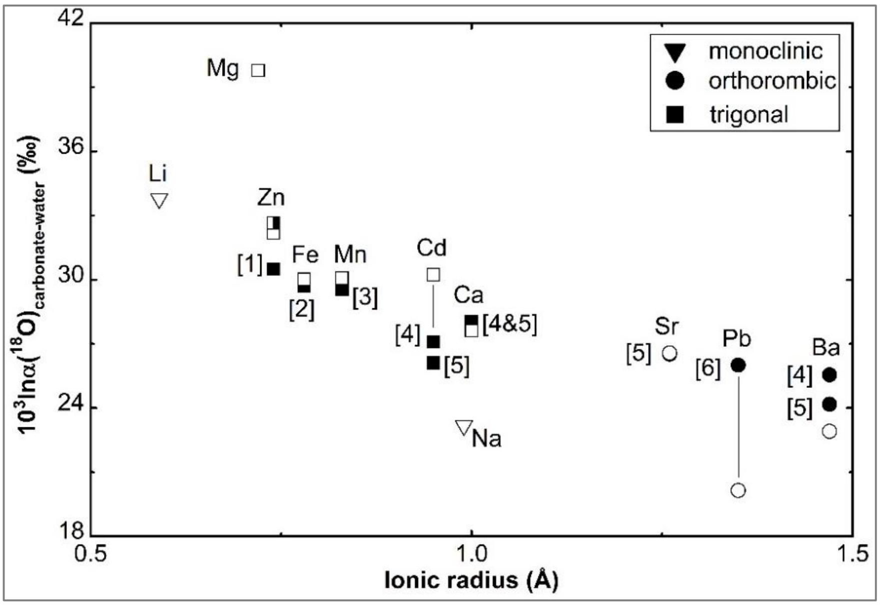

Figure 2.9: Dependence of oxygen isotope fractionation between endmember metal carbonate minerals and water at 25 °C on the respective ionic metal radius. The data given in unfilled symbols are from the ab-initio calculation of Chacko and Deines (2008) and of this study in the half-filled symbol. The data from experimental studies are illustrated in filled symbols from [1] this study; [2] van Dijk et al. (2017); [3] Kim et al. (2009); [4] Kim and O'Neil (1997); [5] O'Neil et al. (1969); [6] Melchiorre et al. (2001).

2.4.6 Implications for natural systems

The temperature-dependent oxygen isotope fractionation between carbonate minerals and water can act as a sensitive indicator for the temperature during their formation (Clayton and Epstein, 1961; O'Neil and Clayton, 1964). However, it has to be considered that the requirements and conditions to use the oxygen isotope fractionation between carbonate minerals and water as an environmental proxy are more complex in natural systems compared to experimental and theoretical studies due to (i) uncertainties in knowledge or estimation of the oxygen isotope composition of the precipitating solution (Gilg et al., 2008), (ii) use of proper mineral-water fractionation factors from literature (Boni et al., 2003; 2007; Gilg et al., 2008; this study), and (iii) unknown and / or varying physicochemical conditions during carbonate formation, such as pH, salinity, CO_2 pressure, which can affect the apparent $\alpha_{carbonate\_mineral\text{-}water}$ values e.g. due to kinetic effects.

In natural surroundings smithsonite formation is mostly related to oxidation of Zn containing solid sulfide phases by water circulation, e.g. in a deep karstic network (Alwan and Williams, 1979; Williams, 1990; Anthony et al., 2003; Boni et al., 2003) as well as in mines and deposits in Sardinia (Boni et al., 2003), in the Irish midlands (Boni et al., 2007) and in Belgium (Coppola et al., 2008). Thus, from another point of view unravelling smithsonite formation conditions may open up new insights into secondary events, which have overprinted the primary depositing mineral association. In particular, geological and environmental events, which create elevated pCO_2, can be recognized and studied by smithsonite formation via decomposition of initially formed hydrozincite.

For instance, in 2003, Boni et al. measured oxygen isotopes of different smithsonite types from the deposits of the Iglesias Valley in the southwest of Sardinia, which are dominated by Paleozoic rocks of sedimentary and igneous origin. They measured $\delta^{18}O$ values for smithsonite of 27.4 ± 0.9 ‰ (given in VSMOW). In order to calculate the smithsonite formation temperature they used the equation of Zheng (1999) and the estimated $\delta^{18}O$ values of De Vivo et al. (1987) for the reactive water between -7.0 and -4.5 ‰ (VSMOW). Hence, they calculated a formation temperature ranging between 20 and 35 °C. However, using the equation (2.5) based on our experimental data the formation temperature is ranging between 10 and 20 °C. As the experimental approach results in most reliable temperature-dependent oxygen isotope fractionation between smithsonite and water (see discussion above), we assume latter lower temperature range to be valid, which is also closer to the average air temperature in the area.

Calculation of the smithsonite formation temperature from natural samples in future studies should include the use of clumped isotopes analyses for naturally formed smithsonite in order to precisely determine the temperatures of mineral formation or overprinting / diagenetic event. Subsequently the oxygen isotopic composition of the reacting fluid can be obtained by Eq. (2.5). Secondly, an advanced approach for studying multi metal carbonate (Me) containing deposits is suggested based on the distinct oxygen isotope signatures of the above mono-cation trigonal Me-carbonate minerals to follow the variability and sequences of post-depositional changes in environmental settings. For this purpose, e.g. siderite might be of special interest as it forms exclusively at reducing conditions (Boni et al., 2003; Coppola et al., 2008). As it can be seen in Fig. 2.8, the regression line for siderite shows a different slope compared to smithsonite. Therefore, the difference in the oxygen isotope fractionation ($\Delta^{18}O_{siderite\text{-}smithsonite} = \delta^{18}O_{siderite} - \delta^{18}O_{smithsonite}$) according to the expression

$$\Delta^{18}O_{siderite\text{-}smithsonite} = 0.31 * 10^6/T^2 - 4.15 \tag{2.8}$$

may provide an interesting tool for the determination of carbonate minerals formation temperatures if close to isotopic equilibrium conditions and the identical precipitating fluid can be reasonably assumed, in particular for elevated temperatures (e.g. $\Delta^{18}O_{siderite\text{-}smithsonite} = -1.66$ ‰ at 80 °C).

2.5 Summary and Conclusions

In the present study first experimental results on the oxygen isotope fractionation between smithsonite and water are presented to study the, until now, poorly constrained $\alpha_{smithsonite\text{-}water}$ and its temperature dependence. Therefore, the formation of smithsonite was induced by the transformation of hydrozincite between 25 and 80 °C. The main conclusions of the experimental and modeling results are as follows:

(1) The temporal evolution of the oxygen isotope fractionation between smithsonite and water indicates the achievement of close to isotopic equilibrium conditions at a reaction time of about 10000 min (~7 days) at T ≥ 25 °C, independent from the hydrodynamic flow / mixing conditions of the experiments.

(2) The oxygen isotope fractionation between smithsonite and water at isotopic equilibrium can be calculated as a function of temperature from 25 to 80 °C according to expression (2.5) based on the experimental data.

(3) The $\alpha(^{18}O)_{\text{smithsonite-water}}$ values from the experimental approach fit within error to the theoretical relationship from the literature and our ab initio calculations. Discrepancies can be explained by the non-precisely described anharmonicity of water and / or by non-entirely approaching isotopic equilibrium throughout formation of smithsonite.

(4) The transformation of hydrozincite, likely forming in sulfide deposits, to smithsonite throughout exposure to solutions at elevated pCO_2 is caused by dissolution and re-crystallization reactions. This reaction paths / mechanisms and its oxygen isotope fractionation behavior can be assessed to evaluate environmental and post-depositional environmental conditions of zinc-bearing sedimentary ores.

Acknowledgements

The research was financially supported by a Marie Skłodowska-Curie Horizon 2020 'European Union Funding Programme for Research and Innovation' Project called BASE-LiNE Earth. The study was conducted at NAWI Graz Central Lab of Water Minerals and Rocks (NAWI Graz Geocentre, Austria). Thanks to A. Geisinger-Haslinger, S. Lindbichler and B. Zirngast for measuring oxygen isotope ratios of the aqueous solutions as well as A. Baldermann and S. Eichinger for measuring element concentrations by ICP-OES. The manuscript also benefited from thoughtful comments by I. Kell-Duivestein. Two anonymous reviewers and Editor-in-Chief, Michael E. Böttcher, are highly acknowledged for their insightful comments on a previous version of this manuscript.

Chapter 3

Effect of growth rate and pH on lithium incorporation in calcite

A. Füger[1,2], F. Konrad[3], A. Leis[2], M. Dietzel[1], V. Mavromatis[1,4,]

[1] Institute of Applied Geosciences, Graz University of Technology, Rechbauerstrasse 12, 8010, Graz, Austria
[2] JR-AquaConSol GmbH, Steyrergasse 21, 8010, Graz, Austria
[3] Omya GmbH, Gersheim Straße 1-2, 9722 Gummern, Austria
[4] Géosciences Environnement Toulouse (GET), CNRS, UMR 5563, Observatoire Midi-Pyrénées, 14 Avenue Edouard Belin, 31400 Toulouse, France

Published in Geochimica et Cosmochimica Acta, 1 March 2019, Vol. 248, Pages 14-24 (https://doi.org/10.1016/j.gca.2018.12.040)

Abstract - Carbonates are only a minor sink of oceanic lithium, yet the presence of this element and its abundance relative to other metal cations in natural carbonate minerals is routinely used as a paleo-environmental proxy. To date, however, experimental studies on the influence of physicochemical parameters that may control lithium incorporation in calcite, like pH and precipitation rate, are scarce. Therefore, we experimentally studied Li incorporation in calcite to quantify the apparent partitioning coefficient ($D^*_{Li} = \frac{(c_{Li}/c_{Ca})_{calcite}}{(m_{Li^+}/m_{Ca^{2+}})_{solution}}$) between calcite and reactive fluid as a function of calcite growth rate and pH. The obtained results suggest that D^*_{Li} increases with calcite growth rate, according to the expression:

$$\mathrm{Log}D^*_{Li} = 1.331\ (\pm 0.116) \times \mathrm{Log}Rate + 6.371\ (\pm 0.880) \qquad (R^2=0.87;\ 10^{-8.1} \le Rate \le 10^{-7.1}\ \mathrm{mol\ m^{-2}\ s^{-1}})$$

Additionally the experimental results suggest that D^*_{Li} values exhibit a strong pH dependence. For experiments conducted at similar growth rates (i.e. *Rate* = $10^{-7.7\pm0.2}$ mol m^{-2} s^{-1}), D^*_{Li} decreases with increasing pH as described by:

$$\mathrm{Log}D^*_{Li} = -0.57\ (\pm 0.047) \times \mathrm{pH} + 0.759\ (\pm 0.366) \qquad (R^2=0.90;\ 6.3 < \mathrm{pH} < 9.5)$$

The positive correlation of D^*_{Li} with calcite growth rate is consistent with an increasing entrapment of traces / impurities at rapidly growing calcite surfaces, although the incorporation of monovalent cations such as Li^+ and Na^+ does not necessarily imply a substitution of Ca^{2+} ions in the calcite crystal lattice. The dependence of D^*_{Li} on pH can be considered as an indication that activity of aqueous HCO_3^- controls the incorporation of Li^+ in calcite. The proposed coupled reaction can be explained by charge balance of these monovalent species, which is likely valid at least during the

initial step of adsorption on the crystal surface. These new findings shed light on the mechanisms controlling Li incorporation in calcite and have direct implications on the use of Li partitioning coefficients in natural carbonates as an environmental proxy.

3.1 Introduction

3.1.1 General Background

The trace elemental and isotopic composition of natural carbonate minerals is routinely used by the geoscientific community in order to elucidate the environmental conditions that occurred during mineral formation. In this regard, the mechanisms controlling chemical and isotopic fractionation during $CaCO_3$ mineral formation have been the subject of numerous experimental studies over the last four decades (e.g. Lorens, 1981; Mucci and Morse, 1983; Busenberg and Plummer, 1985; Mucci, 1988; Dromgoole and Walter, 1990; Dietzel and Usdowski, 1996; Tesoriero and Pankow, 1996; Böttcher, 1998; Dietzel et al., 2004; Lakshtanov and Stipp; 2004; 2007; Gabitov and Watson, 2006; Tang et al., 2008a; 2008b; Mavromatis et al., 2013; 2015; 2017a; 2018; Gabitov et al., 2014a; 2014b; Purgstaller et al., 2016; 2017; Voigt et al., 2017). The incorporation of trace elements in carbonate minerals, however, is not controlled only by physicochemical parameters such as temperature, pH and solution composition. It is also affected by the chemical properties of each element and by the crystal structure of the forming mineral phase. For example, spectroscopic techniques have revealed that the incorporation of divalent cations in calcite and aragonite has been shown to follow an ideal substitution of the Ca^{2+} ion in the crystal lattice (e.g. Reeder et al., 1999). This mechanism is not valid for monovalent or trivalent cations, however, due to ionic radii differences and the charge imbalance that is provoked by such substitution.

In the present study, we investigate the mechanisms controlling the incorporation of lithium ion (Li^+) in calcite. We experimentally study the incorporation behavior of Li^+ as a function of calcite growth rate and pH of the forming fluid. While lithium is readily incorporated into biotite, cordierite, alkali-feldspar, spodumene and petalite, it exhibits low concentrations in carbonate minerals of both biogenic and abiotic origin (Burton and Vigier, 2011). As such, the major source of Li in oceanic waters mainly originates from the weathering of continental silicate rocks and its transport via rivers and groundwaters (e.g. Chan et al., 1992; Huh et al., 2001; Négrel et al., 2010). Once introduced into the oceans, major sinks of Li can be ascribed to sea-floor alteration and partly to incorporation into marine carbonates (Misra and Froelich, 2012). Note here that Li is a strongly hydrophilic element that does not readily form aquo-complexes. Moreover, lithium is not utilized in biological systems, thus Li/Ca ratios of marine carbonates have the potential to provide information about changes of global environmental conditions like continental weathering, marine hydrothermal activity, sea level, and temperature (Misra and Froelich, 2012). Actually the Li content of marine calcites, and more routinely its ratio to major or trace elements in biomineral exoskeletons (i.e. Li/Ca, Li/Mg, Li/Sr), is used to infer physicochemical parameters of forming natural solutions such as dissolved inorganic carbon and / or degree of seawater saturation with respect to calcite (Hall and Chan, 2004; Lear and Rosenthal, 2006; Lear et al., 2010; Vigier et al., 2015), temperature (Hall and Chan, 2004; Marriott et al., 2004a; Bryan and Marchitto, 2008; Lear et al., 2010), and growth rate (Hall and Chan, 2004). To date however, information about the impact of physicochemical conditions on the incorporation of Li in carbonate minerals is still highly ambiguous. Earlier works in geological carbonate samples have shown that the Li/Ca ratio of foraminiferal calcite is not related to the temperature, whereas in brachiopods the Li/Ca ratio decreases with increasing temperature (Delaney et al., 1985; 1989). Moreover, the presence of organics, as well as vital effects of corals and shells, is presumed to influence the mechanisms controlling the incorporation of Li in calcite. To explain the controlling parameters and mechanisms, such as temperature (T), pH, calcification rate, salinity, and incorporation reactions in the carbonate lattice, well constrained laboratory experiments are required. To date, however, only a few studies have investigated the mechanisms controlling the Li/Ca ratio and the Li isotope composition of calcite under laboratory conditions. For instance, Marriott et al. (2004a) demonstrated that the ratio of Li/Ca of calcite decreases with increasing formation temperature and decreasing salinity (Marriott et al., 2004b). However, parameters such as mineral growth rate and pH have not so far been explored. Thus, the aim of the present study is to explore the mechanisms that control the Li incorporation during the growth of calcite focusing on the influence of growth rate and pH.

3.1.2 Mechanisms of monovalent cation incorporation in carbonate minerals

The presence of monovalent metal cations (Me^+) such as Na^+ in naturally-occurring carbonate minerals has been well documented in the literature and a few models have been developed for their position in the crystal lattice (White, 1977; 1978; Busenberg and Plummer; 1985; Yoshimura et al., 2017). We note here that in contrast to divalent cations, the incorporation of monovalent cations (Me^+) is not affected only by size difference between the trace element and the host ion (Wang and Xu, 2001; Mavromatis et al., 2018) but also by the charge imbalance that is imposed by their presence in the solid phase. Earlier studies suggested that Me^+, specially Na^+, may be present in calcite and aragonite at interstitial sites (White, 1977; 1978; Ishikawa and Ichikuni, 1984; Oomori et al., 1985; Okumura and Kitano, 1986), which would result in a positive charge excess that can be compensated by the presence of monovalent anions or anion complexes (like OH^-, HCO_3^- or Cl^-). In a similar double substitution model Busenberg and Plummer (1985) proposed the replacement of one Ca^{2+} ion with two Na^+ ions which is accompanied with structural incorporation of SO_4^{2-}. Finally, the presence of an anion vacancy for the incorporation of Na^+ and K^+ in aragonite has been suggested (White, 1977) in a model where two Ca^{2+} ions are replaced by two Na^+ ions with a CO_3^{2-} vacancy.

3.1.3 Partitioning coefficients

The partitioning of divalent metal cations (Me^{2+}) between $CaCO_3$ minerals and the forming aqueous phase is generally defined as

$$D_{Me^{2+}} = \frac{(c_{Me}/c_{Ca})_{calcite}}{(m_{Me^{2+}}/m_{Ca^{2+}})_{solution}} \tag{3.1}$$

where C_{Me} and C_{Ca} denote the concentration of trace element and calcium in the solid phase, respectively and $m_{Me^{2+}}$ and $m_{Ca^{2+}}$ denote the aqueous concentrations of free Me^{2+} and Ca^{2+} ions, respectively. In experimental studies performed at 1 bar CO_2 and pH of ~ 6.2, the ratio of the molarities in Eq. 3.1 is commonly replaced by the ratio of total aqueous concentrations owing to the fact that free cations comprise typically more than 95% of the total concentration of the dissolved metal ion (Tesoriero and Pankow, 1996; Lakshtanov and Stipp, 2007; Mavromatis et al., 2013). The partitioning coefficient of Me^{2+} in $CaCO_3$ minerals, as defined in Eq. 3.1, is based on the assumption of an ideal substitution between a calcium ion with a divalent cation in the crystal lattice of the $CaCO_3$ phase. In other words, the formation of a dilute ideal solid-solution is assumed. This model is further supported by spectroscopic studies (e.g. Reeder et al., 1999), which suggest that impurities in calcite have a 6-fold coordination with respect to oxygen ions, similar to that of Ca in this mineral phase. This model is also valid for large divalent cations such as Sr^{2+} and Ba^{2+} in the solid phase, although they regularly occur in 9-fold coordination in aqueous media.

The definition of a partitioning coefficient for the incorporation of monovalent cations from an aqueous phase to $CaCO_3$ minerals, however, is not straightforward, as an one-to-one substitution for Ca^{2+} cannot be considered. As such, the apparent partitioning coefficients of Me^{+} in calcium carbonate minerals are commonly expressed as the ratio of total aqueous monovalent metal and Ca concentrations without any correction for the molarities of the free ions (e.g. Ishikawa and Ichikuni, 1984; Marriott et al., 2004a; 2004b). In this study, we report apparent partitioning coefficients of Me^{+} into calcite as:

$$D^{*}_{Me^{+}} = \frac{(c_{Me}/c_{Ca})_{calcite}}{(m_{Me^{+}}/m_{Ca^{2+}})_{solution}} \tag{3.2}$$

where c stands for the concentration of the metal ion in calcite, $m_{Me^{+}}$ denotes the molar concentration of free Me^{+} in the aqueous phase and $m_{Ca^{2+}}$ is the molar concentration of free Ca ions. This approach follows a similar nomenclature for that used in Eq. 3.1 for the formation of a diluted solid-solution from aqueous fluids (Tesoriero and Pankow, 1996; Prieto 2009); we note here, that this does not imply a formation of solid-solution in the case of monovalent ions incorporation in calcite. The use of the molarity of the free ions in Eq. 3.2 considers the formation of aqueous complexes, a process that is significant for Ca within the pH range explored in this study.

3.2 Methods

3.2.1 Experimental set-up

The incorporation of Li in calcite was studied at 25 °C as a function of mineral growth rate and pH of the reactive fluid. The experimental set-up is illustrated in Fig. 3.1 and is similar to that used earlier for pH controlled experiments in our earlier studies (Mavromatis et al., 2015; 2019). Initially, the reactor contained 0.5 L of a 0.3 M NaCl solution that was equilibrated with calcite at the predefined pH conditions in advance of the co-precipitation runs. Prior to the onset of the experiment, ~1 g of calcite seed material (Sigma-Aldrich, > 99 %) was introduced into the reactor, together with a Li (i.e. LiCl) bearing solution. The background electrolyte was fixed at 0.3 M NaCl. Calcite overgrowth on the seed material was induced by the simultaneous pumping of two separate solutions into the reaction vessel using a peristaltic pump, the first containing $CaCl_2$ and LiCl and the second Na_2CO_3. The concentrations of $CaCl_2$ and Na_2CO_3 in the inlet solutions were for each run equal and varied between 0.025 and 0.1 M. The increase in the concentration of the inlet solutions resulted in increasing surface normalized calcite growth rate under chemical steady-state conditions.

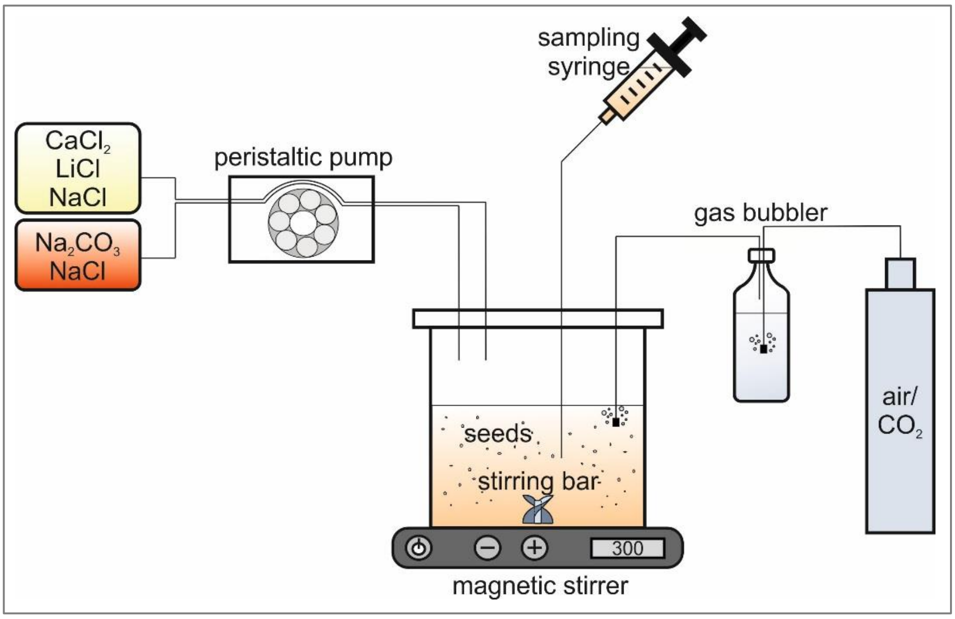

Figure 3.1: Experimental set-up for the calcite growth experiments.

During the course of an experimental run, the pH of the reactive fluid remained constant, as achieved by the continuous bubbling of CO_2 and N_2 gas mixtures. For experiments at pH of ~6.3 the bubbling gas was pure CO_2, whereas at pH of ~8.1 - 8.4 atmospheric air was introduced in the reactor. For experiments conducted at pH > 9.0, constant pH conditions were achieved by titration of 0.5 M NaOH into the reactor vessel. Note here that in order to minimize evaporation, the gas phase was bubbled through a 0.3 M NaCl solution prior to its introduction into the reaction vessel. The inflow of the two inlet solutions in each reactor occurred at a rate of ~10 mL/day for each solution and induced an increase of the volume of the reactive fluid. Thus, every 24 h, a volume of reactive fluid, equal to the sum of the volumes of the inlet solutions added in 24 h by the peristaltic pump, was removed from the reactor so that the fluid volume in the reactor remained constant within ± 4 %. In this study, experiments 5_40 to 5_100 performed at increased inflow rates of ~20 mL/day for each inlet solution in order to increase the actual surface normalized calcite growth rate. In these experiments sampling of the reactive fluid was performed more than once per day. Stirring was stopped shortly prior to sampling to allow the solid material to settle. In this way solid removal was minimized and the solid:solution ratio was kept quasi-constant during the course of a run. Immediately after sampling, the fluid was filtered through a 0.2 µm Millipore cellulose acetate syringe filter and a sub-sample was acidified for further analyses of Ca, Li, and Na concentrations. Reactive fluid carbonate alkalinity was determined in a second sub-sample, whereas the fluid pH was measured *in situ*. At the end of the experimental runs, the fluid was separated from the solid phase via vacuum filtration using a 0.1 µm filter (Millipore, cellulose acetate). The solids were rinsed with Milli-Q water to remove adsorbed ions on the crystal surfaces and subsequently dried at 40 °C.

Table 3.1: Chemical composition of Li and Ca in the reactive fluid at chemical steady-state conditions, pH, estimated growth rate and distribution coefficients of Li and Na in the forming calcite during the experimental runs calculated from both molarities of free ions and total aqueous concentrations.
*indicates samples used in Fig. 3.4

experiment	**Li_{ss} (mM)**	**Ca_{ss} (mM)**	**Alkalinity (mM)**	**pH**	**Log *Rate***	**Log D^*_{Li}**	**Log D^*_{Na}**	**Log D_{Li}**	**Log D_{Na}**
2_30*	0.35	0.99	2.7	8.27	-8.1	-4.7	-5.5	-4.3	-5.1
2_40*	0.34	1.12	2.6	8.29	-8.0	-4.5	-5.5	-4.1	-5.1
2_50	0.34	0.39	3.4	8.56	-8.1	-5.1	-5.7	-4.7	-5.3
2_60*	0.35	1.35	2.3	8.23	-7.8	-4.5	-5.6	-4.1	-5.2
2_70*	0.34	1.37	2.5	8.27	-7.7	-4.5	-5.5	-4.1	-5.1
2_80*	0.36	1.69	2.3	8.29	-7.6	-4.1	-5.4	-3.7	-5.0
2_90	0.35	0.78	2.6	8.40	-7.6	-4.5	-5.5	-4.1	-5.1
2_100*	0.35	1.61	2.3	8.25	-7.5	-3.9	-4.6	-3.5	-4.2
3_25*	0.35	1.32	2.2	8.23	-7.9	-4.5	-5.2	-4.1	-4.8
3_30*	0.35	0.89	2.6	8.35	-7.9	-4.7	-5.7	-4.3	-5.3
3_40*	0.35	1.04	2.4	8.33	-7.8	-4.4	-5.5	-4.0	-5.1
3_50*	0.35	1.73	2.1	8.17	-7.6	-4.3	-4.9	-3.9	-4.5
3_60*	0.34	1.30	2.3	8.30	-7.5	-4.3	-5.3	-3.8	-4.9
3_70*	0.36	1.33	2.2	8.28	-7.4	-4.1	-5.4	-3.7	-5.0
3_80*	0.35	1.85	2.2	8.28	-7.4	-3.9	-4.9	-3.5	-4.5
3_100*	0.35	2.11	2.2	8.34	-7.3	-3.6	-5.0	-3.2	-4.6
5_40*	0.41	1.41	2.6	8.10	-7.5	-3.9	-4.6	-3.5	-4.2
5_50*	0.45	1.49	2.7	8.07	-7.4	-3.6	-4.3	-3.2	-3.9
5_60*	0.44	1.49	2.6	8.13	-7.3	-3.7	-4.5	-3.3	-4.1
5_70*	0.45	1.72	2.5	8.04	-7.3	-3.7	-4.4	-3.3	-4.0
5_80*	0.40	1.27	2.7	8.09	-7.2	-3.7	-4.5	-3.3	-4.1
5_90	0.50	4.55	2.2	7.87	-7.2	-3.3	-4.1	-2.9	-3.7
5_100*	0.40	2.22	2.3	7.99	-7.1	-3.5	-4.4	-3.1	-4.0
7_25	0.31	0.10	2.8	9.59	-8.1	-5.2	-5.7	-4.8	-5.3
7_50	0.31	0.11	2.8	9.43	-7.8	-5.0	-5.7	-4.6	-5.3
7_100	0.31	0.14	2.6	9.54	-7.5	-5.1	-5.5	-4.6	-5.2
12_60	0.24	9.27	20.9	6.29	-7.8	-3.3	-3.3	-2.9	-2.8
12_70	0.26	7.47	20.6	6.34	-7.7	-3.4	-3.5	-3.0	-3.0
12_80	0.28	12.17	21.6	6.31	-7.7	-3.4	-3.5	-2.9	-3.0
12_100	0.24	9.51	22.3	6.31	-7.6	-3.3	-3.6	-2.8	-3.1
13_60	0.24	3.17	5.7	7.41	-7.7	-3.7	-4.1	-3.2	-3.7
13_70	0.25	3.56	5.3	7.49	-7.7	-3.7	-4.1	-3.3	-3.6
13_80	0.23	3.09	6.5	7.50	-7.7	-3.6	-4.2	-3.1	-3.8
13_100	0.24	3.10	5.4	7.44	-7.7	-3.7	-4.2	-3.3	-3.7

3.2.2 Analytical procedures

3.2.2.1 Solution characterization

Elemental concentrations of reactive fluids and digested solids were measured using a Perkin Elmer Optima 8300 DV Inductively coupled plasma optical emission spectrometer (ICP-OES) with an analytical precision of < ± 3 %. The alkalinity of fluid samples was measured by standard HCl titration using an automatic Schott TitroLine alpha plus titrator with an uncertainty of ± 2 %. The pH was measured using a SenTix® 945 pH gel electrode from WTW, calibrated against NIST standard buffers at pH = 4.01, 7.00 and 10.01 at 20 °C. Precision of pH measurements was ± 0.04 units and the slope of the calibration was -57 (± 1) mV per pH unit. Aqueous speciation, ion activities and saturation states (Ω) of the reactive fluids with respect to calcite were calculated using PHREEQC software together with its MINTEQ.V4 database (Parkhurst and Appelo, 1999).

3.2.2.2 Solid characterization

The collected solids were analyzed using an Attenuated Total Reflectance - Fourier Transform Infrared Spectrometer (ATR-FTIR; Perkin Elmer Spectrum 100) in the range of 650 - 4000 cm^{-1}. X-ray powder diffraction (XRD) patterns were recorded using a PANalytical X´Pert PRO diffractometer and Co-Kα-radiation (40 mA, 40 kV) from 4° to 85° at a scan speed of 0.03° min^{-1}. The mineral phases were quantified by Rietveld refinement using the PANalytical X'Pert HighScore Plus software with the PDF-2 database. Selected solids were imaged using a ZEISS DSM 982 Gemini scanning electron microscope (SEM) operating at 2 kV accelerating voltage. The specific surface area of solid samples was determined by multi-point krypton adsorption BET method (Brunauer et al., 1938) using a Quantachrome Gas Sorption system.

3.3 Results

3.3.1 Mineralogy of the precipitated solids

X-ray diffraction patterns of the precipitates suggest calcite was the only mineral phase present, as did FT-IR spectra which matched the calcite reference material. SEM images showed that the precipitated solids (Fig. 3.2B) kept the characteristic rhombohedron-like of the seed material, consistent with the presence of calcite alone (Fig. 3.2A). They consisted of aggregates of rhombohedral crystals with overgrowth features on the seed surface (Fig. 3.2B).

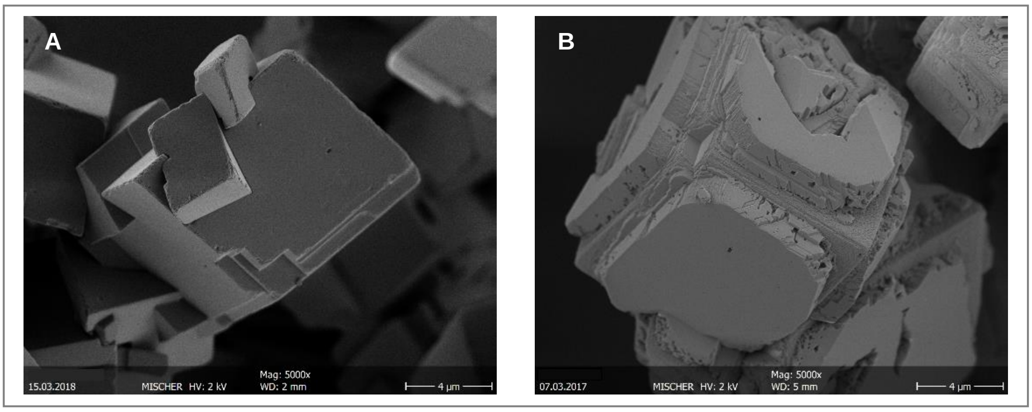

Figure 3.2: Scanning Electron Microphotographs of (A) calcite seeds used for the calcite growth experiments and (B) final overgrow precipitates (Experiment CaLi3_25).

3.3.2 Chemical composition of reactive fluids and growth rate calculation

Steady-state conditions with respect to aqueous calcium concentrations were achieved between 1000 and 3000 min depending on the applied pumping rate (Fig. 3.3). In contrast, Li concentrations appeared to be at steady-state conditions from the onset of the experimental runs (Fig. 3.3). Calcite growth rates expressed in mol m^{-2} s^{-1}, were estimated based on mass balance considerations using the number of moles of Ca introduced in the reactor per unit time and corrected for the number of moles of Ca removed over the same period of time via sampling, after reaching chemical steady-state conditions, according to the expression

$$Rate = \frac{n_{Ca(add)} - n_{Ca(rem)}}{86400} / S \tag{3.3}$$

where *n* stands for the number of moles of calcium added into the reactor and removed from the reactor within 24 h, *S* denotes the total calcite surface (m^2) and *86400* stands for the number of seconds in 24 h (Mavromatis et al. 2013; 2015). Note here that growth rate estimation based on Eq. 3.3 is not taking into account the incorporation of traces such as Li and Na in the precipitated calcite as the respective amounts are negligible compared to Ca. The obtained overall variation in growth rates in experiments conducted herein lays within the range -8.2 ≤ Log*Rate* ≤ -7.1 (see Table 3.1) and it exhibits a linear correlation with saturation degree of the reactive fluid with respect to calcite for experiments conducted under similar inlet solution inflow rates as it can be seen in the Appendix (Appendix B, Figure B.1).

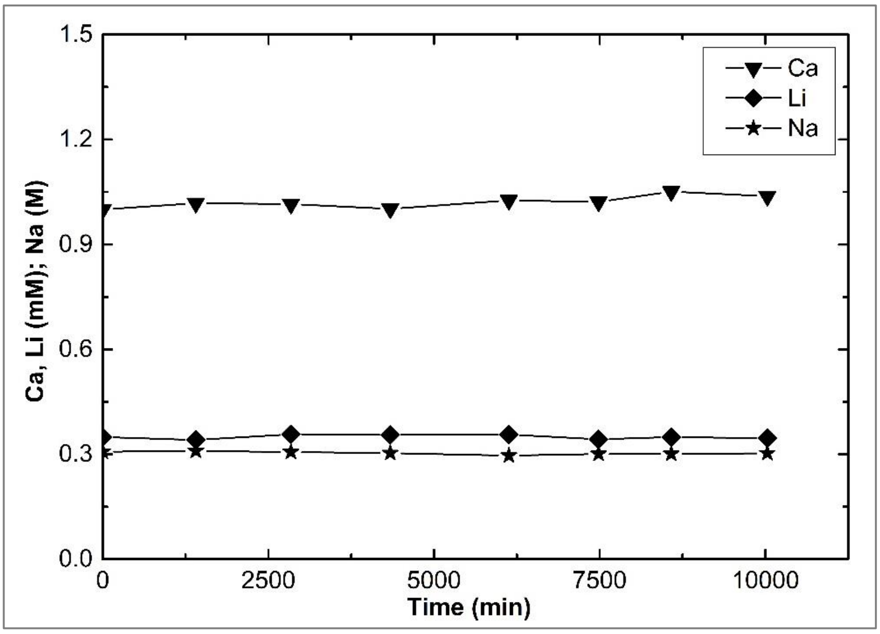

Figure 3.3: Temporal evolution of Ca, Li and Na as a function of time for experimental run CaLi3_40. Analytical uncertainty is included in the symbol size.

3.3.3 Lithium and sodium partitioning between calcite and solution

The apparent partitioning coefficients of Li and Na in the precipitated calcite have been calculated based on the molarities of the respective free aqueous ions after the attainment of chemical steady-state conditions using Eq. 3.2. Note here that no corrections applied to the Na concentrations in experiments performed at pH ~ 9.5 (i.e. 7_25, 7_50 and 7_100) for the amount of Na that was additionally added in the reactive fluid via NaOH titration. This is because the overall amount of Na added in a course of a run was ≤ 3 mmoles and it did not measurably increase the Na concentration of the reactive fluid (see Appendix B, Table B.3). The molarities of aqueous complexes considered in this study are shown in the Appendix Table B.3. Note that the concentration of Me^+ in the solid phase used in Eq. 3.2 has been corrected for the amount of seed material in the bulk precipitate. The amount of the precipitate varied between ~0.2 and ~3.0 g among the experimental runs.

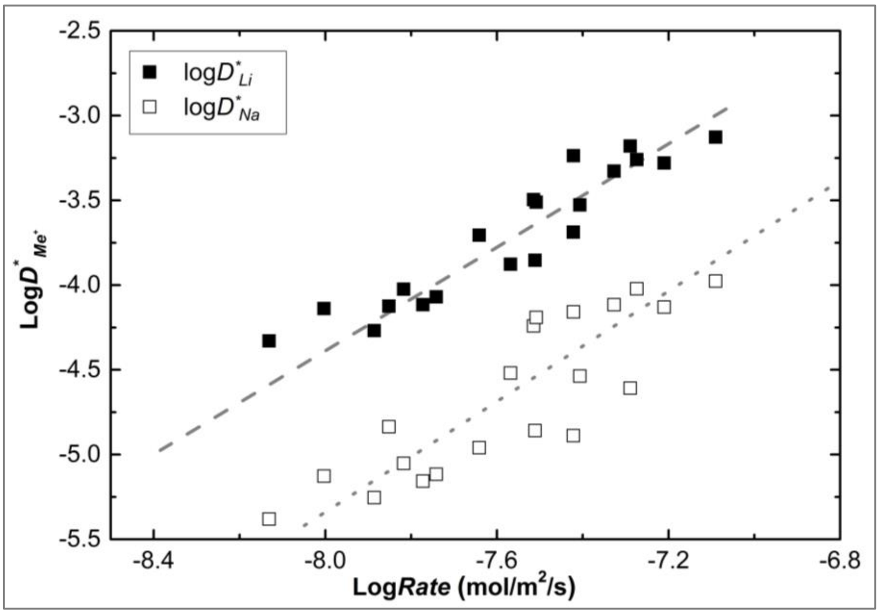

Figure 3.4: Apparent partition coefficient of Li and Na between calcite and reactive fluid plotted as a function of calcite growth rate for experiments conducted in the range 8.0 ≤ pH ≤ 8.3. Analytical uncertainty is included in the symbol size.

Obtained results for D_{Li}^* and D_{Na}^* are provided in Table 3.1. Overall D_{Li}^* and D_{Na}^* values range within -4.8 ≤ LogD_{Li}^* ≤ -2.8 and -5.4 ≤ LogD_{Na}^* ≤ -2.9, respectively. There is a notable correlation of $D_{Li}{}^*$ with growth rate for experiments conducted in the pH range between 8.0 and 8.3 (Fig. 3.4). This correlation is also reflected in the variation of D_{Li}^* with the saturation degree of the reactive fluid with respect to calcite as it is depicted in Appendix B, Fig. B.2. The positive correlation between D_{Li}^* and *Rate* can be described by the linear relationship

$$\mathrm{Log}D_{Li}^* = 1.331\ (\pm\ 0.116) \times \mathrm{Log}Rate + 5.966\ (\pm\ 0.880);\ R^2 = 0.87 \qquad (3.4)$$

In similar terms Na incorporation in calcite, over the same pH range, can be described as a function of growth rate using the linear equation:

$$\mathrm{Log}D^{*}_{Na} = 1.413\ (\pm\ 0.202) \times \mathrm{Log}Rate + 6.039\ (\pm\ 1.527);\ R^2 = 0.72 \quad (3.5)$$

Furthermore, the experimental results indicate that the pH of the reactive fluid has a strong effect on the D^{*}_{Li} value. Indeed, as is illustrated in Fig. 3.5, at the lowest pH value employed in the experiments of this study of about 6.3, D^{*}_{Li} reached its highest value of $10^{-2.9}$. In contrast, at the highest pH value of about 9.5, D^{*}_{Li} yielded its lowest value of $10^{-4.8}$. The negative relation of D^{*}_{Li} with pH for experiments conducted at almost constant growth rates (i.e. $10^{-7.7\pm0.2}$ mol m^{-2} s^{-1}) can be expressed using the linear equation

$$\mathrm{Log}D^{*}_{Li} = -0.57\ (\pm\ 0.047) \times \mathrm{pH} + 0.759\ (\pm\ 0.366);\ R^2 = 0.90;\ 6.3 < \mathrm{pH} < 9.5 \quad (3.6)$$

The observed dependence of the obtained $D^{*}_{Me^{+}}$ values on growth rate calculated in this study is in good agreement with the general behavior of divalent hydrophilic cations with $D_{Me^{2+}} << 1$ values. Those exhibit an increase in partitioning between solid and fluid with increasing growth rates (e.g. Lorens, 1981; Tesoriero and Pankow, 1996; Tang et al., 2008a; Mavromatis et al., 2013). Similarly, for the monovalent cation, Na^{+}, it has previously been shown that its incorporation in calcite is strongly affected by growth rate (Busenberg and Plummer, 1985; Mucci, 1988). Finally, the apparent partitioning coefficients, D^{*}_{Li}, calculated in this study based on Eq. 3.2 are in good agreement with those reported previously by Marriott et al. (2004a; 2004b).

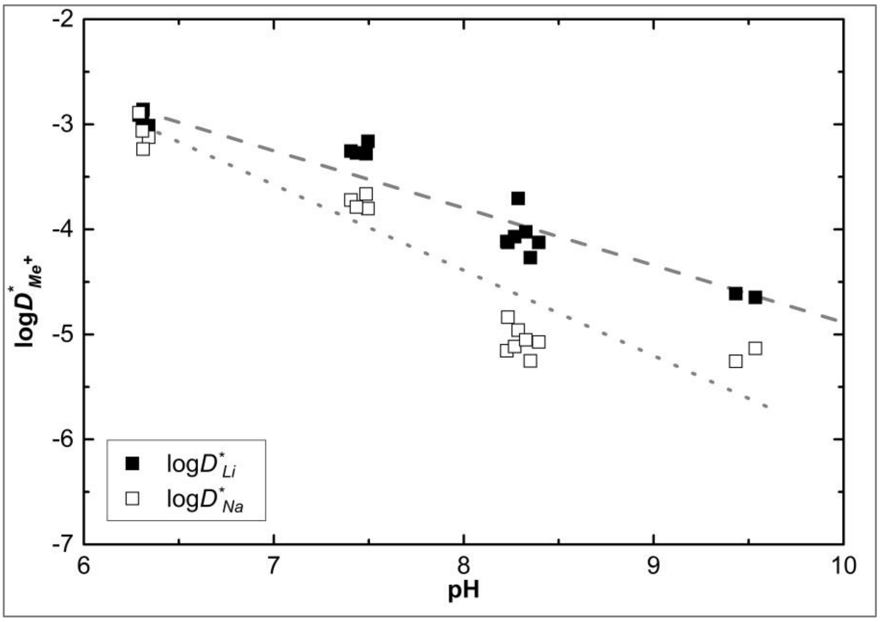

Figure 3.5: Apparent partition coefficient of Li and Na between calcite and reactive fluid plotted as a function of pH for experiments conducted at similar growth rates (i.e. $10^{-7.7\pm0.2}$). Analytical uncertainty is included in the symbol size.

3.4 Discussion

3.4.1 The role of growth rate on Li incorporation in calcite

The results of the present study suggest a strong variation of the D_{Li}^{*} value of about two orders of magnitude over a narrow pH range. Indeed, as depicted in Fig. 3.4, the D_{Li}^{*} values increase from $10^{-4.8}$ to $10^{-2.9}$ as calcite growth rate increases from $10^{-8.1}$ to $10^{-7.1}$ (mol m^{-2} s^{-1}). Considering that this increase in D_{Li}^{*} occurs within a narrow pH range of $8.0 \leq pH \leq 8.3$, and from the constant background electrolyte composition in all experimental runs (i.e. ~0.3 M NaCl) it can be reasonably deduced that under these conditions the parameter controlling the incorporation of Li in calcite is the growth rate.

Growth rate effects on elemental partitioning during calcium carbonate mineral growth have been documented for a large number of traces / impurities. As described by Rimstidt et al. (1998), with increasing growth rate the elemental partitioning of divalent cations during their incorporation in a metal carbonate mineral phase tends towards unity. This behavior implies that at elevated growth rates elemental discrimination, as is postulated by thermodynamic considerations, is no longer valid, and the elemental ratio of trace to major ion in the precipitate approaches that of the forming fluid. Such behavior has been experimentally shown to be valid for a large number of divalent cations during calcite growth (i.e. Ba^{2+}, Cd^{2+}, Co^{2+}, Fe^{2+}, Mn^{2+}, Ni^{2+}, Sr^{2+}, Zn^{2+}; Lorens, 1981; Pingitore and Eastman, 1984, 1986; Dromgoole and Walter, 1990; Tesoriero and Pankow, 1996; Temmam et al., 2000; Lakshtanov and Stipp 2007; Tang et al., 2008a; Mavromatis et al., 2013; 2017a; 2018). A similar behavior has been shown to be valid for anions like borate, sulfate and phosphate, where incorporation in calcite is characterized by small partitioning coefficients (Busenberg and Plummer, 1985; House, 1990; Mavromatis et al., 2015; Uchikawa et al., 2015; 2017; Wynn et al., 2018).

The impact of growth rate on Li partitioning in calcite can be explained by the growth entrapment model (GEM) developed by Watson and co-workers (Watson and Liang, 1995; Watson, 1996, 2004). This model has previously been used to describe the incorporation of divalent metal (Me^{2+}) cations in calcite. The GEM states that during rapid growth of calcite crystals, trace elements that are incompatible with the calcite structure are enriched in a surface layer of the freshly forming crystal. This implies that the partitioning coefficient of hydrophilic divalent cations, $D_{Me^{2+}} < 1$, which can form a solid-solution with calcite via the direct substitution of Me^{2+} with Ca^{2+} in the crystal lattice, would increase at elevated growth rates. Over the last decades GEM has been successfully applied to describe elemental partitioning of divalent cations between carbonate minerals and fluids (Gabitov and Watson, 2006; Gaetani and Cohen, 2006; Gabitov et al., 2008, 2012; Tang et al., 2008a; 2008b; Mavromatis et al., 2013).

In comparison to other impurities in calcite, both cations and anions, Li partitioning exhibits likely the strongest correlation to growth rate as demonstrated in Fig. 3.4. Indeed, with an increase of ~2 orders of magnitude in D_{Li}^{*} values over an increase of about one order of magnitude in growth rate, Li concentrations in calcite are likely a very sensitive indicator of mineral growth in comparison to other ions. For example, Mg exhibits an increase of only about 0.5 orders of magnitude over a two order of magnitude increase in growth rate (Mavromatis et al., 2013). As discussed above, the incorporation of monovalent cations in carbonate minerals is not occurring via direct substitution of Ca^{2+} ion in the calcite structure. In the case of Na^+ incorporation in calcite, D^*_{Na} is suggested to depend on the density of crystal surface defects (Busenberg and Plummer; 1985; Mucci, 1988), a feature that increases with precipitation rate (Teng et al., 2000). Accordingly, it is likely that the reaction mechanism controlling Li^+ incorporation in calcite is the same as that for Na^+. Okumura and Kitano (1986), reached the same conclusion, and inferred this mechanism also for K^+ and Rb^+. The similar mechanism of Li^+ and Na^+ incorporation in calcite is further supported by the very similar rate dependence of $D^*_{Me^+}$ (see data in Fig. 3.4). Indeed the slopes of D^*_{Li} and D^*_{Na} as defined in Eqs. 3.4 and 3.5, respectively, are identical within the error of estimation of apparent partitioning coefficients. The difference in the absolute $D^*_{Me^+}$ values of about one order of magnitude is likely explained by the difference in ionic radii between Li^+ and Na^+ (Okumura and Kitano, 1986). In an aqueous phase, Li^+ occurs as a 6-coordinated ion with a radius of 0.76 Å (Shannon, 1976), whereas 6-fold coordinated Na^+ is ~ 25 % larger with an ionic radius of 1.02 Å (Shannon, 1976). As such, it can be assumed that the introduction of Me^+ ions in the calcite lattice is somewhat affected by their ionic radii.

3.4.2 The role of pH on Li incorporation in calcite

The findings of this study suggest that the growth rate at which calcite forms strongly controls the D^*_{Li} value. As it is depicted in Fig. 3.5, however, pH has also a strong control over the measured D^*_{Li} values. Indeed, for experiments conducted under similar surface normalized growth rates (i.e. $10^{-7.7\pm0.2}$ mol m^{-2} s^{-1}) D^*_{Li} exhibits a strong reduction from $10^{-3.3}$ to $10^{-5.1}$ as pH increases from ~6.3 to ~9.5. A similar pH dependence has previously been shown for B incorporation in calcite and aragonite (Mavromatis et al., 2015; Uchikawa et al., 2015). A comparison between these two elements is not straightforward, however, as aqueous speciation of B (i.e. $^{[III]}B$ and $^{[IV]}B$) is strongly pH dependent, whereas aqueous Li occurs primarily as Li^+ independent of fluid pH. As such, the decreasing D^*_{Li} values at elevated pH conditions are likely associated with the mechanism of Li incorporation in the crystal structure and do not reflect changes in aqueous speciation. The similar incorporation behavior of Na^+ suggests a common mechanism responsible for the incorporation of monovalent cations in the calcite structure. The pH dependence of D^*_{Na}, however, as depicted in Fig. 3.5, follows a somewhat different trend as a function of pH. This difference likely stems from the formation of Na^+ aquo-complexes with HCO_3^- and CO_3^{2-} (i.e. $NaHCO_3^o$ and $NaCO_3^-$; Appendix Table B.2). We note here that an adsorption mechanism controlling Li^+ and Na^+ incorporation in the growing calcite cannot be completely excluded, as at elevated pH cation adsorption tends to increase due to rising electrostatic attraction (e.g. Appelo and Postma, 2007).

One of the major questions raised by the observed pH-dependent Me^+ partitioning in calcite is related to the mechanism of Me^+ incorporation in the crystal lattice. As discussed above, the presence of monovalent cations in the calcite crystal lattice is accompanied by a positive charge excess that can potentially be balanced by the presence of anions. As is illustrated in Fig. 3.6, D^*_{Li} in the experiments conducted in this study exhibits a positive correlation with the activity of aqueous bicarbonate ion (i.e. $a_{HCO_3^-}$). Moreover, as it is depicted in Appendix Fig. B.4, D^*_{Li} exhibits a positive relationship with the activity of aqueous HCO_3^- bearing species (i.e. $CaHCO_3^+$, and $NaHCO_3^o$) and a negative relationship with the activity of CO_3^{2-} bearing species (i.e. CO_3^{2-}, and $NaCO_3^-$) likely due to their pH dependent distribution. The observed correlation between $a_{HCO_3^-}$ and D_{Li}^* is also controlled by the prevailing pH with an overall decrease of $a_{HCO_3^-}$ values at increasing pH, similar to the D_{Li}^* trend presented in Fig. 3.5. Note here that a direct comparison of the $a_{HCO_3^-}$ among experiments conducted at different pH values is not straightforward as the prevailing dissolved inorganic carbon concentration, here presented as alkalinity (Table 3.1), varies among runs due to the pH dependent solubility of calcite. The co-variation of $a_{HCO_3^-}$ with D_{Li}^*, however, likely suggests that HCO_3^- might compensate the Li^+ excess through an ion coupled incorporation mechanism. Note here that recently Andersson et al. (2016) suggested on the basis of density functional theory calculations that HCO_3^- is stable on the calcite surface as an adsorbed species, even at circum-neutral pH conditions where CO_3^{2-} is only a minor dissolved carbon species in the aqueous phase. The correlation observed in Fig. 3.6, however, does not necessarily preclude the association of Li^+ with HCO_3^- in the crystal lattice of the final forming calcite. Indeed, Yoshimura et al. (2017) suggested using synchrotron X-ray spectroscopy that Na^+ in calcite and aragonite is accompanied by a CO_3^{2-} vacancy. This vacancy, however, does not exclude the presence of HCO_3^- surface species during Me^+ uptake on the growing surface and points towards a re-arrangement of this ion during Me^+ incorporation.

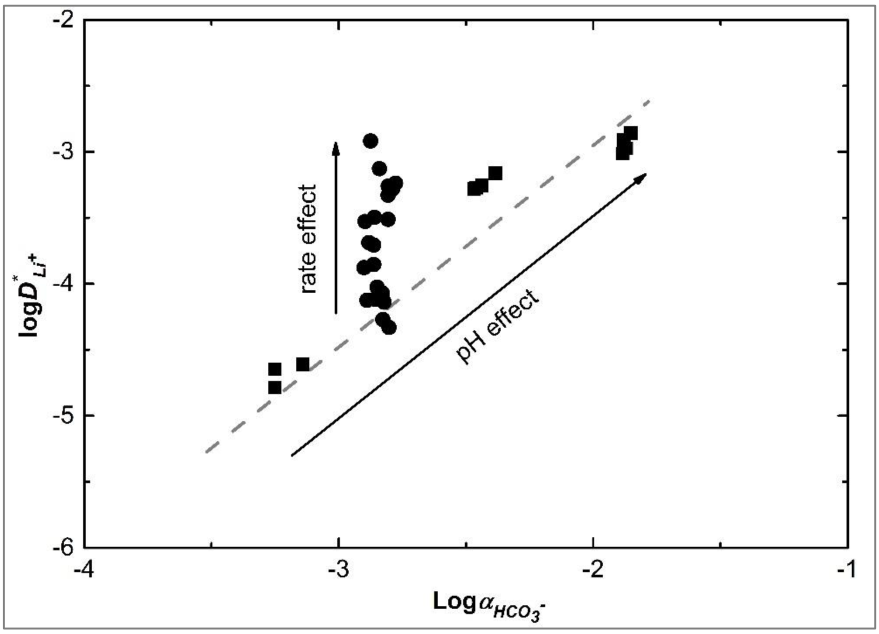

Figure 3.6: Apparent partition coefficient of Li in calcite and reactive fluid plotted as a function of activity of aqueous bicarbonate ion. Experiments at pH 8.1 - 8.4 where growth rate has been increased are represented by circles. Analytical uncertainty is included in the symbol size.

3.4.3 Implications for the Li content of natural calcite

The results of the present study clearly indicate that growth rate plays a major role in the Li content of calcite. We note here that a direct comparison with marine-grown carbonates of either biogenic or abiotic origin may not be straightforward and the proposed growth rate effect as numerically described by Eq. 3.4 may not be directly applicable. This is because in the experiments conducted herein reactive fluids do not contain major ions present in seawater such as Mg^{2+} and SO_4^{2-} that readily incorporate in calcite (Mucci and Morse, 1983; Busenberg and Plummer, 1985; Mavromatis et al., 2017a; 2017b). The different size of such impurities compared to the structural units of calcite (i.e. Ca^{2+} and CO_3^{2-}) may alter the crystallographic structure of the mineral and thus promote increasing incorporation of small ions such as Li^+. Overall, the partitioning of Li in natural calcites can potentially be used as a tool for estimating the formation rate, likely together with ratios of other elements such as Mg/Ca.

Another significant finding of this work that has direct implications for the interpretation of Li/Ca ratios in natural calcites is the strong negative correlation with pH. A dependence of Li content with dissolved inorganic carbon in calcite has previously been shown to exist in marine-derived carbonates such as foraminifera (Dawber and Tripati, 2012; Vigier et al., 2015). Although such dependence, or likely the availability of aqueous HCO_3^-, may be valid for marine carbonates, the highly buffered pH of oceanic waters which has stayed quasi-constant over the last 100 ka (Foster, 2008) together with the biological controls that may affect the composition of the hard parts of calcifies such as foraminifera, suggest that the observed pH-dependence (Fig. 3.5) cannot directly be applied to marine carbonates. In the case of continental carbonate deposits, e.g. travertine formation, where significant pH variations occur, Li/Ca ratios may provide insights on formation conditions.

Finally, our results suggest a positive correlation between the apparent partitioning coefficients of Li and Na according to the equation:

$$\mathrm{Log}D_{Li}^{*} = 0.707\ (\pm\ 0.054) \times \mathrm{Log}D_{Na}^{*} - 0.563\ (\pm\ 0.242)\ ;\ R^2 = 0.84 \qquad (3.7)$$

This relation is valid for all the experimental runs independently of calcite growth rate. Measured Li/Na ratios in natural calcites can thus be used to estimate the Na^+ concentration in the precipitating fluid from Eq. 3.7 if its Li^+ concentration is known or can be reasonably estimated (and vice versa for Na^+). Considering that for natural samples, as for example seawater, the Me^+/Ca concentration ratios are commonly used instead of those for activities, we have plotted in Fig. 3.7B the partitioning coefficient relationship using total Li and Na aqueous concentrations using the notation D_{Me}. This relationship can be expressed as:

$$\mathrm{Log}D_{Li} = 0.699\ (\pm\ 0.052) \times \mathrm{Log}D_{Na} - 0.602\ (\pm\ 0.229)\ ;\ R^2 = 0.85 \qquad (3.8)$$

and it exhibits a slope similar to that of Eq. 3.7. Note here that the application of Eq. 3.8 in natural waters like seawater is not straightforward. This is because it has been calculated for calcites precipitated from a solution with a background electrolyte of ~ 0.3 M NaCl that does not contain other major ions like Mg^{2+} and SO_4^{2-}. The latter ions are abundant at high concentrations in seawater and well known to affect carbonate mineral formation (e.g. Mucci and Morse, 1983; Busenberg and Plummer, 1985).

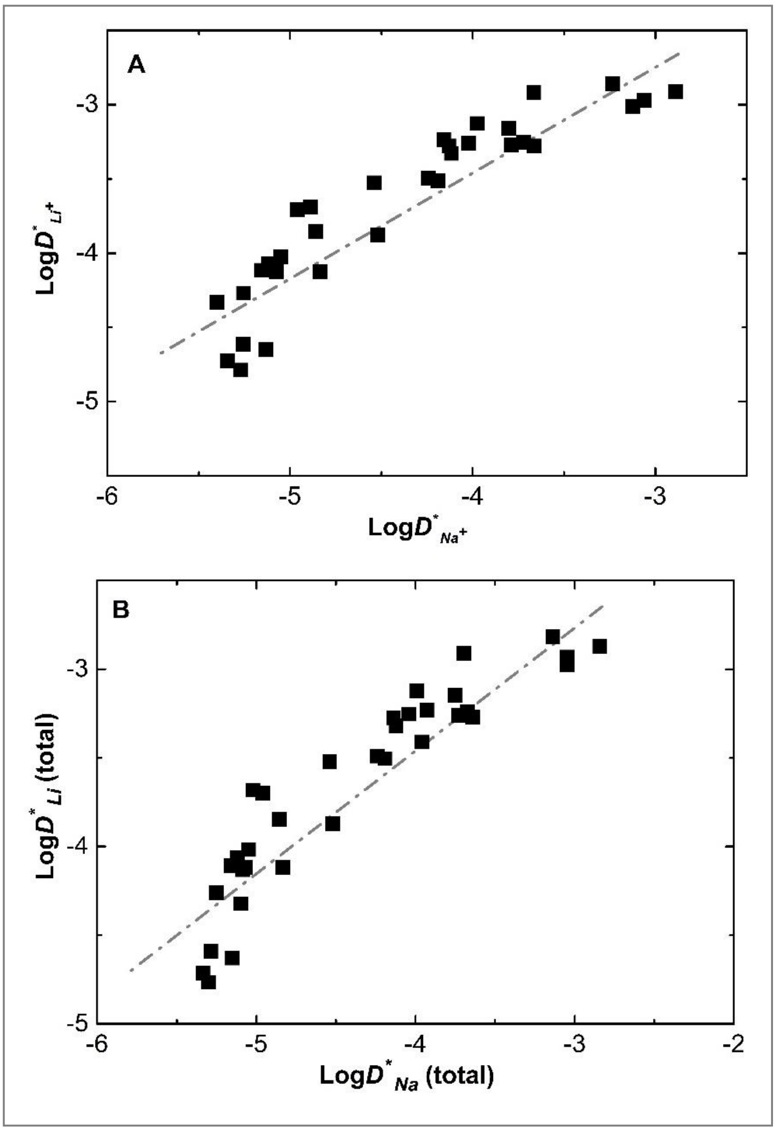

Figure 3.7: Apparent partition coefficient of Li vs Na. in calcite (A) calculated based on the abundance of free ions in the reactive fluid and (B) calculated based on the total concentrations of Li and Na in the reactive fluid. Analytical uncertainty is included in the symbol size.

3.5 Conclusions

The experimental work performed in this study documents that the incorporation of Li in calcite during its growth is affected by at least two parameters, the growth rate and the pH. The observed increase of Li incorporation in the growing calcite can be well explained by the surface entrapment approach that was previously developed by Watson and co-workers (Watson and Liang, 1995; Watson, 1996; 2004). In the case of monovalent cations such as Li^+ and Na^+, entrapment is associated with the presence of defects on crystal surface. The occurrence of such defects is expected to increase at elevated calcite growth rates, similar to the apparent Li partitioning coefficients measured herein. As such, the experimental results imply that Li/Ca ratios in natural calcites can be used as a tool for the estimation of mineral growth rates. Moreover, the similar behavior of sodium and lithium during their incorporation into calcite indicates that the introduction of monovalent cations in calcite is controlled by the same mechanism though absolute partitioning values are affected by ionic radii. The linear correlation of the apparent partitioning coefficients of Li and Na in the forming calcite is independent of growth rate effects, thus Li/Na ratios in natural calcites may be used as a novel tool for reconstructing Na or Li concentration of the aqueous fluids from which calcite formed.

The experimental results suggest that incorporation of monovalent cations in the calcite crystal lattice may be associated with the presence of HCO_3^-. Whether the bicarbonate ion is introduced in the crystal lattice or not cannot be concluded from the present study and has to be assessed in forthcoming high resolution spectroscopic studies.

Acknowledgements

We highly appreciate the support of S. Eichinger, A. Baldermann and B. Purgstaller with ICP-OES measurements. Fruitful discussions with C. Grengg, O. Pokrovsky and J. Schott during the preparation of this manuscript are highly acknowledged. The associated Editor Robert H. Byrne, Wiliam Gray and an anonymous reviewer are highly acknowledged for their insightful comments on a previous version of this manuscript. Additional thank goes to Anna L. Harrison for the help with English. This work was financially supported by Marie Skłodowska-Curie Horizon 2020 Project BASE-LiNE Earth (H2020-MSCA-INT-2014- 643084) and by the FWF-DFG project Charon II (FWF-I3028-N29).

Chapter 4

The role of growth rate and pH on lithium isotope fractionation during its incorporation in calcite

A. Füger[1], M. Kuessner[2], C. Rollion-Bard[2], A. Leis[3], M. Dietzel[1], V. Mavromatis[1,4]

[1] Institute of Applied Geosciences, Graz University of Technology, Rechbauerstraße 12, 8010, Graz, Austria
[2] Department of Geochemistry and Cosmochemistry, Institut de Physique du Globe de Paris, 1 rue Jussieu, 75005 Paris, France
[3] JR-AquaConSol GmbH, Steyrergasse 21, 8010, Graz, Austria
[4] Géosciences Environnement Toulouse (GET), CNRS, UMR 5563, Observatoire Midi-Pyrénées, 14 Avenue Edouard Belin, 31400 Toulouse, France

Abstract – The Li isotope composition of marine calcite is commonly used as an environmental proxy for paleo-seawater reconstructions and continental weathering effects. Physicochemical parameters often significantly influence element incorporation and isotope fractionation and thus corrupt the application as a paleo-proxy. However, the impact of physicochemical parameters, like pH and growth rate, on the behaviour of Li isotope fractionation during its incorporation in calcite are still underexplored. In order to rectify this, the incorporation of Li in calcite at distinct growth rates ($10^{-8.1} \leq r_p$ (mol m^{-2} s^{-1}) $\leq 10^{-7.2}$) and pH ($6.3 \leq pH \leq 9.4$) was performed. The obtained $\Delta^7Li_{calcite-solution}$ ($= \delta^7Li_{calcite} - \delta^7Li_{solution}$) values are significantly affected by both, growth rate and pH. At elevated growth rates ($r_p > 10^{-7.7}$ mol m^{-2} s^{-1}) the lighter Li isotopes are preferentially incorporated into the growing calcite by $\Delta^7Li_{calcite-solution}$ values decreasing from -2.51 ± 0.07 ‰ (2SD) down to -5.33 ± 0.09 ‰ at pH = 8.3 ± 0.2. This growth rate effect of Li isotope fractionation can be explained by kinetically controlled surface entrapment that favors lighter isotopes due to their faster transport and attachment onto the mineral surface. In the range of pH 6.3 to 8.3, smaller Li isotope fractionation during the uptake in the growing calcite is observed ($\Delta^7Li_{calcite-solution}$ = -5.28 ± 0.20 ‰ to -2.51 ± 0.07 ‰, respectively; at constant $r_p = 10^{-7.8\pm0.3}$ mol m^{-2} s^{-1}). This can be explained by the preferential incorporation of $LiHCO_3°$ complexes at defect calcite surface sites. The longer Li-O bond length in aqueous $LiHCO_3°$ versus $Li(H_2O)_n^+$ (n = 1 - 6) favors ^6Li in $LiHCO_3°$ vs. $Li(H_2O)_n^+$. This isotopic behavior is consistent with the decreasing availability of $LiHCO_3°$ for entrapment onto the calcite surface at elevated pH. At pH > 8.3, however, the $\Delta^7Li_{calcite-solution}$ is controlled by strong electrostatic attraction of Li^+ onto the calcite surface which becomes negatively charged. This process is likely dominated by adsorption and subsequent entrapment kinetics which causes the preferential incorporation of the light Li isotope.

4.1 Introduction

Lithium has two stable isotopes ^{6}Li and ^{7}Li with relative abundances of 7.59 % and 92.41 %, respectively (e.g. Rosman and Taylor, 1998). Due to their large relative mass difference (Δ ~ 16.67 %), Li isotopes exhibit a significant range of Li isotopic composition in natural environments (e.g. Hoefs, 2018). This large fractionation is the main reason that Li isotopes have received large attention e.g. during continental weathering where Li isotopes are used to constrain the intensity of continental silicate weathering and secondary mineral formation in the ocean (Chan and Edmond, 1988; Chan et al., 1992; Huh et al., 1998; 2001; Kisakűrek et al., 2005). Lithium is a conservative element that is hosted almost exclusively in trace level concentrations in silicate minerals of continental rocks (e.g. Misra and Froelich, 2012, and references therein). Therefore, beside hydrothermal fluxes (e.g. Bray et al., 2001; Chan et al., 2002), the major source of Li in oceanic water is continental weathering of the silicate host rocks (Huh et al., 1998, Misra and Froelich, 2012). The major sinks of oceanic Li can be ascribed to the neo-formation of clays during sea-floor alteration and incorporation in marine sediments (Chan et al., 1992; 2006; Vigier et al., 2008). Thereby, a lesser extent of the oceanic Li concentration is incorporated in precipitated marine calcium carbonates (e.g. Hoefs and Sywall, 1997).

Up to date, the reaction mechanisms of Li incorporation and its isotope fractionation during e.g. calcite formation have to be assessed. Okumura and Kitano (1986) performed laboratory experiments to understand the mechanisms of Li incorporation into the calcite lattice. Since then, several studies have shown that the Li/Ca ratios of marine calcium carbonates can be used as environmental proxy on past dissolved inorganic carbon (DIC; Hall and Chan, 2004; Vigier et al., 2015), the degree of seawater saturation with respect to calcite (e.g. Lear et al., 2010), salinity (e.g. Marriott et al., 2004b), pH (e.g. Füger et al., 2019, i.e. Chapter 3), temperature (Delaney et al., 1985; 1989; Marriott et al., 2004a, Lear et al., 2010; Dellinger et al., 2018) and calcite precipitation rate (Hall and Chan, 2004; Füger et al., 2019, i.e. Chapter 3). Moreover, the Mg/Li ratio in calcite and aragonite is widely used to determine ambient temperatures during carbonate mineral formation (Bryan and Marchitto, 2008; Hathorne et al., 2013; Raddatz et al., 2013; Dellinger et al., 2018).

In contrast, information about the Li isotope fractionation between carbonate minerals and solution are comparatively rare. Marriott et al. (2004a) demonstrated that the Li isotope fractionation between inorganic calcite and solution is not significantly influenced by temperature. This result is consistent with the latter case studies of Li isotopes in shallow-water and deep-sea corals (Rollion-Bard et al., 2009), foraminifera shells (Vigier et al., 2015) as well as modern calcite and aragonite shells (Dellinger et al., 2018). In addition, the experimental study of Marriott et al. (2004b) showed that with increasing salinity no effect on the Li isotope fractionation between inorganic calcite and solution occurs. In 2009, Rollion-Bard et al. demonstrated that shallow-water and deep-sea corals are not affected by pH and pCO_2 changes of past seawater. The latter study of Vigier et al. (2015) showed that Li isotopes in foraminifera shells can be used as a paleo-ocean DIC indicator. Therefore, it was concluded that the Li isotope composition of marine calcium carbonate minerals is a promising archive to reconstruct the paleo-δ^7Li of seawater in order to unravel past continental weathering rates and / or hydrothermal processes (Marriott et al., 2004a; 2004b; Rollion-Bard et al., 2009; Vigier et al., 2015; Dellinger et al., 2018). Yet, a study by Roberts et al. (2018) demonstrated a correlation of Li isotope fractionation in benthic foraminifera calcite and seawater pH.

These contradict previous observations demonstrate the need of experimental studies in order to develop reliable proxies. Thus, the present study aims to resolve these contradictions by assessing the reaction mechanisms that control Li isotope fractionation during the growth of calcite and in particular to evaluate the influence of growth rate and pH on $\Delta^7Li_{calcite-solution}$ (= $\delta^7Li_{calcite}$ - $\delta^7Li_{solution}$) values. This study is a follow up study of the previous experimental study by Füger et al. (2019; i.e. Chapter 3) which focused on elemental Li distribution between growing calcite and precipitating solution. There was shown that the incorporation of Li in calcite is affected by both, calcite growth rates and pH of the precipitating solution. It was argued that increasing growth rate induces more defect sites at the growing calcite surface and thus elevated amounts of Li in the precipitated calcite. Furthermore, it is assumed that aqueous HCO_3^- is balancing the charge of the Li^+ ion at the calcite surface during a coupled incorporation as $LiHCO_3°$. The decreasing aqueous HCO_3^- concentration at elevated pH, however, is followed by a decrease in aqueous $LiHCO_3°$ complexes and a decrease in Li incorporation in calcite. In the present study, we present and discuss the Li isotope fractionation between calcite and solution at distinct growth rates ($10^{-8.1} \leq$ rp in mol m^{-2} $s^{-1} \leq 10^{-7.2}$) and pH ($6.3 \leq pH \leq 9.4$).

4.2 Methods

4.2.1 Calcite precipitation

The experimental set up for the Li incorporation in calcite is descried in detail in Chapter 3 (i.e. Füger et al., 2019). In this set-up, the reactive solution was doped with traces of Li (0.3 ± 0.1 mM). Besides the incorporation of Li during the precipitation of calcite, in the present contribution the fractionation of the stable Li isotopes was investigated in selected experiments. For Li isotope analyses precipitated calcite at distinct growth rates ($10^{-8.1} \leq r_p$ in mol m^{-2} $s^{-1} \leq 10^{-7.2}$) and pH ($6.3 \leq pH \leq 9.4$) were selected to study the impact of both parameters on the incorporation of Li isotopes during calcite growth (see Table 4.1).

Briefly, the calcite overgrowth was induced by simultaneous pumping of two separate solutions into the reactor solution with the aid of a peristaltic pump (see Fig. C.1 in Appendix C). One solution contained $CaCl_2$ and LiCl and the second Na_2CO_3. The concentration of Ca in the inlet solutions varied between 0.025 to 0.1 M and in all runs it was kept equal to that of the concentration of Na_2CO_3 in the second inlet solution. The reactor solution contained 0.5 L of a 0.3 M NaCl solution, initial ~1 g calcite seed material (Sigma-Aldrich, > 99 %), together with a Li (i.e. LiCl) solution of 3.5×10^{-4} M. During the course of a run the pH of the reactive solution remained constant by the continuous bubbling of a CO_2, N_2 and air gas mixtures. For experiments conducted at pH > 9.0, constant pH was achieved by titration of 0.5 M NaOH into the reactor vessel. The volumes of the reactor solution were kept constant within ± 4 %, by removing every 24 h a volume from the reactor equal to the volume of the inflowing solution. Immediately after sampling, the solution was filtered through a 0.2 µm Millipore cellulose acetate syringe filter for element and isotope measurements. At the end of the experimental runs, the solution was separated from the solid phase via vacuum filtration using a 0.1 µm filter (Millipore, cellulose acetate). The solids were rinsed with deionized water to remove adsorbed Ca, Na and Li from the crystal surfaces and then dried at 40 °C.

Table 4.1: Physicochemical conditions, elemental and isotope fractionation of Li during experimentally grown calcite: pH, calcite growth rate r_p (mol m^{-2} s^{-1}), Li distribution coefficient D^*_{Li} (see Füger et al., 2019), isotopic composition of calcite $\delta^7Li_{calcite}$ ± 2SD (‰), the reactive solution $\delta^7Li_{solution}$ ± 2SD (‰) and the isotope fractionation between the latter given as $\Delta^7Li_{calcite-solution}$ ± 2SD (‰) = $\delta^7Li_{calcite}$ - $\delta^7Li_{solution}$. For calculation of $\Delta^7Li_{calcite-solution}$ the mean $\delta^7Li_{solution}$ = 8.57 ± 0.09 (n = 35) was used, as Li isotope composition of stock solution as well as all initial and final experimental solutions show the identical value within the error of isotope analysis due to Li incorporation in growing calcite at a very low level (D^*_{Li} between $10^{-3.3}$ and $10^{-5.2}$; see Füger et al., 2019; i.e. Chapter 3).

Exp	**pH**	**r_p**	**Log D^*_{Li}**	**$\delta^7Li_{calcite}$**	**$\delta^7Li_{solution}$**	**$\Delta^7Li_{calcite-solution}$**
$LiCl_{stock}$	8.34				8.67 ± 0.16	
$\#1.1_{calcite}$		$10^{-8.13}$	-4.7	5.80 ± 0.21		-2.77 ± 0.15
$\#1.2_{calcite}$		$10^{-8.00}$	-4.5	5.87 ± 0.18		-2.70 ± 0.14
$\#1.3_{calcite}$		$10^{-7.74}$	-4.5	6.06 ± 0.06		-2.51 ± 0.07
$\#1_{solution-initial}$	-				8.36 ± 0.22	
$\#1_{solution-final}$	8.26				8.39 ± 0.05	
$\#2.1_{calcite}$		$10^{-7.82}$	-4.4	5.68 ± 0.32		-2.89 ± 0.20
$\#2.2_{calcite}$		$10^{-7.51}$	-4.3	4.57 ± 0.28		-4.00 ± 0.19
$\#2_{solution-final}$	8.04				8.50 ± 0.12	
$\#3.1_{calcite}$		$10^{-7.33}$	-3.7	3.24 ± 0.09		-5.33 ± 0.09
$\#3.2_{calcite}$		$10^{-7.21}$	-3.7	5.01 ± 0.20		-3.56 ± 0.14
$\#3_{solution-final}$	8.46				8.59 ± 0.33	
$\#4.1_{calcite}$		$10^{-8.11}$	-5.2	4.82 ± 0.07		-3.75 ± 0.08
$\#4.2_{calcite}$		$10^{-7.80}$	-5.0	4.66 ± 0.17		-3.91 ± 0.13
$\#4_{solution-final}$	9.44				8.65 ± 0.15	
$\#5.1_{calcite}$		$10^{-7.72}$	-3.4	3.47 ± 0.18		-5.10 ± 0.14
$\#5.2_{calcite}$		$10^{-7.58}$	-3.3	3.29 ± 0.31		-5.28 ± 0.20
$\#5_{solution-final}$	6.30				8.59 ± 0.06	
$\#6.1_{calcite}$		$10^{-7.75}$	-3.7	5.66 ± 0.25		-2.91 ± 0.17
$\#6.2_{calcite}$		$10^{-7.69}$	-3.7	5.75 ± 0.11		-2.82 ± 0.10
$\#6_{solution-final}$	7.49				8.72 ± 0.11	

4.2.2 Solution and precipitate characterization

Chemical characterization of the reactive solutions and the precipitates yield in the element concentration which was measured using an inductively coupled plasma optical emission spectrometer (ICP-OES Optima 8300 DV, Perkin Elmer). The alkalinity of the reactive solutions was measured by standard HCl titration using an automatic Schott TitroLine alpha plus titrator with an uncertainty of ± 2 %. The pH of the reactive solutions was measured using a SenTix® 945 pH gel electrode from WTW with a precision of ± 0.04 units. In addition, the precipitates were analyzed using Attenuated Total Reflectance - Fourier Transform Infrared Spectroscopy (ATR-FTIR; Perkin Elmer Spektrum 100), X-ray diffraction (XRD; PANalytical X´Pert PRO diffractometer) and scanning electron microscope (SEM; ZEISS DSM 982 Gemini) in order to classify the precipitate mineralogy (Fig. C.2 in Appendix C and for detail see Chapter 3; i.e. Füger et al., 2019). The calculated calcite growth rate is expressed in mol m^{-2} s^{-1}, after reaching chemical steady-state conditions. The estimation is based on mass balance considerations using the number of moles of added Ca in the reactor per 24 h and corrected for the number of moles of removed Ca over 24 h via sampling, divided by the total calcite surface (m^2) and the number of 86400 seconds in 24 h. Elemental concentration, the alkalinity and the pH were used to estimate supersaturation indices with respect to calcite, calculated with PhreeqC together with its MINTEQ.V4 database (Parkhurst and Appelo, 1999). The distribution coefficients between Li and Ca are calculated as $D^{*}_{Me^{+}}$ $\left(= \frac{(c_{Me}/c_{Ca})_{calcite}}{(m_{Me^{+}}/m_{Ca^{2+}})_{solution}}\right)$, where *c* stands for the concentration of the metal ion in calcite, $m_{Me^{+}}$ is the molar concentration of free Me$^+$ in the aqueous phase and $m_{Ca^{2+}}$ is the molar concentration of free Ca ions (compare Table 3.1 in Chapter 3; i.e. Füger et al., 2019).

4.2.3 Li isotope analyses

For the Li isotope analyzes, Li was chemically separated from the respective matrices using a three-step separation protocol for the solid samples which was applied due to very high Ca/Li and Na/Li ratios. For the solution samples only the last separation protocol was used. Lithium separation protocol of Li (and Na) ion from Ca in the precipitates was adapted from Wombacher et al. (2009). This method was originally developed to isolate Ca and Mg using an ionic exchange resin (Biorad AG50-X12, 200-400 mesh). Due to the lower relative selectivity of Li for the AG50-X12 resin compared to Ca and Na, Li ions are eluted more quickly from the columns at equal flow rates. (Near) complete separation of the elution peaks is achieved by lower exchange rates, i.e. lower acid concentration. The protocol was tested with a standard solution containing ~90 mg/L calcite (Sigma-Aldrich, > 99 %), ~500 µg/L Li (MERCK single-element ICP standard, 2 – 3 % HNO_3, 1000 mg/L Li Certipur®) and ~50 mg/L Na (MERCK single-element ICP standard, 2 – 3 % HNO_3, 1000 mg/L Na Certipur®). The elements were eluted using 0.5 mol/L HNO_3 (produced of 2 x distilled 15% HNO_3 and ultrapure water). In order to verify the separation, fractions of 1 mL were collected and analyzed by ICP-OES (see Appendix C, Fig. C.3A and B).

The solid samples, ~0.1 g of finely grained calcite, were treated with concentrated HNO_3 and dried down over night at 90 °C. The residues were digested in 1 mL of 0.5 M HNO_3. Polycarbonate columns with 6 mL volume were packed with 1 mL resin and provide an additional 5 mL reservoir. The columns were conditioned in 0.5 M HNO_3 and the samples loaded in 1 mL of 0.5 M HNO_3. Lithium and Na were eluted from the columns using 20 mL 0.5 M HNO_3. The remaining Ca on the columns after this step was washed off using 5 mL 7 M HNO_3. To ensure complete purification the separation was performed twice. Li yield was routinely tested using ICP-OES.

After these separation steps the collected Li and Na fraction were evaporated and re-dissolved in 1.2 mL 0.2 M HCl (produced of 1 x distilled 36% HCl, VLSI Selectipur, BASF Electronic Materials, and ultrapure water). This separation step was used for the reactive solution samples which were evaporated and equally re-dissolved in 1.2 mL 0.2 M HCl. For the separation of Li from Na and remaining Ca the protocol developed by Kuessner et al. (submitted) was used. This separation was tested using the in-house mixed Na-Li calcite (dissolved) standard from the Ca two-step separation, collecting 1 mL fractions (see Appendix C, Fig. C.3C). This separation was conducted using 6 mL Polypropylene-polyethylene columns (AC-142-TK, TRISKEM, internal diameter: 7 mm). The columns were loaded with 2 mL resin (Biorad AG50W-X12, 200-400 mesh) and provide additional a 4 mL reservoir. The Standard Reference Material NASS-6 (seawater, National Research Council of Canada), the Li stock solution used in the experiments (LiCl, Carl Roth ≥ 98.5 %), the Li MERCK single-element ICP standard that was used for the in-house mixed Na-Li calcite (dissolved) standard, the in-house mixed Na-Li calcite (dissolved) standard and a 0.2 M HCl blank solution were systematically processed in each session to control the reliability of the separation. Before the separation of Li from Na and the matrix (remaining Ca), the columns were conditioned twice with 4 mL 0.2 M HCl. The Li-Na fraction of the sample dissolved in 1 mL of 0.2 M HCl were loaded onto the resin. To insure complete loading of the sample onto the resin and its total removal from the column's reservoir, 1.5 mL Milli-Q H_2O were used. After addition of 10 mL 0.2 M HCl, the Li fraction was collected using 18 mL of 0.2 M HCl. The remaining matrix after this step on the columns was washed off using first 4 mL 3 M HCl and afterwards 4 mL H_2O.

The collected solutions were evaporated and in order to remove organic residual (from the resin) in the Li fraction, the samples were cooked for at least 48 h in concentrated HNO_3 and HCl and subsequently evaporated over night at 90 °C. Thereafter, the samples were dissolved in 1 mL 0.5 M HNO_3 for Li isotope analyses. Lithium isotope ratios were determined with a MC-ICP-MS (Neptune + Thermo Scientific) at IPGP, France, coupled with an APEX-HF desolvation system and measurements were typically performed on solutions with a Li concentration of 20 – 30 ppb. Each sample was measured 3 times within a standard-sample bracketing (SSB) sequence. The long-term reproducibility of the measurement was checked by repeated measurements of IRMM-16 and Li-SVEC standard. The Li isotope ratios are reported as

$$\delta^7\mathrm{Li} = \frac{(^7\mathrm{Li}/^6\mathrm{Li})_{sample}\,/\,(^7\mathrm{Li}/^6\mathrm{Li})_{standard}}{(^7\mathrm{Li}/^6\mathrm{Li})_{standard}} * 10^3 \qquad (4.1)$$

relative to the L-SVEC Li-isotope standard. The uncertainties are reported as the 2 standard deviation (2SD). The overall reproducibility and accuracy were checked by the measurement of the Standard Reference Material (NASS-6, δ^7Li = 31.51 ± 0.18 ‰, n = 25), the Li stock solution (LiCl, δ^7Li = 8.67 ± 0.16 ‰, n = 15), the in-house mixed Na-Li calcite (dissolved) standard (δ^7Li = 4.25 ± 0.23 ‰, n = 30), the Li MERCK single-element ICP standard (δ^7Li = 3.92 ± 0.17 ‰, n = 71) that was used for the in-house mixed Na-Li calcite (dissolved) standard and a 0.5 M HNO_3 blank.

4.3 Results

The measured Li isotopic composition of aqueous solutions ($\delta^7\mathrm{Li}_{solution}$), precipitates ($\delta^7\mathrm{Li}_{calcite}$) and the calculated $\Delta^7\mathrm{Li}_{calcite\text{-}solution}$ values (= $\delta^7\mathrm{Li}_{calcite}$ - $\delta^7\mathrm{Li}_{solution}$) are given in Table 4.1. The Li isotopic composition of the LiCl stock solution (δ^7Li = 8.67 ± 0.16 ‰, n = 15) as well as the initial solution (8.59 ± 0.16 ‰, n = 5) and the final reactive solution at the four different final pH values (mean $\delta^7\mathrm{Li}_{solution}$ value = 8.57 ± 0.09, n = 35) exhibit a very small variation (see Fig. C.4 in Appendix C) that is lower than the analytical precision of Li isotope measurements (see Table 4.1).

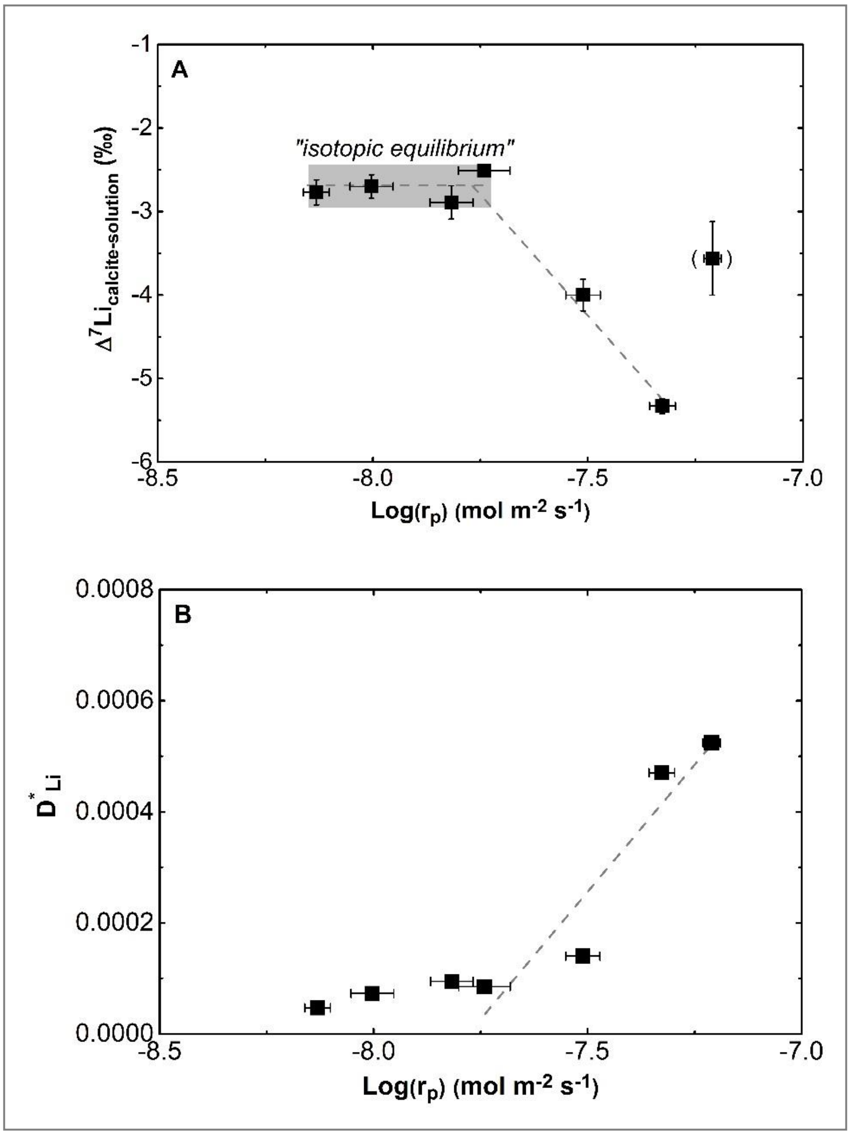

Figure 4.1: Calcite growth rate at constant pH = 8.3 ± 0.2 plotted as a function of (A) $\Delta^7Li_{calcite\text{-}solution}$ values; and (B) D^*_{Li} values.

The $\Delta^7Li_{calcite\text{-}solution}$ values as a function of growth rate and pH can be seen in Fig. 4.1A and 4.2, respectively. All experiments exhibit a preferential incorporation of ^6Li in the precipitated calcite compared to the precipitating solution. This preferential uptake of ^6Li in the precipitated calcite becomes higher at elevated calcite growth rates, starting from $10^{-8.1}$ to $10^{-7.2}$ mol m^{-2} s^{-1} (Fig. 4.1A). One data point (see Fig. 4.1A) is excluded due to the high Na/Li ratio in the measured Li faction of the precipitate after the three-step separation which might affected the Li isotope measurement.

At constant calcite growth rate ($r_p = 10^{-7.8\pm0.3}$ mol m^{-2} s^{-1}) $\Delta^7Li_{calcite\text{-}solution}$ values between calcite and solution increase from -5.28 ± 0.20 ‰ to -2.51 ± 0.07 ‰ from pH 6.3 to 8.3 (Fig. 4.2), respectively. Above pH 8.3, the $\Delta^7Li_{calcite\text{-}solution}$ values decrease from -2.51 ± 0.07 ‰ to -3.91 ± 0.13 ‰.

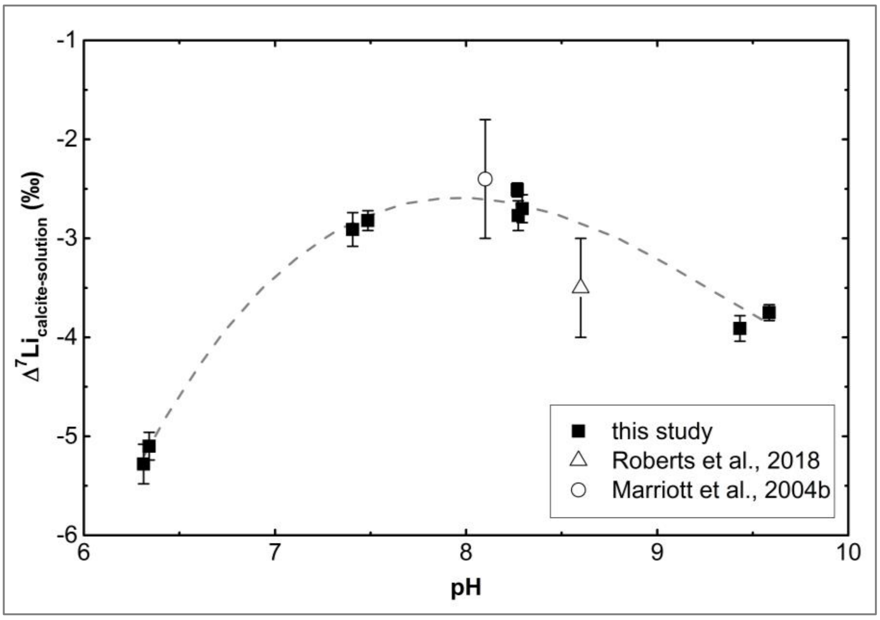

Figure 4.2: $\Delta^7Li_{calcite-solution}$ values plotted as a function of pH at constant calcite growth rate ($r_p = 10^{-7.8 \pm 0.3}$ mol m^{-2} s^{-1}). Analytical uncertainty of pH is included in the symbol size.

4.4 Discussion

4.4.1 Effect of growth rate on Li isotopic fractionation

4.4.1.1 Approaching equilibrium isotope fractionation

The obtained results (see Fig. 4.1A) suggest a preferential incorporation of lighter Li isotopes as calcite growth rates increase from $10^{-8.1}$ to $10^{-7.2}$ (mol m^{-2} s^{-1}). This observed dependence of $\Delta^7Li_{calcite-solution}$ values on the calcite growth rate likely reflects non-equilibrium isotopic conditions at elevated growth rates. In order to assess the deviation from equilibrium, however, its absolute value has to be defined. At isotopic equilibrium conditions elemental and isotopic exchange between reactant and product phases are controlled by the interplay between the net reaction rate of a forward and a backward reaction. Thereby, the forward reaction rate is described as precipitation rate, whereas the backward reaction rate is described as dissolution rate. At isotopic equilibrium conditions the rates of the forward and the backward reaction are equal as it has been formulated using transition state theory (TST; Lasaga, 1981; Aagaard and Helgeson, 1982; Oelkers, 2001; Schott et al., 2009) and later on applied to the case of Ca isotopes in calcite by the surface reaction kinetic model from DePaolo (2011). Note here, however, that in the case of Li the notion of equilibrium between solid and solution may not be straightforward. This is because in contrast to divalent cation incorporation in calcite lattice, the introduction of Li in the solid phase does not follow an one-to-one replacement of the Ca ion but it rather occurs in interstitial positions (see Chapter 3; i.e. Füger et al., 2019).

If we consider a linear deviation from isotopic equilibrium in this study that is related to increasing growth rates, we can use the diagrams of D^*_{Li} values (Fig. 4.1B) and $\Delta^7Li_{calcite-solution}$ values (Fig. 4.1A) plotted as a function of growth rate in order to calculate and extract the value of Li isotope fractionation between calcite and solution at near equilibrium. As it can be seen in Fig. 4.1A and B at calcite growth rates ≤ $10^{-7.7}$ mol m^{-2} s^{-1} at pH 8.3 the D^*_{Li} and $\Delta^7Li_{calcite\text{-}solution}$ values obtain an almost constant value. These $\Delta^7Li_{calcite\text{-}solution}$ values at calcite growth rates ≤ $10^{-7.7}$ mol m^{-2} s^{-1} are slightly negative. This result is in good agreement with the literature inasmuch as at equilibrium the light isotope (^6Li) partitions preferentially into the solid compared to the solution as it was shown previously for melts and carbonates (e.g. Marriott et al., 2004a; Wunder et al., 2006; Tomascak et al., 2016). Assuming as a working hypothesis, however, that the equilibrium D^*_{Li} value of calcite is close to zero as it is valid for Sr (D_{Sr} ~ 0.021; e.g. Tesoriero and Pankow, 1996) and Mg (D_{Mg} ~ 0.008; e.g. Mavromatis et al., 2013) we can use the linear equation (4.2) from Fig. 4.1B in order to estimate the equilibrium Li isotope fractionation between calcite and solution

$$D^*_{Li} = 9.12 * 10^{-4} (\pm 2.3 * 10^{-4}) * \mathrm{Log} r_p + 0.0071 (\pm 0.0017); R^2 = 0.94 \tag{4.2}$$

The calculated calcite growth rate and $\Delta^7Li_{calcite\text{-}solution}$ value at near equilibrium conditions is about $10^{-7.8}$ mol m^{-2} s^{-1} and -2.3 ‰. This calculated value is in good agreement with the measured $\Delta^7Li_{calcite\text{-}solution}$ values in Fig. 4.1A which approach -2.66 ± 0.12 ‰ at calcite growth rates ≤ $10^{-7.7}$ mol m^{-2} s^{-1} at pH 8.3. Just slightly faster calcite growth rate values for Sr isotope equilibrium fractionation ($10^{-8.2} \leq r_p$ mol m^{-2} s^{-1} ≤ $10^{-8.6}$; e.g. Tesoriero and Pankow, 1996; Böhm et al., 2012) and Mg isotope equilibrium fractionation (rp ~ $10^{-8.6}$ mol m^{-2} s^{-1}; e.g. Mavromatis et al., 2013) between calcite and solution were previously reported.

4.4.1.2 Kinetic isotope fractionation

A deviation from isotope equilibrium conditions is observed with increasing growth rate and lighter isotopes are preferential incorporated in the crystal structure as it can be seen in Fig. 4.1A. In the case of Li two points have to be considered related to (i) its elemental properties and (ii) the incorporation mechanism.

For (i), the Li ion is different in charge, cation size and hydration sphere compared to divalent cations. Indeed, the hydration sphere of Li is different compared to e.g. Sr, but similar to Mg. It was previous shown that in particular the hydration sphere is a controlling parameter during the incorporation of divalent cations (e.g. Nielsen, 1984). Strontium isotope fractionation shows the same disequilibrium trend for stable isotope fractionation between solid and solution at elevated growth rates as Li (e.g. Böhm et al., 2012), whereas Mg isotope fractionation shows the opposite trend (e.g. Mavromatis et al., 2013). The different isotope fractionation behavior between Sr and Mg likely stems from the different dehydration behavior. The Mg ion dehydrates only partially when it is incorporated into the calcite crystal lattice compared to Sr which dehydrates completely related to weaker hydration complexes (e.g. Tang et al., 2008a; Böhm et al., 2012; Mavromatis et al., 2013). A direct comparison between Li with Mg and Sr, however, is not straightforward due to the incorporation in different sites (ideal substitution for the Ca ion of the Sr and Mg ion versus Li incorporation in interstitial position of the calcite lattice) during the growth of calcite (see (ii)). Lithium, in general, forms rather weak hydration complexes, so that the Li^+-water complex is unstable with rapid water exchange rates between the hydration shell and the surrounding medium (i.e. $5.8 * 10^{9}$ s^{-1}; Loeffler et al., 2006). The dehydration involves a bond breaking that is favored for the lighter isotopic species (Bigeleisen, 1949). These facts may lead to a complete dehydration of Li prior to its incorporation. In contrast, owing to the small radius of Li (i.e. 0.59 - 0.76 Å; Shannon, 1976) and the short Li-O bond lengths of the Li^+ aquo-ion (i.e. ~1.95 Å; Marcus, 1988) there might be no reason for the dehydration of Li before its incorporation into the interstitial position. In any case, whether Li is introduced in the crystal lattice in its hydrated form or not cannot be concluded from the present study.

However, for (ii), Nielsen et al. (2012) and Eiler (2013) mentioned that different incorporation sites might control differently the isotopic behavior during the element incorporation. Lithium is most likely incorporated in defect sites at the calcite surface and shows no ideal substitution for the Ca ion in contrast to divalent metals such as Sr and Mg (e.g. Tang et al., 2008a; 2008b; Böhm et al., 2012; Mavromatis et al., 2013; Chapter 3). DePaolo (2011) mentioned that the isotopic composition of the solid is affected by transport to the reactive site as well as attachment / detachment kinetics on the minerals surface. At higher growth rates, the transport and attachment of the ions to the mineral surface is fast which is favored for isotopic species with higher reaction rates. It is known that the lighter isotopes exhibit a higher vibrational energy and molecular velocity with higher reaction rates (e.g. Criss, 1999; Zeebe and Wolf-Gladrow, 2001; Richter et al., 2003; Hoefs, 2018). According to the relative mass difference of the two Li isotopes (~16.67 %; e.g. Hoefs, 2018), the Li transport and attachment is favored for the lighter Li isotopes at elevated growth rates.

4.4.2 Effect of pH on the Li isotopic fractionation

The $\Delta^7Li_{calcite-solution}$ value, for experiments conducted under similar surface normalized growth rates (i.e. $r_p = 10^{-7.8 \pm 0.3}$ mol m^{-2} s^{-1}), reaches a maximum around pH 8.3 (see Fig. 4.2). We note here that the Li isotope fractionation shows a different behavior as a function of pH compared to the corresponding Li distribution coefficient which exhibits a strong reduction as pH increases from ~6.3 to ~9.4 (see Füger et al., 2019; Chapter 3). Actually, as it can be seen in Fig. 4.3A, a direct comparison between the distribution coefficient and the Li isotope fractionation as a function of pH is not straightforward. Thus, it is suggested that Li isotope fractionation can be divided in two parts depending on the pH of the reactive solution: (i) 6.3 ≤ pH ≤ 8.3; and (ii) 8.3 ≤ pH ≤ 9.4.

For (i), 6.3 ≤ pH ≤ 8.3, with increasing pH, a smaller Li isotope fractionation can be seen (Fig. 4.2). The results of Füger et al. (2019; i.e. Chapter 3) lead to the suggestion that the incorporation of Li in calcite as a function of pH is accompanied by a positive charge excess at the calcite crystal structure which is balanced by the presence of bicarbonate. With decreasing presence of bicarbonate in the solution less Li is incorporated in calcite. This correlation is accompanied with a smaller Li isotope fractionation, as it can be seen in Fig. 4.3B. The good correlation, however, of the activity of aqueous bicarbonate with (i) Li distribution coefficient in Chapter 3 (Füger et a., 2019), and (ii) the Li isotope fractionation (see Fig 4.3B) supports the assumption of Li^+ aquo-complex formation with HCO_3^- (e.g. $LiHCO_3^0$). This observed fractionation can be likely explained by changes in the mean Li-O bond distance between aqueous $[Li(H_2O)_n]^+$ (n = 1 - 6) and aqueous $LiHCO_3$ complexes as earlier studies argued (e.g. Wunder et al., 2011). In aqueous solutions Li forms $[Li(H_2O)_n]^+$ (n = 1 – 6; e.g. Yamaji et al. 2001) complexes with Li-O distances of ~1.8 Å ($[Li(H_2O)_1]^+$), ~1.9 Å ($[Li(H_2O)_4]^+$) and ~2.1 Å ($[Li(H_2O)_6]^+$), respectively (e.g. Marcus, 1988; Yamaji et al. 2001). To the best of our knowledge, until now no Li-O distance data of $LiHCO_3$ complexes are available.

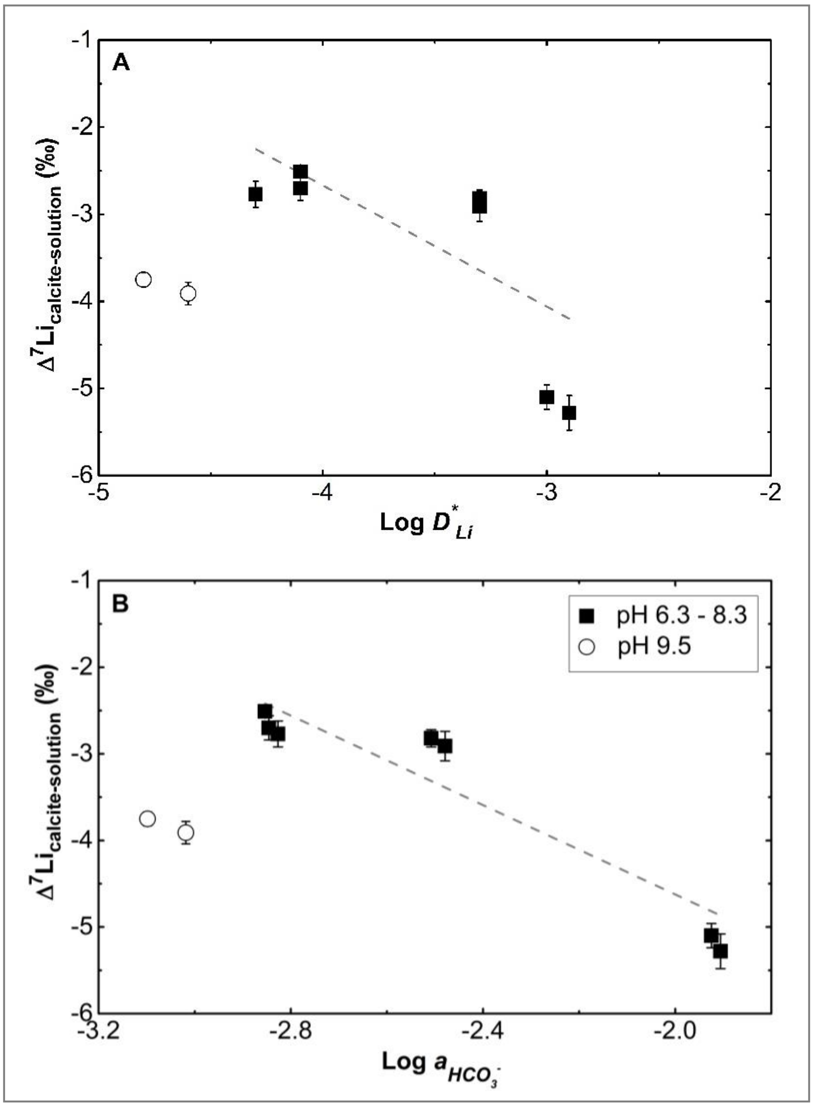

Figure 4.3: $\Delta^7Li_{calcite-solution}$ shown as a function of (A) distribution coefficient for Li concentration in precipitating calcite and growing solution; and (B) aqueous HCO_3^- activity. Analytical uncertainty of the distribution coefficient and the a_{HCO3-} are included in the symbol size.

Owing to the lack of relevant data, one can assume that the behavior of Li-O bond length is similar to that observed for the Na-O bond length. We note here that as it has been shown earlier in Chapter 3 (i.e. Füger et al., 2019) the incorporation of Na in calcite follows a similar behavior to that of Li as a function of pH. Thus, as a working hypothesis it can be assumed that changes in the Na-O distance between hydrated Na^+ and aqueous $NaHCO_3$ complexes can be applied for Li. The reported Na-O distances for hydrated Na^+ are ~2.4 Å (Kameda et al. 1998), whereas the same distance in $NaHCO_3$ complexes is ~2.5 Å (Zachariasen, 1933). It is known, that the lighter isotope would be concentrated in longer and consequential weaker bonds compared to the heavy isotope (e.g. Hoefs, 2018). Therefore, the high concentration of bicarbonate in the solution at low pH intensifies the affinity for cation-anion complexation. This step is accompanied with longer Li-O bonds in the aqueous $LiHCO_3^0$ complexes compared to hydrated Li^+ and is therefore favored for the light Li isotope. With increasing pH, the aqueous bicarbonate concentration decreases as well as the cation-anion complexation so that a smaller Li isotope fractionation is observed.

For (ii), $8.3 < pH \leq 9.4$, it can be seen that lighter isotopes are preferential incorporated in the solid phase (Fig. 4.2). We note here that the low aqueous bicarbonate concentration at elevated pH provides a very low affinity for cation-anion complexation so that a preferential incorporation of the heavy Li isotope can be expected. Although the distribution coefficient is decreasing at elevated pH, an adsorption mechanism controlling Li^+ incorporation in the growing calcite was not excluded (Füger et al., 2019; i.e. Chapter 3). Following this assumption of adsorption, the surface charge of calcite as a function of pH has to be considered. It is known that at the point of zero charge (pH_{PZC} = ~8.6) the calcite surface charge is changing with increasing pH from positive to negative (e.g. Somasundaran and Agar, 1967). The negative surface charge of calcite promotes the adsorption of positive charged ions (e.g. Appelo and Postma, 2007). This strong electrostatic attraction of an initial adsorption and subsequent entrapment process is strong kinetically controlled related to transport rates (e.g. Hoefs, 2018). Due to the faster transport of the lighter isotopes for adsorption on the mineral surface, the lighter Li isotopes are favored.

4.4.3 Implications for Li isotope composition of natural calcites

The obtained results of this study indicate that the growth rate plays a major role for the Li isotope fractionation between calcite and solution. Up to the best of our knowledge, no growth rate data from natural grown carbonates for comparison exists. However, we have to note here that due to the fact that our experimental solutions do not contain other major ions such as Mg^{2+} and SO_4^{2-} that are present in seawater (e.g. Broecker, 1974), a direct comparison to marine-grown carbonates is not straightforward. In any case, we suppose the partitioning of Li in natural calcites accompanied with the Li isotope fractionation between calcite and solution as a potential tool in order to estimate the formation rate of natural grown calcite.

The other observed finding in this study is that Li isotope fractionation between calcite and water is dependent on the solution pH. Former studies of measured Li isotope composition in foraminifera shells as well as shallow-water and deep-sea corals demonstrated no dependence on the pH (e.g. Rollion-Bard et al., 2009; Vigier et al., 2015). In contrast, a later study by Roberts et al. (2018) showed a pH-dependence of $\delta^7Li_{foraminifera}$ values in benthic foraminifera calcite. The results of their study indicate an anti-correlation between $\delta^7Li_{calcite}$ values and the pH in the pH range between 7.9 and 8.6 from ~30.3 ‰ down to ~27.5 ‰. Using a $\delta^7Li_{seawater}$ value of +31 ‰ for the modern sea water (Misra and Froelich, 2012), the $\Delta^7Li_{calcite-solution}$ values range from -0.7 ‰ down to -3.5 ‰. Using the $\Delta^7Li_{calcite-solution}$ value from Roberts et al. (2018) at pH 8.6 (-3.5 ‰) it fits well to our data (see Fig. 4.2). Furthermore, a dependence of the Li isotope composition and dissolved inorganic carbon in calcite has previously been shown to exist in marine-derived carbonates such as foraminifera shells. Vigier et al. (2015) provided an increase of the heavier Li isotopes ($\delta^7Li_{foraminifera}$) from ~31.8 to ~37.7 ‰ in calcite with increasing DIC (from 2 to 3 mmol/kg). The data of the present study show a similar trend of the $\delta^7Li_{calcite}$ values ($4.7 \leq \delta^7Li_{calcite}$ ‰ ≤ 6.1) in the same DIC range compared to the data of Vigier et al. (2015). The absolute Li isotope fractionation values of the natural grown marine carbonates, however, are increasing ($1.8 \leq \Delta^7Li_{calcite\text{-}solution}$ ‰ ≤ 7.7) compared to the values of the present study ($-2.5 \geq \Delta^7Li_{calcite\text{-}solution}$ ‰ ≥ -3.9). Such a discrepancy of the $\Delta^7Li_{calcite\text{-}solution}$ values in comparison to the studies of Vigier et al. (2015) and Roberts et al. (2018) indicates that the implication of Li isotopes as a pH and / or DIC proxy is not straightforward for biogenic induced marine carbonates as vital effects have to be considered.

Moreover, a reliable Li isotopic composition of the precipitating solution, seawater / internal solution has to be postulated. According to this, the formation of crystalline $CaCO_3$ via an ACC (amorphous calcium carbonate) precursor phase has become of interest as it can be of relevance for biogenic and abiogenic carbonate mineral precipitation (e.g. Brečević and Nielsen, 1989). A hint on a potential mechanism for lower isotope fractionation during $CaCO_3$ formation can be given from Mg isotope fractionation during ACC formation and subsequent transformation to calcite (Mavromatis et al., 2017a). Magnesium isotopes were trapped into ACC with low fractionation (without sorting), which might be also valid for Li. Indeed, the different incorporation sites, as mentioned above, between Mg and Li have to be considered. However, fast precipitation of calcite which may result in larger Li isotope fractionation, might be well distinguishable with calcite formed by ACC transformation within internal limited systems by Li isotopes in calcite if the same precipitating solution can be reasonably considered. In any case, further investigations on Li isotope fractionation (i) throughout the formation and transformation of ACC; (ii) during the growth of biogenic induced calcite by analyzing besides the solid also the solution Li isotopic composition at controlled culturing conditions; and (iii) forthcoming high resolution spectroscopic studies in order to verify whether Li is incorporated with its hydration sphere or not, are highly encouraged.

4.5 Conclusions

In the present study we experimentally demonstrated a significant isotope fractionation of Li between the growing calcite and the precipitating solution which is affected by both, growth rate and pH (T = 25 °C). The observed Li isotope fractionation between calcite and reactive solution can be explained by surface kinetic models and surface reactions. With increasing growth rates a preferential incorporation of lighter Li isotopes into the growing calcite with $\Delta^7Li_{calcite\text{-}solution}$ values from -2.51 ± 0.07 ‰ down to -5.33 ± 0.09 ‰ is observed. Differences in reaction rates between the two Li isotopes based on their different isotopic masses lead to the faster transport and attachment of lighter Li isotopes onto the calcite surface at elevated growth rates. Accordingly, the good correlation of the Li isotope distribution and the Li/Ca values with the growth rate can be used in order to calculate formation rates of natural grown calcite.

In the pH range between 6.3 and 8.3 it is suggested that Li is in particular incorporated in calcite as $LiHCO_3^\circ$ complex (see Füger et al., 2019; i.e. Chapter 3 for detail). The longer Li-O bond length (less bond energy) in the $LiHCO_3^\circ$ complex compared to hydrated Li^+ leads to the preferential incorporation of lighter Li isotopes into the growing calcite at lower pH. Indeed, with increasing pH the bicarbonate concentration and its incorporation as cation-anion complex is decreasing accompanied by smaller Li isotope fractionation from -5.28 ± 0.20 ‰ to -2.51 ± 0.07 ‰. At pH

> 8.3, however, strong electrostatic attraction controls the adsorption of Li^+ onto the negatively charged calcite surface. This process is strong kinetically dominated with a preferential incorporation of lighter Li isotopes. The use of Li isotope fractionation in order to calculate paleo-seawater pH or DIC is up to date not straightforward and needs further investigations.

Acknowledgements

We acknowledge the support of J. A. Stammeier, B. Purgstaller, K. Götschl, P. Louvat, J. Bouchez and J. Gaillardet for enlightening discussions. This project has received funding by Marie Skłodowska-Curie Horizon 2020 Project BASE-LiNE Earth (H2020-MSCA-INT-2014- 643084) and by the FWF-DFG project Charon II (FWF-I3028-N29).

Chapter 5

The role of pH on chromium partitioning and isotopic fractionation during its incorporation in calcite

A. Füger[1], S. Bruggmann[2], R. Frei[2], A. Leis[3], M. Dietzel[1], V. Mavromatis[1,4]

[1] Institute of Applied Geosciences, Graz University of Technology, Rechbauerstraße 12, 8010, Graz, Austria
[2] Department of Geosciences and Natural Resource Management, University of Kopenhagen, Øster Voldgade 10, 1350, Copenhagen, Denmark
[3] JR-AquaConSol GmbH, Steyrergasse 21, 8010, Graz, Austria
[4] Géosciences Environnement Toulouse (GET), CNRS, UMR 5563, Observatoire Midi-Pyrénées, 14 Avenue Edouard Belin, 31400 Toulouse, France

Abstract – The Cr(VI) incorporation and chromium stable isotope composition in calcite has been studied in experiments performed in the pH range between 8.0 and 10.6 at constant temperature (T = 25 ± 1 °C), precipitation rate ($r_p = 10^{-7.7 \pm 0.2}$ mol m^{-2} s^{-1}) and total aqueous Cr(VI) concentration (Cr(VI) = 49.6 ± 1.3 mM). The obtained results indicate that Cr(VI) incorporation in calcite is pH-dependent and it is significantly affected by the formation of the aqueous $CaCrO_4^0$ species. Indeed, the experimental findings suggest that during calcite growth at pH < 9.4 Cr(VI) uptake in the solid phase is likely controlled by the initial adsorption and subsequent incorporation of $CaCrO_4^0$ complexes, whereas this process is balanced by the additional uptake of aqueous CrO_4^{2-} species when the reaction solution has a pH ≥ 9.4. This distinct mechanism of Cr(VI) incorporation into calcite is further confirmed by the Cr(VI) isotope fractionation between calcite and the precipitating solution. Owing to the longer Cr-O bond lengths in aqueous $CaCrO_4^0$ compared to CrO_4^{2-} species the lighter ^{52}Cr(VI) isotope is preferentially abundant in the aqueous $CaCrO_4^0$. The preferential uptake of the isotopically lighter $CaCrO_4^0$ in the growing calcite results in Cr(VI) isotope fractionation, $\Delta^{53}Cr_{calcite\text{-}solution} = \delta^{53}Cr_{calcite} - \delta^{53}Cr_{solution}$, as low as -0.7 ‰ at pH 8. In contrast, at pH > 9.4 the smaller contributions of $CaCrO_4^0$ in the total concentration of Cr(VI) in calcite yields in a $\Delta^{53}Cr_{calcite\text{-}solution}$ value close to zero ($\Delta^{53}Cr_{calcite\text{-}solution}$ = 0.05 ± 0.01‰).

Our results imply that the chromium isotope tracer system applied to calcite, and to carbonates in general, as an environmental proxy for the reconstruction of ocean redox, is not solely a mirror of redox effects in the aqueous fluid from which the carbonates precipitate, but additionally is controlled by the effect of pH and consequently by the relative stability and the distribution of aquo-complexes, in particular the occurrence of $CaCrO_4^0$. Speciation calculations that include the presence of $CaCrO_4^0$ for calcite precipitated from seawater predict isotope fractionation values that lay within -0.67 ‰ < $\Delta^{53}Cr_{calcite\text{-}solution}$ < -0.43 ‰, and come in excellent agreement with the experimental results of this study at similar pH conditions. This theoretic perspective predicts that calcite formation under pH conditions below 8.5 results in depletion of ^{53}Cr(VI) in the growing calcite

crystal. In contrast, the Cr(VI) isotopic composition of precipitating calcite in alkaline solutions can be reasonably taken to directly depict the Cr(VI) isotopic signature of the aqueous solution from which the calcite forms, at least within the above range of experimental conditions.

5.1 Introduction

The trace elemental composition of carbonate rocks, as well as their isotopic ratios, are widely used for the reconstruction of marine and lacustrine environmental conditions that prevailed in the geological past. The incorporation of trace elements and / or impurities into the lattice of carbonate minerals, however, is controlled by physicochemical parameters such as temperature, pH or salinity, and it is affected by the mineralogy of the precipitated $CaCO_3$ phase (e.g. Mucci and Morse, 1983; Busenberg and Plummer, 1985; Dietzel and Usdowski, 1996; Tesoriero and Pankow, 1996; Dietzel et al., 2004; Tang et al., 2008a; Mavromatis et al., 2013; 2015; 2017b; 2018; 2019; Füger et al., 2019). To date the majority of scientific contributions in this field have mainly focused on the incorporation behavior of divalent metal cations (Me^{2+}), owing to the fact that they ideally substitute for Ca^{2+} in the lattice of $CaCO_3$ minerals, e.g. calcite and aragonite (e.g. Reeder et al., 1999; Finch and Allison, 2007). So far, less attention has been given to the incorporation of oxyanions, although studies for sulfate (e.g. Busenberg and Plummer, 1985; Wynn et al., 2018), arsenate (e.g. Yokoyama et al., 2012) and selenite substitution (e.g. Cowan et al., 1990; Reeder et al., 1994; Hebling et al., 2014) exist. Likely the most well studied example of oxyanion substitution in $CaCO_3$ minerals is that of borate and its isotopic composition (Mavromatis et al., 2015; Noireaux et al., 2015; Uchikawa et al., 2015; 2017), owing to its use as a potential pH proxy (Hemming and Hanson, 1992). Interestingly, although chromate content and its Cr(VI) isotope composition in marine carbonates are increasingly used as paleo-redox proxies, e.g. aimed to be eventually useful in the reconstruction of atmospheric oxygen levels (e.g. Frei et al., 2009; Crowe et al., 2013; Reinhard et al., 2013; Planavsky et al., 2014), the reaction mechanisms and the Cr isotope discrimination during chromate incorporation in calcite are not well explored (Tang et al., 2007; Rodler, 2015; Rodler et al., 2015). The topic of this study is to contribute to the understanding of the mechanisms controlling the incorporation of Cr(VI) and the potential chromium isotope fractionation during its incorporation in calcite. The ultimate goal is to set a framework that can be used in the evaluation and characterization of marine depositional environments in the past that rely on the isotope signature of chromium in carbonates.

Owing to its significant redox sensitivity, the chromium isotope system has become a modern tool to study the evolution of oceanic and atmospheric O_2 levels in Earth's history (Frei et al., 2009; 2011; Konhauser et al., 2011; Bonnand et al., 2013; Crowe et al., 2013; Frei and Polat, 2013; Planavsky et al., 2014; Gilleaudeau et al., 2016; 2018; Rodler et al., 2016; 2017). Chromium occurs mainly in the oxidation states (VI) and (III). The oxidized Cr(VI) species can be mobilized as aqueous chromates CrO_4^{2-}, $HCrO_4^{-}$ and $CaCrO_4^{0}$. Aqueous Cr(VI) complexes can be incorporated into carbonate minerals, ideally replacing CO_3^{2-} in their lattice (Tang et al., 2007). In contrast, dissolved reduced Cr(III) species are strongly particle reactive and usually form oxides or oxyhydroxides that are insoluble and immobile in the pH range met in natural waters. However, likely through its complexation with inorganic (McClain and Maher, 2016) and / or organic molecules (Nakayama et al., 1981; Kaczynski and Kieber, 1994), Cr(III) can readily form soluble organometallic complexes that may or may not have a significant control on the dissolved Cr pool in a specific water column.

The common view of the Cr isotope paleo-redox proxy is grounded in the idea that oxidative weathering of Cr(III)-containing minerals by manganese (Mn) oxides, the formation of which requires free oxygen, is required for Cr redox cycling and Cr isotope fractionation. During this oxidation process, soluble Cr(VI) is released and transported to the oceans, reduced to Cr(III) under reducing environments, and deposited in marine sediments (Schoenberg et al., 2008; Frei et al., 2009). Thus, authigenic marine sediments, such as carbonates, capture an integrated isotopic signature reflective of the redox processes involved in Cr(III) oxidative mobilization, partial Cr(VI) reduction during riverine transport, and ultimate Cr(III)/Cr(VI) burial in sediments.

Thus, oxidation of Cr(III) to Cr(VI) from e.g. igneous terrestrial reservoirs leads to mobilization of Cr(VI) that eventually ends up in oceanic waters (e.g. Robles-Camacho and Armienta, 2000; Oze et al., 2007; Izbicki et al., 2008). The (partial) reduction of Cr(VI) during the transport via groundwater and rivers results in an enrichment of ^{53}Cr(VI) vs ^{52}Cr(VI) as the immobile Cr(III) is ^{53}Cr depleted (e.g. Ellis et al., 2002; 2004; Jamieson-Hanes et al., 2012; Kitchen et al., 2012; Crowe et al., 2013; Šillerová et al., 2014). The shift in δ^{53}Cr(VI) values during Cr(VI) reduction reflects the breaking of Cr-O bonds of the Cr(VI) oxyanions (Ellis et al., 2002; Schauble et al., 2004; Hoefs, 2018).

Under oxidizing conditions Cr(VI) remains mobile in seawater (Rai et al., 1987; Palmer and Puls, 1994) and may react with minerals such as sulfides, oxides, silicates and carbonates (e.g. Fendorf, 1995; Wei et al., 2002). Experimentally the study by Tang et al. (2007) was the first one that mechanistically studied the incorporation of Cr(VI) in calcium carbonate and later on Rodler et al. (2015) reported on the Cr(VI) isotope fractionation between calcite and solution using rapid Cr(VI)calcite co-precipitation experiments in the absence of Cr(III). These co-precipitation experiments of chromate and calcite at pH ≈ 8.3 conducted using the CO_2 diffusion technique (Dietzel and Usdowski, 1996; Dietzel et al., 2004) and showed a preferential incorporation of light Cr isotopes on the precipitates (Rodler, 2015). Depending on the initial Cr concentrations, the authors observed Cr isotopic offsets ranged between -2.65 ± 0.06 ‰ (~0.6 μg g^{-1}) and -0.84 ± 0.03 ‰ (60 μg g^{-1}).

In the present study, we examine the hitherto not assessed effect of pH on the Cr(VI) incorporation and its isotopic fractionation during calcite growth in inorganic precipitation experiments at well-defined physicochemical conditions.

5.2 Methods

5.2.1 Precipitation experiments

Experiments of Cr(VI) co-precipitation with calcite were performed at the pH range between 8.0 and 10.6, reaction temperature of 25 ± 1 °C and at constant aqueous Cr(VI) concentration (i.e. 49.6 ± 1.3 mM). The experiments were conducted in reactive fluids with a KCl background electrolyte concentration of 0.2 M using a mixed flow reactor (Fig. 5.1) previously described in Mavromatis et al. (2013; 2015) and Füger et al. (2019). Initially, about 0.5 g of calcite seed material (Sigma-Aldrich, ReagentPlus®, > 99 %) was introduced into the reactor containing a solution at near equilibrium conditions with respect to calcite.

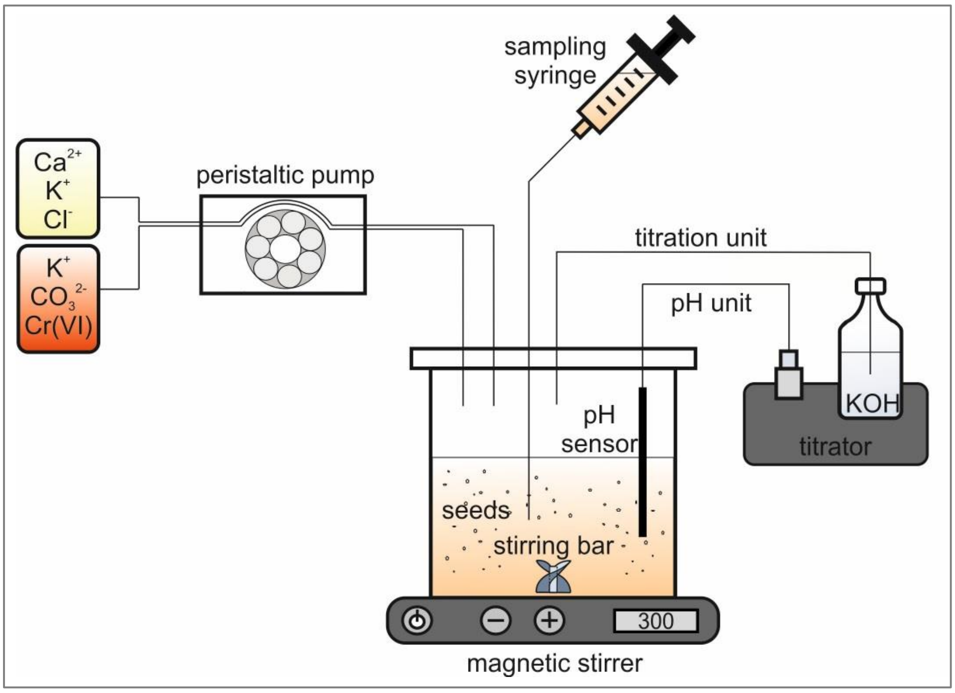

Figure 5.1: Experimental set-up for the Cr(VI) incorporation in calcite.

The subsequent overgrowth of calcite was evoked by simultaneous pumping of two separate inlet solutions into the reaction vessel using a peristaltic pump. One solution contained dissolved KCl and $CaCl_2$ and the other K_2CO_3 with $K_2Cr_2O_7$ as Cr(VI) source (see Table 5.1 for more details). The precipitation rate was held constant using similar pumping rates of the inlet solutions in all runs (i.e. ~20 mL/24 h). Note here that in the experiments performed at pH ≥ 9.4 additional titration of up to 7 mL KOH (in 7 d experimental duration) was necessary in order to keep the pH constant. As it can be seen in Table 5.1, this amount of additional K did not significantly affect the K concentration in the reactive solution.

Initially the reactor vessel contained 500 mL of a KCl solution and was equipped with a Teflon-coated floating stir bar rotating at 300 rpm. The initial Cr(VI) concentration of the reactor solution was set to half of the concentration of the inlet solution. The concentration of Ca in the inlet solution was kept equal to the concentration of K_2CO_3. All solutions were prepared using analytical grade $CaCl_2$ (Carl Roth, ≥ 99 %, ACS) and K_2CO_3 (Merck, ≥ 99 %, ACS, ISO) as well as high purity deionized water (resistivity 18.2 M Ω cm^{-1}). Note here that in all experimental runs a single Cr(VI) source was used ($K_2Cr_2O_7$; Carl Roth, ≥ 99.5 %, ACS, ISO).

In order to keep the volume of the reactive solution in the reactor constant during the experimental runs, every 24 h a volume of the reactive solution equal to the volume that was added within 24 h by the peristaltic pump was sampled. These solutions were filtered instantly after sampling through a 0.1 µm filter (Millipore cellulose acetate) and measured for pH as well as alkalinity. Subsequently, the samples were acidified using 2 % HNO_3 for Ca, K and Cr analyses. At the end of the experimental runs, the experimental solutions were separated from the precipitate phases via vacuum filtration using 0.1 µm filters. The precipitates were rinsed with deionized water to remove the experimental solution and adsorbed Ca, K and Cr on the crystal surfaces and subsequently dried at 40 °C. The duration of each precipitation run was set to 7 days.

Table 5.1: Chemical and isotopic composition as pH of reactive solution at steady state conditions, sampling time (min), precipitation rate r_p (mol m^{-2} s^{-1}), concentration of the final solution for HCO_3^-, CO_3^{2-}, total Cr(VI), Ca and K (mM).

Exp	pH	time	r_p	HCO_3^-	CO_3^{2-}	Cr(VI)	Ca	K
$K_2Cr_2O_{7stock}$	3.85	-						
#1.1	7.96	10457	$10^{-7.98}$	2.49	0.03	50.85	15.01	194.87
$\#1.1_{solution\_initial}$	-	0						
#1.2	8.00		$10^{-7.95}$	2.40	0.03	50.40	13.97	193.79
#2.1	8.50		$10^{-7.64}$	1.51	0.05	49.79	6.25	218.91
#2.2	8.54	9760	$10^{-7.61}$	1.44	0.06	49.41	6.42	213.38
#3.1	9.36		$10^{-7.72}$	0.53	0.14	49.38	5.07	207.89
#3.2	9.41	9715	$10^{-7.59}$	0.49	0.14	48.87	4.85	207.51
#4.1	10.46		$10^{-7.63}$	0.05	0.16	49.07	5.15	210.20
#4.2	10.57	9855	$10^{-7.56}$	0.04	0.15	48.98	4.10	208.53
$\#4.2_{solution\_initial}$	-	0						
$\#4.2_{solution}$	10.60	1365						
$\#4.2_{solution}$	10.67	2905						
$\#4.2_{solution}$	10.46	4095						
$\#4.2_{solution}$	10.51	5795						
$\#4.2_{solution}$	10.69	7320						
$\#4.2_{solution}$	10.59	8605						

Table 5.1 (continued): Chemical and isotopic composition as Cr(VI) concentration of precipitate (mg/kg), distribution coefficient ($D_{Cr(VI)}$), SI with respect to calcite, $\delta^{53}Cr_{solution}$ ± 2SD (‰), $\delta^{53}Cr_{calcite}$ ± 2SD (‰) and $\Delta^{53}Cr_{calcite\text{-}solution}$ ± 2SD (‰).

Exp	Cr(VI)	$D_{Cr(VI)}$	SI	δ^{53}Cr	δ^{53}Cr	Δ^{53}Cr
	calcite			solution	calcite	calcite-solution
$K_2Cr_2O_{7stock}$				-0.26 ± 0.06		
#1.1	1121.7	-5.67	0.71	-0.14 ± 0.01	-0.86 ± 0.08	-0.72 ± 0.05
$\#1.1_{solution\_initial}$				-0.13 ± 0.06		
#1.2	956.6	-5.67	0.70		-0.81 ± 0.01	-0.67 ± 0.01
#2.1	729.6	-5.50	0.64		-0.36 ± 0.02	-0.26 ± 0.02
#2.2	679.0	-5.52	0.67	-0.10 ± 0.02	-0.37 ± 0.08	-0.27 ± 0.05
#3.1	682.7	-5.13	0.95	-0.11 ± 0.05	-0.06 ± 0.06	0.05 ± 0.06
#3.2	469.7	-5.28	0.95		-0.11 ± 0.04	0 ± 0.05
#4.1	710.7	-5.07	1.01		0.01 ± 0.01	0.12 ± 0.05
#4.2	514.0	-5.15	0.90	-0.11 ± 0.09	-0.08 ± 0.05	0.03 ± 0.07
$\#4.2_{solution\_initial}$				-0.09 ± 0.05		
$\#4.2_{solution}$				-0.18 ± 0.09		
$\#4.2_{solution}$				-0.11 ± 0.05		
$\#4.2_{solution}$				-0.26 ± 0.13		
$\#4.2_{solution}$				-0.14 ± 0.03		
$\#4.2_{solution}$				-0.07 ± 0.03		
$\#4.2_{solution}$				-0.07 ± 0.06		

5.2.2 Solution characterization

The pH was measured using a SenTix 945 from WTW combined with a SenTix® 945 pH gel electrode with a glass shaft from WTW, calibrated on the activity scale with NBS buffers (pH = 4.01, 6.87 and 9.18 at 25 °C). Precision of pH measurements was ± 0.04 units. The DIC (dissolved inorganic carbon) of the solution was measured using a SHIMADZU Total Organic Carbon Analyzer accompanied with an ASI-V autosampler at a precision ≤ 2 %. The total K, Ca and Cr concentrations of the solutions were measured using a Perkin Elmer Optima 8300 DV ICP-OES with an analytical precision of ± 3 %. Cr content was additionally assessed to be equal to Cr(VI) concentration by ion chromatography (Dionex IC S 3000, IonPac, AS19 and CS16 column) with an analytical precision of ± 5 %.

Aqueous chromate speciation (e.g. CrO_4^{2-}, $HCrO_4^-$, $KCrO_4^-$ and $CaCrO_4^0$) was modeled using PHREEQC software (Parkhurst and Appelo, 1999) together with its MINTEQ.V4 database after the addition of the aqueous $KCrO_4^-$ and $CaCrO_4^0$ species. The complex formation constants of $10^{-2.745}$ and $10^{-1.144}$ for $CaCrO_4^0$ and $KCrO_4^-$, respectively, at 25 °C were taken from Accomero et al. (2010).

5.2.3 Solid characterization

The collected precipitates were analyzed using an Attenuated Total Reflectance - Fourier Transform Infrared Spectrometer (ATR-FTIR; Perkin Elmer Spectrum 100) in the range of 650 to 4000 cm^{-1}. Xray powder diffraction (XRD) patterns of the precipitates were recorded using a PANalytical X´Pert PRO diffractometer and Co-Kα-radiation (40 mA, 40 kV) over the range from 4° to 85° and a scan speed of 0.03° min^{-1}. The mineral phases were quantified by Rietveld refinement using the PANalytical X'Pert HighScore Plus software with the PDF-2 database. Selected precipitates were imaged using a ZEISS DSM 982 Gemini scanning electron microscope (SEM) operating at 2 kV accelerating voltage. The chemical composition of the bulk solid was obtained by digestion using 6 % suprapure HNO_3 and subsequent analyses similar to the ICP-OES technique described above. The specific surface area of solid samples was determined by multi-point krypton adsorption BET method (Brunauer et al., 1938) using a Quantachrome Gas Sorption system.

5.2.4 Chromium isotope separation

Chromium was separated from carbonate, chloride, calcium and potassium using a single-step (solutions) or a double-step (solids) ion chromatographic separation protocol (e.g. D'Arcy et al., 2017). Aliquots of the dissolved Cr bearing precipitates containing ~500 ng Cr were spiked with a ^{50}Cr-^{54}Cr double spike to achieve a ratio of Cr concentrations between spike and sample of 1:4 (Ellis et al., 2002; Schoenberg et al., 2008). Samples were evaporated in Savillex™ Teflon beakers on a hotplate at 130 °C and re-dissolved in aqua regia and again evaporated to ensure complete mixing of sample and spike. In the next step, samples were dissolved in 20 mL of high purity deionized Milli-Q® water (18.2 MΩ; MQ) and 0.5 mL of 1 M HCl, as well as 0.5 mL of 0.2 M $(NH_4)_2S_2O_8$ were added. The capped beakers were heated at 130 °C and the samples boiled for 1 hour to achieve oxidation of Cr(III) to Cr(VI). After cooling, samples were flushed through columns

containing 2 ml pre-cleaned Dowex AG 1 X8 anion resin. Subsequently, 10 mL 0.2 M HCl, 2 mL 2 M HCl and 5 mL MQ were passed through the columns to elute matrix elements while Cr(VI)-oxyanions are strongly attached to the surface of the resin. Cr(VI) was then reduced to Cr(III) by addition of 2 M HNO_3 doped with 5 % H_2O_2 (6 mL in total), eluted and collected. After drying down, the samples were re-dissolved in 100 µL concentrated double distilled HCl, heated for 10 minutes on a hotplate at 120 °C and diluted with 2.3 mL MQ. The weakly acidic samples were then passed over pre-cleaned cation exchange columns with Dowex AG50W-X8 resin, adopting a slightly modified recipe by Trinquier et al. (2008). Cr was eluted and collected in 8 mL 0.5 M HCl.
Solutions containing 500 ng Cr and an adequate amount of double spike were evaporated, re-dissolved in 100 µL concentrated double distilled HCl and subjected to the cation exchange column as described above.

5.2.5 Chromium isotope analyses

Chromium isotope compositions were measured by thermal ionization mass spectrometry. All samples were evaporated to dryness before loading onto outgassed Re filaments in a mixture of 3:2:1 (total of 3 µL) of silica gel, 0.5 M H_3PO_4 and 0.5 M H_3BO_4 (Frei et al., 2009). The Cr loads were analyzed on a IsotopX Phoenix thermal ionization mass spectrometer (TIMS) at the University of Copenhagen. The simultaneous measurement of $^{50}Cr^+$, $^{52}Cr^+$, $^{53}Cr^+$ and $^{54}Cr^+$, $^{49}Ti^+$, $^{51}V^+$ and $^{56}Fe^+$ in eight Faraday cups monitors potential interferences during the analyses. Analyses were conducted in static mode with 120 cycles per run (2 runs per sample) at a ^{52}Cr ion beam intensity of 1 V. Chromium isotopic compositions ($\delta^{53}Cr$) are reported relative to the Standard Reference Material SRM 979 as:

$$\delta^{53}Cr = ((^{53}Cr/^{52}Cr)_{sample}/\ (^{53}Cr/^{52}Cr)_{SRM979} - 1) * 1000 \qquad (5.1)$$

in ‰ (± 2σ). Double spiked NIST SRM 979 standards were repeatedly analyzed to determine external reproducibility and return $\delta^{53}Cr$ values of -0.05 ‰ ± 0.05 2 σ (n = 8), which was used to correct the resulting $\delta^{53}Cr$ values of the samples (Frei et al., 2014). With amounts of ≤ 2 ng of Cr, procedural blanks are very low compared to the 500 ng Cr in the samples used during chromatographic Cr separation, and therefore no blank corrections of the samples were undertaken.

5.3 Results

5.3.1 Mineralogy of the precipitates

The collected FT-IR spectra of the precipitates match with the spectrum of reference calcite. In analogy, the X-ray diffraction pattern of the precipitates correspond to the reference calcite with no shift in d(hkl)-values. The SEM images show that the precipitates (Fig. 5.2B) keep the rhombohedral structure of the seed calcite (Fig. 5.2A). Accordingly, the precipitates consist of aggregates of rhombohedral calcite crystals with typical overgrowth features at the calcite surface.

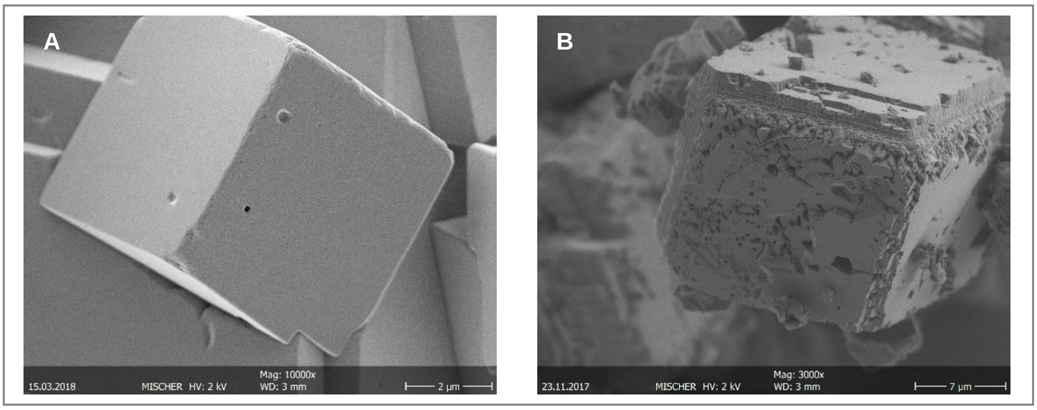

Figure 5.2: Characteristic scanning electron microphotographs of (A) calcite seeds, (B) final precipitate with Cr(VI)-$CaCO_3$-overgrowth (exemplarily shown for experiment #4.2; see Table 5.1).

5.3.2 Chemical composition of the fluid and precipitation rate

Steady-state conditions with respect to aqueous Ca concentration within the experimental runs were reached earlier than 1500 min (see Fig. 5.3). Note here that all experiments were conducted under oxidizing conditions, thus potential reduction of Cr(VI) to Cr(III) can be ruled out. This is substantiated by analyses of dissolved total Cr that remained equal to Cr(VI) concentration within the analytical precision (see methods).

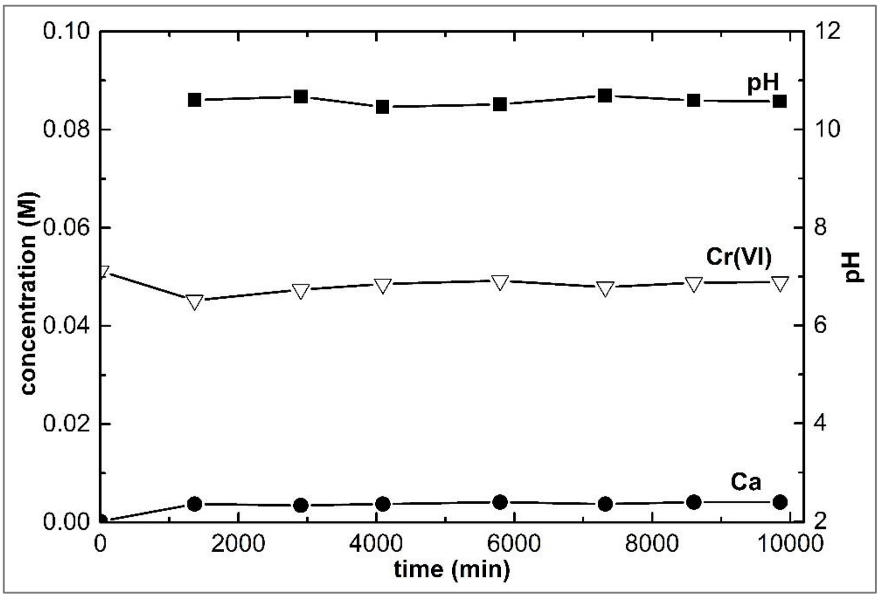

Figure 5.3: Temporal evolution of Ca and Cr(VI) aqueous concentration and pH for experiment #4.2. Analytical uncertainty is included in the symbol size.

The precipitation rate, r_p (mol m^{-2} s^{-1}), has been calculated according to Mavromatis et al. (2013; 2015; 2017b) from the number of moles of Ca added to the reactor within 24 h, $n_{Ca(add)}$, corrected for the number of moles of this element removed via sampling during the same period of time, $n_{Ca(rem)}$, by the expression

$$r_p = \frac{n_{Ca(add)} - n_{Ca(rem)}}{86400} / S \qquad (5.2)$$

where *S* is the total surface area of $CaCO_3$ in m^2 and *86400* the number of seconds in 24 h. Calculated precipitation rates in all experimental runs are quasi constant and about $10^{-7.7 \pm 0.2}$ mol m^{-2} s^{-1} as shown in Table 5.1.

5.3.3 Cr(VI) distribution between calcite and solution

The incorporation of divalent cations (Me^{2+}) in carbonate minerals commonly follows an ideal substitution of Me^{2+} for the Ca^{2+} ion in the crystal lattice (e.g. Reeder et al., 1999). In similar terms, the incorporation of divalent anions such as SO_4^{2-}, SeO_4^{2-}, $HAsO_4^{2-}$ and CrO_4^{2-} can be assumed to follow an ideal substitution of CO_3^{2-} in the crystal lattice during mineral formation (e.g. Cowan et al., 1990; Reeder et al., 1994; Staudt et al., 1994; Hemming et al., 1998; Alexandratos, 2004; Tang et al., 2007; Yokoyama et al., 2012; Wynn et al., 2018). This assumption is based on earlier characterization of solid speciation using EXAFS, XAFS and XANES spectroscopy (e.g. Reeder et al., 1994; Alexandratos, 2004; Tang et al., 2007; Yokoyama et al., 2012). The similarity of the substitution mechanism can be used to parameterize the relation between aqueous concentrations with that measured in the forming solid as suggested by Tang et al. (2007) for CrO_4^{2-} uptake in calcite. Accordingly, the distribution coefficient between calcite and solution can be defined according to

$$D_{Cr(VI)} = \frac{\left(c_{Cr(VI)} / c_{CO_3}\right)_{calcite}}{\left(m_{CrO_4{}^{2-}} / m_{CO_3{}^{2-}}\right)_{solution}} \qquad (5.3)$$

where *c* denotes concentration of Cr(VI) and carbonate in calcite and *m* stands for the concentrations of free aqueous CrO_4^{2-} and CO_3^{2-} ions, respectively.

As it can be seen in Table 5.1 and Fig. 5.4A, the pH of the reactive solution has a strong effect on the $\log D_{Cr(VI)}$ value. Note here that this effect cannot be assigned to calcite growth kinetics because the experiments in this study were conducted at a similar surface normalized precipitation rate of $10^{-7.7 \pm 0.2}$ mol m^{-2} s^{-1}. As depicted in Fig. 5.4A, pH and $\log D_{Cr(VI)}$ values increase according to the equation

$$\log D_{Cr(VI)} = 0.23\ (\pm 0.03) \times pH - 7.42\ (\pm 0.31)\ (8.0 \leq pH \leq 10.6;\ R^2 = 0.86) \qquad (5.4)$$

In contrast, the Cr(VI) content of calcite decreased from ~1122 ppm in experiments conducted at pH = 8.0 to 594 ppm in experiments conducted at pH = 10.6 (Fig. 5.4B). Indeed, at the lowest pH value employed in this study of 8.0, the content of Cr(VI) incorporated in calcite reached its highest value. At pH between 9.4 and 10.6, the Cr(VI) content of calcite remained nearly constant. Note here that similar to the constant precipitation rates, the supersaturation degrees of the reactive solutions with respect to calcite were quasi constant at $SI_{calcite} = 0.8 \pm 0.1$ (n = 8) in all experiments. This is illustrated in Table 5.1.

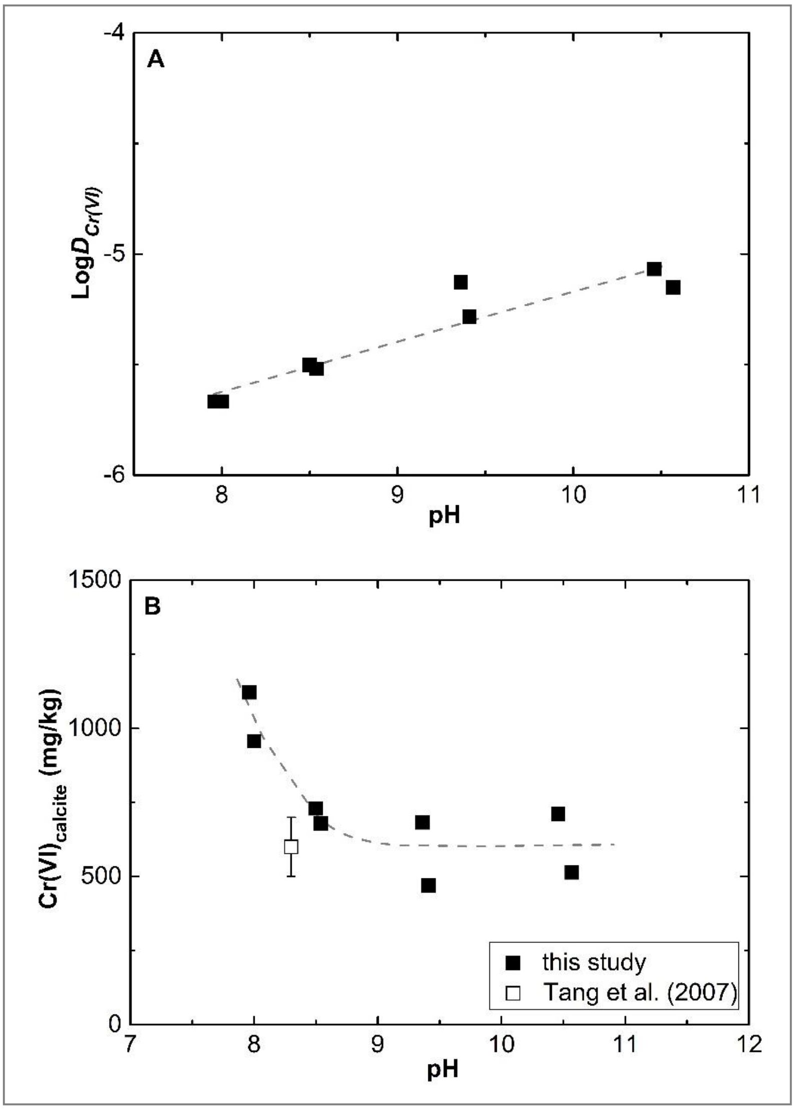

Figure 5.4: Cr(VI) partitioning coefficient in calcite as a function of pH (A) and amount of chromate ($\mathrm{Cr(VI)}_{calcite}$) incorporated in calcite (B). Analytical uncertainty is included in the symbol size.

5.3.4 Cr(VI) isotopic fractionation between reactive solution and precipitate

The measured $\delta^{53}\mathrm{Cr}_{solution}$ values are given in Table 5.1. The temporal evolution of the $\delta^{53}\mathrm{Cr}_{solution}$ value remained constant during the entire duration of the experimental runs as it is depicted in the Appendix D Fig. D.1A. Indeed, in experiment #4.2, $\delta^{53}\mathrm{Cr}_{solution}$ values exhibit a temporal variation of only -0.13 ± 0.06 ‰ which lies within the analytical precision of individual Cr(VI) isotope measurements (see Table 5.1). For all experiments, the isotopic composition of the reactor solution ($\delta^{53}\mathrm{Cr}_{solution}$ = -0.13 ± 0.06 ‰; n = 2) and the reactive solution (-0.15 ± 0.09 ‰; n = 4) was similar to that of the Cr(VI) stock solution (-0.19 ± 0.08 ‰). Thus, calcite precipitation did not induce a measurable change in the Cr(VI) isotopic composition of the reactive solution (see Fig. D.1B in Appendix D). Constant solution Cr(VI) isotope compositions are consistent with constant aqueous Cr(VI) concentrations during all experimental runs. The latter is further supported by only trace amounts of Cr(VI) that co-precipitated with calcite. The $\delta^{53}\mathrm{Cr}_{calcite}$ values can be seen in Table 5.1

and they vary between 0.01 and -0.86 ‰. It is worth noting here that experiments performed at similar pH conditions exhibit similar $\delta^{53}Cr_{calcite}$ values.

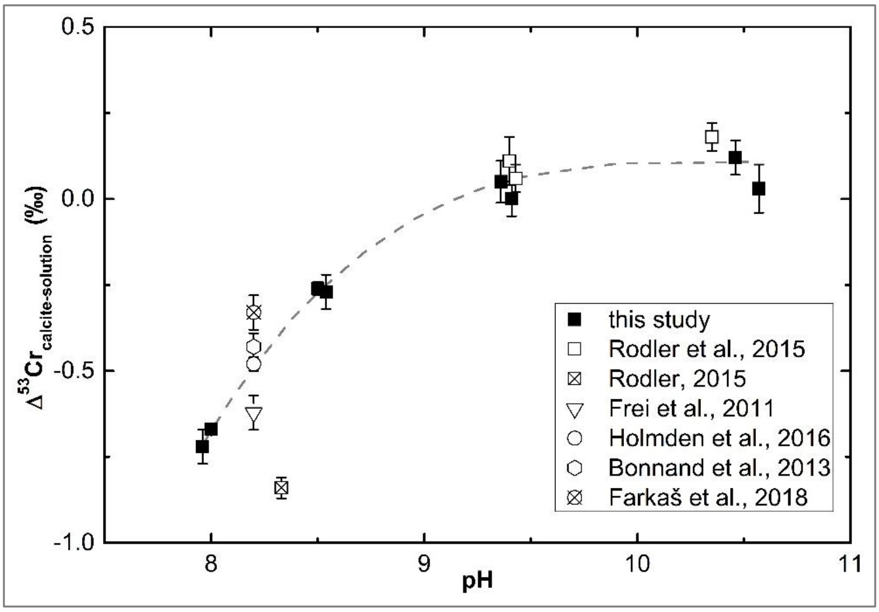

Figure 5.5: Cr(VI) isotope fractionation plotted as a function of pH in the synthetic precipitates of this study and literature data. Dashed regression line:

$\Delta^{53}Cr_{calcite-solution}$ = -67.43 (± 33.12) + 19.65 (± 11.04) * pH – 1.91 (± 1.22) * pH^2 + 0.06 (± 0.04) * pH^3.

Analytical uncertainty is included in the symbol size.

The Cr(VI) isotope fractionation between the solution and calcite is defined according to the equation

$$\Delta^{53}Cr_{calcite-solution} = \delta^{53}Cr_{calcite} - \delta^{53}Cr_{solution} \quad (5.5)$$

and calculated using the $\delta^{53}Cr_{solution}$ value at the corresponding pH value. The $\Delta^{53}Cr_{calcite-solution}$ values indicate a decreasing isotope fractionation from pH 8.0 up to pH 8.5 (Fig. 5.5; -0.72 ± 0.02 ‰ < $\Delta^{53}Cr_{calcite-solution}$ < -0.27 ± 0.03 ‰). At pH above 9.4, Cr(VI) isotope fractionation between calcite and solution is close to zero ($\Delta^{53}Cr_{calcite-solution}$ = 0.05 ± 0.01 ‰; n = 4).

5.4 Discussion

5.4.1 Effect of pH on chromate incorporation into calcite

As it is depicted in Fig. 5.4B, the measured $Cr(VI)_{calcite}$ (mg/kg) concentrations are decreasing with increasing pH. The $Cr(VI)_{calcite}$ (mg/kg) values obtained in this study are in good agreement with those of Tang et al. (2007) who conducted experiments at pH 8.3 (Fig. 5.4B). The observed trend of decreasing anion incorporation in calcite at elevated pH is a feature commonly occurring during the incorporation of divalent anions in calcite. Indeed, similar trends were previously reported for sulfate (Wynn et al., 2018), arsenate (Yokoyama et al., 2012) and selenite (Cowan et al., 1990). In order to explain this systematic behavior, Wynn et al. (2018) suggested that increasing pH results in increasing carbonate ion concentration in the reactive fluid at the expense of bicarbonate, and that a divalent anion competition between aqueous sulfate and carbonate during calcite growth likely takes place. In similar terms, Yokoyama et al. (2012) showed that arsenate (i.e. $HAsO_4^{2-}$) substitution in calcite is decreasing with increasing pH. They attributed the elevated content of arsenate in their experimental products to the formation of the aqueous $CaHAsO_4^o$ aquo-complex and they proposed an incorporation model whereby incorporation in the solid phase is controlled by the initial adsorption and latter incorporation of the aqueous $CaHAsO_4^o$ species. Taken together, the similarities observed in oxyanion contents in calcite as a function of pH, it can be assumed that oxyanion incorporation is likely affected by two processes: (i) the competition with aqueous CO_3^{2-} and (ii) the initial adsorption and subsequent incorporation anion aquo-complexes (e.g. Ca^{2+}-bearing). Both processes are controlled by the prevailing pH in the calcite forming solution.

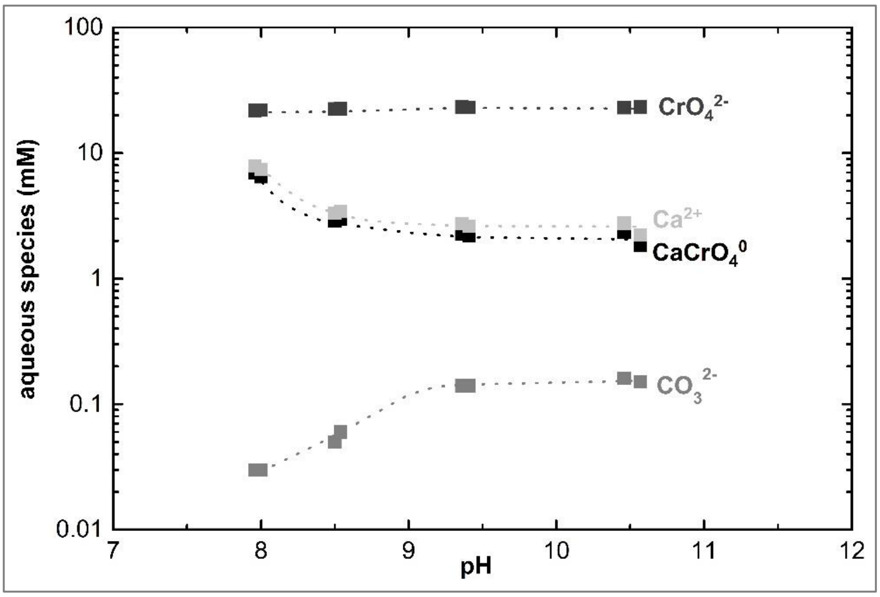

Figure 5.6: Species distribution as a function of experimental pH for aqueous CrO_4^{2-}, $CaCrO_4^0$, Ca^{2+} and CO_3^{2-} (see Table 5.1 and Appendix D Table D.2). Analytical uncertainty is included in the symbol size.

In contrast to the Cr(VI) concentration in calcite, as depicted in Fig. 5.4A, the log$D_{Cr(VI)}$ values calculated using Eq. 5.3 increase as a function of pH. This contrasting behavior between the distribution coefficient and the concentration of Cr(VI) in the solid is likely the result of $D_{Cr(VI)}$ estimation using Eq. 5.3. This is because an increase of the formation pH from 8.0 to 10.6 results in an increase of the aqueous CO_3^{2-} concentration by a factor of about 8, whereas aqueous Cr(VI) remains quasi constant. At the same time, the concentration of Cr(VI) in calcite is decreasing by a factor of 0.5 as pH is increasing from 8.0 to 10.6, and this results in an overall increase of the $D_{Cr(VI)}$ value. This observation suggests that the classical distribution coefficient is suitable for deciphering incorporation mechanisms, but not straight forward for the estimation of the total Cr(VI) concentration during calcite growth. Hence, the following discussion is focused on the $Cr(VI)_{calcite}$ (mg/kg) concentration of calcite as a function of pH. Based on the observed behavior of Cr(VI) incorporation into calcite as a function of pH it is suggested that Cr(VI) incorporation is affected by the two mechanisms. The incorporation of Cr(VI) as a free ion occurs independently of prevailing pH of the reactive solution as it is imposed by Eq. 5.3. As it can be seen in Fig. 5.6 and in the Appendix D Table D.2 the dissolved Cr(VI) in the experiments of this study is present as aqueous CrO_4^{2-} (43 - 48 %) and $KCrO_4^-$ complexes (41 - 48 %) whereas the aqueous $CaCrO_4^0$ complex constitutes only a small proportion, ranging between 5 and 16 % of the total dissolved Cr(VI). Despite the small abundance of aqueous $CaCrO_4^0$ in the reactive solution, the obtained results suggest that the presence of this aquo-complex is likely controlling Cr(VI) incorporation in calcite. Indeed, as it can be seen in Fig. 5.7, the Cr(VI) concentration in calcite (expressed as mg/kg) is linearly correlated with the aqueous $CaCrO_4^0$ complex that can be described by the equation:

$$C(VI)_{calcite}\ (mg/kg) = 88.48\ (\pm 14.65) \times (CaCrO_4^0)\ [mM] + 375.29\ (\pm 66.82);\ R^2 = 0.84 \qquad (5.6)$$

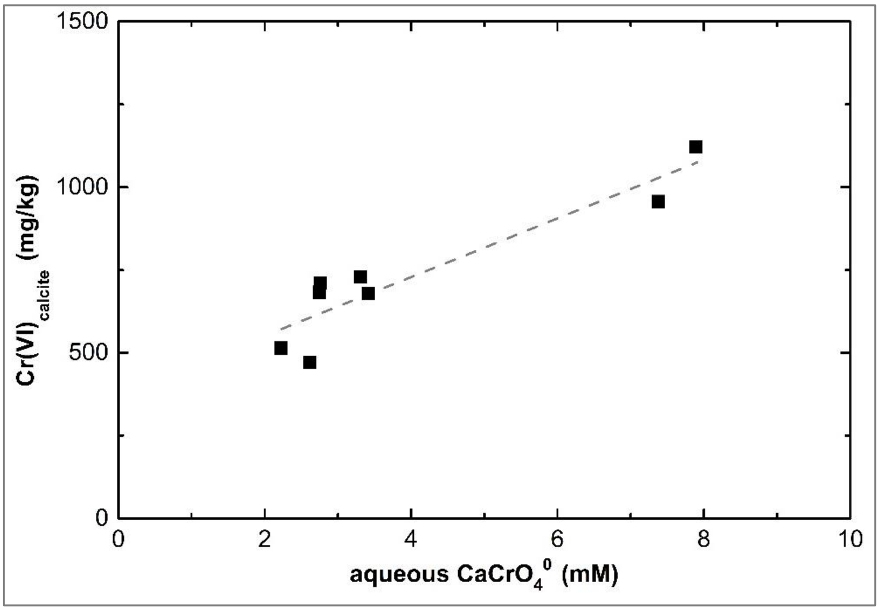

Figure 5.7: Relationship between the amount of incorporated chromate ($Cr(VI)_{calcite}$) and the concentration of the aqueous $CaCrO_4^0$ complex according to Eq. 5.6. Analytical uncertainty is included in the symbol size.

As it can be calculated from the Eq. 5.6, in the absence of $CaCrO_4^0$ complex, a concentration of $Cr(VI)_{calcite}$ (mg/kg) of 375.3 ppm would be expected from the incorporation of solely CrO_4^{2-} in calcite. We also consider that incorporation of Cr(VI) as a $CaCrO_4^0$ complex is a pH dependent process and affected by the abundance of Ca^{2+} and CrO_4^{2-} ions in the reactive solution (Fig. 5.6). At elevated pH ≥ 9.4 however, solubility of calcite decreases and subsequently the availability of aqueous Ca^{2+} in the reactive fluid that can eventually complex with aqueous Cr(VI) is readily reduced (see Table D.1 in Appendix D). At these elevated pH conditions Cr(VI) incorporation in calcite is controlled by the abundance of $CaCrO_4^0$ and the direct incorporation of CrO_4^{2-} ions. At pH conditions lower than 9.4, the good correlation between the Cr(VI) concentration in calcite and the concentration of the aqueous $CaCrO_4^0$ complex suggest that the formation of the latter species is likely the dominant parameter controlling Cr(VI) incorporation in the calcite structure. The incorporation of Cr(VI) in calcite likely occurs via the adsorption and subsequent incorporation of the $CaCrO_4^0$ complex, however the formation of surface complexes cannot be ruled out.

5.4.2 Cr(VI) isotope fractionation during calcite growth

Another novel finding of this study is that the $\Delta^{53}Cr_{calcite\text{-}solution}$ values exhibit pH-dependent fractionation. Although in the experimental runs Cr occurs in all cases in its oxidized form, fractionation exhibits variations larger than 0.7 ‰ that cannot be assigned to redox phenomena. Indeed, as it can be seen in Fig. 5.5, $\Delta^{53}Cr_{calcite\text{-}solution}$ values increase from -0.7 ± 0.03 ‰ at pH 8.0 to about 0.1 ‰ at pH 10.6 (see also Table 5.1). At this elevated pH, the observed $\Delta^{53}Cr_{calcite\text{-}solution}$ values are in good agreement with those of Rodler et al. (2015) (i.e. $\Delta^{53}Cr_{calcite\text{-}solution} \approx +0.15 \pm 0.03$ ‰) who conducted experiments of Cr(VI) co-precipitation with calcite at pH 9.4 and 10.4. Our results are also in good agreement with those of Rodler (2015) who identified $\Delta^{53}Cr_{calcite\text{-}solution}$ values of -0.84 ± 0.03 ‰ ($Cr_{precipitate}$ concentration 55.37 µg g^{-1}). The $\Delta^{53}Cr_{calcite\text{-}solution}$ values and Cr concentrations show a positive correlation ($R^2 = 0.55$), indicating that $\Delta^{53}Cr_{calcite\text{-}solution}$ values are also dependent on the Cr concentration of the precipitating calcite.

Owing to the fact that the observed isotopic fractionation cannot be attributed to reduction of Cr(VI) to Cr(III), we assign the observed variations in isotopic fractionation in the bonding environment of Cr(VI) in the crystal lattice. It is worth noting here that the incorporation of aqueous CrO_4^{2-} is accompanied by a significant distortion of the calcite crystal lattice. This is because the replacement of the planar CO_3^{2-} ion (C-O = 1.28 Å; Hemming et al., 1998) by the tetrahedral CrO_4^{2-} ion (Cr-O = 1.62-1.69 Å; Arroyo-de Dompablo et al., 2015) results in an increase of the required geometrical volume of the crystal lattice in order to accommodate the larger anion. This is also reflected in the changes of the mean Cr-O bond length between the aqueous Cr(VI) ion and the Cr in calcite. Indeed, as it has been defined by EXAFS spectroscopy the Cr-O bond length of CrO_4^{2-} incorporated in calcite is about 1.64 Å (Tang et al., 2007) and somewhat shorter compared to the aqueous CrO_4^{2-} tetrahedral anion which is characterized by a mean Cr-O bond length of 1.656 Å (Hoffmann et al., 2001). This change in the average Cr-O bond length provides insight to the Cr isotope fractionation during Cr(VI) incorporation in calcite. If we consider that shorter / stronger bonds preferentially involve the heavier isotopes (e.g. Schauble et al., 2004), it would be expected that the solid phase, which is characterized by shorter bonds, would be enriched in the heavier ^{53}Cr isotope. In contrast to what could be expected however, as it is depicted in Fig. 5.5, a preferential incorporation of the lighter ^{52}Cr isotope is observed. However, the incorporation of Cr(VI) via the aqueous $CaCrO_4^0$ complex in calcite still holds. The isotopic effect can be explained by the fact that the formation of aqueous $CaCrO_4^0$ is accompanied by an increase of the mean Cr–O distance (i.e. 1.66 Å; Tang et al., 2007) compared to the aqueous CrO_4^{2-} ion which results in the preferred complexation of lighter Cr isotopes. In other words, due to the longer Cr-O bond length the $CaCrO_4^0$ complex should be depleted in the heavier ^{53}Cr isotope and its direct incorporation into calcite explains well the observed isotope fractionation pattern. In addition, the high affinity for aqueous $CaCrO_4^0$ formation and its preferential incorporation in calcite leads to the incorporation of lighter Cr(VI) isotopes at lower pH values (see Fig. 5.8). The relation between $Cr(VI)_{calcite}$ (mg/kg) value and Cr(VI) isotope fractionation in our study can be expressed as:

$$\Delta^{53}Cr_{calcite\text{-}solution}\ (‰) = -0.001\ (\pm 0.0003) * Cr(VI)_{calcite}\ (mg/kg) + 0.75\ (\pm 0.24);\ R^2 = 0.70 \qquad (5.7)$$

In the absence of $CaCrO_4^0$ complex incorporation in calcite, Eq. 5.6 predicts a Cr(VI) content in calcite to result in about 375 mg/kg. The use of this value in Eq. 5.7 leads to a $\Delta^{53}Cr_{calcite\text{-}solution}$ value of + 0.38 ‰ (again only if $CaCrO_4^0$ is non-existent). Such formation conditions prevail at increasing pH conditions where the low solubility of calcite controls the concentration of aqueous Ca^{2+} and subsequently suppresses the formation of $CaCrO_4^0$ complexes. The constant concentrations of aqueous $CaCrO_4^0$ and CrO_4^{2-} complexes at high pH (see Fig. 5.6), and the likely incorporation of both aqueous species in the forming experimental calcite precipitates herein, both seem to control the near zero $\Delta^{53}Cr_{calcite\text{-}solution}$ values at pH ≥ 9.4.

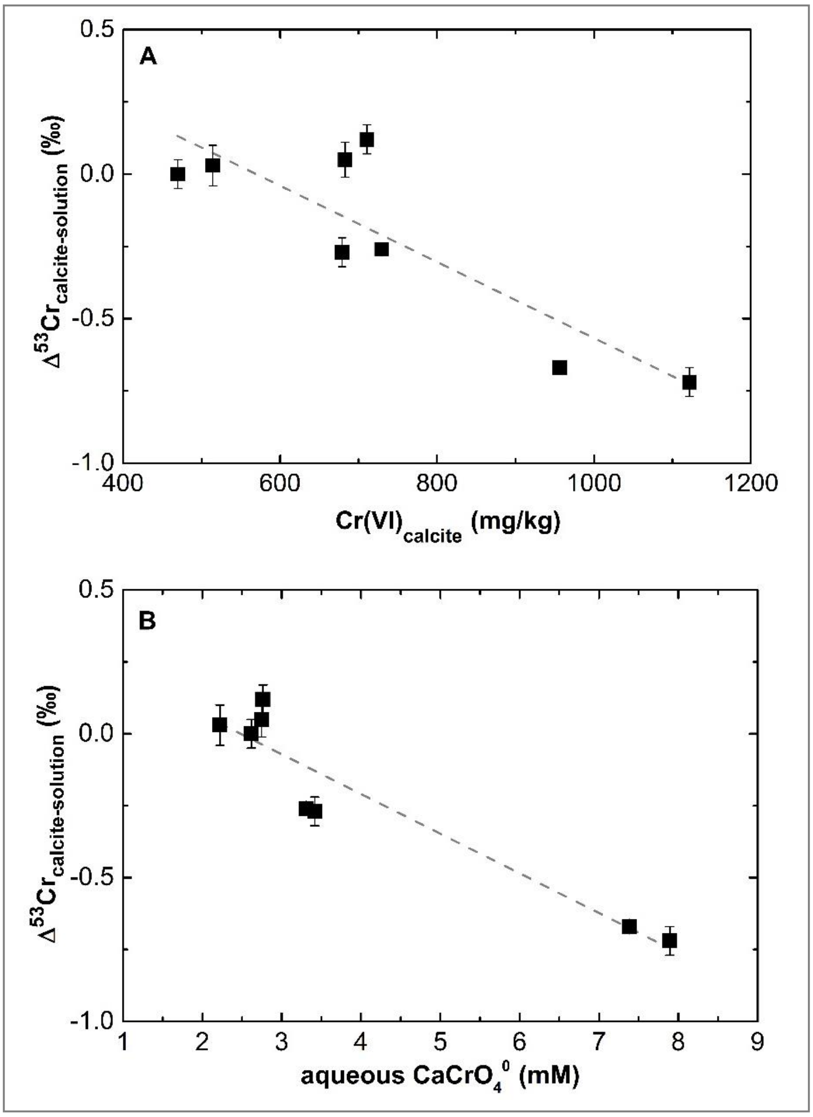

Figure 5.8: Relation between Cr(VI) isotope fractionation and (A) amount of incorporated chromate ($Cr(VI)_{calcite}$); (B) aqueous $CaCrO_4^0$ concentration. The dashed regression line is described by the linear equation: $\Delta^{53}Cr_{calcite\text{-}solution}$ = -0.14 (±0.02) * $CaCrO_4^0$ (mM) + 0.34 (±0.09); R^2 = 0.88. Analytical uncertainty is included in the symbol size.

5.4.3 Implications for Cr(VI) incorporation and isotope fractionation in natural calcite

The novel finding of this study, namely that the Cr content and Cr isotope composition of calcite is pH dependent, has significant implications for the use of Cr isotopes in natural carbonate samples. To date the Cr(VI) content of natural calcites and in particular its isotope composition has been used to interpret oxygenation events of the paleo-atmosphere (e.g. Crowe et al., 2013; Gilleaudeau et al., 2016), and to describe changes in ocean oxygenation and glaciation periods (e.g. Frei et al., 2011; Gueguen et al., 2016). The differences in isotopic composition have been assigned to changes in the redox state of aqueous Cr species that can reach 6 ‰ between co-existing aqueous Cr(VI) and Cr(III) species (Wang et al., 2015). Only recently, Holmden et al. (2016) considered that carbonates might record the δ^{53}Cr value of the Cr(VI) pool in seawater without the necessity for its reduction to Cr(III). The present study confirms the finding of Holmden et al. (2016) since our results clearly indicate that the pH of the forming fluid plays a major role on the incorporation and isotope composition of Cr(VI) in calcite. Actually, a closer look at the composition of Cr in natural samples compared to ambient seawater from which they formed, suggests that the measured and estimated $\Delta^{53}Cr_{calcite\text{-}solution}$ values might simply be the result of aqueous Cr(VI) complexation with Ca^{2+} rather than stemming from partial reduction to Cr(III) which is associated with an isotope shift towards lighter isotopes in the reduced species. This is evident in the studies by Frei et al. (2011), Bonnand et al. (2013), Holmden et al. (2016) and Farkaš et al. (2018) in which they report $\Delta^{53}Cr_{calcite\text{-}solution}$ values from marine carbonate sediments which fit well with our experimental data plotted as a function of pH (see Fig. 5.5). In the above mentioned studies, δ^{53}Cr values of the carbonates have been measured whereas the $\Delta^{53}Cr_{calcite}$solution values have been calculated by estimating $\delta^{53}Cr_{seawater}$ using total aqueous Cr composition and Eq. 5.5. In detail, Frei et al. (2011) reported $\Delta^{53}Cr_{calcite\text{-}solution}$ values of about -0.62 ‰ for Ediacaran carbonates of the Ediacaran Polanco Formation in Uruguay, assuming a seawater δ^{53}Cr value of 0.5‰. The Cr isotopes in marine carbonate sediments from the modern Caribbean Sea measured by Holmden et al. (2016) are isotopically fractionated from ambient Caribbean seawater ($\delta^{53}Cr = +1.14$ ‰) by 0.48 ‰. Bonnand et al. (2013) reported a $\Delta^{53}Cr_{calcite\text{-}solution}$ value of -0.43 ‰ from limestone samples and the Southampton Sea ($\delta^{53}Cr = +1.32$ ‰). Furthermore, Farkaš et al. (2018), presented Cr isotope fractionation values of calcite ($\delta^{53}Cr_{calcite} = +0.42$ ‰; $\delta^{53}Cr_{seawater} = +0.76$ ‰; $\Delta^{53}Cr_{calcite\text{-}seawater} = -0.34$ ‰) from the Lady Elliot Island of the southern-most tropical coral cay of the Great Barrier Reef. The results presented in Fig. 5.9 were computed assuming the formation of aqueous complexes of CrO_4^{2-} with Ca^{2+} ions in seawater based on the seawater concentrations reported by Millero (1974). A pH value of 8.2 for modern seawater from Foster (2008) was used in these calculations. As it can be seen in Fig. 5.9A, the $\Delta^{53}Cr_{calcite\text{-}solution}$ values of the naturally precipitated carbonates indicate a significant trend for incorporation of lighter isotopes with increasing aqueous $CaCrO_4^0$ complex formation, as shown and validated in our experimental approach (Fig. 5.8). This trend is well explained in Fig. 5.9B, where the comparison of the aqueous molar $(CaCrO_4^0)/(totalCr(VI))$ ratio between the experimental and natural $\Delta^{53}Cr_{calcite\text{-}solution}$ values show lighter Cr(VI) isotopes with increasing affinity for $CaCrO_4^0$ complex formation.

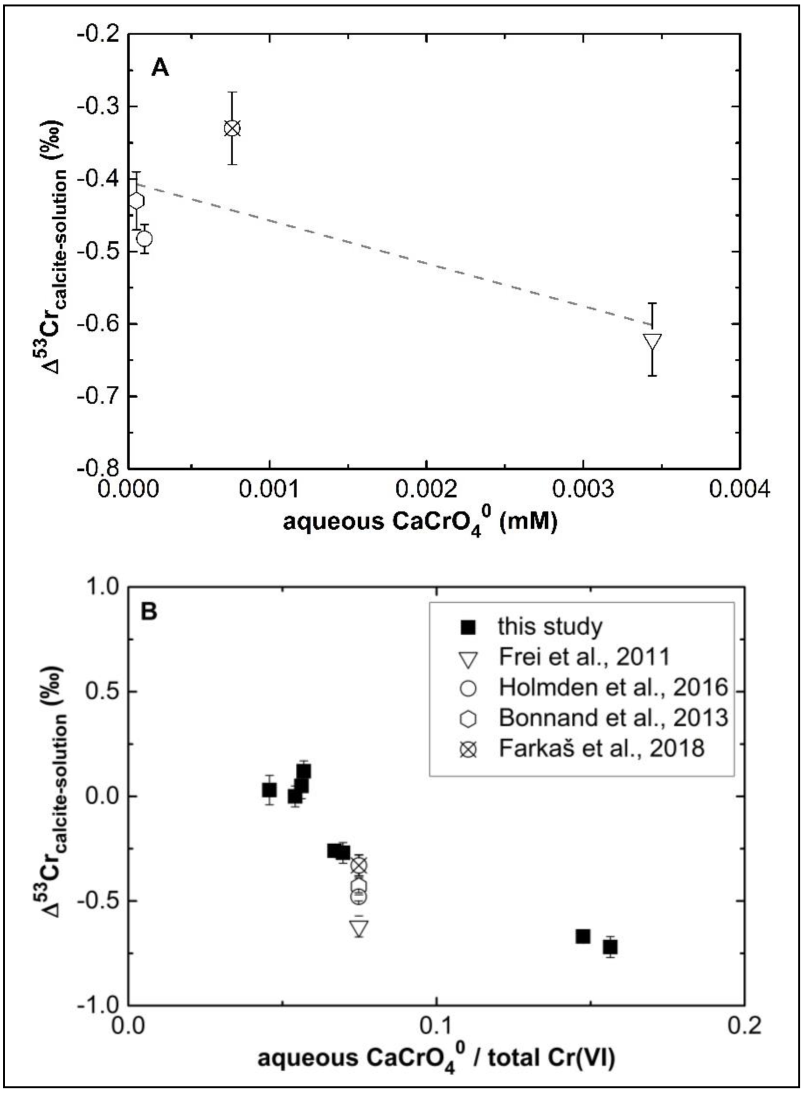

Figure 5.9: Correlation between $\Delta^{53}Cr_{calcite-solution}$ and (A) the concentration of $CaCrO_4^0$ complex of natural carbonate samples from the literature (Frei et al., 2011; Bonnand et al., 2013; Holmden et al., 2016 and Farkaš et al., 2018) according to the equation: $\Delta^{53}Cr_{calcite-solution}$ = -58.8 (± 36.04) * $CaCrO_4^0$ (mM) - 0.40 (± 0.06); $R^2 = 0.36$.; and (B) the aqueous ratio of $CaCrO_4^0$ complexes and total Cr(VI) of our experimental and natural carbonate samples from the literature (Frei et al., 2011; Bonnand et al., 2013; Holmden et al., 2016 and Farkaš et al., 2018). Analytical uncertainty is included in the symbol size.

The results obtained in this study clearly show that aqueous speciation is a critical parameter in the application and interpretation of Cr isotopes as a paleo redox proxy and further research on the Cr isotope fractionation between carbonate minerals and forming fluids are necessary, especially considering and emphasizing the importance of the aqueous $CaCrO_4^0$ complex. Thus, reconstruction of dissolved Cr(VI) concentration and its isotopic composition of seawater strongly requires knowledge of the chemical composition of the forming solution which constitutes a true challenge to the application of this tracer in marine paleo redox reconstructions. We emphasize here the potential of its use as a possible tracer for the solution / seawater pH. This perspective renders the use of the Cr(VI) isotope system in calcite as an environmental proxy rather challenging. For example, the shift of $\delta^{53}Cr$ values in carbonate minerals towards a lighter isotope composition compared to ambient seawater is, according to our study, induced by elevated $CaCrO_4^0$

concentrations which conversely hint on pH significantly below 8.5 and / or the presence of elevated Ca^{2+} concentration in the forming solution. In contrast, the Cr(VI) isotopic composition of precipitating calcite in alkaline waters can reasonably suggest to depict and trace the aqueous Cr(VI) isotopic signature within the range of the experimental conditions explored in this study. The latter parameters can unravel local and / or temporal changes in past environmental conditions during calcite formation.

5.5 Conclusions

The results obtained in this study show that pH is a controlling parameter for the incorporation of Cr(VI) in calcite at constant precipitation rate and T = 25 °C. In accordance the Cr(VI) isotope distribution indicates a significant fractionation between Cr(VI) in the precipitated calcite and the solution which is also pH-dependent. The observed pH-dependent incorporation and isotope fractionation of Cr(VI) during formation of calcite can be explained considering Cr(VI) aquo-complex formation and surface reactions as follows:

(1) Cr(VI) in solution is complexing with dissolved Ca^{2+} to form the aqueous $CaCrO_4^0$ complex which, compared to CrO_4^{2-}, is preferentially incorporated into calcite via an initial adsorption step. Thus, Cr(VI) incorporation in calcite decreases from pH 8.0 to 9.4 following the increase of $CaCrO_4^0$ concentration. From pH 9.4 to 10.6 $CaCrO_4^0$ and CrO_4^{2-} concentrations reach almost constant values which limit Cr(VI) incorporation into calcite at a constant level.

(2) CrO_4^{2-} and $CaCrO_4^0$ formation is accompanied with distinct Cr-O bond lengths and energy levels. In the pH range between 8.0 and 9.4, the longer Cr-O bond length (less bond energy) in incorporated $CaCrO_4^0$ compared to incorporated CrO_4^{2-} leads to the preferential incorporation of lighter Cr isotopes into the growing calcite with $\Delta^{53}Cr_{calcite\text{-}solution}$ from -0.7 to -0.27 ‰. At pH ≥ 9.4, however, $CaCrO_4^0$ and CrO_4^{2-} concentrations are constant yielding in $\Delta^{53}Cr_{calcite\text{-}solution}$ close to zero ($\Delta^{53}Cr_{calcite\text{-}solution} = 0.05 \pm 0.01$ ‰).

(3) Based on the experimental findings the incorporation of Cr(VI) in calcite only from aqueous CrO_4^{2-} bearing solutions and in the total absence of $CaCrO_4^0$ leads to a calculated $\Delta^{53}Cr_{calcite\text{-}solution}$ value of about +0.38 ‰. This finding indicates the incorporation of lighter Cr isotopes via aqueous $CaCrO_4^0$ uptake into the growing calcite crystal.

(4) The findings suggest that carbonate minerals likely record the $\delta^{53}Cr$ value of the Cr(VI) pool in seawater and the fractionated Cr is not necessarily related to redox processes, but more likely controlled by Cr(VI) aquo-complex formation and, hence, by the concentrations of calcium, DIC and Cr(VI) in the precipitating solution.

Acknowledgements

We acknowledge the support of Stephanie Eichinger, Bettina Purgstaller and Andre Baldermann with ICP-OES, Judith Jernej with IC and Maria Hierz with DIC measurements. For the enlightening discussions during the preparation of this manuscript, we would like to thank Alexandra Rodler, Cyrill Grengg, Jessica Stammeier and Katja Goetschl. This project has received funding by Marie Skłodowska-Curie Horizon 2020 Project BASE-LiNE Earth (H2020-MSCA-INT-2014- 643084) and by the FWF-DFG project Charon II (FWF-I3028-N29).

Chapter 6

Conclusions and Perspectives

6.1 Conclusions

With the experimental work performed in this study new insights are offered related to controlling mechanism for (i) oxygen isotope fractionation between smithsonite and water as a function of temperature; (ii) Li distribution and its isotope fractionation between calcite and solution during formation as a function of precipitation rate and pH; and (iii) Cr(VI) distribution and isotope fractionation between calcite and solution during the growth of calcite as a function of pH.

Oxygen isotope fractionation between smithsonite and water in experimental data was studied in the temperature range between 25 and 80 °C and compared to theoretical calculations (**Chapter 2**). The temporal evolution of the pH, supersaturation with respect to smithsonite in the water as well as the oxygen isotope fractionation between smithsonite and water indicates thermodynamic equilibrium was achieved after a reaction time of 7 days at 25 °C. At the same experimental set-up but at higher temperature (80°C) the oxygen isotope fractionation between smithsonite and water was observed to be smaller. In order to verify the experimental data, these values from the experimental approach were compared with both (i) theoretical calculations and (ii) different trigonal-carbonate minerals. For (i), the observed experimental results are well in the range of theoretical calculations. For (ii), the experimental data fit within the sequence of $Zn^{2+} < Fe^{2+} < Mn^{2+} < Ca^{2+}$ for trigonal-carbonate minerals. This can be expected from thermodynamics that with increasing cation radius the oxygen isotope fractionation decreases.

The results of **Chapter 3** and **4** indicate that the Li distribution and isotope fractionation between calcite and solution is affected by both, precipitation rate and pH. With increasing growth rate Li was increasingly incorporated in calcite which can be explained by an increasing amount of defect surface sites at elevated growth rates which are entrapped by impurities such as monovalent cations (e.g. Na^+ and Li^+). This increasing Li incorporation at elevated growth rates is accompanied with faster transport and attachment of the lighter Li isotopes at the calcite surface based on their higher reaction rates. Further, with increasing pH, the HCO_3^- concentration in the solution and equally the Li incorporation in calcite is decreasing. It is suggested that bicarbonate balances the positive charge excess during Li incorporation. This correlation is assumed to be caused by a coupled incorporation of Li with HCO_3^-. An adsorption process at elevated pH, however, cannot be excluded completely. The lighter Li isotopes are preferentially incorporated in calcite at lower pH values (e.g. pH range between 6.3 and 8.3). This is related to longer Li-O distance in $LiHCO_3^0$ complexes compared to $[Li(H_2O)_n]^+$ (n = 1 - 6) complexes which are favored for lighter Li isotopes. At pH > 8.3, strong electrostatic attraction controls the adsorption and subsequent incorporation of Li^+ onto the negatively charged calcite surface accompanied by the preferentially incorporation of lighter Li isotopes.

The experimental results show that the observed distribution of Cr(VI) and Cr isotopes in calcite versus precipitating solution can be explained by considering aquo-complex formation and surface reactions (**Chapter 5**). With increasing pH ($8 \leq pH \leq 9.4$), aqueous Cr(VI) is forming $CaCrO_4^0$ aquo-complexes with dissolved Ca^{2+} which are preferentially incorporated in calcite via an initial adsorption step. At elevated pH ($9.4 \leq pH \leq 10.6$), the CrO_4^{2-} species is also affecting the Cr(VI) incorporation due to the decreasing concentration of aqueous Ca^{2+} for complexation. Therefore, the Cr(VI) incorporation reaches a constant level. The formation of aqueous $CaCrO_4^0$ and CrO_4^{2-} is accompanied with differences of Cr-O bond lengths and energy levels between the two Cr(VI) species. The longer Cr-O bond length (i.e. less bonding energy) leads to the preferential incorporation of lighter Cr isotopes in calcite via $CaCrO_4^0$ complexes rather than via CrO_4^{2-}. At pH ≥ 9.4, however, $CaCrO_4^0$ and CrO_4^{2-} concentrations are constant yielding $\Delta^{53}Cr_{calcite\text{-}solution}$ values close to zero ($\Delta^{53}Cr_{calcite\text{-}solution} = 0.05 \pm 0.01$ ‰).

The results of the present PhD thesis clearly highlight the necessity of experimental work i.e. inorganic carbonate precipitation experiments, in understanding natural processes. As could be shown, the underlying mechanisms are complex. Detailed knowledge is crucial in order to understand and identify kinetics in natural surroundings related to elemental and isotopic distribution behavior, especially when any of these are used as an environmental proxy. With the results of the current study, new proxies can be developed e.g. for the reconstruction of the paleo-seawater composition. In order to sum up, this PhD thesis makes a significant contribution in understanding precipitation and kinetic mechanisms of well-established, i.e. oxygen isotopes in smithsonite; and also new and non-traditional isotopes, e.g. Li distribution and isotope composition in calcite as a function of growth rate and pH; and Cr(VI) distribution and its isotope fractionation behavior as a function of pH. The oxygen isotope fractionation between smithsonite and water can be used to determine in combination with other trigonal-carbonate minerals (i.e. siderite) the formation temperature of carbonate minerals, or identify post-depositional alteration. The Li/Ca and Li isotope composition can be a potentially tool for estimating the precipitation rate in natural grown carbonates or provide insights on formation conditions in continental carbonate deposits. The Cr(VI) distribution and isotope composition can be used as tracer in alkaline surroundings to directly predict the Cr(VI) isotopic signature of the aqueous solution from which the calcite forms.

6.2 Perspectives

The experimental studies in this PhD thesis placed milestones in order to understand the controlling parameters on carbonate precipitation, and their influence on the incorporation of elements and isotopes. In addition, the results of this project offer new proxies to constrain formation mechanisms of carbonate minerals in natural environments. Yet, in order to compare data from experimental work with naturally formed carbonates as well as to assess and understand geochemical processes in natural carbonates in their entity, more parameters as well as their competing influences need to be taken into account. The results of the current study offer several directions for such investigations.

In this study it was shown that oxygen isotope fractionation in smithsonite can be used to recalculate environmental temperatures during formation (see **Chapter 2**). However, the calculation of the formation temperature of smithsonite in nature with theoretical or experimental equations is not straightforward, related to a lack of information about the physicochemical parameters during the formation such as solution chemistry and pCO_2. In order to develop this new temperature proxy better in paleo-environments further investigations are needed such as carbonate clumped isotope (Δ_{47}) thermometry. The Δ_{47} thermometry involves the estimation of ^{13}C and ^{18}O in the carbonate mineral structure which are chemically bound to one another within the same carbonate ion group. Because it involves a homogeneous equilibrium (reaction among components of a single phase), the Δ_{47} thermometry is independent of the isotopic composition of the solution from which the carbonate precipitate (e.g. Ghosh et al., 2006a; 2006b; 2007; Schauble et al., 2006; Came et al., 2007; Huntington et al., 2011). Temperature evaluation from clumped isotope data have great potential to calculate smithsonite formation temperatures and thus to decipher the isotopic composition of the precipitating solution, which gives information on the origin of the zinc carbonate deposit.

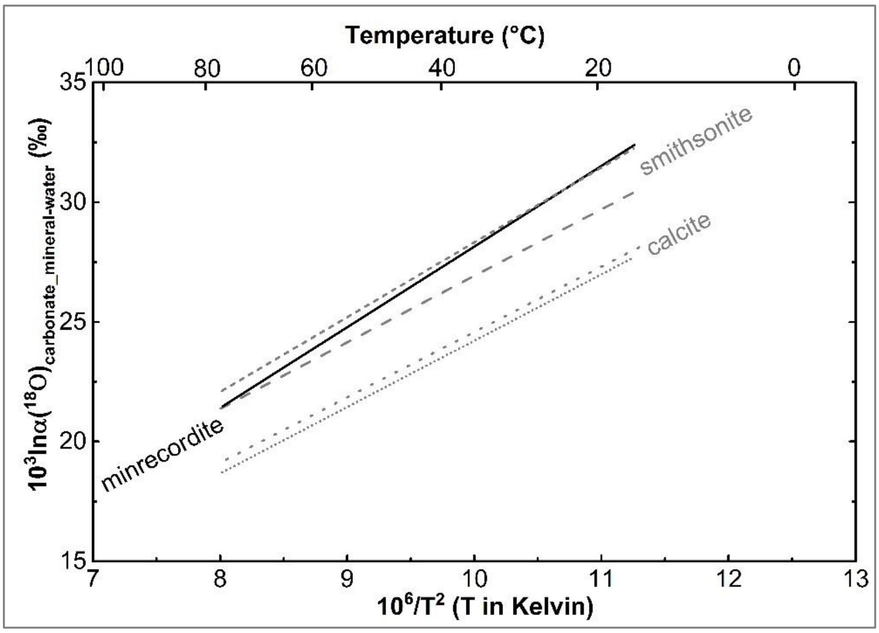

Figure 6.1: Oxygen isotope fractionation between the two Zn and Ca carbonate end-member minerals, smithsonite and calcite, and water as well as between minrecordite ($CaZn[CO_3]_2$) and water (black line; Zheng and Böttcher, 2016) plotted as a function of temperature. The small dashed line represents the oxygen isotope fractionation between smithsonite and water and the small dotted line the oxygen isotope fractionation between calcite and water of the theoretical calculation by Chacko and Deines (2008). The dashed line shows the experimental fit of the oxygen isotope fractionation between smithsonite and water (of Chapter 2; i.e. Füger et al., 2018) and the dotted line the experimental fit of the oxygen isotope fractionation between calcite and water (Kim and O'Neil, 1997).

In regard to Zn carbonate deposits, double carbonates such as $CaZn[CO_3]_2$ (minrecordite) occur in nature. In order to understand their formation conditions, their stable oxygen isotope composition and that of the respected carbonate mineral end-members could be used (e.g. Zheng and Böttcher, 2016, and references therein). As it can be seen in Fig. 6.1 the oxygen isotope fractionation between minrecordite and solution is close to the oxygen isotope fractionation between $ZnCO_3$ (smithsonite) and water, but far from those of $CaCO_3$ (calcite) and water. Smithsonite occurs in the calcite structure (Farmer, 1974). Therefore, the oxygen isotope fractionation behavior of smithsonite compared to calcite is not caused e.g. by coordination effects, but rather by smaller Zn-O in contrast to Ca-O bonds. Shorter / stronger bonds (higher bond energy) involve the heavier isotopes (e.g. Schauble et al., 2004) and are related to the smaller cation radius of Zn^{2+} compared to Ca^{2+} (e.g. Chacko and Deines, 2008). The minrecordite structure is referred to the calcite group and cell unit dimensions lay between the above mentioned end-member minerals (e.g. Zheng and Böttcher, 2016). Thus, oxygen isotope fractionation between minrecordite and solution should be in between these end-member minerals, although structural ordering effects of distinct cations in minrecordite have to be additionally considered. This relative behavior is somehow valid depending on the used values from the literature (see Fig. 6.1). However, up to date studies on the oxygen isotope fractionation between minrecordite and solution are rare. In order to better understand the coordination effects as well as exchange kinetics on oxygen isotope fractionation behavior in respect to minrecordite and solution, further investigations are highly requested. Furthermore, previous studies demonstrated that Zn isotope fractionation might be temperature (e.g. Ducher et al., 2016) and pH dependent (Mavromatis et al., 2019). It is known that smithsonite is formed via its precursor phase (hydrozincite) from solution in oxidized zone of Pb-Zn ore bodies initiated by an increase of the partial pressure of CO_2 (e.g. Alwan and Williams, 1979; Williams, 1990). Therefore, the Zn isotope composition of smithsonite may be used as proxies to calculate temperatures and pH conditions during the (trans-)formation.

The present studies of Li distribution and its isotope fractionation have offered new insights in controlling Li incorporation mechanism and kinetics in calcite (**Chapter 3** and **4**). As a function of pH the Li incorporation is balanced by the entrapment of bicarbonate to the calcite surface. Yet, it is still unclear whether the bicarbonate ion is introduced in the crystal lattice or simply adsorbed on the surface. Simultaneously, it is up to date unclear, if the incorporation of Li is influenced by dehydration processes at the mineral surface. Therefore, forthcoming high resolution spectroscopic studies would be a good tool in order to unravel these mysteries. However, in seawater environments in addition to calcite, aragonite is formed, e.g. in corals and sponges (e.g. Böhm et al., 2000; Marriott et al., 2004a; Rollion-Bard et al., 2009; Wombacher et al., 2011; Hathorne et al., 2013; Rollion-Bard and Blamart, 2015). It is known that ions are incorporated differently in calcite and aragonite which might be related to the difference due to the denser structure of aragonite (e.g. Okumura and Kitano, 1986; Morse et al., 2007). Therefore, it would be useful to conduct analogous experiments to those in the present studies with initial aragonite seed material. Furthermore, a direct comparison between experimental and natural marine carbonates might not be straightforward due to major ions which are present in seawater such as Mg^{2+} and SO_4^{2-} and which incorporate readily in calcite (e.g. Broecker, 1974; Mucci and Morse, 1983; Busenberg and Plummer, 1985; Mavromatis et al., 2017a; 2017b). Especially, Mg^{2+} plays an important role because it is present in marine carbonates with up to 30 mol-% in Mg-calcites (e.g. Appelo and Postma, 2007). These major ions might not only affect the Li distribution but also the Li isotope fractionation behavior. Therefore, further experimental studies should include major ions, e.g. resembling seawater composition, to identify the behavior of Li distribution and its isotope fractionation during the growth of carbonate minerals.

The present study about Cr(VI) was one of the first experimental studies beside Hua et al. (2007), Tang et al. (2007), Sánchez-Pastor et al. (2011), Rodler (2015) and Rodler et al. (2015), which investigated the incorporation of Cr(VI) and its isotope distribution during the growth of calcite. In addition, it was shown that Cr isotope fractionation between calcite and solution can occur without redox processes (see **Chapter 5**). Therefore, further studies should be carried out in order to understand the controlling parameter such as temperature, growth rate, partial pressure of CO_2, salinity and formation rate during Cr(VI) incorporation in calcite without former reduction to Cr(III). Moreover, sulfate is one of the most important elements in the ocean which is readily incorporated in calcite (e.g. Broecker, 1974; Busenberg and Plummer, 1985). Thereby, the SO_4^{2-} incorporation is affected by a competition with the carbonate ion at elevated pH values (e.g. Wynn et al., 2018). The competition between CrO_4^{2-}, CO_3^{2-} and SO_4^{2-} might also affecting the Cr(VI) distribution and isotope fractionation behavior as a function of pH. This information would be indispensable to compare data from experimental and natural grown carbonate minerals. In addition, the different incorporation behavior of cations in calcite and aragonite is also valid for anions as it was previously shown for B (e.g. Kitano et al., 1978). Therefore, studies with initial aragonite seeds instead of calcite seeds would be necessary in order to unravel mysteries during Cr(VI) incorporation and isotope fractionation.

References

Aagaard P. and Helgeson H. C. (1982) Thermodynamic and kinetic constraints on reaction-rates among minerals and aqueous solutions. 1. Theoretical considerations. Am. J. Sci. 282, 237–285.

Accomero M., Marini L. and Lelli M. (2010) Prediction of the thermodynamic properties of metal–chromate aqueous complexes to high temperatures and pressures and implications for the speciation of hexavalent chromium in some natural waters. Appl. Geochemistry 25, 242–260.

Alexandratos V. G. (2004) Macroscopic and spectroscopic studies of arsenate uptake by calcite. State University of New York at Stony Brook.

Alwan A. K. and Williams P. A. (1979) Transition Metal Chemistry. 4th ed., Dordrecht, Netherlands.

Andersson M. P., Rodriguez-Blanco J. D. and Stipp S. L. S. (2016) Is bicarbonate stable in and on the calcite surface? Geochim. Cosmochim. Acta 176, 198–205.

Anthony J. W., Bideaux R. A., Bladh K. W. and Nichols M. C. (2003) Handbook of Mineralogy, Mineral Data Publishing., Tiscon, AZ, USA.

Appelo C. A. J. and Postma D. (2007) Geochemistry, Groundwater and Pollution. 2nd ed., A. A. Balkema Publisher, Leiden.

Arroyo-de Dompablo M. E., Fernández-González M. A. and Fernández-Diaz L. (2015) Computational investigation of the influence of tetrahedral oxoanions (sulphate, selenate and chromate) on the stability of calcium carbonate polymorphs. R. Soc. Chem. 5, 59845–59852.

Baroni S., de Gironcoli S., Dal Corso A. and Giannozzi P. (2001) Phonons and related crystal properties from density-functional perturbation theory. Rev. Mod. Phys. 73.

Beck W. C., Grossman E. L. and Morse J. W. (2005) Experimental studies of oxygen isotope fractionation in the carbonic acid system at 15°, 25°, and 40°C. Geochim. Cosmochim. Acta 69, 3493–3503.

Becker R. H. and Clayton R. N. (1976) Oxygen isotope study of a Precambrian banded iron-formation, Hamerslay Range, Western Australia. Geochim. Cosmochim. Acta 40, 1153–1165.

Bigeleisen J. (1949) The relative reaction velocities of isotopic molecules. J. Chem. Phys. 17, 675–678.

Bigeleisen J. and Mayer M. G. (1947) Calculation of Equilibrium Constants for Isotopic Exchange Reactions. J. Chem. Phys. 15, 261–267.

Böhm F., Eisenhauer A., Tang J., Dietzel M., Krabbenhöft A., Kisakürek B. and Horn C. (2012) Strontium isotope fractionation of planktic foraminifera and inorganic calcite. Geochim. Cosmochim. Acta 93, 300–314.

Böhm F., Joachimski M. M., Dullo W.-C., Eisenhauer A., Lehnert H., Reitner J. and Wörheide G. (2000) Oxygen isotope fractionation in marine aragonite of coralline sponges. Geochim. Cosmochim. Acta 64, 1695–1703.

Boni M., Balassone G., Gilg H. A. and Stanley G. (2007) Non-sulphide Zn-Pb mineralization in the Irish Midlands (Tynagh, Silvermines and Galmoy). Digging Deep., 1377–1380.

Boni M., Gilg H. A., Aversa G. and Balassone G. (2003) The "Calamine" of southwest Sardinia: Geology, mineralogy, and stable isotope geochemistry of supergene Zn mineralization. Econ. Geol. 98, 731–748.

Bonnand P., James R. H., Parkinson I. J., Connelly D. P. and Fairchild I. J. (2013) The chromium isotopic composition of seawater and marine carbonates. Earth Planet. Sci. Lett. 382, 10–20.

Böttcher M. E. (1998) Manganese(II) partitioning during experimental precipitation of rhodochrosite-calcite solid solutions from aqueous solutions. Mar. Chem. 62, 287–297.

Bouchard M. and Smith D. C. (2001) Evaluating Raman Microscopy for the non-destructive archaeometry of corroded coins: a powerful technique for conservation studies. Invited paper. Asian Chem. Lett. 5, 157–170.

Brand U., Azmy K., Bitner M. A., Logan A., Zuschin M., Came R. and Ruggiero E. (2013) Oxygen isotopes and $MgCO_3$ in brachiopod calcite and a new paleotemperature equation. Chem. Geol. 359, 23–31.

Brand U., Azmy K., Griesshaber E., Bitner M. A., Logan A., Zuschin M., Ruggiero E. and Colin P. L. (2015) Carbon isotope composition in modern brachiopod calcite: A case of equilibrium with seawater? Chem. Geol. 411, 81–96.

Brand U., Logan A., Hiller N. and Richardson J. (2003) Geochemistry of modern brachiopods: applications and implications for oceanography and paleoceanography. Geo. Chem. 198, 305–334.

Bray A. M., Chan L. H. and von Damm K. L. (2001) Constancy of the Li-Isotopic Signature in Mid-Ocean Ridge Hydrothermal Fluids: Evidence for Equilibrium Control. In American Geophysical Union, Fall Meeting 2001

Brečević L. and Nielsen A. E. (1989) Solubility of amorphous calcium carbonate. J. Cryst. Growth 98, 504–510.

Broecker W. S. (1974) Chemical Oceanography. Harcourt Brace Jovanovich, Inc. USA.

Brunauer S., Emmet P. H. and Teller E. (1938) Adsorption of gases in multimolecular layers. J. Am. Chem. Soc. 60, 309–319.

Bryan S. P. and Marchitto T. M. (2008) Mg/Ca-temperature proxy in benthic foraminifera: New calibrations from the Florida Straits and a hypothesis regarding Mg/Li. Paleoceanography, 1–17.

Burke W. H., Denison R. E., Hetherington E. A., Koepnick R. B., Nelson H. F. and Otto J. B. (1982) Variation of seawater $^{87}Sr/^{86}Sr$ throughout Phanerozoic time. Geology 10, 516–519.

Burton K. W. and Vigier N. (2011) Lithium isotopes as tracers in marine and terrestrial environment. In Handbook of environmental isotope geochemistry (ed. M. Baskaran).

Busenberg E. and Plummer L. N. (1985) Kinetic and thermodynamic factors controlling the distribution of SO_4^{2-} and Na^+ in calcites and selected aragonites. Geochim. Cosmochim. Acta 49, 713–725.

Came R. E., Eiler J. M., Veizer J., Azmy K., Brand U. and Weidman C. R. (2007) Coupling of surface temperatures and atmospheric CO_2 concentrations during the Palaeozoic era. Nature 449, 198–201.

Carothers W. W., Adami L. H. and Rosenbauer R. J. (1988) Experimental Oxygen Isotope Fractionation between Siderite-Water and Phosphoric-Acid liberated CO_2-Siderite. Geochim. Cosmochim. Acta 52, 2445–2450.

Carpenter S. J. and Lohmann K. C. (1995) $\delta^{18}O$ and $\delta^{13}C$ values of modern brachiopod shells. Goechim. Cosmochim. Acta 59, 3749–3764.

Chacko T., Cole D. R. and Horita J. (2001) Equilibrium Oxygen, Hydrogen and Carbon Isotope Fractionation Factors applicable to Geologic Systems. In Stable Isotope Geochemistry, pp. 1–81.

Chacko T. and Deines P. (2008) Theoretical calculation of oxygen isotope fractionation factors in carbonate systems. Geochim. Cosmochim. Acta 72, 3642–3660.

Chacko T., Mayeda T. K., Clayton R. N. and Goldsmith J. R. (1991) Oxygen and carbon isotope fractionations between CO_2 and calcite. Geochim. Cosmochim. Acta 55, 2867–2882.

Chan L.-H., Alt J. C. and Teagle D. A. H. (2002) Lithium and lithium isotope profiles through the upper oceanic crust: a study of seawater-basalt exchange at ODP Sites 504B and 896A. Earth Planet. Sci. Lett. 201, 187–201.

Chan L.-H. and Edmond J. M. (1988) Variation of lithium isotope composition in the marine environment: A preliminary report. Geochim. Cosmochim. Acta 52, 1711–1717.

Chan L.-H., Edmond J. M., Thompson G. and Gillis K. (1992) Lithium isotopic composition of submarine basalts: implications for the lithium cycle in the oceans. Earth Planet. Sci. Lett. 108, 151–160.

Chan L.-H., Gieskes J. M., You C.-F. and Edmond J. M. (1994) Lithium isotope geochemistry of sediments and hydrothermal fluids of the Guaymas Basin, Gulf of California. Geochim. Cosmochim. Acta 20, 4443–4454.

Chan L.-H., Leeman W. P. and Plank T. (2006) Lithium isotopic composition of marine sediments. Geochemistry, Geophys. Geosystems 7, 1–25.

Cheng L., Sturchio N. C., Woicik J. C., Kemmer K. M., Lyman P. F. and Bedzyk M. J. (1998) High-resolution structural study of zinc ion incorporation at the calcite cleavage surface. Surf. Sci. Lett. 415, 976–982.

Clarkson J. R., Price T. J. and Adams C. J. (1992) Role of Metastable Phases in the Spontaneous Precipitation of Calcium Carbonate. J. Chem. Soc., Faraday Trans. 88, 243–249.

Clayton R. N. and Epstein S. (1961) The Use of Oxygen Isotopes in High-Temperature Geological Thermometry. J. Geol. 69, 447–452.

Coplen T. B., Kendall C. and Hopple J. (1983) Comparison of stable isotope reference samples. Nature 302, 236–238.

Coppola V., Boni M., Gilg H. A., Balassone G. and Dejonghe L. (2008) The “calamine” nonsulfide Zn-Pb deposits of Belgium: Petrographical, mineralogical and geochemical characterization. Ore Geol. Rev. 33, 187–210.

Cowan C. E., Zachara J. M. and Resch C. T. (1990) Solution ion effects on the surface exchange of selenite on calcite. Geochim. Cosmochim. Acta 54, 2223–2234.

Cowley E. R. and Pant A. K. (1973) Lattice Dynamics of Calcite. Phys. Rev. B 8, 4795–4800.

Criss R. E. (1999) Principles of stable Isotope Distribution., Oxford University Press Inc., New York.

Crowe S. A., Døssing L. N., Beukes N. J., Bau M., Kruger S. J., Frei R. and Canfield D. E. (2013) Atmospheric oxygenation three billion years ago. Nature 501, 535–538.

D'Arcy M., Whittaker A. C. and Roda-Boluda D. (2017) Measuring alluvial fan sensitivity to past climate changes using a self-similarity approach to grain-size fining, Death Valley, California. Sedimentology 64, 388–424.

Dal Corso A. (2014) Pseudopotentials periodic table: From H to Pu. Comput. Mater. Sci. 95, 337–350.

Dawber C. F. and Tripati A. K. (2012) Relationships between bottom water carbonate saturation and element/Ca ratios in coretop samples of the benthic foraminifera Oridorsalis umbonatus. Biogeosciences 9, 3029–3045.

Deines P. (2004) Carbon isotope effects in carbonate systems. Geochim. Cosmochim. Acta 68, 2659–2679.

Delaney M. L., Bé A. W. H. and Boyle E. A. (1985) Li, Sr, Mg, and Na in foraminiferal calcite shells from laboratory culture, sediment traps, and sediment cores. Geochim. Cosmochim. Acta 49, 1327–1341.

Delaney M. L., Popp B. N., Lepzlter C. G. and Anderson T. F. (1989) Lithium-to-calcium ratios in modern, cenozoic, and paleozoic articulate brachiopod shells. Paleoceanography 4, 681–691.

Dellinger M., West A. J., Paris G., Adkins J. F., Pogge von Strandmann P. A. E., Ullmann C. V., Eagle R. A., Freitas P., Bagard M. L., Ries J. B., Corsetti F. A., Perez-Huerta A. and Kampf A. R. (2018) The Li isotope composition of marine biogenic carbonates: Patterns and mechanisms. Geochim. Cosmochim. Acta.

DePaolo D. J. (2011) Surface kinetic model for isotopic and trace element fractionation during precipitation of calcite from aqueous solutions. Geochim. Cosmochim. Acta 75, 1039–1056.

Dietzel M. (2011) Carbonates. In Encyclopedia of Geobiology Springer, Netherlands. pp. 261–266.

Dietzel M., Gussone N. and Eisenhauer A. (2004) Co-precipitation of Sr^{2+} and Ba^{2+} with aragonite by membrane diffusion of CO_2 between 10 and 50 °C. Chem. Geol. 203, 139–151.

Dietzel M., Tang J., Leis A. and Köhler S. J. (2009) Oxygen isotopic fractionation during inorganic calcite precipitation - Effects of temperature, precipitation rate and pH. Chem. Geol. 268, 107–115.

Dietzel M. and Usdowski E. (1996) Coprecipitation of Ni^{2+}, Co^{2+}, and Mn^{2+} with galena and covellite, and of Sr^{2+} with calcite during crystallization via diffusion of H_2S and CO_2 through polyethylene at 20°C: Power law and Nernst law control of trace element partitioning. Chem. Geol. 131, 55–65.

van Dijk J., Fernandez A., Müller I. A., Lever M. and Bernasconi S. M. (2017) Oxygen isotope fractionation in the siderite-water system between 8.5 and 62 °C. Geochim. Cosmochim. Acta.

Døssing L. N., Dideriksen K., Stipp S. L. S. and Frei R. (2011) Reduction of hexavalent chromium by ferrous iron: A process of chromium isotope fractionation and its relevance to natural environments. Chem. Geol. 285, 157–166.

Dove P. M., De Yoreo J. J. and Weiner S. (2003) Biomineralization. In Reviews in Mineralogy and Geochemistry 54

Dromgoole E. L. and Walter L. M. (1990) Iron and manganese incorporation into calcite - effects of growth-kinetics, temperature and solution chemistry. Chem. Geol. 81, 311–336.

Ducher M., Blanchard M. and Balan E. (2016) Equilibrium zinc isotope fractionation in Zn-bearing minerals from first-principles calculations. Chem. Geol. 443, 87–96.

Effenberger H., Mereiter K. and Zemann J. (1981) Crystal structure refinements of magnesite, calcite, rhodochrosite, siderite, smithonite, and dolomite, with discussion of some aspects of the stereochemistry of calcite type carbonates. Zeitschrift für Krist. - Cryst. Mater. 156, 233–243.

Eiler J. M. (2013) The Isotopic Anatomies of Molecules and Minerals. Annu. Rev. Earth Planet. Sci. 41, 411–441.

Eisenhauer A., Bitner M. A., Rollion-Bard C., Angiolini L., Magne T., Komarek M., Tomašovych A., Frei R., Fiebig J., Griesshaber E., Lazar B., Bouman C., Leis A., Dietzel M., Brand U., Azmy K., Bücker C., Jansen U., Antia A., Farkaš J. and Henkel D. (2014) Grand Agreement (MSCA-ITN-2014-ETN: Marie Skłodowska-Curie Innovative Training Networks): BASE-LiNE Earth ("Brachiopods As SEnsitive tracers of gLobal marINe Environment: Insights from alkaline, alkaline Earth metal, and metalloid trace element ratios and isotope systems"), Annex 1, Part B.

Elderfield H. and Schultz A. (1996) Mid-ocean ridge hydrothermal fluxes and the chemical composition of the ocean. Annu. Rev. Earth Planet. Sci. 24, 191–224.

Ellis A. S., Johnson T. M. and Bullen T. D. (2002) Chromium Isotopes and the Fate of Hexavalent Chromium in the Environment. Science 295, 2060–2062.

Ellis A. S., Johnson T. M. and Bullen T. D. (2004) Using chromium stable isotope ratios to quantify Cr(VI) reduction: Lack of sorption effects. Environ. Sci. Technol. 38, 3604–3607.

Epstein S., Buchsbaum R., Lowenstam H. A. and Urey H. C. (1953) Revised carbonate-water isotopic temperature scale. Geol. Soc. Am. 64, 1315–1326.

Epstein S. and Mayeda T. (1953) Variation of O^{18} content of waters from natural sources. Geochim. Cosmochim. Acta 4, 213–224.

Farkaš J., Böhm F., Eisenhauer A., Wallmann K., Blenkinsop J., Eisenhauer A., van Geldern R., Munnecke A., Voigt S. and Veizer J. (2007) Calcium isotope record of Phanerozoic oceans: Implications for chemical evolution of seawater and its causative mechanisms. Geochim. Cosmochim. Acta 71, 5117–5134.

Farkaš J., Frýda J., Paulukat C., Hathorne E. C., Matoušková Š., Rohovec J., Frýdová B., Francová M. and Frei R. (2018) Chromium isotope fractionation between modern seawater and biogenic carbonates from the Great Barrier Reef, Australia: Implications for the paleo-seawater δ^{53}Cr reconstruction. Earth Planet. Sci. Lett. 498, 140–151.

Farmer V. C. (1974) Mineralogical Society Monograph 4: The Infrared Spectra of Minerals.

Fendorf S. E. (1995) Surface reaction of chromium in soils and waters. Geoderma 67, 55–71.

Finch A. A. and Allison N. (2007) Coordination of Sr and Mg in calcite and aragonite. Mineral. Mag. 71, 539–552.

Fortier S. M. (1994) An on-line experimental/analytical method for measuring the kinetics of oxygen isotope exchange between CO_2 and saline/hypersaline salt solutions at low (25-50°C) temperatures. Chem. Geol. 116, 155–162.

Foster G. L. (2008) Seawater pH, pCO_2 and CO_3^{2-} variations in the Caribbean Sea over the last 130 kyr: A boron isotope and B/Ca study of planktic foraminifera. Earth Planet. Sci. Lett. 271, 254–266.

Frei R., Gaucher C., Døssing L. N. and Sial A. N. (2011) Chromium isotopes in carbonates - A tracer for climate change and for reconstructing the redox state of ancient seawater. Earth Planet. Sci. Lett. 312, 114–125.

Frei R., Gaucher C., Poulton S. W. and Canfield D. E. (2009) Fluctuations in Precambrian atmospheric oxygenation recorded by chromium isotopes. Nature 461, 250–253.

Frei R., Poiré D. and Frei K. M. (2014) Weathering on land and transport of chromium to the ocean in a subtropical region (Misiones, NW Argentina): A chromium stable isotope perspective. Chem. Geol. 381, 110–124.

Frei R. and Polat A. (2013) Chromium isotope fractionation during oxidative weathering — implications from the study of a Paleoproterozoic (ca. 1.9 Ga) paleosol, Schreiber Beach, Ontario, Canada. Precambrian Res. 224, 434–453.

Frost R. L., Hales M. C. and Wain D. L. (2008a) Raman spectroscopy of smithsonite. J. Raman Spectrosc. 39, 108–114.

Frost R. L., Martens W. N., Wain D. L. and Hales M. C. (2008b) Infrared and infrared emission spectroscopy of the zinc carbonate mineral smithsonite. Spectrochim. Acta - Part A Mol. Biomol. Spectrosc. 70, 1120–1126.

Füger A., Konrad F., Leis A., Dietzel M. and Mavromatis V. (2019) Effect of growth rate and pH on lithium incorporation in calcite. Geochim. Cosmochim. Acta 248, 14–24.

Füger A., Méheut M., Mavromatis V., Leis A. and Dietzel M. (2018) Oxygen isotope fractionation during smithsonite formation from aqueous solutions. Chem. Geol. 495, 76–89.

Gabitov R. I. (2013) Growth-rate induced disequilibrium of oxygen isotopes in aragonite: An in situ study. Chem. Geol. 351, 268–275.

Gabitov R. I., Gaetani G. A., Watson E. B., Cohen A. L. and Ehrlich H. L. (2008) Experimental determination of growth rate effect on U^{6+} and Mg^{2+} partitioning between aragonite and fluid at elevated U^{6+} concentration. Geochim. Cosmochim. Acta 72, 4058–4068.

Gabitov R. I., Rollion-Bard C., Tripati A. and Sadekov A. (2014b) In situ study of boron partitioning between calcite and fluid at different crystal growth rates. Geochim. Cosmochim. Acta 137, 81–92.

Gabitov R. I., Sadekov A. and Leinweber A. (2014a) Crystal growth rate effect on Mg/Ca and Sr/Ca partitioning between calcite and fluid: An in situ approach. Chem. Geol. 367, 70–82.

Gabitov R. I. and Watson E. B. (2006) Partitioning of strontium between calcite and fluid. Geochemistry Geophys. Geosystems 7.

Gabitov R. I., Watson E. B. and Sadekov A. (2012) Oxygen isotope fractionation between calcite and fluid as a function of growth rate and temperature: An in situ study. Chem. Geol. 306, 92–102.

Gaetani G. A. and Cohen A. L. (2006) Element partitioning during precipitation of aragonite from seawater: A framework for understanding paleoproxies. Geochim. Cosmochim. Acta 70, 4617–4634.

Gautier Q., Bénézeth P., Mavromatis V. and Schott J. (2014) Hydromagnesite solubility product and growth kinetics in aqueous solution from 25 to 75 °C. Geochim. Cosmochim. Acta 138, 1–20.

Ghosh P., Adkins J., Affek H., Balta B., Guo W. F., Schauble E. A., Schrag D. and Eiler J. M. (2006a) ^{13}C-^{18}O bonds in carbonate minerals: a new kind of paleothermometer. Geochim. Cosmochim. Acta 70, 1439–1456.

Ghosh P., Eiler J., Campana S. E. and Feeney R. F. (2007) Calibration of the carbonate 'clumped isotope' paleothermometer for otoliths. Geochim. Cosmochim. Acta 71, 2736–2744.

Ghosh P., Eiler J. M. and Garzione C. (2006b) Rapid uplift of the Altiplano revealed in abundances of ^{13}C-^{18}O bonds in paleosol carbonate. Science 311, 511–515.

Giannozzi P., Baroni S., Bonini N., Calandra M., Car R., Cavazzoni C., Ceresoli D., Chiarotti G. L., Cococcioni M., Dabo I., Dal Corso A., de Gironcoli S., Fabris S., Fratesi G., Gebauer R., Gerstmann U., Gougoussis C., Kokalj A., Lazzeri M., Martin-Samos L., Marzari N., Mauri F., Mazzarello R., Paolini S., Pasquarello A., Paulatto L., Sbraccia C., Scandolo S., Sclauzero G., Seitsonen C., Smogunov A., Umari P. and Wentzcovitch R. M. (2009) QUANTUM ESPRESSO: a modular and open-source software project for quantum simulations of materials. J. Phys. Condens. Matter 21, 1–19.

Gilg H. A., Boni M., Hochleitner R. and Struck U. (2008) Stable isotope geochemistry of carbonate minerals in supergene oxidation zones of Zn-Pb deposits. Ore Geol. Rev. 33, 117–133.

Gilg H. A., Struck U., Vennemann T. and Boni M. (2003) Phosphoric acid fractionation factors for smithsonite and cerussite between 25 and 72 °C. Geochim. Cosmochim. Acta 67, 4049–4055.

Gilleaudeau G. J., Frei R., Kaufman A. J., Kah L. C., Azmy K., Bartley J. K., Chernyavskiy P. and Knoll A. H. (2016) Oxygenation of the mid-Proterozoic atmosphere: clues from chromium isotopes in carbonates. Geochemical Perspect. Lett., 178–187.

Gilleaudeau G. J., Voegelin A. R., Thibault N., Moreau J., Ullman C. V., Klaebe R. M., Korte C. and Frei R. (2018) Stable isotope records across the Cretaceous-Paleogene transition, Stevns Klint, Denmark: New insights from the chromium isotope system. Geochim. Cosmochim. Acta 235, 305–332.

Gillet P., Biellmann C., Reynard B. and McMillan P. (1993) Raman spectroscopic studies of carbonates part I: High-pressure and high-temperature behaviour of calcite, magnesite, dolomite and aragonite. Phys. Chem. Miner. 20, 1–18.

Gillet P., Mcmillan P., Schott J., Badro J. and Grzechnik A. (1996) Thermodynamic properties and isotopic fractionation of calcite from vibrational spectroscopy of ^{18}O-substituted calcite. Geochim. Cosmochim. Acta 60, 3471–3485.

Golyshev S. I., Padalko N. L. and Pechenkin S. A. (1981) Fractionation of stable oxygen and carbon isotopes in carbonate systems. Geochem. Intl. 10, 85–99.

Gueguen B., Reinhard C. T., Algeo T. J., Peterson L. C., Nielsen S. G., Wang X., Rowe H. and Planavsky N. J. (2016) The chromium isotope composition of reducing and oxic marine sediments. Geochim. Cosmochim. Acta 184, 1–19.

Hales M. C. and Frost R. L. (2007) Synthesis and vibrational spectroscopic characterisation of synthetic hydrozincite and smithsonite. Polyhedron 26, 4955–4962.

Hall J. M. and Chan L. H. (2004) Li/Ca in multiple species of benthic and planktonic foraminifera: Thermocline, latitudinal, and glacial–interglacial variation. Geochim. Cosmochim. Acta 68, 529–545.

Hathorne E. C., Felis T., Suzuki A., Kawahata H. and Cabioch G. (2013) Lithium in the aragonite skeletons of massive Porites corals: A new tool to reconstruct tropical sea surface temperatures. Paleoceanography 28, 143–152.

Hebling F., Vinograd V. L., Polly R., Gale J. D., Heck S., Rothe J., Bosbach D., Geckeis H. and Winkler B. (2014) A thermodynamic adsorption/entrapment model for selenium(IV) coprecipitation with calcite. Geochim. Cosmochim. Acta 134, 16–38.

Hellwege K. H., Lesch W., Plihal M. and Schaack G. (1970) Two phonon absorption spectra and dispersion of phonon branches in crystals of calcite structure. Zeitschrift für Phys. A Hadron. Nucl. 232, 61–86.

Hemming N. G. and Hanson G. N. (1992) Boron isotopic composition and concentration in modern marine carbonates. Geochim. Cosmochim. Acta 56, 537–543.

Hemming N. G., Reeder R. J. and Hart S. R. (1998) Growth-step-selective incorporation of boron on the calcite surface. Geochim. Cosmochim. Acta 62, 2915–2922.

Henisch H. K. (1970) Crystal Growth in Gels. The Pennsylvania State Univ. Press, University Park, Pennsylvania.

Hoefs J. (2015) Stable Isotope Geochemistry. 7th ed., Springer-Verlag, Heidelberg.

Hoefs J. (2018) Stable Isotope Geochemistry. 8th ed., Springer-Verlag, Heidelberg.

Hoefs J. and Sywall M. (1997) Lithium isotope composition of Quaternary and Tertiary biogenic carbonates and a global lithium isotope balance. Geochim. Cosmochim. Acta 61, 2679–2690.

Hoffmann M. M., Darab J. G. and Fulton J. L. (2001) An Infrared and X-ray Absorption Study of the Equilibria and Structures of Chromate, Bichromate, and Dichromate in Ambient Aqueous Solutions. J. Phys. Chem. 105, 1772–1782.

Hohenberg P. and Kohn W. (1964) Inhomogeneous Electron Gas. Phys. Rev. 136, 864–871.

Holmden C., Jacobson A. D., Sageman B. B. and Hurtgen M. T. (2016) Response of the Cr isotope proxy to Cretaceous Ocean Anoxic Event 2 in a pelagic carbonate succession from the Western Interior Seaway. Geochim. Cosmochim. Acta 186, 277–295.

Hönisch B. and Hemming N. G. (2005) Surface ocean pH response to variations in pCO_2 through two full glacial cycles. Earth Planet. Sci. Lett. 236, 305–314.

Horita J., Ueda A., Mizukami K. and Takatori I. (1989) Automatic δD and $\delta^{18}O$ analyses of multi-water samples using H_2- and CO_2-water equilibration methods with a common equilibration set-up. Int. J. Radiat. Appl. Instrumentation. 40, 801–805.

Horita J. and Wesolowski D. J. (1994) Liquid-vapor fractionation of oxygen and hydrogen isotopes of water from the freezing to the critical temperature. 58, 3425–3437.

House W. A. (1990) The prediction of phosphate co-precipitation with calcite in fresh-waters. Water Res. 24, 1017–1023.

Hua B., Deng B., Thornton E. C., Yang J. and Amonette J. E. (2007) Incorporation of chromate into calcium carbonate structure during coprecipitation. Water. Air. Soil Pollut. 179, 381–390.

Huh Y., Chan L.-H. and Edmond J. M. (2001) Lithium isotopes as a probe of weathering processes: Orinoco River. Earth Planet. Sci. Lett. 194, 189–199.

Huh Y., Chan L.-H., Zhang L. and Edmond J. M. (1998) Lithium and its isotopes in major world rivers: Implications for weathering and the oceanic budget. Geochim. Cosmochim. Acta 62, 2039–2051.

Huntington K. W., Budd D. W., Wernicke B. P. and Eiler J. M. (2011) Use of clumped isotope thermometry to constrain temperature of crystallization for diagenetic calcite. J. Sediment. Res. 81, 656–669.

Ishikawa M. and Ichikuni M. (1984) Uptake of Sodium and Potassium by Calcite. 42, 137–146.

Izbicki J. A., Ball J. W., Bullen T. D. and Sutley S. J. (2008) Chromium, chromium isotopes and selected elements, western Mojave Desert, USA. Appl. Geochemistry 23, 1325–1352.

Jambor J. L. (1964) Studies of basic copper and zinc carbonates: 1-synthetic zinc carbonates and their relationship to hydrozincite. Cabadian Mineral., 92–108.

Jamieson-Hanes J. H., Amos R. T. and Blowes D. W. (2012) Reactive transport modeling of chromium isotope fractionation during Cr(VI) reduction. Environ. Sci. Technol. 46, 13311–13316.

Jiménez-López C., Caballero E., Huertas F. J. and Romanek C. S. (2001) Chemical, mineralogical and isotope behavior, and phase transformation during the precipitation of calcium carbonate minerals from intermediate ionic solution at 25 °C. Geochim. Cosmochim. Acta 65, 3219–3231.

Kaczynski S. E. and Kieber R. J. (1994) Hyrophobic C^{18} Bound Organic Complexes of Chromium and Their Potential Impact on the Geochemistry of Chromium in Natural Waters. Environ. Sci. Technol. 28, 799–804.

Kameda Y., Sugawara K., Usuki T. and Uemura O. (1998) Hydration Structure of Na^+ in Concentrated Aqueous Solutions. Bull. Chem. Soc. Jpn. 71, 2769–2776.

Kampschulte A. and Strauss H. (2004) The sulfur isotopic evolution of Phanerozoic seawater based on the analysis of structurally substituted sulfate in carbonates. Chem. Geol. 204, 255–286.

Kim S.-T., Coplen T. B. and Horita J. (2015) Normalization of stable isotope data for carbonate minerals: Implementation of IUPAC guidelines. Geochim. Cosmochim. Acta 158, 276–289.

Kim S.-T., Hillaire-Marcel C. and Mucci A. (2006) Mechanisms of equilibrium and kinetic oxygen isotope effects in synthetic aragonite at 25 °C. Geochim. Cosmochim. Acta 70, 5790–5801.

Kim S.-T., Kang J. O., Seong-taek Y., O'Neil J. R. and Mucci A. (2009) Experimental studies of oxygen isotope fractionation between rhodochrosite ($MnCO_3$) and water at low temperatures. Geochim. Cosmochim. Acta 73, 4400–4408.

Kim S.-T. and O'Neil J. R. (1997) Equilibrium and nonequilibrium oxygen isotope effects in synthetic carbonates. Geochim. Cosmochim. Acta 61, 3461–3475.

Kinniburgh D. G. and Cooper D. M. (2011) PhreePlot: Creating graphical output with PhreeqC.

Kisakűrek B., James R. H. and Harris N. B. W. (2005) Li and δ^7Li in Himalayan rivers: Proxies for silicate weathering? Earth Planet. Sci. Lett. 237, 387–401.

Kitano Y., Okumura M. and Idogaki M. (1978) Coprecipitation of borate-boron with calcium carbonate. Geochem. J. 12, 183–189.

Kitchen J. W., Johnson T. M., Bullen T. D., Zhu J. and Raddatz A. (2012) Chromium isotope fractionation factors for reduction of Cr(VI) by aqueous Fe(II) and organic molecules. Geochim. Cosmochim. Acta 89, 190–201.

Kohn W. and Sham L. J. (1965) Self-Consistent Equations Including Exchange and Correlation Effects. Phys. Rev. 140, 1133–1138.

Konhauser K. O., Lalonde S. V., Planavsky N. J., Pecoits E., Lyons T. W., Mojzsis S. J., Rouxel O. J., Barley M. E., Rosiere C., Fralick P. W., Kump L. R. and Bekker A. (2011) Aerobic bacterial pyrite oxidation and acid rock drainage during the Great Oxidation Event. Nature 478, 369–373.

Kuessner M. L., Gourgiotis A., Manhès G., Bouchez J. and Gaillardet J. Automated analyte separation by ion chromatography using a Cobot applied to geological reference materials for Li isotope composition. Submitted to Geostand. Geoanalytical Res.

Lakshtanov L. Z. and Stipp S. L. S. (2004) Experimental study of europium(III) co-precipitation with calcite. Geochim. Cosmochim. Acta 68.

Lakshtanov L. Z. and Stipp S. L. S. (2007) Experimental study of nickel(II) interaction with calcite: Adsorption and co-precipitation. Geochim. Cosmochim. Acta 71, 3686–3697.

Lasaga A. C. (1981) Transition state theory. Rev. Mineral. 8, 135–169.

Lear C. H., Mawbey E. M. and Rosenthal Y. (2010) Cenozoic benthic foraminiferal Mg/Ca and Li/Ca records: Toward unlocking temperatures and saturation states. Paleoceanography 25, 2–11.

Lear C. H. and Rosenthal Y. (2006) Benthic foraminiferal Li/Ca: Insights into Cenozoic seawater carbonate saturation state. Geology 34, 985–988.

Lécuyer C., Hutzler A., Amiot R., Daux V., Grosheny D., Otero O., Martineau F., Fourel F., Balter V. and Reynard B. (2012) Carbon and oxygen isotope fractionations between aragonite and calcite of shells from modern molluscs. Chem. Geol. 332–333, 92–101.

Lemarchand D., Gaillardet J., Lewin É. and Allégre C. J. (2000) The influence of rivers on marine boron isotopes and implications for reconstructing past ocean pH. Nature 408, 951–954.

Loeffler H. H., Inada Y. and Funahashi S. (2006) Water Exchange Dynamics of Lithium(I) Ion in Aqueous Solution. J. Phys. Chem. 110, 5690–5696.

Lorens R. B. (1981) Sr, Cd, Mn and Co distribution coefficients in calcite as a function of calcite precipitation rate. Geochim. Cosmochim. Acta 45, 553–561.

Lowenstam H. A. (1961) Mineralogy, O^{18}/O^{16} ratios, and strontium and magnesium contents of recent and fossil brachiopods and their bearing on the history of the oceans. J. Geol. 69, 241–260.

Lyons T. W. and Reinhard C. T. (2009) Oxygen for heavy-metal fans. Nature 461, 179–181.

Marcus Y. (1988) Ionic Radii in Aqueous Solutions. Chem. Rev. 88, 1475–1498.

Marriott C. S., Henderson G. M., Belshaw N. S. and Tudhope A. W. (2004a) Temperature dependence of δ^7Li, δ^{44}Ca and Li/Ca during growth of calcium carbonate. Earth Planet. Sci. Lett. 222, 615–624.

Marriott C. S., Henderson G. M., Crompton R., Staubwasser M. and Shaw S. (2004b) Effect of mineralogy, salinity, and temperature on Li/Ca and Li isotope composition of calcium carbonate. Chem. Geol. 212, 5–15.

Mavromatis V., Schmidt M., Botz R., Comas-Bru L. and Oelkers E. H. (2012) Experimental quantification of the effect of Mg on calcite-aqueous fluid oxygen isotope fractionation. Chem. Geol. 310–311, 97–105.

Mavromatis V., Goetschl K. E., Grengg C., Konrad F., Purgstaller B. and Dietzel M. (2018) Barium partitioning in calcite and aragonite as a function of growth rate. Geochim. Cosmochim. Acta 237, 65–78.

Mavromatis V., Gonzàlez G. A., Dietzel M. and Schott J. (2019) Zinc isotope fractionation during the inorganic precipitation of calcite - Towards a new pH proxy. Geochim. Cosmochim. Acta 244, 99–112.

Mavromatis V., Immenhauser A., Buhl D., Purgstaller B., Baldermann A. and Dietzel M. (2017b) Effect of organic ligands on Mg partitioning and Mg isotope fractionation during low-temperature precipitation of calcite in the absence of growth rate effects. Geochim. Cosmochim. Acta 207, 139–153.

Mavromatis V., Montouillout V., Noireaux J., Gaillardet J. and Schott J. (2015) Characterization of boron incorporation and speciation in calcite and aragonite from co-precipitation experiments under controlled pH, temperature and precipitation rate. Geochim. Cosmochim. Acta 150, 299–313.

Mavromatis V., Purgstaller B., Dietzel M., Buhl D., Immenhauser A. and Schott J. (2017a) Impact of amorphous precursor phases on magnesium isotope signatures of Mg-calcite. Earth Planet. Sci. Lett. 464, 227–236.

Mavromatis V., Gautier Q., Bosc O. and Schott J. (2013) Kinetics of Mg partition and Mg stable isotope fractionation during its incorporation in calcite. Geochim. Cosmochim. Acta 114, 188–203.

McClain C. N. and Mahler K. (2016) Chromium fluxes and speciation in ultramafic catchments and global rivers. Chem. Geol. 426, 135–157.

McConnaughey T. (1989) ^{13}C and ^{18}O isotopic disequilibrium in biological carbonates: II. In vitro simulation of kinetic isotope effects. Geochim. Cosmochim. Acta 53, 163–171.

McCrea J. M. (1950) On the Isotopic Chemistry of Carbonates and a Paleotemperature Scale. J. Chem. Phys. 18, 849–857.

Méheut M., Lazzeri M., Balan E. and Mauri F. (2007) Equilibrium isotopic fractionation in the kaolinite, quartz, water system: Prediction from first-principles density-functional theory. Geochim. Cosmochim. Acta 71, 3170–3181.

Melchiorre E. B., Williams P. A. and Bevins R. E. (2001) A low temperature oxygen isotope thermometer for cerussite, with applications at Broken Hill, New South Wales, Australia. Geochim. Cosmochim. Acta 65, 2527–2533.

Miller K. G., Kominz M. A., Browning J. V., Wright J. D., Mountain G. S., Katz M. E., Sugarman P. J., Cramer B. S., Christie-Blick N. and Pekar S. F. (2005) The Phanerozoic Record of Global Sea-Level Change. Science 310, 1293–1298.

Millero F. J. (1974) The Physical Chemistry of Seawater. Annu. Rev. Earth Planet. Sci., 101–150.

Mills G. A. and Urey H. C. (1940) The Kinetics of Isotopic Exchange between Carbon Dioxide, Bicarbonate Ion, Carbonate Ion and Water. J. Am. Chem. Soc. 62, 1019–1026.

Misra S. and Froelich P. N. (2012) Lithium Isotope History of Cenozoic Seawater: Changes in Silicate Weathering and Reverse Weathering. Science 335, 818–824.

Monkhorst H. J. and Pack J. D. (1976) Special points for Brillouin-zone integrations. Phys. Rev. B 13, 5188–5192.

Morse J. W., Arvidson R. S. and Lüttge A. (2007) Calcium carbonate formation and dissolution. Chem. Rev. 107, 342–381.

Morse J. W. and Mackenzie F. T. (1990) Geochemistry of Sedimentary Carbonates., Elsevier Science Publishers B.V., Amsterdam, Netherlands.

Mucci A. (1988) Manganese uptake during calcite precipitation from seawater - conditions leading to the formation of a pseudokutnahorite. Geochim. Cosmochim. Acta 52, 1859–1868.

Mucci A. (1981) The solubility of calcite and aragonite and the composition of calcite overgrowths in seawater and related solutions. PhD Thesis, University of Miami.

Mucci A. and Morse J. W. (1983) The Incorporation of Mg^{2+} and Sr^{2+} Into Calcite Overgrowths - Influences of Growth-Rate and Solution Composition. Geochim. Cosmochim. Acta 47, 217–233.

Nakayama E., Kuwamoto T., Tsurubo S., Tokoro H. and Fujinaga T. (1981) CHEMICAL SPECIATION OF CHROMIUM IN SEA WATER Part 1. Effect of Naturally Occurring Organic Materials on the Complex Formation, of Chromium(III). Anal. Chim. Acta 130, 289–294.

Négrel P., Millot R., Brenot A. and Bertin C. (2010) Lithium isotopes as tracers of groundwater circulation in a peat land. Chem. Geol. 276, 119–127.

Nielsen A. E. (1984) Electrolyte crystal growth mechanisms. J. Cryst. Growth 67, 289–310.

Nielsen L. C., DePaolo D. J. and De Yoreo J. J. (2012) Self-consistent ion-by-ion growth model for kinetic isotopic fractionation during calcite precipitation. Geochim. Cosmochim. Acta 86, 166–181.

Noireaux J., Mavromatis V., Gaillardet J., Schott J., Montouillout V., Louvat P., Rollion- Bard C. and Neuville D. R. (2015) Crystallographic control on the boron isotope paleo-pH proxy. Earth Planet. Sci. Lett. 430, 398–407.

O’Neil J. R. and Clayton R. N. (1964) Oxygen isotope geothermometry. Isot. Cosm. Chem., 157–168.

O’Neil J. R., Clayton R. N. and Toshiko M. K. (1969) Oxygen Isotope Fractionation in Divalent Metal Carbonates. J. Chem. Phys. 51, 5547–5558.

Oelkers E. H. (2001) General kinetic description of multioxide silicate mineral and glass dissolution. Geochim. Cosmochim. Acta 65, 3703–3719.

Okumura M. and Kitano Y. (1986) Coprecipitation of alkali metal ions with calcium carbonate. Geochim. Cosmochim. Acta 50, 49–58.

Oomori T., Nakasone M., Kanechima K. and Kitano Y. (1985) Incorporation of Sodium into Calcium Carbonate and Protodolomite. Bull. Coll. Sci. 39, 51–56.

Oze C., Bird D. K. and Fendorf S. (2007) Genesis of hexavalent chromium from natural sources in soil and groundwater. Proc. Natl. Acad. Sci. 104, 6544–6549.

Oze C., Fendorf S., Bird D. K. and Coleman R. G. (2004) Chromium Geochemistry in serpentinized ultramafic Rocks and serpentine Soil from Franciscan Complex of California. Am. J. Sci. 304, 67–101.

Palmer C. D. and Puls R. W. (1994) Natural Attenuation of Hexavalent Chromium in Ground Water and Soils. In EPA Environmental Assessment Sourcebook (ed. J. R. Boulding).

Palmer M. R., Pearson P. N. and Cobb S. J. (1998) Reconstructing Past Ocean pH-Depth Profiles. Science 282, 1468–1471.

Parkhurst D. L. and Appelo C. A. J. (1999) User's guide to PHREEQC (Version 2)—a computer program for speciation, bath-reaction, one-dimensional transport, and inverse geochemical calculations., Water-Resources Investigations Report 99–4259. USGS, Denver, USA.

Parkinson D., Curry G. B., Cusack M. and Fallick A. E. (2005) Shell structure, patterns and trends of oxygen and carbon stable isotopes in modern brachiopod shells. Chem. Geol. 219, 193–235.

Paul D. and Skrzypek G. (2007) Assessment of carbonate-phosphoric acid analytical technique performed using GasBench II in continuous flow isotope ratio mass spectrometry. Int. J. Mass Spectrom. 262, 180–186.

Pearson P. N. and Palmer M. R. (2000) Atmospheric carbon dioxide concentrations over the past 60 million years. Nature 406, 695–699.

Pearson P. N. and Palmer M. R. (1999) Middle Eocene Seawater pH and Atmospheric Carbon Dioxide Concentrations. Science 284, 1824–1826.

Perdew J. P., Burke K. and Ernzerhof M. (1996) Generalized Gradient Approximation Made Simple. Phys. Rev. 77, 3865–3868.

Pingitore N. E. J. and Eastman M. P. (1986) The co-precipitation of Sr^{2+} with calcite at 25 °C and 1 atm. Geochim. Cosmochim. Acta 50, 2195–2203.

Pingitore N. E. J. and Eastman M. P. (1984) The experimental partitioning of Ba^{2+} into calcite. Chem. Geol. 45, 113–120.

Pingitore Jr. N. E., Lytle F. W., Davies B. M., Eastman M. P., Eller P. G. and Larson E. M. (1992) Mode of incorporation of Sr^{2+} in calcite: Determination by X-ray absorption spectroscopy. Geochim. Cosmochim. Acta 56, 1531–1538.

Planavsky N., Reinhard C., Wang X., Thomson D., McGoldrick P., Rainbird R., Johnson T., Fischer W. and Lyons T. (2014) Low Mid-Proterozoic atmospheric oxygen levels and the delayed rise of animals. Science 346, 635–638.

Polyakov V. B. (1998) On anharmonic and pressure corrections to the equilibrium isotopic constants for minerals. Geochim. Cosmochim. Acta 62, 3077–3085.

Popp B. N., Anderson T. F. and Sandberg P. A. (1986) Brachiopods as indicators of original isotopic compositions in some Paleozoic limestones. Geol. Soc. Am. Bull. 97, 1262–1269.

Prieto M. (2009) Thermodynamics of solid solution – aqueous solution systems. In Reviews in Mineralogy and Geochemistry 70, pp. 47–85.

Prieto M., Fernández-González A., Putnis A. and Fernández-Díaz L. (1997) Nucleation, growth, and zoning phenomena in crystallizing $(Ba,Sr)CO_3$, $Ba(SO_4,CrO_4)$,$(Ba,Sr)SO_4$, and $(Cd,Ca)CO_3$ solid solutions from aqueous solutions. Geochim. Cosmochim. Acta 61, 3383–8897.

Purgstaller B., Konrad F., Dietzel M., Immenhauser A. and Mavromatis V. (2017) Control of Mg^{2+}/Ca^{2+} Activity Ratio on the Formation of Crystalline Carbonate Minerals via an Amorphous Precursor. Cryst. Growth Des. 17, 1069–1078.

Purgstaller B., Mavromatis V., Immenhauser A. and Dietzel M. (2016) Transformation of Mg-bearing amorphous calcium carbonate to Mg-calcite – In situ monitoring. Geochim. Cosmochim. Acta 174, 180–195.

Raddatz J., Liebetrau V., Rüggeberg A., Harthorne E., Krabbenhöft A., Eisenhauser A., Böhm F., Vollstaedt H., Fietzke J., López Correa M., Freiwald A. and Dullo W.-C. (2013) Stable Sr-isotope, Sr/Ca, Mg/Ca, Li/Ca and Mg/Li ratios in the scleractinian cold-water coral Lophelia pertusa. Chem. Geol. 352, 143–152.

Rai D., Sass B. M. and Moore D. A. (1987) Chromium(III) hydrolysis constants and solubility of chromium(III) hydroxide. Inorg. Chem. 26, 345–349.

Reddy M. M. and Nancollas G. H. (1976) The crystallization of calcium carbonate. J. Cryst. Growth 35, 33–38.

Reeder R. J., Lamble G. M., Lee J. and Staudt W. J. (1994) Mechanism of SeO_4^{2-} substitution in calcite: an XAFS study. Geochim. Cosmochim. Acta 58, 5639–5646.

Reeder R. J., Lamble G. M. and Northrup P. A. (1999) XAFS study of the coordination and local relaxation around Co^{2+}, Zn^{2+}, Pb^{2+}, and Ba^{2+} trace elements in calcite. Am. Mineral. 84, 1049–1060.

Reinhard C. T., Planavsky N. J., Robbins L. J., Partin C. A., Gill B. C., Lalonde S. V., Bekker A., Konhauser K. O. and Lyons T. (2013) Proterozoic ocean redox and biogeochemical stasis. Proc. Natl. Acad. Sci. U. S. A. 110, 5357–5362.

Renne P. R., Black M. T., Zichao Z., Richards M. A. and Basu A. R. (1995) Synchrony and Causal Relations Between Permian-Triassic Boundary Crises and Siberian Flood Volcanism. Science 269, 1412–1416.

Révész K. M. and Landwehr J. M. (2002) $\delta^{13}C$ and $\delta^{18}O$ isotopic composition of $CaCO_3$ measured by continuous flow isotope ratio mass spectrometry: Statistical evaluation and verification by application to Devils Hole core DH-11 calcite. Rapid Commun. Mass Spectrom. 16, 2102–2114.

Richet P., Bottinga Y. and Javoy M. (1977) A Review of Hydrogen, Carbon, Nitrogen, Oxygen, Sulphur, and Chlorine Stable Isotope Fractionation among gaseous Molecules. Ann. Rev. Earth Planet 5, 65–110.

Richter F. M., Davis A. M., DePaolo D. J. and Watson A. B. (2003) Isotope fractionation by chemical diffusion between molten basalt and rhyolite. Geochim. Cosmochim. Acta 67, 3905–3923.

Rimstidt J. D., Balog A. and Webb J. (1998) Distribution of trace elements between carbonate minerals and aqueous solutions. Geochim. Cosmochim. Acta 62, 1851–1863.

Roberts J., Kaczmarek K., Langer G., Skinner L. C., Bijma J., Bradbury H., Turchyn A. V., Lamy F. and Misra S. (2018) Lithium isotopic composition of benthic foraminifera: A new proxy for paleo-pH reconstruction. Geochim. Cosmochim. Acta 236, 336–350.

Robles-Camacho J. and Armienta M. A. (2000) Natural chromium contamination of groundwater at León Valley, México. J. Geochemical Explor. 68, 167–181.

Rodler A. (2015) Chromium Isotope Uptake in Carbonates: Chromium isotope fractionation during coprecipitation with calcite using a CO_2-diffusion technique. PhD Thesis, University of Copenhagen.

Rodler A. S., Frei R., Gaucher C., Korte C., Rosing S. A. and Germs G. J. B. (2017) Multiproxy isotope contraints on ocean compositional changes across the late Neoproterozoic Ghaub glaciation, Otavi Group, Namibia. Precambrian Res. 298, 306–324.

Rodler A. S., Hohl S. V., Guo Q. and Frei R. (2016) Chromium isotope stratigraphy of Ediacaran cap dolostones, Doushantuo Formation, South China. Chem. Geol. 436, 24–34.

Rodler A., Sánchez-Pastor N., Fernández-Díaz L. and Frei R. (2015) Fractionation behavior of chromium isotopes during coprecipitation with calcium carbonate: Implications for their use as paleoclimatic proxy. Geochim. Cosmochim. Acta 164, 221–235.

Rollion-Bard C. and Blamart D. (2015) Possible controls on Li, Na and Mg incorporation into aragonite coral skeletons. Chem. Geol. 396, 98–111.

Rollion-Bard C., Vigier N., Meibom A., Blamart D., Reynaud S., Rodolfo-Metalpa R., Martin S. and Gattuso J. P. (2009) Effect of environmental conditions and skeletal ultrastructure on the Li isotopic composition of scleractinian corals. Earth Planet. Sci. Lett. 286, 63–70.

Rosenbaum J. M. (1997) Gaseous, liquid, and supercritical fluid H_2O and CO_2: Oxygen isotope fractionation behavior. Geochim. Cosmochim. Acta 61, 4993–5003.

Rosenthal Y., Boyle E. A. and Slowey N. (1997) Temperature control on the incorporation of magnesium, strontium, fluorine, and cadmium into benthic foraminiferal shells from Little Bahama Bank: Prospects for thermocline paleoceanography. Geochim. Cosmochim. Acta 61, 3633–3643.

Rosman K. J. R. and Taylor P. D. P. (1998) Isotopic composition of the elements. Pure Appl. Chem. 70, 217–235.

Rudnick R. L., Tomascak P. B., Njo H. B. and Gardner L. R. (2004) Extreme lithium isotopic fractionation during continental weathering revealed in saprolites from South Carolina. Chem. Geol. 212, 45–57.

Saenger C. and Wang Z. (2014) Magnesium isotope fractionation in biogenic and abiogenic carbonates: Implications for paleoenvironmental proxies. Quat. Sci. Rev. 90, 1–21.

Sánchez-Pastor N., Gigler A. M., Cruz J. A., Park S. H., Jordan G. and Fernández-Díaz L. (2011) Growth of calcium carbonate in the presence of Cr(VI). Cryst. Growth Des. 11, 3081–3089.

Schauble E. A., Ghosh P. and Eiler J. M. (2006) Preferential formation of ^{13}C-^{18}O bonds in carbonate minerals, estimated using first-principles lattice dynamics. Geochim. Cosmochim. Acta 70, 2510–2529.

Schauble E., Rossman G. R. and Taylor H. P. (2004) Theoretical estimates of equilibrium chromium-isotope fractionations. Chem. Geol. 205.

Schindler P., Reinert M. and Gamsjäger H. (1969) Löslichkeitskonstanten und Freie Bildungsenthalpien von $ZnCO_3$ und $Zn_5(OH)_6(CO_3)_2$ bei 25°. Helv. Chim. Acta 52, 2327–2332.

Schmidt M., Xeflide S., Botz R. and Mann S. (2005) Oxygen isotope fractionation during synthesis of CaMg-carbonate and implications for sedimentary dolomite formation. Geochim. Cosmochim. Acta 69, 4665–4674.

Schoenberg R., Zink S., Staubwasser M. and von Blanckenburg F. (2008) The stable Cr isotope inventory of solid Earth reservoirs determined by double spike MC-ICP-MS. Chem. Geol. 249, 294–306.

Schott J., Pokrovsky O. S. and Oelkers E. H. (2009) The link between mineral dissolution/precipitation kinetics and solution chemistry. In Thermodynamics and Kinetics of Water-Rock Interaction. In Reviews in Mineralogy and Geochemistry, pp. 207–258.

Shannon R. D. (1976) Revised Effective Ionic Radii and Systematic Studies of Interatomic Distances in Halides and Chaleogenides. Acta Crystallogr. Sect. 32, 751–767.

Sikora E. R., Johnson T. M. and Bullen T. D. (2008) Microbial mass-dependent fractionation of chromium isotopes. Geochim. Cosmochim. Acta 72, 3631-3641.

Šillerová H., Chrastný V., Čadková E. and Komárek M. (2014) Isotope fractionation and spectroscopic analysis as an evidence of Cr(VI) reduction during biosorption. Chemosphere 95, 402–407.

Smith S. V., Buddemeier R. W., Redaije R. C. and Houck J. E. (1979) Strontium-Calcium Thermometry in Coral Skeletons. Science 204, 404–407.

Somasundaran P. and Agar G. E. (1967) The Zero Point of Charge of Calcite. J. Colloid Interface Sci. 24, 433–440.

Spötl C. and Vennemann T. W. (2003) Continuous-flow isotope ratio mass spectrometric analysis of carbonate minerals. Rapid Commun. mass Spectrom. 17, 1004–1006.

Staudt W. J., Reeder R. J. and Schoonen M. A. A. (1994) Surface structural controls on compositional zoning of SO_4^{2-} and SeO_4^{2-} in synthetic calcite single crystals. Geochim. Cosmochim. Acta 58, 2087–2098.

Steuber T. and Veizer J. (2002) Phanerozoic record of plate tectonic control of seawater chemistry and carbonate sedimentation. Geology 30, 1123–1126.

Stoilova D., Koleva V. and Vassileva V. (2002) Infrared study of some synthetic phases of malachite ($Cu_2(OH)_2CO_3$)-hydrozincite ($Zn_5(OH)_6(CO_3)_2$) series. Spectrochim. Acta - Part A Mol. Biomol. Spectrosc. 58, 2051–2059.

Stoll H. M. and Schrag D. P. (2000) Coccolith Sr/Ca as a new indicator of coccolithophorid calcification and growth rate. Geochemistry, Geophys. Geosystems 1, 1–24.

Tang J., Dietzel M., Boehm F., Koehler S. J. and Eisenhauer A. (2008b) Sr^{2+}/Ca^{2+} and $^{44}Ca/^{40}Ca$ fractionation during inorganic calcite formation: II. Ca isotopes. Geochim. Cosmochim. Acta 72, 3733–3745.

Tang J., Köhler S. J. and Dietzel M. (2008a) Sr^{2+}/Ca^{2+} and $^{44}Ca/^{40}Ca$ fractionation during inorganic calcite formation: I. Sr incorporation. Geochim. Cosmochim. Acta 72, 3718–3732.

Tang J., Niedermayr A., Köhler S. J., Böhm F., Kisakürek B., Eisenhauer A. and Dietzel M. (2012) Sr^{2+}/Ca^{2+} and $^{44}Ca/^{40}Ca$ fractionation during inorganic calcite formation: III. Impact of salinity / ionic strength. Geochim. Cosmochim. Acta 77, 432–443.

Tang Y., Elzinga E. J., Jae Lee Y. and Reeder R. J. (2007) Coprecipitation of chromate with calcite: Batch experiments and X-ray absorption spectroscopy. Geochim. Cosmochim. Acta 71, 1480–1493.

Tarutani T., Clayton R. N. and Mayeda T. K. (1969) The effect of polymorphism and magnesium substitution on oxygen isotope fractionation between calcium carbonate and water. Geochim. Cosmochim. Acta 33, 987–996.

Temmam M., Paquette J. and Vali H. (2000) Mn and Zn incorporation into calcite as a function of chloride aqueous concentration. Geochim. Cosmochim. Acta 64, 2417–2430.

Teng H. H., Dove P. M. and DeYoreo J. J. (2000) Kinetics of calcite growth; surface processes and relationships to macroscopic rate laws. Geochim. Cosmochim. Acta 64, 2255–2266.

Tesoriero A. J. and Pankow J. F. (1996) Solid solution partitioning of Sr^{2+}, Ba^{2+}, and Cd^{2+} to calcite. Geochim. Cosmochim. Acta 60, 1053–1063.

Tomascak P. B., Langmuir C. H., le Roux P. J. and Shirey S. B. (2008) Lithium isotopes in global mid-ocean ridge basalts. Geochim. Cosmochim. Acta 72, 1626–1637.

Tomascak P. B., Magna T. and Dohmen R. (2016) Advances in Lithium Isotope Geochemistry., Springer International Publishing Switzerland.

Trinquier A., Birck J. L. and Allègre C. J. (2008) High-precision analysis of chromium isotopes in terrestrial and meteorite samples by thermal ionization mass spectrometry. J. Anal. At. Spectrom. 23, 1565–1574.

Trotter J., Montagna P., McCulloch M., Silenzi S., Reynaud S., Mortimer G., Martin S., Ferrier-Pagès C., Gattuso J.-P. and Rodolfo-Metalpa R. (2011) Quantifying the pH ‘vital effect’ in the temperate zooxanthellate coral Cladocora caespitosa: Validation of the boron seawater pH proxy. Earth Planet. Sci. Lett. 303, 163–173.

Uchikawa J., Harper D. T., Penman D. E., Zachos J. C. and Zeebe R. E. (2017) Influence of solution chemistry on the boron content in inorganic calcite grown in artificial seawater. Geochim. Cosmochim. Acta 218, 291–307.

Uchikawa J., Penman D. E., Zachos J. C. and Zeebe R. E. (2015) Experimental evidence for kinetic effects on B/Ca in synthetic calcite: Implications for potential $B(OH)_4^-$ and $B(OH)_3$ incorporation. Geochim. Cosmochim. Acta 150, 171–191.

Urey H. C. (1947) The Thermodynamic Properties of Isotopic Substances. J. Chem. Soc., 562–581.

Ushatinskaya G. T. (2008) Origin and Dispersal of the Earliest Brachiopods. Paleontol. J. 42, 776–791.

Veizer J., Ala D., Azmy K., Bruckschen P., Bruhn F., Buhl D., Carden G. A. F., Diener A., Ebneth S., Godderis Y., Jasper T., Korte C., Pawellek F., Podlaha O. G. and Strauss H. (1999) $^{87}Sr/^{86}Sr$, ^{13}C and ^{18}O evolution of Phanerozoic seawater. Chem. Geol. 161, 59–88.

Veizer J., Bruckschen P., Pawellek F., Diener A., Podlaha O. G., Carden G. A. F., Jasper T., Korte C., Strauss H., Azmy K. and Ala D. (1997) Oxygen isotope evolution of Phanerozoic seawater. Palaeogeogr. Palaeoclimatol. Palaeoecol. 132, 159–172.

Veizer J., Fritz P. and Jones B. (1986) Geochemistry of brachiopods: oxygen and carbon isotopic records of Paleozoic oceans. Geochim. Cosmochim. Acta 50, 1679–1696.

Verney-Carron A., Vigier N. and Millot R. (2011) Experimental determination of the role of diffusion on Li isotope fractionation during basaltic glass weathering. Geochim. Cosmochim. Acta 75, 3452–3468.

Vigier N., Decarreau A., Millot R., Carignan J., Petit S. and France-Lanord C. (2008) Quantifying Li isotope fractionation during smectite formation and implications for the Li cycle. Geochim. Cosmochim. Acta 72, 780–792.

Vigier N., Rollion-Bard C., Levenson Y. and Erez J. (2015) Lithium isotopes in foraminifera shells as a novel proxy for the ocean dissolved inorganic carbon (DIC). Comptes Rendus - Geosci. 347, 43–51.

De Vivo B., Maiorani A., Perna G. and Turi B. (1987) Fluid inclusion and stable isotope studies of calcite, quartz and barite from karstic caves in the Masua mine, south-western Sardinia, Italy. Chemie der Erde 46, 259–273.

Voigt M., Mavromatis V. and Oelkers E. H. (2017) The experimental determination of REE partition coefficients in the water-calcite system. Chem. Geol. 462, 30–43.

Vollstaedt H., Eisenhauser A., Wallmann K., Böhm F., Fietzke J., Liebetrau V., Krabbenhöft A., Farkaš J., Tomašových A., Raddatz J. and Veizer J. (2014) The Phanerozoic $\delta^{88/86}$Sr record of seawater: New constraints on past changes in oceanic carbonate fluxes. Geochim. Cosmochim. Acta 128, 249–265.

Wahab R., Ansari S. G., Kim Y. S., Dar M. A. and Shin H. S. (2008) Synthesis and characterization of hydrozincite and its conversion into zinc oxide nanoparticles. J. Alloys Compd. 461, 66–71.

Wallmann K. (2001) Controls on the cretaceous and cenozoic evolution of seawater composition, atmospheric CO_2 and climate. Geochim. Cosmochim. Acta 65, 3005–3025.

Wallmann K. (2004) Impact of atmospheric CO_2 and galactic cosmic radiation on Phanerozoic climate change and the marine δ^{18}O record. Geochemistry, Geophys. Geosystems 5, 1–29.

Wang X. L., Johnson T. M. and Ellis A. S. (2015) Equilibrium isotopic fractionation and isotopic exchange kinetics between Cr(III) and Cr(VI). Geochim. Cosmochim. Acta 153, 72–90.

Wang Y. F. and Xu H. F. (2001) Prediction of trace metal partitioning between minerals and aqueous solutions: A linear free energy correlation approach. Geochim. Cosmochim. Acta 65, 1529–1543.

Watkins J. M., Hunt J. D., Ryerson F. J. and DePaolo D. J. (2014) The influence of temperature, pH, and growth rate on the δ^{18}O composition of inorganically precipitated calcite. Earth Planet. Sci. Lett. 404, 332–343.

Watson E. B. (2004) A conceptual model for near-surface kinetic controls on the trace-element and stable isotope composition of abiogenic calcite crystals. Geochim. Cosmochim. Acta 68, 1473–1488.

Watson E. B. (1996) Surface enrichment and trace-element uptake during crystal growth. Geochim. Cosmochim. Acta 60, 5013–5020.

Watson E. B. and Liang Y. (1995) A simple model for sector zoning in slowly grown crystals: implications for growth rate and lattice diffusion, with emphasis on accessory minerals in crustal rocks. Am. Mineral. 80, 1179–1187.

Wei Y., Chiu S., Tsai H., Yang Y. and Lee J. (2002) Thermal stabilization of chromium(VI) in kaolin. Environ. Sci. Technol. 36, 4633–4641.

White A. F. (1977) Sodium and potassium coprecipitation in aragonite. Geochim. Cosmochim. Acta 41, 687–690.

White A. F. (1978) Sodium Coprecipitation in Calcite and Dolomite. Chem. Geol. 23, 65–72.

White W. B. (1974) The carbonates minerals. In The Infrared Spectra of Minerals (ed. V. C. Farmer). London. pp. 227–284.

Williams P. A. (1990) Oxide Zone Geochemistry., Ellis Horwood Ltd., Chichester, West Sussex, England.

Wombacher F., Eisenhauer A., Böhm F., Gussone N., Regenberg M., Dullo W.-C. and Rüggeberg A. (2011) Magnesium stable isotope fractionation in marine biogenic calcite and aragonite. Geochim. Cosmochim. Acta 75, 5797–5878.

Wombacher F., Eisenhauer A., Heuser A. and Weyer S. (2009) Separation of Mg, Ca and Fe from geological reference materials for stable isotope ratio analyses by MC-ICP-MS and double-spike TIMS. J. Anal. At. Spectrom. 24, 627–636.

Wray J. L. and Daniels F. (1957) Precipitation of Calcite and Aragonite. J. Am. Chem. Soc. 79, 2031–2034.

Wunder B., Meixner A., Romer R. L. and Heinrich W. (2006) Temperature-dependent isotopic fractionation of lithium between clinopyroxene and high-pressure hydrous fluids. Contrib. to Mineral. Petrol. 151, 112–120.

Wunder B., Meixner A., Romer R. L. and Jahn S. (2011) Li-isotope fractionation between silicates and fluids: Pressure dependence and influence of the bonding environment. Eur. J. Mineral. 23, 333–342.

Wynn P. M., Fairchild I. J., Borsato A., Spötl C., Hartland A., Baker A., Frisia S. and Baldini J. U. L. (2018) Sulphate partitioning into calcite: Experimental verification of pH control and application to seasonality in speleothems. Geochim. Cosmochim. Acta 226, 69–83.

Yamaji K., Makita Y., Watanabe H., Sonoda A., Kanoh H., Hirotsu T. and Ooi K. (2001) Theoretical estimation of lithium isotopic reduced partition function ratio for lithium ions in aqueous solution. J. Phys. Chem. 105, 602–613.

Yokoyama Y., Tanaka K. and Takahashi Y. (2012) Differences in the immobilization of arsenite and arsenate by calcite. Geochim. Cosmochim. Acta 91, 202–219.

Yoshimura T., Tamenori Y., Suzuki A., Kawahata H., Iwasaki N., Hasegawa H., Nguyen L. T., Kuroyanagi A., Yamazaki T., Kuroda J. and Ohkouchi N. (2017) Altervalent substitution of sodium for calcium in biogenic calcite and aragonite. Geochim. Cosmochim. Acta 202, 21–38.

Zachariasen W. H. (1933) The Crystal Lattice of Sodium Bicarbonate, $NaHCO_3$. J. Chem. Phys. 1, 634–639.

Zeebe R. E. and Wolf-Gladrow D. (2001) CO_2 in Seawater: Equilibrium, Kinetics, Isotopes. ed. D. Halpern, Elsevier Oceanography Series.

Zheng Y.-F. (2011) On the theoretical calculations of oxygen isotope fractionation factors for carbonate-water systems. Geochem. J. 45, 341–354.

Zheng Y.-F. (1999) Oxygen isotope in carbonate fractionation and sulfate minerals. Geochem. J. 33, 109–126.

Zheng Y.-F. and Böttcher M. E. (2016) Oxygen isotope fractionation in double carbonates. Isotopes Environ. Health Stud. 52, 29–46.

Zhou G.-T. and Zheng Y.-F. (2003) An experimental study of oxygen isotope fractionation between inorganically precipitated aragonite and water at low temperatures. Geochim. Cosmochim. Acta 67, 387–399.

Zhou G.-T. and Zheng Y.-F. (2002) Kinetic mechanism of oxygen isotope disequilibrium in precipitated witherite and aragonite at low temperatures: An experimental study. Geochim. Cosmochim. Acta 66, 63–71.

Zhu, F., Persson, D. and Thierry D. (2001) Formation of Corrosion Products on Open and Confined Metal Surfaces Exposed to Periodic Wet/Dry Conditions—A Comparison between Zinc and Electrogalvanized Steel. Corrosion 57, 582–590.

van Zuilen K., Müller T., Nägler T. F., Dietzel M. and Küsters T. (2016) Experimental determination of barium isotope fractionation during diffusion and adsorption processes at low temp. Geochim. Cosmochim. Acta 186, 226–241.

Appendix A

1/ Frequency scaling procedure to correct the carbonate-vapor fractionation factor

For calcite, a good agreement is observed between calculated frequencies and experimental (Table 2.3) ones. Generally, the calculated frequencies underestimate experiment by a few %, but the relative error is varying depending on the modes.

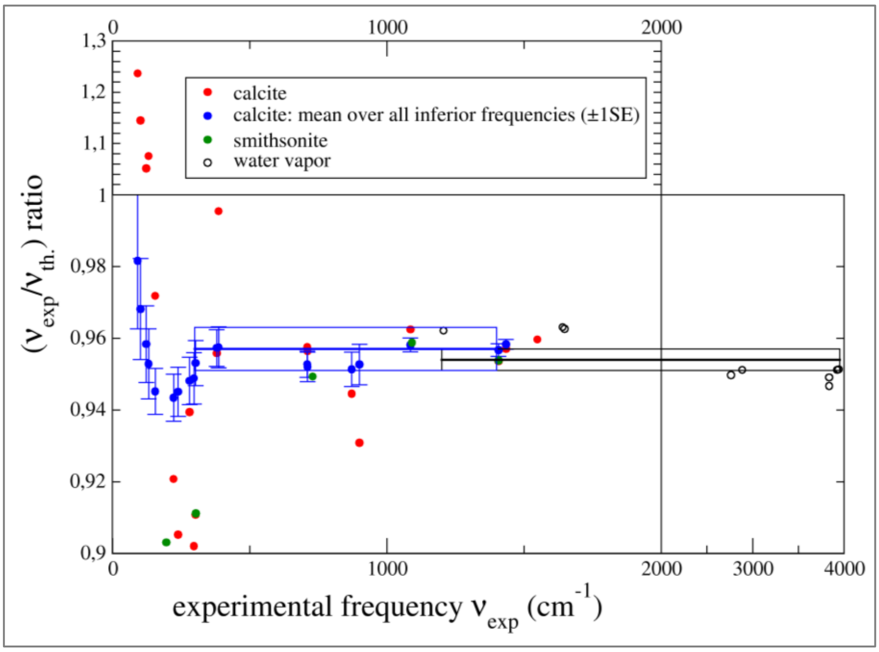

Figure A.1: Ratio between calculated frequencies and their experimental counterpart. Red and green plain circles are the ratios of each mode taken from Table 2.3, for calcite and smithsonite, respectively. Blue symbols are averages of the ratios of calcite over all the modes with frequencies equal or lower than the corresponding experimental frequency. The chosen values for the correction procedure are the blue line (0.957 ± 0.006), for calcite and smithsonite, and the black line (0.954 ± 0.003) for the water molecule (see text for details).

As can be seen on Figure A.1, the four lowest frequencies of calcite (around 100 - 150 cm^{-1}) are significantly overestimated, on the contrary to the rest, and for the above frequencies up to about 300 cm^{-1}, the ratio is varying significantly. Looking at the average ratio, we find 0.982 ± 0.019 (1SE) if we consider all the modes, but 0.957 ± 0.006 (1SE) if we consider only the frequencies higher than 350 cm^{-1}. Since the low frequency modes are not expected to strongly impact fractionation, we will choose this value of 0.957 ± 0.006 (blue box on Figure A.1) to discuss the consequences of this error on the fractionation properties. Also, Figure A.1 suggests no difference between the frequency ratio of calcite and of smithsonite. This is consistent with Schauble et al. 2006 who concluded on the adequacy of a unique scale factor for several anhydrous carbonate minerals.

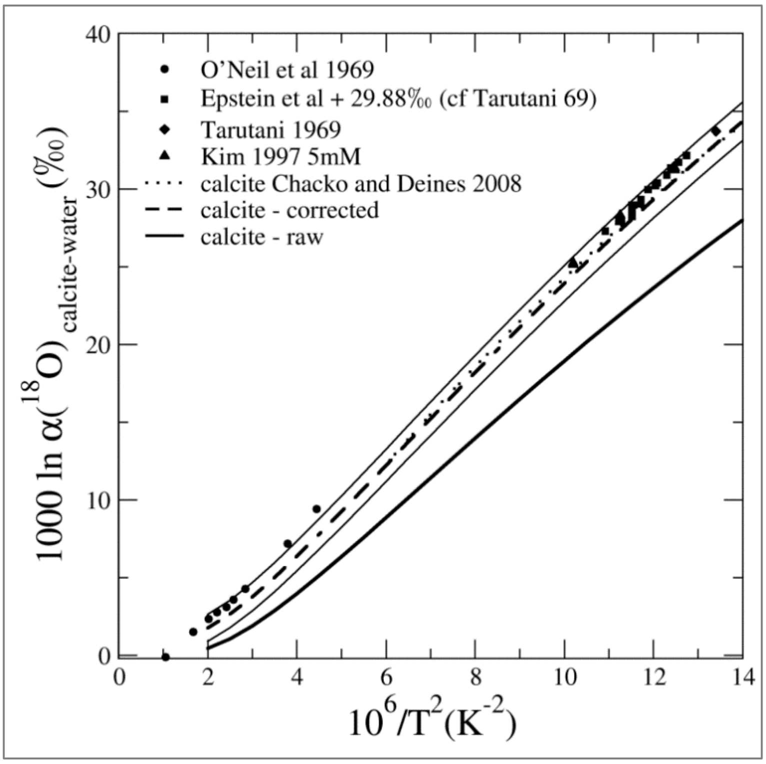

Figure A.2: Oxygen isotope fractionation between calcite and fluid as a function of temperature (this study) compared to previous studies. The two thin plain lines framing the corrected law correspond to the estimated error of this corrected calculation (see text).

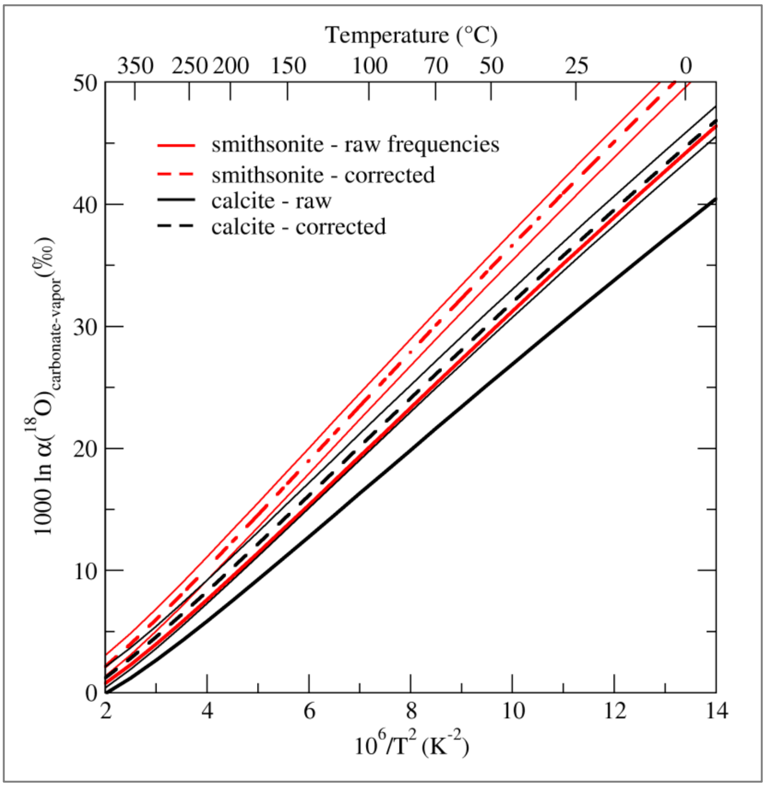

Figure A.3: Calculated fractionation factors between carbonates and an isolated water molecule. Plain line: obtained with the harmonic frequencies calculated from ab initio methods. Dashed line: fractionation factors corrected and their associated error (see text).

The mineral-water vapor fractionation factors, calculated directly from these ab initio-based harmonic frequencies, are shown as a function of temperature on Figure A.3. To correct for the approximations inherent to our methodology, we realized two corrections. First, to correct for the error on harmonic frequencies, we rescaled them. For calcite and smithsonite, the scaling factor considered was 0.957 ± 0.006. For water vapor, based on our previous calculation (see Table 2 of Méheut et al., 2007), we obtain a mean scaling factor of 0.954 ± 0.003 (1SE). Second, to correct for anharmonicity, we added the anharmonic contribution determined by Richet et al. (1977). To obtain a calcite-water law, we combined the calcite-vapor calculation with the experimental liquid-vapor law proposed by Horita and Wesolowski (1994) (Figure A.3). For calcite, the corrected law is in good agreement with both experimental data and previous theoretical studies.

Table A.4: Temperature, pH, pCO_2, alkalinity, duration, added $NaHCO_3$ and $Zn(NO_3)_2$, final $NaHCO_3$ and $Zn(NO_3)_2$ of the experimental solution. $\delta^{18}O$ values of the precipitates and water relative to Vienna Standard Mean Ocean Water (VSMOW). $10^3\ln\alpha(^{18}O)_{precipitate–water}$: Oxygen isotopic fractionation between the precipitate and water.
[1] hydrozincite precipitated at the initial stage of the experiments at 25 °C
s = precipitation of smithsonite by using a stirred reactor.

No.	T (°C)	pH	alkalinity (mmol/L)	pCO_2 (atm)	t (min)	added $NaHCO_3$ (mM)	added $Zn(NO_3)_2$ (mM)	final $NaHCO_3$ (mM)	final $Zn(NO_3)_2$ (mM)	$\delta^{18}O$ precipitate	$\delta^{18}O_{water}$	$10^3\ln\alpha(^{18}O)$ precipitate-water	$\Omega_{precipitate}$
Precursor phase (hydrozincite)													
T25_0[1]	25	6.83	70.0	$10^{-3.4}$	0	199.8	40.94	189.9	5.22	22.75	-9.57	32.11	$10^{7.01}$
Smithsonite (non-stirring)													
T25_1.1	25	5.31	38.6	9.3	465	228.7	43.5	138.4	2.70	19.43	-9.68	28.97	13.49
T25_1.2	25	5.42	51.9	9.5	1160	199.5	44.2	118.9	3.53	20.11	-9.69	29.64	26.30
T25_1.3	25	5.35	42.8	9.5	1410	249.5	43.2	108.2	2.39	20.49	-9.62	29.95	13.80
T25_1.4	25	5.46	56.0	9.8	4485	199.6	42.1	107.0	0.97	21.24	-9.63	30.69	8.32
T25_1.5	25	5.41	49.3	9.3	10050	201.4	42.8	117.0	0.53	20.77	-9.72	30.32	3.80
T25_1.6	25	5.40	48.0	9.5	20150	199.4	43.2	118.9	0.47	20.74	-9.68	30.26	3.24
T25_1.7	25	5.48	58.5	9.3	30270	202.0	42.8	201.2	0.23	20.87	-9.66	30.36	2.09
T25_1.8	25	5.39	46.1	9.8	58790	201.2	43.0	101.8	0.27	21.05	-9.53	30.41	1.74
T25_1.9	25	5.38	38.0	9.9	72620	207.7	44.2	97.2	0.21	21.06	-9.61	30.50	1.05
T40_1	40	5.32	30.9	9.5	24240	98.1	21.8	140.8	0.48	17.93	-9.53	27.35	3.89
T40_2	40	5.54	54.3	10	4125	199.8	39.1	109.6	0.40	18.09	-9.31	27.28	6.17
T60_1	60	5.50	37.6	10.5	18815	100.2	20.0	163.4	0.33	14.41	-9.43	23.79	7.24
T60_2	60	5.06	13.0	11	26930	103.0	21.1	61.6	0.43	14.23	-10.14	24.32	2.14
T80	80	5.48	29.1	12.9	10035	100.0	21.0	81.9	0.36	12.22	-9.19	21.38	10.96
Smithsonite (stirring)													
T25s_1.1	25	5.61	81.6	9.3	490	226.4	36.9	201.3	4.40	21.06	-9.55	30.44	57.54
T25s_1.2	25	5.51	64.4	9.1	930	188.5	39.8	200.6	4.56	20.6	-9.58	30.02	44.67
T25s_1.3	25	5.45	55.8	9.1	1345	170.1	39.8	204.5	4.94	19.99	-9.67	29.51	39.81
T25s_1.4	25	5.40	48.9	8.9	4490	179.0	38.5	197.7	4.12	20.14	-9.66	29.64	28.18
T25s_1.5	25	5.38	46.5	8.9	10170	166.4	39.5	202.4	4.25	19.87	-9.62	29.34	26.92
T25s_1.6	25	5.43	51.1	9.1	20040	202.1	39.9	111.6	0.50	19.84	-9.66	29.35	3.80

Appendix B

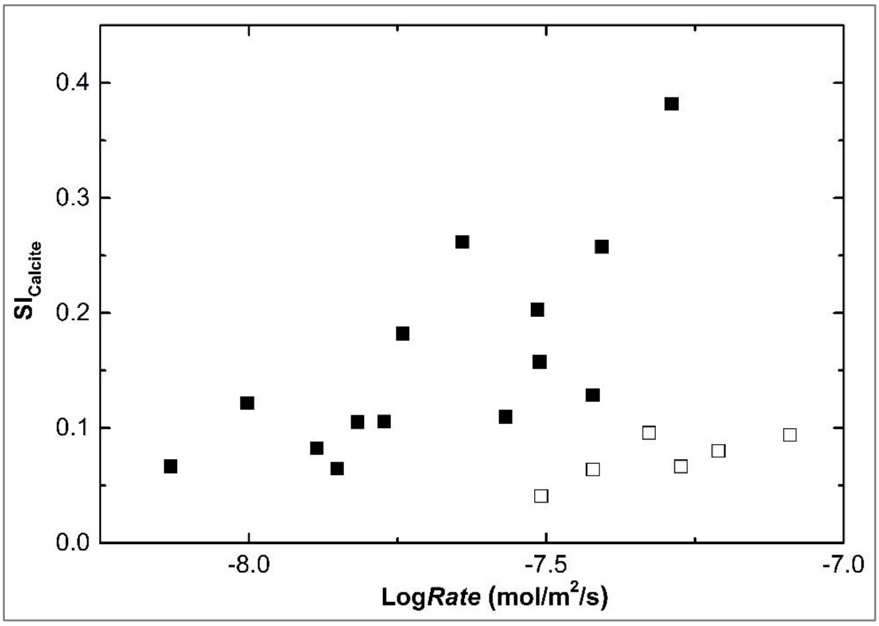

Figure B.1: Calcite growth rate as a function of the saturation degree of the fluid with respect to this mineral phase for experiments conducted in the range 8.0 ≤ pH ≤ 8.3. As it can be seen two distinct trends can be recognised, closed rectangulars are experiments conducted with inflow rate of ~10 mL/day and open symbols experiments conducted with inflow rate of ~20 mL/day.

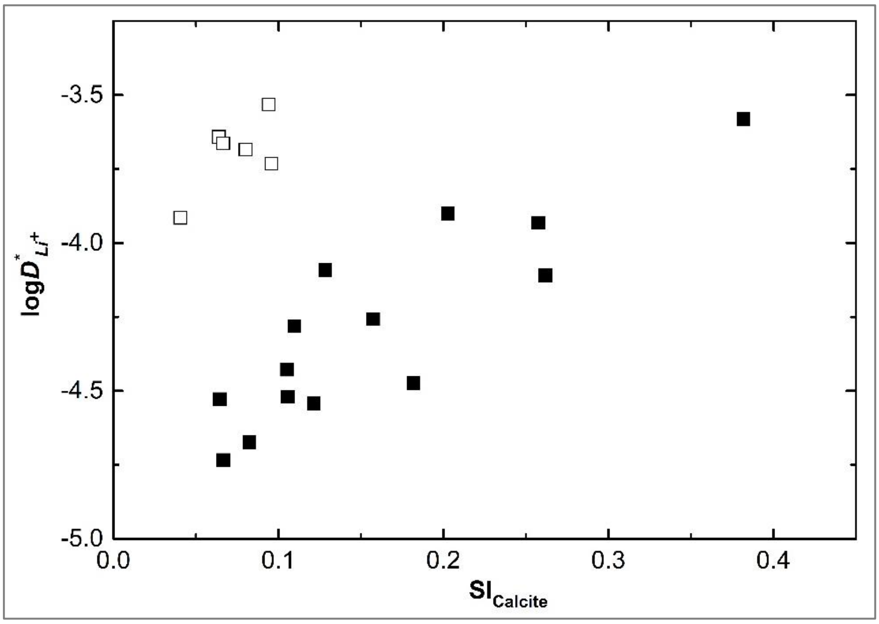

Figure B.2: Apparent partition coefficient of Li as a function of the saturation degree of the fluid with respect to this mineral phase for experiments conducted in the range 8.0 ≤ pH ≤ 8.3. As it can be seen two distinct trends can be recognised, closed rectangulars are experiments conducted with inflow rate of ~10 mL/day and open symbols experiments conducted with inflow rate of ~20 mL/day.

Table B.3: Molar concentrations of aqueous species calculated using PHREEQC software together with its Minteq.v4 database and saturation index of the reactive fluid with respect to calcite.

experiment	**Ca^{2+}**	**$CaCO_3^o$**	**$CaHCO_3^+$**	**$CaOH^+$**	**Na^+**	**$NaCO_3^-$**
2_30	1.10E-03	6.92E-06	1.21E-05	1.68E-08	3.00E-01	7.81E-05
2_40	3.77E-04	5.47E-06	5.15E-06	1.07E-08	3.02E-01	1.81E-04
2_50	1.33E-03	6.72E-06	1.35E-05	1.77E-08	2.99E-01	6.24E-05
2_60	1.35E-03	7.98E-06	1.46E-05	1.96E-08	2.99E-01	7.33E-05
2_70	1.67E-03	9.57E-06	1.68E-05	2.55E-08	2.98E-01	7.08E-05
2_80	7.65E-04	6.15E-06	8.37E-06	1.51E-08	3.00E-01	9.99E-05
2_90	1.59E-03	8.39E-06	1.61E-05	2.22E-08	2.99E-01	6.51E-05
2_100	1.30E-03	6.11E-06	1.23E-05	1.73E-08	2.99E-01	5.82E-05
3_25	8.77E-04	6.29E-06	9.60E-06	1.54E-08	3.00E-01	8.90E-05
3_30	1.02E-03	6.64E-06	1.06E-05	1.71E-08	3.00E-01	8.05E-05
3_40	1.71E-03	6.82E-06	1.57E-05	1.98E-08	2.98E-01	4.92E-05
3_50	1.28E-03	7.51E-06	1.29E-05	2.00E-08	2.99E-01	7.27E-05
3_60	1.31E-03	7.04E-06	1.26E-05	1.96E-08	2.99E-01	6.64E-05
3_70	1.83E-03	9.48E-06	1.70E-05	2.73E-08	2.98E-01	6.40E-05
3_80	9.70E-04	6.11E-06	1.12E-05	1.42E-08	3.00E-01	7.82E-05
3_100	2.08E-03	1.26E-05	1.96E-05	3.57E-08	2.97E-01	7.41E-05
5_40	1.38E-03	5.84E-06	1.59E-05	1.37E-08	2.99E-01	5.22E-05
5_50	1.46E-03	6.18E-06	1.80E-05	1.35E-08	2.99E-01	5.22E-05
5_60	1.46E-03	6.62E-06	1.68E-05	1.55E-08	2.99E-01	5.59E-05
5_70	1.69E-03	6.23E-06	1.94E-05	1.45E-08	2.98E-01	4.55E-05
5_80	1.25E-03	5.37E-06	1.49E-05	1.20E-08	2.99E-01	5.33E-05
5_90	4.50E-03	9.55E-06	4.41E-05	2.61E-08	2.92E-01	2.57E-05
5_100	2.19E-03	6.65E-06	2.33E-05	1.68E-08	2.97E-01	3.73E-05
7_25	9.49E-05	4.45E-06	3.91E-07	2.90E-08	3.02E-01	5.84E-04
7_50	1.07E-04	4.46E-06	5.66E-07	2.25E-08	3.02E-01	5.21E-04
7_100	1.33E-04	5.55E-06	5.46E-07	3.60E-08	3.01E-01	5.21E-04
12_60	8.45E-03	4.64E-06	8.17E-04	1.29E-09	3.00E-01	6.89E-06
12_70	6.81E-03	4.16E-06	6.53E-04	1.17E-09	3.04E-01	7.74E-06
12_80	1.11E-02	6.50E-06	1.10E-03	1.77E-09	2.95E-01	7.27E-06
12_100	8.62E-03	5.28E-06	8.89E-04	1.38E-09	3.01E-01	7.73E-06
13_60	3.08E-03	6.21E-06	8.26E-05	6.20E-09	2.99E-01	2.49E-05
13_70	3.47E-03	7.83E-06	8.67E-05	8.39E-09	2.98E-01	2.79E-05
13_80	2.99E-03	8.36E-06	9.05E-05	7.40E-09	3.00E-01	3.48E-05
13_100	3.01E-03	6.19E-06	7.69E-05	6.51E-09	2.99E-01	2.54E-05

Table B.3 (continued): Molar concentrations of aqueous species calculated using PHREEQC software together with its Minteq.v4 database and saturation index of the reactive fluid with respect to calcite.

experiment	$NaHCO_3^o$	Li^+	CO_3^{2-}	HCO_3^-	$SI_{calcite}$
2_30	1.86E-04	3.46E-04	4.76E-05	2.09E-03	0.07
2_40	2.32E-04	3.45E-04	1.10E-04	2.58E-03	0.12
2_50	1.71E-04	3.54E-04	3.81E-05	1.92E-03	0.04
2_60	1.83E-04	3.48E-04	4.48E-05	2.06E-03	0.11
2_70	1.69E-04	3.48E-04	4.34E-05	1.90E-03	0.18
2_80	1.85E-04	3.48E-04	6.07E-05	2.07E-03	0.26
2_90	1.70E-04	3.47E-04	3.98E-05	1.92E-03	0.08
2_100	1.59E-04	3.47E-04	3.56E-05	1.79E-03	0.20
3_25	1.85E-04	3.40E-04	5.41E-05	2.07E-03	0.06
3_30	1.75E-04	3.50E-04	4.91E-05	1.96E-03	0.08
3_40	1.54E-04	3.47E-04	3.01E-05	1.74E-03	0.11
3_50	1.69E-04	3.45E-04	4.44E-05	1.90E-03	0.11
3_60	1.62E-04	3.46E-04	4.06E-05	1.82E-03	0.16
3_70	1.56E-04	3.42E-04	3.92E-05	1.76E-03	0.13
3_80	1.95E-04	3.50E-04	4.76E-05	2.19E-03	0.26
3_100	1.57E-04	3.43E-04	4.55E-05	1.78E-03	0.38
5_40	1.93E-04	4.07E-04	3.19E-05	2.17E-03	0.04
5_50	2.06E-04	4.08E-04	3.19E-05	2.32E-03	0.06
5_60	1.93E-04	4.08E-04	3.42E-05	2.17E-03	0.10
5_70	1.93E-04	4.08E-04	2.78E-05	2.17E-03	0.07
5_80	2.01E-04	4.04E-04	3.25E-05	2.26E-03	0.08
5_90	1.61E-04	4.21E-04	1.61E-05	1.85E-03	0.25
5_100	1.77E-04	4.08E-04	2.29E-05	2.00E-03	0.09
7_25	6.98E-05	3.21E-04	3.54E-04	7.78E-04	0.09
7_50	8.98E-05	3.17E-04	3.15E-04	1.00E-03	0.16
7_100	6.98E-05	3.15E-04	3.16E-04	7.78E-04	0.18
12_60	1.63E-03	2.44E-04	4.20E-06	1.84E-02	0.06
12_70	1.63E-03	2.56E-04	4.67E-06	1.82E-02	0.11
12_80	1.64E-03	2.77E-04	4.51E-06	1.89E-02	0.09
12_100	1.75E-03	2.39E-04	4.70E-06	1.97E-02	0.10
13_60	4.50E-04	2.43E-04	1.53E-05	5.08E-03	0.06
13_70	4.18E-04	2.53E-04	1.71E-05	4.74E-03	0.16
13_80	5.10E-04	2.25E-04	2.12E-05	5.74E-03	0.19
13_100	4.28E-04	2.42E-04	1.56E-05	4.83E-03	0.16

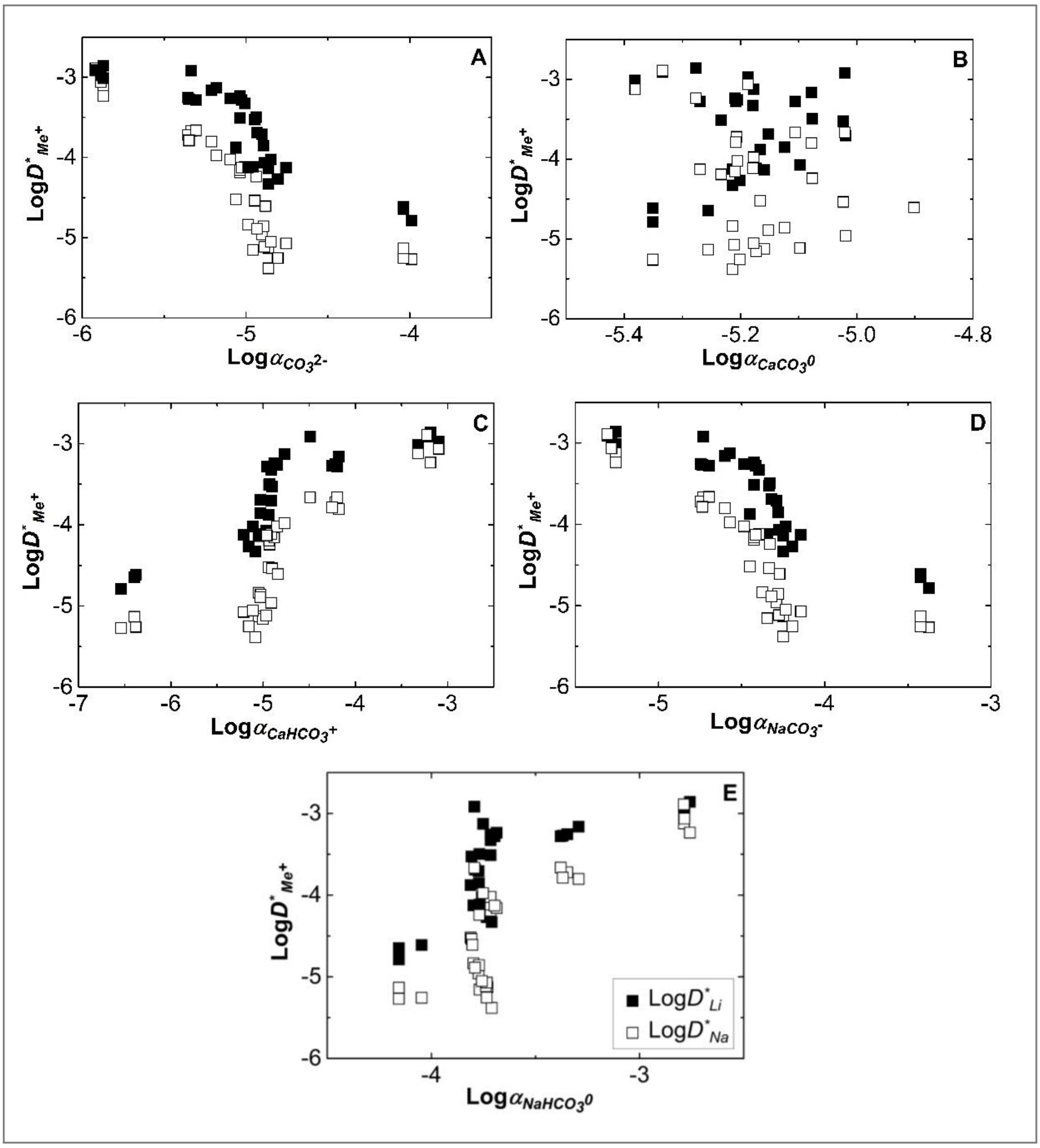

Figure B.4: Apparent partition coefficient of Li and Na in calcite and reactive fluid plotted as a function of activity of aqueous (A) CO_3^{2-} (aq), (B) $CaCO_3^{o}$ (aq), (C) $CaHCO_3^{-}$ (aq), (D) $NaCO_3^{-}$ (aq) and (E) $NaHCO_3^{o}$ (aq).

Appendix C

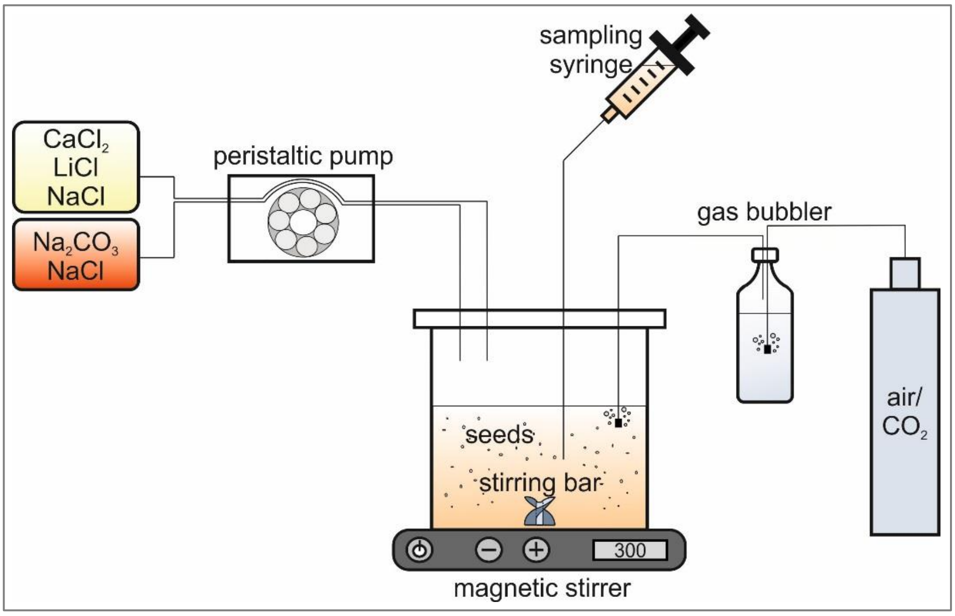
sampling syringe
$CaCl_2$
LiCl
NaCl
peristaltic pump
Na_2CO_3
NaCl
gas bubbler
air/
CO_2
seeds
stirring bar
300
magnetic stirrer

Figure C.1: Experimental set-up for the calcite growth experiments.

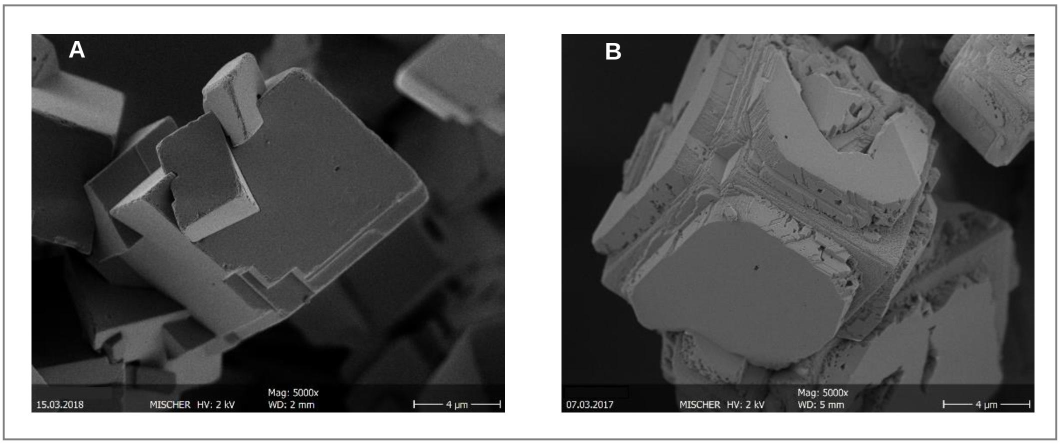
A
15.03.2018
MISCHER HV: 2 kV
Mag: 5000x
WD: 2 mm
4 µm
B
07.03.2017
MISCHER HV: 2 kV
Mag: 5000x
WD: 5 mm
4 µm

Figure C.2: Scanning Electron Microphotographs of (A) calcite seeds used for the calcite growth experiments and (B) final overgrow precipitates (Experiment CaLi3_25).

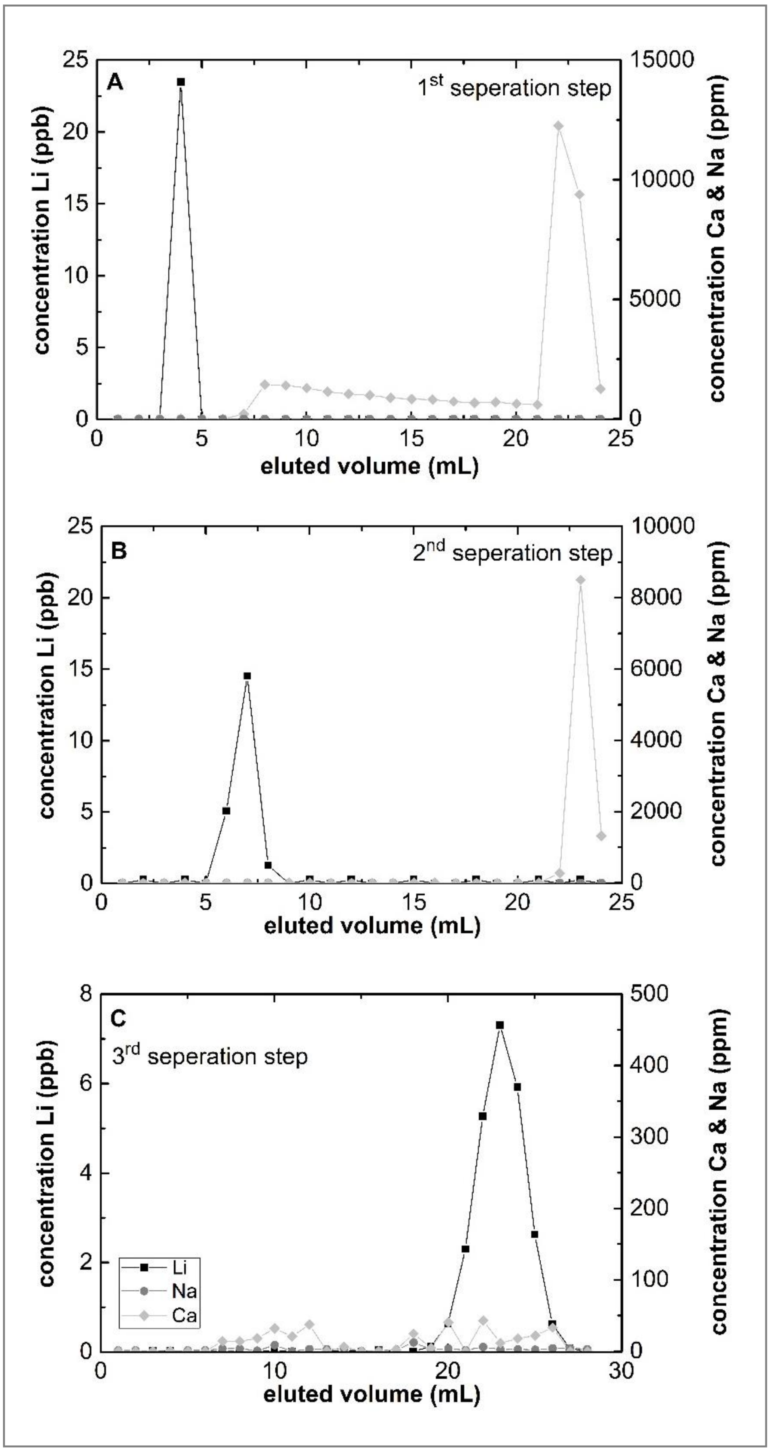

Figure C.3: Three step separation chemistry of the solids (A) Li & Na seperation - 1st step; (B) Li & Na seperation - 2nd step; and (C) Li seperation – 3rd step.

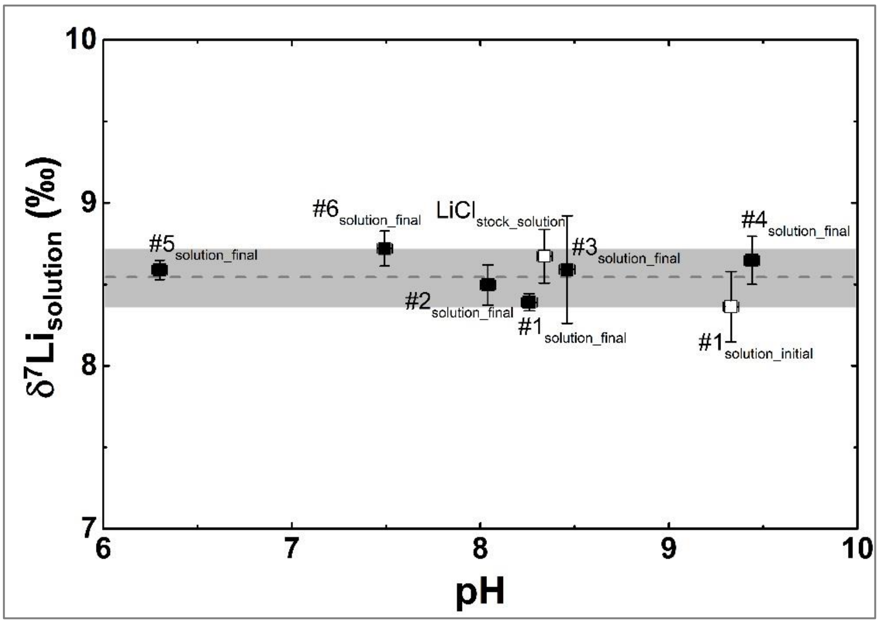

Figure C.4: The δ^{7}Li$_{solution}$ values of the LiCl stock solution, initial solution and the final solutions at different pH values and different calcite growth rates for experiments conducted at 25 °C. Analytical errors of the pH are within the symbols.

Appendix D

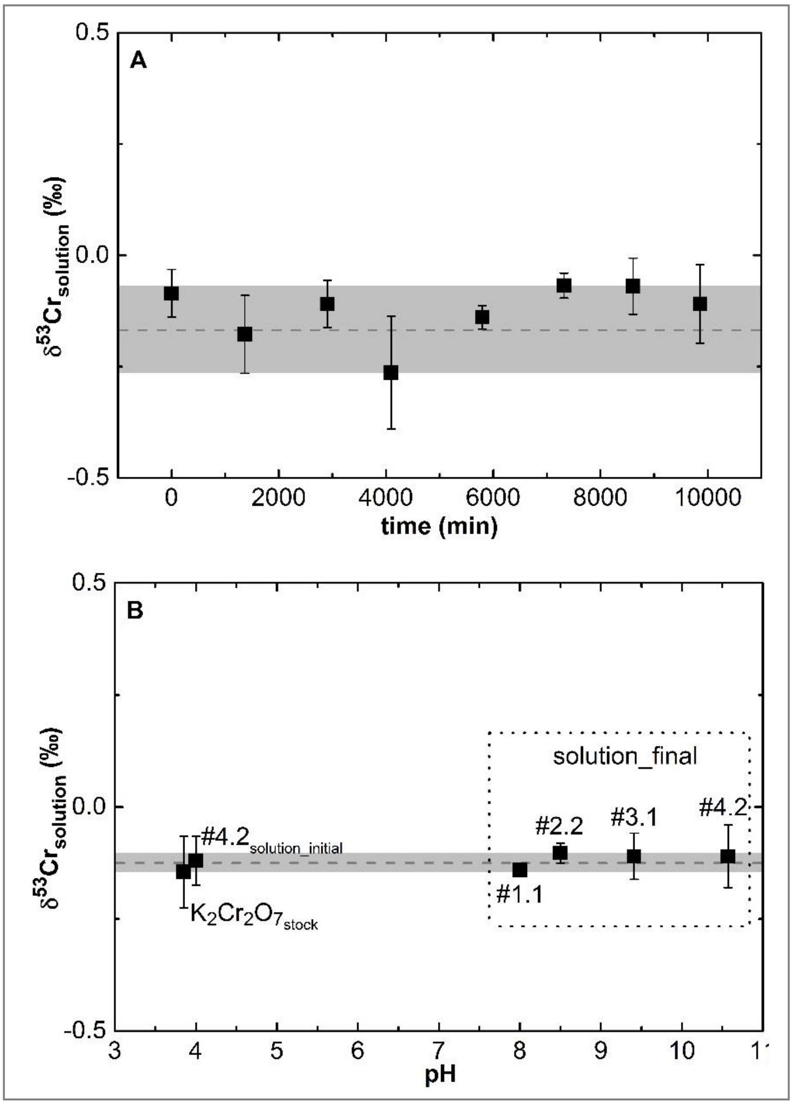

Figure D.1: The measured $\delta^{53}Cr_{solution}$ values for experiments conducted at 25 °C and constant growth rate (~$10^{-7.7}$ mol m^{-2} s^{-1}): (A) temporal evolution of solutions for experiments #4.2; (B) $K_2Cr_2O_{7stock}$, #4.2$_{solution\_initial}$ and final experimental solution at different pH values (see Table 5.1). Analytical uncertainty is included in the symbol size.

Table D.2: Calculated concentrations from geochemical modelling for HCO_3^-, CO_3^{2-}, $CaCrO_4^0$, $KCrO_4^-$, CrO_4^{2-} and Ca^{2+} in mM.

Exp	HCO_3^-	CO_3^{2-}	$CaCrO_4^0$	$KCrO_4^-$	CrO_4^{2-}	Ca^{2+}
#1.1	2.49	0.03	7.89	20.71	21.81	6.99
#1.2	2.4	0.03	7.38	20.69	21.92	6.47
#2.1	1.51	0.05	3.31	23.91	22.45	2.89
#2.2	1.44	0.06	3.42	23.36	22.53	2.95
#3.1	0.53	0.14	2.74	23.38	23.24	2.27
#3.2	0.49	0.14	2.62	23.18	23.06	2.18
#4.1	0.05	0.16	2.76	23.37	22.94	2.33
#4.2	0.04	0.15	2.22	23.48	23.28	1.83

Appendix E

E.1 Curriculum Vitae

Anja Füger was born on April 13th 1988 in Karlsruhe, Germany. She attended high school at the Helmholtz Gymnasium from which she graduated 2007. After four semesters studying Mathematics at the Ruprecht-Karls-University in Heidelberg and Chemistry at the Institute of Technology in Karlsruhe, she enrolled for studying Applied Earth Science at the Institute of Technology in Karlsruhe. After finishing her Bachelor degree in 2011 she enrolled for the Master in Applied Earth Science at the Institute of Technology in Karlsruhe specializing Hydrogeology, Geochemistry and Hydro-geochemistry, which she finished in 2015. During her study period she was working as student assistant at the hydrogeology company hydrag in Karlsruhe. In the same year she started working at the JR-AquaConSol GmbH in collaboration with the Graz University of Technology as part of the Doctoral School of Geoscience within the BASE-LiNE Earth project, an initiative funded by Marie Skłodowska-Curie Horizon 2020 'European Union Funding Programme for Research and Innovation' Project.

E.2 Publications

Oxygen isotope fractionation during smithsonite formation from aqueous solutions
A. Füger, M. Méheut, V. Mavromatis, A. Leis, M. Dietzel
Chemical Geology (2018), Vol. 495, pp. 76-89.

Effect of growth rate and pH on lithium incorporation in calcite
A. Füger, F. Konrad, A. Leis, M. Dietzel, V. Mavromatis
Geochimica et Cosmochimica Acta (2019), Vol. 248, pp. 14-24.

The role of growth rate and pH on lithium isotope fractionation during its incorporation in calcite
A. Füger, M. Kuessner, C. Rollion-Bard, A. Leis, M. Dietzel, V. Mavromatis

The role of pH on chromium partitioning and isotopic fractionation during its incorporation in calcite
A. Füger, S. Bruggmann, R. Frei, A. Leis, M. Dietzel, V. Mavromatis
(under review)

E.3 Conference Distribution

BASE-LiNE Earth Workshop 2015, Kiel, Germany

EGU 2016, Vienna, Austria (Poster)
A. Füger, M. Méheut, V. Mavromatis, A. Leis and M. Dietzel *Stable oxygen isotope fractionation between smithsonite and fluid in the temperature range 25 and 80 °C*

BASE-LiNE Earth Workshop 2016, Prague, Czech Republic (Presentation)
A. Füger, V. Mavromatis, A. Leis and M. Dietzel *Calibration of elemental and isotope proxies by inorganic precipitation experiments*

EGU 2017, Vienna, Austria (Poster)
A. Füger, V. Mavromatis, F. Konrad, A. Leis and M. Dietzel *Control of growth rate on Li/Ca ratio of calcite - An experimental approach*

Goldschmidt 2017, Paris, France (Poster)
A. Füger, V. Mavromatis, F. Konrad, A. Leis and M. Dietzel *Mechanisms controlling lithium incorporation in calcite - an experimental approach*

BASE-LiNE Earth Workshop 2017, Graz, Austria (Presentation)
A. Füger, V. Mavromatis, A. Leis and M. Dietzel *Control Of Growth Rate On Li/Ca Values During The Growth Of Calcite – An Experimental Approach*

EGU 2018, Vienna, Austria (Poster)
A. Füger, S. Bruggmann, R. Frei, A. Leis, M. Dietzel and V. Mavromatis *Effect of pH on chromate incorporation during the growth of calcite*

BASE-LiNE Earth Workshop 2018, Milan, Italy
A. Füger, V. Mavromatis, A. Leis and M. Dietzel *Calibration of elemental and isotope proxies by inorganic precipitation experiments*

Brachiopod-conference 2018, Milan, Italy (Poster)
A. Füger, M. Kuessner, C. Rollion-Bard, F. Konrad, A. Leis, M. Dietzel and V. Mavromatis *Mechanisms controlling lithium incorporation and lithium isotopes in calcite - An experimental approach*

SINA Meeting 2018, Graz, Austria (Presentation)
A. Füger, M. Méheut, V. Mavromatis, A. Leis and M. Dietzel *Oxygen Isotope Fractionation During Smithsonite Formation From Aqueous Solutions*

SINA Meeting 2018, Graz, Austria (Poster)
A. Füger, M. Kuessner, C. Rollion-Bard, F. Konrad, A. Leis, M. Dietzel and V. Mavromatis *Mechanisms controlling lithium incorporation and lithium isotopes in calcite - An experimental approach*

E.4 BASE-LiNE Earth - Secondments

19.06.2017 – 07.07.2017 & 29.01.2018 – 16.02.2018	Collaboration at the Institute de Physique du Globe de Paris in collaboration with Dr. Claire Rollion-Bard and Marie Kuessner. Separation of lithium in inorganic calcite samples and measurement of lithium isotopes with a Neptun Thermo Scientific Multicollector Inductively Coupled Plasma Mass Spectrometer (MC-ICP-MS).
19.02.2018 – 02.03.2018	Collaboration at the University of Copenhagen - Department of Geosciences and Natural Resource Management with Prof. Dr. Robert Frei and Sylvie Bruggmann. Separation of chromium in inorganic calcite samples and measurement of chromium isotopes with a IsotopX Phoenix Thermal Ionization Mass Spectrometer (TIMS).